

Nonlinear electro-mechanical coupling and thermally stimulated currents in relaxor ferroelectrics

Présentée le 6 mai 2022

Faculté des sciences et techniques de l'ingénieur
Groupe SCI STI DD
Programme doctoral en science et génie des matériaux

pour l'obtention du grade de Docteur ès Sciences

par

Lukas RIEMER

Acceptée sur proposition du jury

Dr A. Hessler-Wyser, présidente du jury
Prof. D. Damjanovic, directeur de thèse
Prof. C. A. Randall, rapporteur
Prof. K. G. Webber, rapporteur
Dr I. Stolichnov, rapporteur

Acknowledgments

Above all, I would like to thank my supervisor Prof. Dragan Damjanovic for giving me the opportunity to pursue a Ph.D. with him in the Group for Ferroelectrics and Functional Oxides at EPFL. My greatest appreciation for sharing his passion for science, answering my questions, trusting my work, continuously supporting me, and for his generosity. It was a great pleasure to discuss results and to spend time in the lab with him. Thank you, Dragan.

I would like to thank the members of the jury of my doctoral exam Prof. Clive A. Randall, Prof. Kyle G. Webber, and Dr. Igor Stolichnov for their valuable time, their motivating lectures, and their inspiring talks.

Many thanks to Prof. Andrew Bell, Prof. Brahim Dkhil, Dr. Hana Uršič and Liu for providing PMN single crystals and ceramics and the insightful discussions of results.

I would like to thank Prof. Jürgen Rödel for sparking my interest in ferroelectrics and the opportunity to perform diffraction experiments at the Technical University of Darmstadt.

I would like to thank Prof. Tadej Rojac for hosting me at the Electronics Ceramics Department at Jožef Stefan Institute in Ljubljana for sharing his expertise about electromechanical characterization and his passion for science.

I would like to thank Prof. Thomas Shrout for providing single crystals used in this work.

I would like to thank Prof. Nazanin Bassiri-Gharb for supporting my candidature as IEEE Student Representative for Ferroelectrics.

I would like to thank Prof. Shujun Zhang for welcoming me at the Institute for Superconducting and Electronic Materials at the Australian Institute for Innovative Materials in Wollongong, for insightful discussions about single crystal growth and domain structures.

I would like to thank Ms. Sandra Roux for her kind support during the last weeks of this work.

My sincere gratitude goes to Mr. Pierre-André Despont and the team of the Atelier de l'Institut des Matériaux at EPFL for our discussions and the fabrication of experimental setups. Many ex-

Acknowledgements

perimental results of this thesis would not have been possible without their valuable contribution.

I would like to thank Dr. Stuart Burns for the shared time as Student Representatives and for welcoming me in Sydney.

I would like to thank Ms. Yuko Kagata and Mr. Enrico Colla for administrative and technical support.

I would like to thank Dr. Robin Nigon for sharing his expertise and for his helpfulness in the lab.

I would like to thank my colleagues, Dr. Milica Vasiljevic, Dr. Kanghyun Chu, Dr. Ramin Matloub, Dr. Mahmoud Hadad, and Dr. Daesung Park for their shared knowledge, technical support, lessons learned, and free time activities.

I would like to acknowledge the help from Ms. Barbara Althaus, Ms. Kristin Andrikopoulus, Ms. Sylvia Goetze Wake, and Ms. Jayshri Mizeret-Lad from the Language Centre at EPFL over the years.

I would like to thank Ms. An-Phuc Hoang for her outstanding support. Without you, this would not have been possible.

I am deeply indebted to Ms. Maria Magarita Ariza for her tremendous emotional support, for continuously offering help, and for my personal pink coloured pen used for proofreading this thesis.

I would like to thank Dr. Malte Oppermann for his remarks and his friendship. My time in Lausanne would not have been the same without you.

I would like to thank Dr. Giulia Bini, Dr. Jessica Pidoux and Ms. Judith Riemer for reviewing parts of the manuscript.

I would like to thank Mr. Jorge Andres Madrid for his passion for words and for sharing it with me.

I was exceptionally fortunate to meet Mr. Sergio Daniel Hernandez. Thank you for including me into the Colombo-Austrian empire.

I deeply thank Dr. Louis, Mr. Gabriel Laupré, Ms. Aysu Ceren Okur, Ms. Alice Comberlato, Ms. Sarah, Mr. Johannes Hentschel, Mr. Timo Schuler, and Dr. Simon Dumas Primbault for shared free time activities.

I would like to thank my family for continued support and love, and for the privilege to explore the world.

Lausanne, 27 February 2022

Lukas M. Riemer

Abstract

In this work, the emergence of polarization and electro-mechanical coupling in $\text{Pb}(\text{Mg}_{1/3}\text{Nb}_{2/3})\text{O}_3$ and $\text{Pb}(\text{Mg}_{1/3}\text{Nb}_{2/3})\text{O}_3 - \text{PbTiO}_3$ was investigated using thermally stimulated current, and nonlinear dielectric and electro-mechanical measurements. The presence of complex time-dependent and interrelated mechanisms, and their influence on macroscopic functional properties was demonstrated. Widely accepted interpretations related to the nature of relaxor ferroelectrics were questioned.

Persistent macroscopic polarization in the nominally ergodic and centrosymmetric relaxor state of pristine $\text{Pb}(\text{Mg}_{1/3}\text{Nb}_{2/3})\text{O}_3$ single crystals was revealed by dynamic pyroelectric measurements. Annealing experiments below and above the Burns temperature, T_B , related this polarization then to the presence of nano-sized polar entities. Poling experiments of $\text{Pb}(\text{Mg}_{1/3}\text{Nb}_{2/3})\text{O}_3$ associated a maximum in the electric-field dependent nonlinear dielectric permittivity and an attendant anomaly in the second harmonic polarization response to the reorientation of nano-sized polar entities.

In the following, changes in the polar structure of $\text{Pb}(\text{Mg}_{1/3}\text{Nb}_{2/3})\text{O}_3$ were characterized *in-situ* with thermally stimulated depolarization current measurements. It was shown that electrical or mechanical poling can induce anomalies at temperatures related to static and dynamic nano-sized polar regions. An aging effect was revealed with dynamic dielectric and thermally stimulated current measurements. A current reversal was observed around the coherence temperature in electrical poled and unpoled aged samples, suggesting a direct or indirect correlation between oxygen vacancies and nano-sized polar regions.

Based on these observations, the effect of aging on macroscopic functional properties was investigated in $\text{Pb}(\text{Mg}_{1/3}\text{Nb}_{2/3})\text{O}_3 - \text{PbTiO}_3$ utilizing thermally stimulated depolarization current, and dielectric and electro-mechanical measurements. For this purpose, the response of unpoled, direct current poled and alternating current poled samples was compared for annealed and aged samples. Aging was related to reduced piezoelectric properties and depolarization temperatures. An apparent contradicting duality of polarization stabilization and property enhancement was observed for alternating current poling. It was proposed that the applied bipolar poling field leads to a distribution of oriented defect clusters throughout the volume, which could improve dielectric and piezoelectric properties through locally broken symmetry and mediated reversible polarization rotation.

The existence of an ergodic relaxor state and the model of a single polar entity below T_B are not consistent with the results presented in this work. It is proposed that functional and structural properties of undoped $\text{Pb}(\text{Mg}_{1/3}\text{Nb}_{2/3})\text{O}_3$ and undoped $\text{Pb}(\text{Mg}_{1/3}\text{Nb}_{2/3})\text{O}_3 - \text{PbTiO}_3$

Acknowledgements

are considerably affected by defect structures, which depend on the thermal, electric field, and mechanical field history, and on time. It was speculated that the multitude of sometimes contradicting experimental results reported in the literature are related to these findings. The outcomes of this work are expected to further the fundamental understanding of relaxor ferroelectrics and to contribute to an enhanced reproducibility of experimental results found in the literature.

Key words: relaxor, ferroelectrics, dielectric, piezoelectric, defects, lead magnesium niobate, alternating current poling, single crystal

Zusammenfassung

In dieser Arbeit wurde das Auftreten von Polarisation und elektromechanischer Kopplung in $\text{Pb}(\text{Mg}_{1/3}\text{Nb}_{2/3})\text{O}_3$ und $\text{Pb}(\text{Mg}_{1/3}\text{Nb}_{2/3})\text{O}_3 - \text{PbTiO}_3$ mittels thermisch stimuliertem Strom und nichtlinearen dielektrischen und elektromechanischen Messungen untersucht. Das Vorhandensein komplexer zeitabhängiger und miteinander verbundener Mechanismen und deren Einfluss auf die makroskopischen Funktionseigenschaften wurde nachgewiesen. Weithin akzeptierte Interpretationen in Bezug auf die Natur von Relaxor-Ferroelektrika wurden in Frage gestellt.

Durch dynamische pyroelektrische Messungen wurde eine anhaltende makroskopische Polarisation im nominell ergodischen und zentrosymmetrischen Relaxor-Zustand von unberührten $\text{Pb}(\text{Mg}_{1/3}\text{Nb}_{2/3})\text{O}_3$ -Einkristallen nachgewiesen. Glühexperimente unterhalb und oberhalb der Burns-Temperatur bezogen diese Polarisation auf das Vorhandensein von polaren Einheiten in Nanogröße. Polungsexperimente an $\text{Pb}(\text{Mg}_{1/3}\text{Nb}_{2/3})\text{O}_3$ brachten ein Maximum in der vom elektrischen Feld abhängigen nichtlinearen dielektrischen Permittivität und eine damit einhergehende Anomalie mit der Reorientierung diesen polaren Einheiten in Verbindung.

Im Folgenden wurden Veränderungen in der polaren Struktur von $\text{Pb}(\text{Mg}_{1/3}\text{Nb}_{2/3})\text{O}_3$ *in-situ* mit thermisch stimulierten Depolarisationsstrommessungen charakterisiert. Es wurde gezeigt, dass Anomalien durch elektrisches oder mechanisches Polen bei Temperaturen induziert werden können, die mit statischen und dynamischen nanogroßen Regionen zusammenhängen. Ein Alterungseffekt wurde mit dynamischen dielektrischen und thermisch stimulierten Strommessungen aufgedeckt. Eine Stromumkehr wurde um die Kohärenztemperatur in elektrisch polarisierten und unpolarisierten gealterten Proben beobachtet, was auf eine direkte oder indirekte Korrelation zwischen Sauerstoffleerstellen und polaren Regionen in Nanogröße hindeutet.

Auf der Grundlage dieser Beobachtungen wurde die Auswirkung der Alterung auf die makroskopischen funktionellen Eigenschaften von $\text{Pb}(\text{Mg}_{1/3}\text{Nb}_{2/3})\text{O}_3 - \text{PbTiO}_3$ mit Hilfe von thermisch stimuliertem Depolarisationsstrom sowie dielektrischen und elektromechanischen Messungen untersucht. Zu diesem Zweck wurde die Reaktion von ungepolten, gleichstromgepolten und wechselstromgepolten Proben für thermisch ausgelagerte und gealterte Proben verglichen. Die Alterung wurde mit reduzierten piezoelektrischen Eigenschaften und Depolarisationstemperaturen in Verbindung gebracht. Eine scheinbar widersprüchliche Dualität von Polarisationsstabilisierung und Eigenschaftsverstärkung wurde für Wechselstrompolung festgestellt. Es wurde vorgeschlagen, dass das angelegte bipolare Polungsfeld zu einer Verteilung von orientierten Defektclustern im gesamten Volumen führt, was die dielektrischen und piezoelektrischen Eigenschaften durch lokal gebrochene Symmetrie und vermittelte reversible Polarisationsrotation verbessern könnte.

Die Existenz eines ergodischen Relaxor-Zustands und das Modell einer einzelnen polaren

Acknowledgements

Einheit unterhalb von TB sind nicht mit den in dieser Arbeit vorgestellten Ergebnissen vereinbar. Es wird vorgeschlagen, dass die funktionellen und strukturellen Eigenschaften von undotiertem $\text{Pb}(\text{Mg}_{1/3}\text{Nb}_{2/3})\text{O}_3$ und undotiertem $\text{Pb}(\text{Mg}_{1/3}\text{Nb}_{2/3})\text{O}_3 - \text{PbTiO}_3$ erheblich durch Defektstrukturen beeinflusst werden, die von der thermischen, elektrischen und mechanischen Feldgeschichte sowie von der Zeit abhängen. Es wurde spekuliert, dass die Vielzahl von manchmal widersprüchlichen experimentellen Ergebnissen, die in der Literatur berichtet werden, mit diesen Erkenntnissen zusammenhängen.

Es wird erwartet, dass die Ergebnisse dieser Arbeit das grundlegende Verständnis von Relaxor-Ferroelektrika fördern und zu einer verbesserten Reproduzierbarkeit experimenteller Ergebnisse in der Literatur beitragen.

Stichwörter: Relaxor, Ferroelektrika, Dielektrika, Piezoelektrisch, Defekt, Bleimagnesiumniobat, Wechselstrompolen, Einkristall

Contents

Acknowledgements	iii
Abstract	v
List of figures	xiii
List of tables	xvii
List of symbols	xix
1 Introduction	1
1.1 Lead magnesium niobate	1
1.2 Lead magnesium niobate lead titanate	6
1.3 Relaxor models	8
2 Experimental techniques	11
2.1 Sample preparation	11
2.1.1 Lead zirconate titanate	11
2.1.2 Lead magnesium niobate	11
2.1.3 Lead magnesium niobate lead titanate	13
2.1.4 Electroding	13
2.1.5 Cutting	14
2.1.6 Poling	14
2.2 Characterization	14
2.2.1 Temperature-dependent dielectric permittivity	14
2.2.2 Dynamic pyroelectric current measurements	15
2.2.3 Thermally stimulated current measurements	17
2.2.4 Direct piezoelectric measurements	18
2.2.5 Ferroelectric hysteresis measurements	19
2.2.6 Dynamic nonlinear polarization and strain measurements	20
3 Dielectric and electro-mechanical nonlinearities in ferroelectric materials	23
3.1 Motivation	23
3.2 Dielectric and electro-mechanical nonlinearities	23
3.3 Nonlinear description	24
3.4 Harmonic analysis of ferroelectrics	26
3.5 Geometric interpretation	28

Contents

3.6	Theoretical interpretation	32
3.7	Phenomenological interpretation	34
3.8	Summary	41
4	Macroscopic polarization in lead magnesium niobate	43
4.1	Motivation	43
4.2	Introduction	43
4.3	Nonlinearities of lead magnesium niobate	45
4.4	Dynamic pyroelectric measurements of lead magnesium niobate	52
4.5	Summary and conclusions	59
5	Thermally stimulated depolarization currents in lead magnesium niobate	61
5.1	Motivation	61
5.2	Introduction	61
5.2.1	Dipolar relaxation	62
5.2.2	Space charge relaxation	63
5.3	Thermally stimulated depolarization currents of lead magnesium niobate	65
5.4	Aging in lead magnesium niobate	74
5.5	Summary and Conclusions	76
6	Aging and alternate current poling in relaxor ferroelectric solid solutions	79
6.1	Motivation	79
6.2	Introduction	79
6.3	Results	83
6.4	Summary and conclusions	96
7	Summary, conclusions, and perspectives	99
A	Circuit schematics for pyroelectric measurements	105
B	Circuit schematics for Sawyer Tower measurements	109
C	Technical drawings of rectilinear precision spring	113
D	Circuit schematics for nonlinear polarization measurements	123
E	Supplementary data for Chapter 3	125
F	Supplementary data for Chapter 4	127
G	Derivation of Bucci-Fieschi equation	135
H	Supplementary data for Chapter 5	137
I	Approximation of stored energy in polarized and in strained crystals	139
J	Estimation of flexoelectric poling efficiency	141
K	Supplementary data for Chapter 6	143

Bibliography	170
Curriculum Vitae	171

List of Figures

1.1	Electron diffraction pattern of lead magnesium niobate (PMN) and dark-field image of chemical ordered regions.	2
1.2	Structural models of chemical ordered regions.	3
1.3	Atomistic structure of PMN as calculated from scanning transmission electron microscopy data.	3
1.4	Reverse Monte Carlo simulations of nano-sized polar regions in PMN.	4
1.5	Relative dielectric permittivity and elastic susceptibility of PMN.	5
1.6	Correlations between structural and functional properties of lead magnesium niobate lead titanate (PMN- x PT).	7
1.7	Domain structures obtained by transmission electron microscopy of PMN- x PT. . .	7
1.8	Polar-slush model for relaxor ferroelectric solid solution PMN-25PT.	10
2.1	Optical microscopy images of [001]-PMN crystals in as-received conditions.	12
2.2	Optical microscopy images of PMN- x PT crystals in as-received conditions.	13
2.3	Experimental setup for measurements of the dielectric permittivity.	14
2.4	Experimental setup for measurements of dynamic pyroelectric currents.	15
2.5	Basic electronic measurement circuits.	16
2.6	Custom-made furnace for thermally stimulated current measurements.	17
2.7	Custom-made Berlincourt-meter.	19
2.8	Sample fixture for strain and polarization measurements.	20
3.1	Comparison between polarization electric field hysteresis loop and their Fourier expansion for a lead zirconate titanate (PZT) sample.	27
3.2	Representation of the first three harmonic vs. the fundamental sinusoids for various values of the phase angles.	28
3.3	Geometric description of the combination between first and second harmonic components.	30
3.4	Geometric description of the combination between first and third harmonic components, and phasor diagram for commonly observed phase angles of the third harmonic of polarization.	31
3.5	Dielectric and electro-mechanical nonlinearities of poled Nb- and Fe-doped PZT ceramics with rhombohedral composition.	35
3.6	Dielectric and piezoelectric nonlinearities of Nb-doped PZT ceramics with rhombohedral, tetragonal, and morphotropic phase boundary composition.	36

List of Figures

3.7	Amplitudes of the first three harmonic sinusoids of strain and polarization for different PZT compositions with 1 at.% Nb-doping.	37
3.8	Asymmetry of polarization electric-field hysteresis loops of poled ferroelectric samples.	38
3.9	Dielectric and piezoelectric response of a poled PMN-20PT ceramic measured with an applied electric dc-bias field.	39
3.10	Harmonic components of polarization and strain response of a poled PMN-20PT ceramic measured with an applied electric dc-bias field.	40
3.11	Comparison between harmonic measurements and polarisation electric-field hysteresis loops obtained with the Sawyer-Tower method for a PMN ceramic measured at 200 K.	41
4.1	Dielectric nonlinearities of PMN ceramics.	45
4.2	Dielectric nonlinearities of a [001]-PMN crystal.	46
4.3	Subsequent measurements of harmonic phase angles of polarization for different sample orientations of a [001]-PMN crystal.	47
4.4	Longitudinal piezoelectric coefficients of polarized PMN ceramics and crystals. . .	49
4.5	Dielectric and electro-mechanical nonlinearities of an unpoled and poled [001]-PMN crystal.	50
4.6	Dielectric and electro-mechanical nonlinearities of electric field-trained PMN ceramics.	51
4.7	Dynamic pyroelectric measurements of field-trained PMN ceramics.	52
4.8	Proof of persistent macroscopic polarization in the ergodic phase of PMN.	53
4.9	Dynamic pyroelectric response of a [001]-PMN-crystal measured at different temperatures.	55
4.10	Dynamic pyroelectric response of a pristine, poled, and annealed [001]-PMN crystal. . .	57
4.11	Relative dielectric permittivity of a [001]-PMN crystal as a function of driving field amplitude for various frequencies.	58
5.1	Thermally stimulated depolarization current (TSDC) experimental setup and procedure.	65
5.2	Comparison of TSDC spectra of a PMN ceramic and crystal.	66
5.3	TSDC spectra of a [001]-PMN crystal as a function of electric poling field.	67
5.4	TSDC spectra in the vicinity of Burns temperature for a [001]-PMN crystal.	68
5.5	TSDC spectra in the vicinity of the coherence temperature for a [001]-PMN crystal. . .	69
5.6	Results of peak fitting of TSDC peaks in the vicinity of T^*	70
5.7	TSDC spectra for electric field-cooled [001]-PMN crystal.	71
5.8	TSDC spectra of mechanically poled [001]-PMN crystal.	72
5.9	TSDC spectra for field-cooled and fractional-poled [001]-PMN-crystal.	74
5.10	Thermally stimulated current response of [001]-PMN crystal during cooling.	75
5.11	Dynamic pyroelectric response of [001]-PMN crystal measured after TSDC measurement.	76
5.12	TSDC spectra of aged PMN ceramics.	77

6.1	Domain states for different poling conditions and symmetries in pseudocubic coordinates.	80
6.2	Piezoresponse force microscopy images for direct current (DCP) and alternate current poling (ACP) of [001]-PMN- <i>x</i> PT crystals.	81
6.3	Evolution of domain structure during ACP according to phase-field simulations. .	82
6.4	Dielectric permittivity and TSDC spectra of unpoled and aged [001]-PMN-29PT crystals.	84
6.5	Comparison between temperature-dependent dielectric permittivity and TSDC spectra for DCP and ACP of [001]-PMN-29PT crystals.	86
6.6	TSDC spectra and polarization for aged and then polarized [001]-PMN-29PT crystals.	87
6.7	TSDC spectra and polarization for annealed and aged samples.	88
6.8	TSDC spectra and derived polarization for ACP of [001]-PMN-29PT crystals.	89
6.9	Polarization and thermally stimulated currents for different sample orientations for ACP of [001]-PMN-30PT.	91
6.10	Change of polarization electric field hysteresis loops during ACP of [001]-PMN- <i>x</i> PT crystals obtained from different providers.	92
6.11	Comparison of subcoercive dielectric and electro-mechanical nonlinearities for DCP and ACP of [001]-PMN-29PT.	93
6.12	Normalized dielectric and electro-mechanical nonlinearities and third harmonic phase angle of polarization for DCP and ACP of [001]-PMN-29PT.	93
6.13	Anisotropic electric field-dependent nonlinear polarization response for DCP of various relaxor ferroelectric solid solutions.	95
6.14	Polarized light microscopy images and third harmonic phase angle of polarization of a [111]-PMN-28PT crystal.	96
A.1	Block diagram of <i>Dynopyro</i> , a device for dynamic pyroelectric measurements. . . .	105
B.1	Block diagram of modified Sawyer Tower circuit.	109
C.1	Rectilinear precision spring for measurements of strain and electrical signals. . . .	113
D.1	Equivalent circuit of the experimental configuration for measurements of polarization harmonics.	123
E.1	Phasor diagram for commonly observed phase angles of the third harmonic of polarization.	125
E.2	Anomalies in the amplitude of the real part of the second harmonic in polarization for Nb-doped lead zirconate titanate ceramics.	126
F.1	Dielectric nonlinearities of [001] strontium titanate single crystal.	127
F.2	Orientation dependence of harmonic phase angle for poled [111]-PMN-28PT crystal.	127
F.3	Dielectric nonlinearities of [001]-PMN crystal.	128
F.4	Dielectric and electromechanical nonlinearities of PMN ceramic for three subsequent measurements.	129

List of Figures

E.5	Dynamic pyroelectric measurements for [001]-PMN crystals of different origin, electrodes, thicknesses, and surface finishing.	130
E.6	Pyroelectric response of PMN crystals and ceramics.	131
E.7	Dielectric nonlinearities of PMN crystal for various frequencies.	132
E.8	Decay of pyroelectric response of a [001]-PMN crystal after poling.	132
E.9	Sequential measurements of the first harmonic permittivity for PMN crystal and ceramic.	133
E.10	Two subsequent measurements with different measurement parameters of the field dependent relative dielectric permittivity for a [001]-PMN crystal.	133
E.11	Third harmonic phase angle of polarization for [001] strontium titanate single crystal at cryogenic temperatures.	134
H.1	Fit procedure of TSDC response of [001]-PMN-A crystal.	137
H.2	Comparison between electrometers.	138
K.1	Temperature dependent dielectric permittivity and loss tangent obtained during heating and cooling for different [001]-PMN-29PT samples.	143
K.2	Polarization for unpoled, and unpoled and then aged PMN-29PT.	144
K.3	TSDC spectra and polarization for two unpolarized lead-based relaxor ferroelectric solid solutions.	145
K.4	Aging for DCP of [111]-PMN-28PT single crystal.	146
K.5	Third harmonic phase angle of polarization for various driving field frequencies for DCP of PMN-28PT.	146
K.6	Third harmonic phase angle or polarization and strain for barium titanate single crystals.	147
K.7	Second harmonic of polarization and stain for DCP of [111]-PMN-28PT.	147
K.8	Real part of the second harmonic of polarization and strain of $0.93\text{Pb}(\text{Zn}_{1/3}\text{Nb}_{2/3}) - 0.07\text{PbTiO}_3$ crystals.	148



List of Tables

2.1 Investigated PMN- <i>x</i> PT crystals by manufacturer.	13
---	----

List of symbols and acronyms

A	electroded sample area
C	capacitance
C_{Nb}	niobium concentration
d	piezoelectric coefficient
d_{33}	longitudinal piezoelectric coefficient
d_{33}^*	effective macroscopic longitudinal piezoelectric coefficient
$d^{(1)}$	first harmonic piezoelectric coefficient
d_{init}	intrinsic piezoelectric coefficient
E	electric field
E_0	driving field amplitude
$E_{0,m}$	ac electric field amplitude of maximum permit-
	tivity
E_a	activation energy
E_c	coercive field
E_c^-	negative coercive field
E_c^+	positive coercive field
E_{dc}	electric dc bias field
E_M	dc electric field strength for polarization reversal
E_p	electric poling field
F	excitation signal
F_0	excitation signal amplitude
f	ordinary frequency
f_0	-3dB cut-off frequency
h	height
I_B	input bias current
I_D	depolarization current density
i_{max}	Current density maximum
i_p	pyroelectric current
$j_{0,m}$	mean pyroelectric current density amplitude
j_D	depolarization current density
j_{max}	current density maximum
j_p	pyroelectric current density
$j_{p,m}$	mean pyroelectric current density

List of symbols and acronyms

k_B	Boltzmann constant
M	electrostrictive coefficient
M_A	monoclinic A-phase
M_B	monoclinic B-phase
M_C	monoclinic C-phase
m	material coefficient
n	order of harmonic component
n_{CVS}	Curie von Schweidler power exponent
O	orthogonal phase
P	polarization
P_{300K}	polarization at 300 K
$P^{(1)}$	amplitude of first harmonic of polarization
$P^{(2)}$	amplitude of second harmonic of polarization
$P^{(n)}$	amplitude of n^{th} harmonic of polarization
P_e	equilibrium polarization
P_M	macroscopic polarization
P_r	remnant polarization
p	pyroelectric coefficient
Q_D	total ionic depolarization charge
Q	electrostrictive coefficient
q	heating rate
R	response
R_0	response amplitude
R-phase	rhombohedral phase
R_{const}	constant of Fourier series
R_f	feedback resistor
R_{shunt}	shunt resistance
S_u	sensitivity of photonic displacement sensor
T	temperature
T_0	initial temperature
T_{0P}	temperature of zero polarization
T^*	coherence temperature
T_B	Burns temperature
T_C	Curie temperature
T_f	freezing temperature
T_m	temperature of maximum permittivity
T_{max}	Temperature of current density maximum
T_p	poling temperature
T_{RT}	rhombohedral to tetragonal phases transition
T_ω	period
t	time
$\tan \delta$	dielectric loss tangent
u	displacement
V_{OS}	input offset voltage

V_{OUT}	output voltage
x	strain
$x^{(1)}$	amplitude of first harmonic of strain
$x^{(2)}$	amplitude of second harmonic of strain
$x^{(3)}$	amplitude of third harmonic of strain
$x^{(n)}$	amplitude of n^{th} harmonic of strain
α	Rayleigh coefficient
α_d	piezoelectric Rayleigh coefficient
α_ϵ	dielectric Rayleigh coefficient
ΔE_c	internal bias field
δ	phase angle of polarization
$\delta^{(1)}$	first harmonic phase angle of polarization
$\delta^{(2)}$	second harmonic phase angle of polarization
$\delta^{(3)}$	third harmonic phase angle of polarization
$\delta^{(n)}$	phase angle of n^{th} polarization harmonic
ϵ	dielectric permittivity
ϵ_0	vacuum permittivity
ϵ_{33}	longitudinal dielectric permittivity
$\epsilon^{(1)}$	first harmonic dielectric permittivity
ϵ_{init}	intrinsic dielectric permittivity
ϵ_r	relative dielectric permittivity
ω	angular frequency
ϕ	phase angle of strain
$\phi^{(1)}$	first harmonic phase angle of strain
$\phi^{(2)}$	second harmonic phase angle of strain
$\phi^{(3)}$	third harmonic phase angle of strain
$\phi^{(n)}$	phase angle of n^{th} strain harmonic
ρ_d	dislocation density
τ	time constant
τ_0	dipolar relaxation time
θ	phase angle
$\theta^{(2)}$	phase angle of second harmonic
$\theta^{(n)}$	phase angle of n^{th} harmonic
ac	alternate current
ACP	alternate current poling
BST	barium strontium titanate
BT	barium titanate
COR	chemically ordered region
CvS	Curie von Schweidler law
dc	direct current
DCP	direct current poling
FC	field cooling

List of symbols and acronyms

FP	fractional poling
HREM	high-resolution electron microscopy
IP	isothermal poling
MPB	morphotropic phase boundary
ODR	octahedral distortion regions
OTR	octahedral tilt regions
PFM	piezoresponse force microscopy
PID	proportional-integral-derivative (controller/al- gorithm)
PIN-PMN-PT	$\text{Pb}(\text{In}_{0.5}\text{Nb}_{0.5})\text{O}_3 - \text{Pb}(\text{Mg}_{1/3}\text{Nb}_{2/3})\text{O}_3 - \text{PbTiO}_3$
PLM	polarized light microscope
PMN	lead magnesium niobate
PMN- <i>x</i> PT	lead magnesium niobate lead titanate
PNR	polar nano region
PP	pulse poling
PTFE	polytetrafluorethylene
PVDF	polyvinylidene fluoride
PZN- <i>x</i> PT	lead zinc niobate lead titanate
PZT	lead zirconate titanate
RES	resonant electrostriction spectroscopy
RPS	resonant piezoelectric spectroscopy
RTD	resistance temperature detector
SCLD	space charge limited drift
STEM	scanning transmission electron microscopy
STO	strontium titanate
TSC	thermally stimulated current
TSDC	thermally stimulated depolarization current
UNP	unpolarized
WLF	Williams, Landel and Ferry

1 Introduction

Relaxor ferroelectric solid solutions are the material class of choice for high-performance piezoelectric coupling devices today. While much research has been done to clarify the mechanistic origin of their properties, the fundamental understanding of electro-mechanical coupling has remained limited. A complex local structure and various simultaneously acting mechanisms on different length scales, combined with strong history dependence, make these materials extremely difficult to analyze. A predictive atomistic structural model or even a general physical definition of *relaxor* and *relaxor ferroelectric* is yet missing.

The terms *relaxor*, *ferroelectric relaxor*, and *relaxor ferroelectric* are themselves ill-defined and often used interchangeably in the literature. In the following, ferroelectric relaxor or relaxor ferroelectric refer to the single compounds that exhibit characteristic dielectric relaxation, while relaxor ferroelectric solid solution refers to solid solutions, where at least one endmember is ferroelectric. The field of relaxors and their solid solutions is notorious for a certain degree of ambiguity when it comes to the interpretation of experimental results. Often several contradictory interpretations can be found in the literature for a given phenomenon, and great care must be exercised when comparing experimental results of different origins. Models and interpretations have been revised several times over the past decades, and inconsistent nomenclatures are found between different theoretical models and disciplines.

The eponymous characteristic of relaxors is a broad peak in the temperature-dependent weak-field dielectric permittivity, with marked frequency dependence below the temperature of its maximum. It is commonly attributed to the relaxation dynamics of polar entities in the nanometre scale, often called polar nano regions, PNRs, the nature of which is subject to this thesis. In the following chapter, a short review of the investigated material systems and relaxor models is provided.

1.1 Lead magnesium niobate

Lead magnesium niobate, $\text{Pb}(\text{Mg}_{1/3}\text{Nb}_{2/3})\text{O}_3$ (PMN), is a complex perovskite oxide with Pb^{2+} on the A-sites and either Mg^{2+} or Nb^{5+} on the B-sites.¹ The Pb^{2+} ions have 12 oxygen ion next neighbors while B-site atoms reside in corner linked oxygen octahedra. The difference in valences and ionic radii between Mg^{2+} ($d = 0.72 \text{ \AA}$)² and Nb^{5+} ($d = 0.64 \text{ \AA}$)² cause local inhomogeneities in polarization and lattice strain. The average structure obtained by X-ray and neutron scattering experiments is cubic $\text{Pm}\bar{3}\text{m}$ at ambient temperatures, with local displacements of ions from the special positions of the ideal cubic perovskite structure.^{3–5} The origin, spatial correlations,

dynamic properties, and temperature dependencies of these shifts are still not fully clarified. For example, several authors have proposed antiparallel^{5–7} displacement of Pb ions in $\langle 111 \rangle$ directions^{5,8–11} while alternative views suggest a superposition of $\langle 110 \rangle$ displacements.^{12–16}

It is generally accepted, however, that local polarization arises due to the displacement of the highly polarizable Pb and to a lesser extent from Nb ions, while Mg ions remain approximately in the center of their respective oxygen octahedra.^{10,17,18} This is attributed to the covalent nature of Pb–O, and Nb–O bonds in contrast to the ionic Mg–O bonds.^{10,19} Oxygen ions do not only influence the structure via tilting and rotation of oxygen octahedra,^{6,20,21} but the saturation of oxygen bonds also influences ionic shifts of the surrounding cations.^{10,17} The local displacement of Pb ions, and with it the local polarization is therefore strongly correlated to their coordination on the B-sublattice.^{10,20,22}

Local short-range order on the B-sublattice has been identified based on superlattice reflections of $\{h/2\ k/2\ l/2\}$ -type in electron diffraction pattern.^{23–25} Dark-field imaging of these superlattice reflections revealed chemically ordered regions, CORs, with a diameter of ~ 5 nm dispersed in a disordered matrix (Figure 1.1).^{23–25} The absence of coarsening of CORs upon annealing was correlated to growth-inhibiting space charges, resulting from a rock-salt type 1:1 ordering of Mg and Nb on the B-sublattice.^{16,23,25,26} The local structure in this *space charge* model is given as $\text{Pb}(\text{Mg}_{1/2}\text{Nb}_{1/2})\text{O}_3$ with a formal negative charge, which is compensated by positively charged disordered regions.^{23,24} However, this 1:1 ordering could not be experimentally verified, and an alternative charge-balanced random site model was proposed.²⁷ In this model, the B-sublattice is divided into alternating $[111]$ -layers of different occupancies denoted as B' and B".^{28–30} B' layers are randomly occupied by Mg and Nb in a 2:1 ratio, and B" layers are predominantly occupied by Nb atoms. The resulting CORs formally described as $\text{Pb}[(\text{Mg}_{2/3}\text{Nb}_{1/3})_{1/2}\text{Nb}_{1/2}]\text{O}_3$ are charge-neutral, while the random population on B' layers causes random local electric fields.^{31–33} The atomistic structure for the space charge and charge-balanced random site model are compared

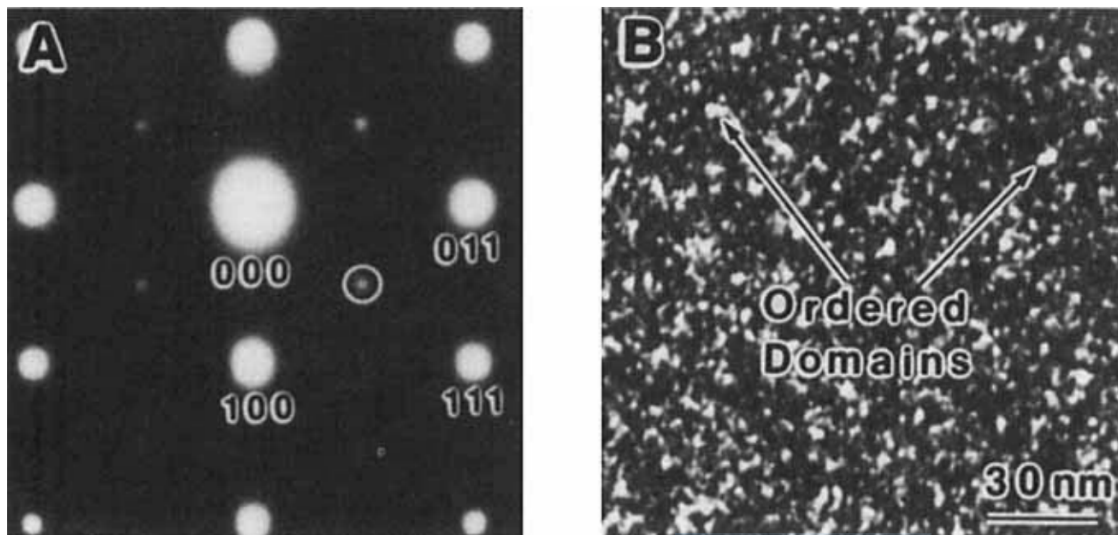


Figure 1.1. (a) Electron diffraction pattern of lead magnesium niobate, PMN, in $[0\bar{1}1]$ zone. (b) Chemically ordered regions in PMN obtained by dark-field imaging of $(\frac{1}{2}\ \frac{1}{2}\ \frac{1}{2})$ superlattice reflection. Adapted from Chen *et al.*, Ref. [23].

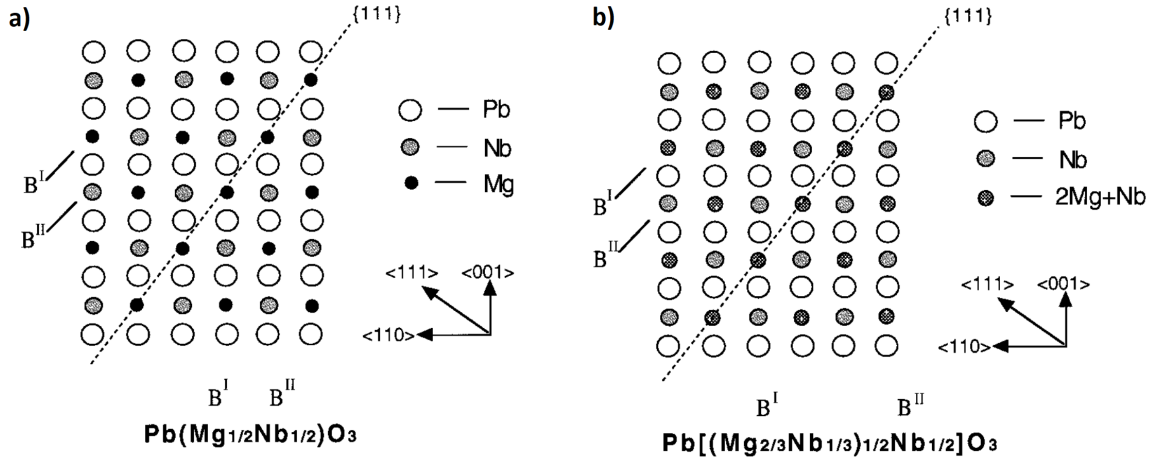


Figure 1.2. Structural models of chemical ordered regions, CORs, in PMN. Oxygen ions are omitted. (a) Space charge model, (b) charge-balanced random site model. Adapted from Xu *et al.*, Ref. [43].

in Figure 1.2. Theoretical calculations attributed the formation of CORs to a balance between configurational entropy and hybridization energy of Pb6s and O2p states on otherwise under bonded oxygen.³⁴ High-resolution, HREM, and scanning transmission electron microscopy, STEM, images have suggested the presence of antiphase boundaries between CORs with an order gradient towards these boundaries.^{31,35} Due to a phenomenological correlation between local ordering and dielectric relaxation,^{36,37} it was long believed that CORs and PNRs are of the same origin.^{38–40} Later studies, on the other hand, suggest that PNRs and CORs are separate entities.^{10,20,41,42}

Atomistic correlations between the local polarization and chemical order have been investigated in the recent past by advanced aberration-corrected STEM techniques.²⁰ In this study, the projected polarization appears to change continuously in 2 to 12 nm-sized areas that are separated by low-angle domain walls. In addition, a method to correlate polarization, CORs, octahedral distortion regions, ODRs, and octahedral tilt regions, OTRs, was presented (Figure 1.3). It has been calculated that CORs, ODRs, and OTRs are located close to PNR boundaries. An interesting finding of this study is a correlation between antiferrodistortive displacements of Pb

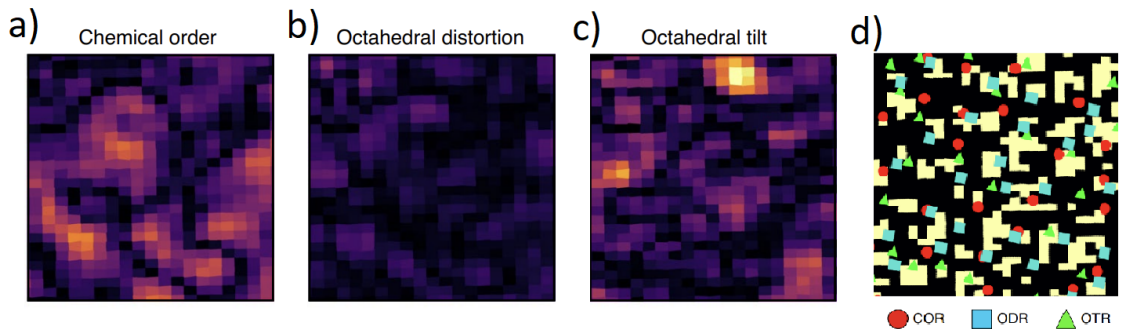


Figure 1.3. Atomistic structure of PMN as calculated from scanning transmission electron microscopy data. (a) Chemical ordered regions, COR, (b) octahedral distortion regions, ODR, (c) octahedral tilt regions, OTR, and (d) spatial correlations between polarized regions, COR, ODR, and OTR. The yellow blocks indicate where domain walls are expected. Adapted from Kumar *et al.*, Ref. [20].

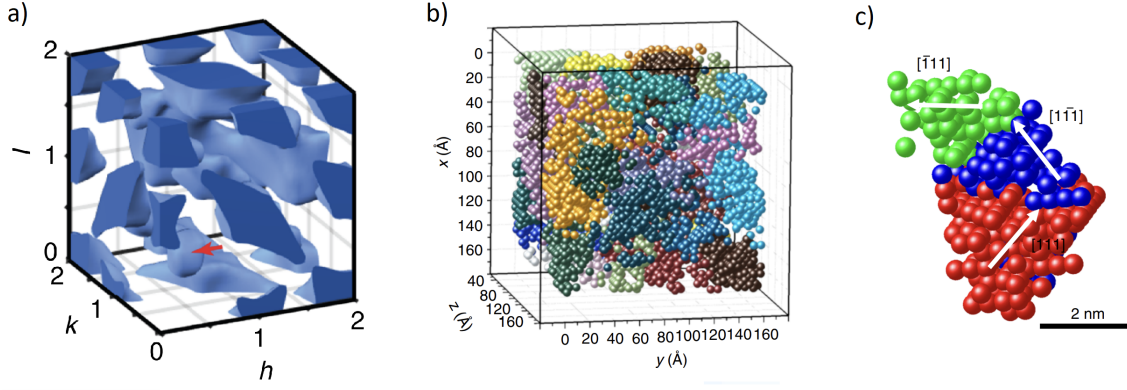


Figure 1.4. (a) Experimental X-ray diffuse scattering pattern of PMN, (b) angle correlation of Pb atoms calculated by Reverse Monte Carlo simulation, (c) rendering of PNRs as aggregated regions of collective Pb shifts along $\langle 111 \rangle$. The polarization in adjacent $\langle 111 \rangle$ variants span an angle of 71° . Adapted from Eremenko *et al.*, Ref. [10].

and COR centers.²⁰ Theoretical studies have reached a similar conclusion.^{10,22} Three-dimensional correlations of Pb ions have been modeled by means of Reverse Monte Carlo simulations to diffraction and spectroscopy data.¹⁰ Space filling clusters of Pb atoms have been identified through displacement-angle correlations, as depicted in Figure 1.4(b). Furthermore, the formation of clusters of spatially correlated Pb and Nb shifts along $\langle 111 \rangle$ directions and the formation of aggregated PNRs, as shown in Fig. 1.4(c), have been proposed.¹⁰

Despite this complex local structure, a temperature-driven macroscopic structural phase transition is absent in PMN. The average structure obtained by X-ray and neutron diffraction techniques is cubic $Pm\bar{3}m$ between 5 K and 1020 K with weak rhombohedral distortions below 300 K.^{3–5} The cubic lattice constant decreases linearly between approximately 900 K and 600 K before deviating and becoming roughly constant with $a \approx 4.05 \text{ \AA}$ below 300 K.^{3,44,45} This anomalous behavior is accompanied by anomalies in the refraction index,⁴⁶ the elastic⁴⁷ and dielectric modulus,⁴⁸ and onset of diffuse X-ray and neutron scattering.⁶ These observations have been interpreted as the first emergence of local polarization^{46,49} related to the correlated displacement of ions at the so-called *Burns temperature*, $T_B \approx 600\text{--}650 \text{ K}$.^{6,45}

Over the years, several patterns of the diffuse scattering intensity have been identified: butterfly-shaped intensities around (h00) Bragg peaks,^{6,45} ellipsoidal-shaped intensities along (hh0) reflections, as well as intensities at the zone-boundary M- and R-points of the Brillouin-zone.^{6,39,45,50,51} They have been attributed to polar-nanoregions,^{12,14,45,52} domain walls,¹⁸ chemically ordered regions,^{38,53} and Huang scattering due to defect induced lattice deformations.^{6,54}

Probably the most prominent diffuse scattering component of relaxors are butterfly-shaped patterns, which appear around 650 K and increase in intensity with decreasing temperature.^{6,45} Due to its temperature dependence and its reaction to applied electric fields, it has often been correlated to nano-sized polar regions.^{9,45,52} This interpretation is contrasted by diffuse scattering studies of lead zirconate titanate⁵⁴ and molecular dynamics simulations of nano-sized ferroelectric domains,¹⁸ for which similar patterns have been obtained. Despite its elusive origin, the ferroic nature of butterfly-shaped diffuse scattering patterns is widely accepted.^{18,39,54} By mapping large volumes of the reciprocal space with X-ray and neutron scattering techniques,

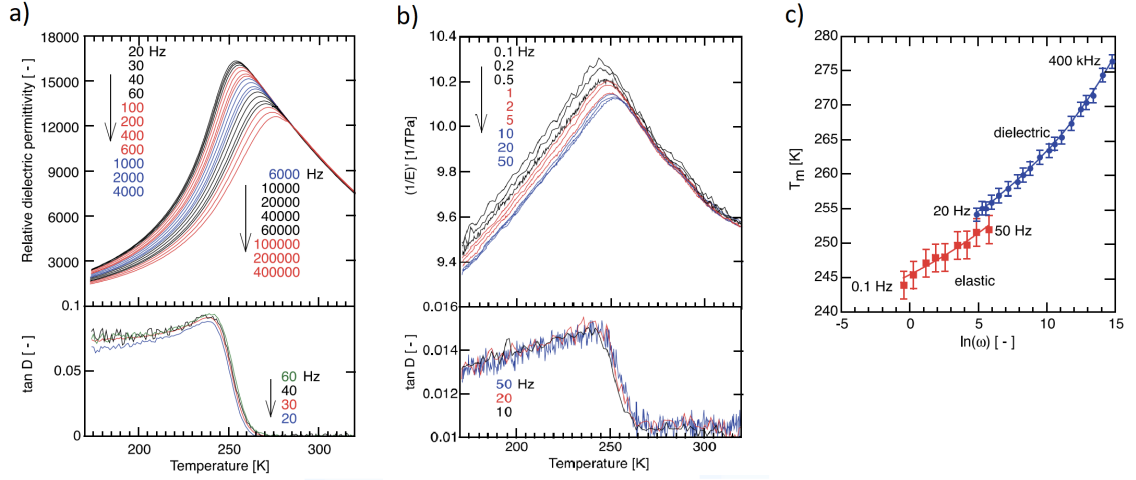


Figure 1.5. (a) The relative dielectric permittivity and loss tangent, (b) elastic susceptibility and loss tangent, and (c) the temperature of the maximum dielectric permittivity (circles) and elastic susceptibility (squares) as a function of $\ln \omega$, where ω is the measurement frequency. Full lines are fits to the data using the Vogle-Fulcher equation. Adapted from Uršič *et al.*, Ref. [57].

systematic intensity modulations of these characteristic patterns have been revealed.⁵⁰ They are more pronounced for neutron scattering than for X-ray scattering data and have therefore been attributed to collective oxygen displacements.⁵⁰ Subsequent STEM studies have suggested that these modulations originate from oxygen octahedra tilt ordering associated with Mg–O–Mg arrangements in the chemically disordered matrix of PMN.²⁰ Other common diffuse scattering patterns in PMN are temperature-dependent rods at zone boundary centers that have been assigned to antiferroelectric distortions,¹⁶ and temperature-independent bow-tie and rod patterns which have often been attributed to CORs.^{45,50} The correlation of antiferroelectric ordering and CORs has been highlighted by several authors.^{50,55,56}

The complex dielectric permittivity of PMN has been studied over a wide temperature range and several decades of frequency.^{58–63} The most notable feature is a broad peak in the real part of the temperature-dependent dielectric permittivity with substantial dielectric dispersion below its maximum T_m , as evident in Figure 1.5(a). The shift of T_m for a certain frequency range, ΔT_m , is often used as a measure for the strength of relaxation.^{50,64,65} For PMN, T_m shifts from $T_m \approx 390\text{--}420\text{ K}$ ⁶³ at 74 GHz to $T_m \approx 220\text{--}250\text{ K}$ at 3 mHz.^{60,63}

Different approaches have been applied to model the dielectric response of PMN,^{1,66–69} often involving cumulative contributions of Debye-type relaxations with a continuous distribution of relaxation times.^{60,66} The validity of an underlying Debye-type relaxation is thereby an assumption that is difficult to verify in practice.¹ In other words, the model of cumulative Debye-like processes with a distribution of relaxation times can approximate most dielectric data, and the obtained fitting parameters do not need to carry physical meaning.¹ Alternatively, dielectric data of PMN have been described by the empirical Havriliak-Negami function⁶⁹ or as a superposition of the Kohlrausch-Williams-Watt stretched exponential and the Curie von Schweidler power-law dependence.¹

It has been shown that the characteristic dielectric response is accompanied by anelastic

relaxation, providing evidence that the underlying mechanism is simultaneously electrically and mechanically active [Fig. 1.5(b)].^{47,57} The frequency shift of maximum dielectric permittivity and maximum elastic susceptibility can thereby be satisfactorily described by the Vogel-Fulcher law⁷⁰

$$\omega = \omega_0 \exp \left[-\frac{E_a}{k_B(T_m - T_f)} \right], \quad (1.1)$$

as depicted in Fig. 1.5(c), where ω is measurement frequency, ω_0 a characteristic frequency, E_a the activation energy, k_B the Boltzmann constant, and T_f the freezing temperature. It may be interpreted as a temperature shift of the characteristic relaxation time, $\tau \sim 1/\omega$, with a temperature-dependent activation energy, predicting a divergence of τ at T_f .⁷¹ On the other hand, it has been theoretically derived that the Vogel-Fulcher law may also be obtained without divergence of τ if the static permittivity has a maximum at T_f .⁷² Interestingly, fitting parameters result in activation energies equivalent to the thermal energy at $T \sim 900$ K and predict freezing of the domain state at $T_f \approx 220$ K. Many studies have reported the existence of diffuse scattering intensities correlated to chemical ordering up to 900 K,^{45,50} and the onset of pronounced history dependence of properties below T_f has been investigated intensively.^{4,73–77}

It has been widely accepted that PMN is in a metastable state below T_f that can be transformed into a rhombohedral-like ferroelectric state when a strong enough electric field is applied.^{4,66,73,75,76} In contrast to the slim polarization hysteresis loops obtained at ambient temperatures, characteristic ferroelectric hysteresis loops can be measured below T_f .⁷⁸ Not only can the ferroelectric state be induced when the electric field is applied under isothermal conditions, but also when it is applied during cooling from ambient temperatures.^{73,76,79,80} The threshold field for this transformation has been determined to be ~ 1.7 kV/cm.^{73,76,79,80} An electric-field-temperature phase diagram for the induced ferroelectric, non-ergodic, and ergodic relaxor state has been constructed.⁷⁸ In this framework, the non-ergodic relaxor state is assigned to the metastable state below T_f that can be transformed into a ferroelectric state, and the ergodic relaxor state has been introduced to distinguish the relaxor state with dynamic locally correlated polarization from the paraelectric state above T_B .⁷⁷ A more recent discovery is the coherence temperature $T^* \sim 400$ –500 K.^{45,81,82} It has been attributed to the first appearance of static PNRs^{18,45,81,82} and a local ferroelectric phase transition.^{11,48,83}

1.2 Lead magnesium niobate lead titanate

Today's high-performance electro-mechanical coupling devices are based on lead-based relaxor-ferroelectric solid solutions.^{84,85} One of the most relevant systems is lead magnesium niobate lead titanate, $(100-x)\text{Pb}(\text{Mg}_{1/3}\text{Nb}_{2/3})\text{O}_3 - x\text{PbTiO}_3$, (PMN- x PT).^{84,85} The system features a morphotropic phase boundary, MPB, in its composition temperature phase diagram at which the piezoelectric properties are strongly enhanced [Figure 1.6(a)]. This enhancement is correlated to a polarization rotation mechanisms through a monoclinic phase that bridges the rhombohedral and tetragonal phases.^{86–88}

PMN- x PT becomes progressively ferroelectric with enhanced PT content.⁶⁵ For PT additions up to $x \approx 38$, complex phase mixtures and hierarchical domain structures are observed, while a tetragonal symmetry and simple lamellar domain structures are present for higher concentrations (Figure 1.7).^{50,65} The addition of Ti-ions on the B-site increases chemical disorder on the local

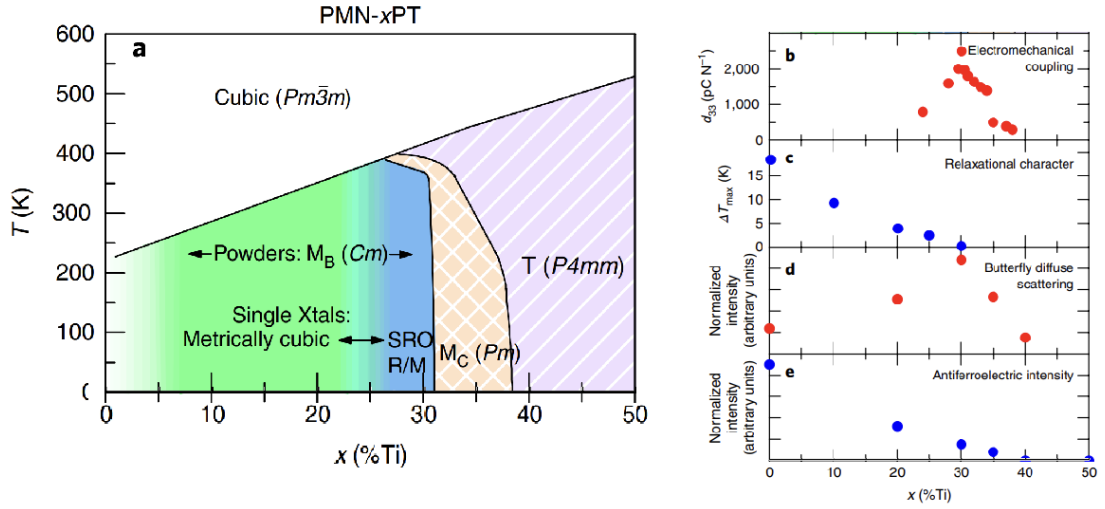


Figure 1.6. Correlation between structural and functional properties of PMN- x PT. (a) Phase diagram, and (b-e) correlation between functional properties and normalized diffuse scattering intensities. Adapted from Krogstad *et al.*, Ref. [50].

scale.^{20,25,50} With increasing x , the amount of CORs and OTRs is reduced while the amount of ODRs is increased.²⁰ For $x = 40$ superlattice reflections related to CORs are absent.²⁵

The comparison between functional properties and characteristic diffuse scattering intensities has led to the hypothesis that enhanced piezoelectric properties are related to the coexistence of ferroic and antiferroic order.⁵⁰ Similar correlations have been derived by other authors.^{33,89} However, it was highlighted that neither diffuse scattering feature alone can explain the improved piezoelectric properties, as butterfly-shaped peaks are also present in PMN that is not considered piezoelectric.⁵⁰ The diffuse scattering may therefore be a necessary but not sufficient condition for large piezoelectricity. More importantly, neither the MPB, nor relaxor properties alone can fully explain the superior electro-mechanical properties of PMN- x PT. In fact, only lead-based relaxor ferroelectric solid solutions show outstanding properties, while other relaxor-systems with MPB are less competitive.⁹⁰

The description of electro-mechanical coupling in relaxor ferroelectrics and even in con-

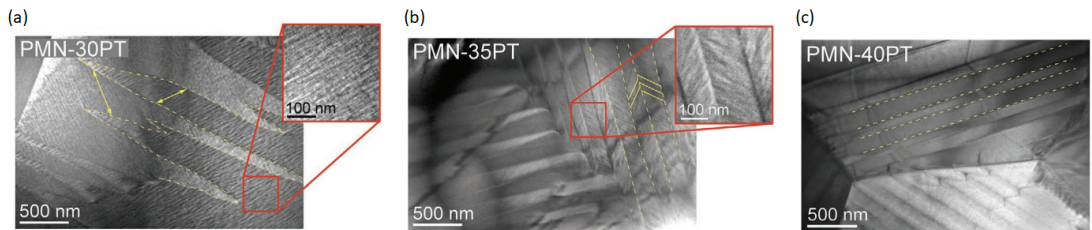


Figure 1.7. Domain structures obtained by transmission electron microscopy of (a) PMN-30PT, (b) PMN-35PT, and (c) PMN-40PT. Hierarchical domain structures with nanodomains (yellow arrows and full lines) within parent ferroelectric domains (dashed yellow lines) are observed for PMN-30 and PMN-35PT. Adapted from Otoničar *et al.*, Ref. [65].

ventional ferroelectrics is still subject to intensive research. Many different contributing effects have been discovered, but their interactions and individual magnitude are not well understood. Electro-mechanical coupling and its enhancements may arise from intrinsic piezoelectricity and electrostriction, dynamics of domain walls and their interactions with defects in response to homogeneous fields⁹¹ and gradients,^{91,92} field-induced phase transitions,⁸⁷ adaptive domain structures,⁹³ strain accommodation mechanisms,⁹⁴ static charged domain walls,⁹⁵ dynamics of electrically conducting domain walls,⁹⁶ chemical expansion,⁹⁷ oxygen-octahedra tilting,⁹⁸ intermediate monoclinic⁸⁶ or triclinic²⁰ phases, coupling of polar regions to lattice vibrations,⁹⁹ and instability due to the system's proximity to a critical endpoint,¹⁰⁰ softening due to polarization and strain disorder,⁶⁵ or complex ferroelectric domain states.¹⁸ Given the variety of possible mechanisms, the dynamic polarization behavior and its contribution to electro-mechanical coupling in these materials remains one of the most discussed subjects in this research area.¹⁰¹

Counter-intuitively, the effective macroscopic longitudinal piezoelectric coefficient, d_{33}^* , in many technologically relevant systems is dominated by a polarization rotation mechanism.⁸⁷ The essential condition for this is a sufficiently large piezoelectric shear coefficient, such as d_{15} in tetragonal materials.¹⁰² In that case, a maximum of d_{33}^* can be obtained along non-polar crystallographic directions.⁸⁷ By poling crystals along specific non-polar directions, stable multi-domain configurations with high shear contributions can be engineered.¹⁰³ Domain-engineered single crystals with compositions close to a morphotropic phase boundary can combine ultrahigh piezoelectric coefficients, almost no hysteresis, and high coupling coefficients.⁷⁹ Piezoelectric coefficients of $d_{33}^* \sim 4000$ pC/N have been recently obtained for domain-engineered Sm-doped single crystals.⁸⁵

However, domain engineering, doping, as well as the MPB concept are general concepts of ferroelectric systems.⁸⁸ Only a few concepts take relaxor characteristics into account to explain their outstanding electro-mechanical properties. Xu *et al.* proposed that the interaction of polar entities with phonons destabilize the ferroelectric state.⁹⁹ Thereby, the coupling of PNR to lattice vibrations that induce a shear deformation of the polar vector is thought to enhance the piezoelectric shear coefficient.¹⁰⁴ Based on this concept, 50-80 % of the piezoelectric property's magnitude was recently attributed to the presence of polar regions within ferroelectric domains based on cryogenic experiments.¹⁰⁵ It is proposed that PNRs within ferroelectric domains increase the transverse dielectric permittivity, which results in high piezoelectric shear coefficients.¹⁰⁵ Several authors have questioned the model of PNRs, on the other hand.^{18,75,101} It has been argued that the available experimental results can also be modeled by complex domain structures.

Lately, the performance of domain-engineered PMN-PT crystals has been considerably enhanced by a simple poling procedure.^{106,107} The application of several bipolar electric field cycles with an electric field above the coercive field (alternating current, ac, poling) has been proven to increase d_{33}^* by about 40 % compared to conventional direct current, dc, poling.^{106–108} The origin of this unexpected effect has not been identified conclusively. Enhanced¹⁰⁷ and reduced domain wall densities¹⁰⁸ have been proposed as possible explanations.

1.3 Relaxor models

During the last 60 years, several models have been proposed to explain the intriguing properties of relaxors and their solid solutions. The first model was reported by Smolenskii *et al.*,¹⁰⁹ who

correlated the observed dielectric relaxation to local fluctuations of the Curie temperature, T_C , causing a coexistence of ferroelectric and paraelectric states. Burns *et al.* interpreted an anomalous deviation from the linear temperature dependence of the optical refractive index as the first emergence of randomly oriented polarization in a glassy state below T_B .⁴⁶

One of the most popular models was introduced by Cross *et al.*⁴⁹ In his *superparaelectric model*, relaxors are described as an ensemble of individual Debye-like relaxors, the characteristic frequencies of which follow an Arrhenius-like temperature shift with a distribution of activation energies. Individual relaxors are thought to originate from nano-sized volumes of correlated orientational polarization, so-called polar nano regions, PNRs. It has been proposed that PNRs firstly emerge around T_B , dispersed in a non-polar matrix, and undergo thermally activated flipping between equivalent sites. The disordered nature of relaxors is thought to result in a distribution of activation energies so that the cumulative contribution of PNRs to the dielectric permittivity gradually fades out with reduced temperature.

Shortly after, the *dipolar glass model* was introduced by Viehland *et al.*⁷¹ The fundamental assumption of this model is a temperature-dependent interaction between ferroelectric clusters that increases during cooling. Inhomogeneities in the material result in conflicting interactions that cause a cooperative frustration of the polar structure. Such a system is then characterized by a static freezing temperature and short-range order. The onset of non-ergodic behavior below $T \sim 220$ K and the fidelity of the Vogle Fulcher law have been used to justify this model.

The very existence of a non-polar matrix was disputed in the *random-field model* by Westphal *et al.*⁷⁵ It has been pointed out that the absence of a macroscopic phase transition and freezing characteristics are not exclusive to glassy behavior. Instead, it has been argued that random electric fields “destroy” the phase transition. As a result, dynamic nano-sized ferroelectric domains are present above and frustrated nano-sized ferroelectric domains below $T \approx 200$ K. Experimentally observed Barkhausen jumps, which are not expected for glassy states, have been related to avalanche-like depinning of ferroelectric domains.

A *breathing model* was introduced by Glazounov *et al.*, questioning the reorientation of dipoles as the origin of dielectric relaxation.¹¹⁰ From measurements of the anisotropic dielectric response of PMN to ac and dc electric driving fields, two contributions to the dielectric response have been derived. A depinning of interphase boundaries between polar regions and a non-polar matrix dominant in ac-fields, and a slow reorientation of dipoles in response to dc fields. In this model, dielectric relaxation originates from a time-dependent depinning process of interphase boundaries that vibrate in weak ac-fields.

The recent *polar-slush model*, derived from molecular dynamics calculations for PMN-0.25PT, describes a multi-domain state with domain sizes of 2-10 nm and a large fraction of low-angle domain walls, as presented in Figure 1.8.¹⁸ These low-angle domain walls are facilitated by the off-centering of Pb from its oxygen cuboctahedra with small energy differences between the $\langle 100 \rangle$, $\langle 110 \rangle$, and $\langle 111 \rangle$ orientations. At T_B , dynamic nanodomains form throughout the material with weak polarization correlations within and between nanodomains. Below T^* the correlation strength increases within domains resulting in enhanced order and reduced dynamics, while the correlation between individual domains remains weak. In this state, a mixture of ferroelectric- and paraelectric-like unit cells is thought to allow for slow and correlated polarization rotation of individual nanodomains. Below T_f , the increasing interactions between nanodomains result in a frustrated state. In this frozen state, only local polarization fluctuations appear, which are

more pronounced than in conventional ferroelectrics, however. Even though the absence of a non-polar matrix is stated, the model relies on the presence of paraelectric regions. It would be interesting to see whether the polar-slush model would also predict a nanodomain state for single component PMN.

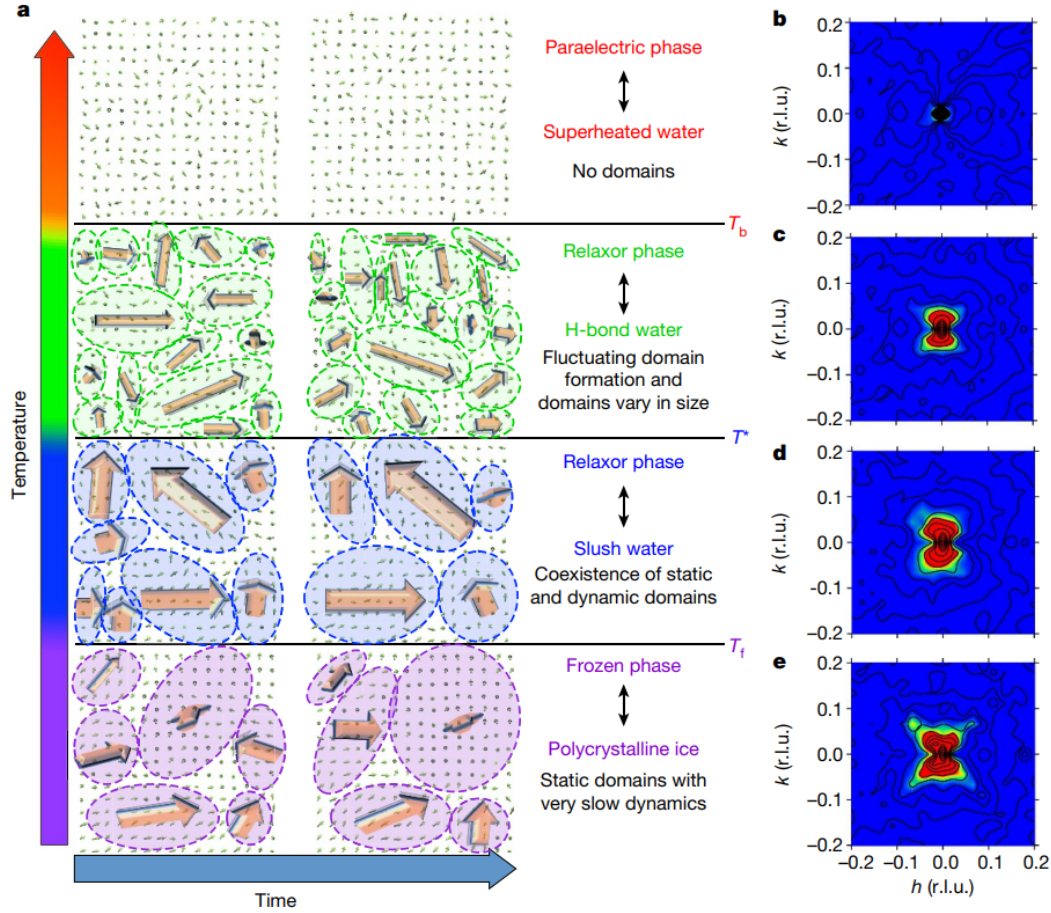


Figure 1.8. Polar-slush model for relaxor ferroelectric solid solution PMN-25PT and diffuse scattering intensities according to molecular dynamics simulations. (a) Four characteristic states are defined. A high-temperature paraelectric state with randomly oriented dipoles. Below T_B , dynamic nanodomains appear throughout the volume. Local correlations become stronger upon cooling, increasing the domain size and local order. Below T^* , polarization is strongly correlated within but weakly between nanodomains. A slow collective polarization rotation within individual nanodomains is facilitated by the coexistence of ferroelectric and paraelectric unit cells. Below T_f the domain state is mainly frozen. (b)-(e) The calculated diffuse scattering intensity around the (100) Bragg peak is consistent with experimental observations. Below T_B , a butterfly-shaped pattern appears, the intensity of which increases with reduced temperature. Adapted from Takenaka *et al.*, Ref. [18].

2 Experimental techniques

2.1 Sample preparation

All samples investigated in this study were purchased or provided by collaborators. The preparation of the individual compounds is described below.

2.1.1 Lead zirconate titanate

Samples were synthesized following a mixed oxide route.¹¹¹ Starting powders of PbO (99.9+ %, Sigma-Aldrich, U.S.), ZrO₂ (99.96 %, Tosho Corporation, JPN), Ti₂ (99.8 %, Alfa Aesar, U.S.), Nb₂O₅ (99.975 %, Alfa Aesar, U.S.), Fe₂O₃ (99.945 %, Alfa Aesar, U.S.), were weighed according to the desired composition and milled in isopropanol for 6 h. The mixtures were dried at ≈ 323 K and subsequently calcined in covered high-density alumina crucibles at 1223 K for 120 min with a 5 K/min heating rate. Calcined powders were milled in isopropanol for 6 h. A 5 % polyvinyl alcohol-water solution was used as binder to prepare mixtures with a 1:20 binder-powder ratio. The mixtures were uniaxially pressed into pellets with a nominal diameter of 10 mm and a pressure of 125 MPa. The pellets were sintered in covered alumina crucibles filled with powder of the same composition to prevent evaporation of volatile components. A two-step sintering procedure was applied with a heating rate of 3 K/min, 2 h dwell time at 873 K and 1473 K, and natural cooling in the furnace. The density of the samples was determined by Archimedes' method, and 96 % or more of the theoretical density was achieved. More details can be found in Ref. [111].

2.1.2 Lead magnesium niobate

PMN-A

The lead magnesium niobate (PMN) crystal named PMN-A was grown by a modified Bridgman approach.¹¹² The raw materials of (MgCO₃)₄ · Mg(OH)₂ · 5 H₂O (99 %, Alfa Aesar, Massachusetts, U.S.), Nb₂O₅, and PbO, (99.9 %, Sigma-Aldrich, Massachusetts, U.S.) powders are commercially available. The precursor PMN ceramics were synthesized by two steps columbite precursor method. The MgNb₂O₆ powders were pre-synthesized at 1423 K for 4 h. The precursor MgNb₂O₆ was mixed with PbO and calcined at 1073 K for 4 h to form PMN powders. The calcined powders with the addition of 1 wt.% binder were uniaxially pressed into pellets. To improve the green density, pellets were further cold isostatic pressed at 200 MPa for 5 min by using a Stansted Isolab EPG2540 (A) hydraulic press. Then PMN pellets were sintered at 1423 K for 2 h after a binder burn out process at 873 K for 2 h. The prepared pellets were charged into a cone-shaped platinum crucible (XRF Scientific Europe GmbH) with a diameter of 20 mm and 70 mm length

and sealed with a platinum lid. The conical space of the platinum crucible was filled with a stoichiometric mixture of MgNb_2O_6 and Pb_3O_4 powders. Here Pb_3O_4 (99 %, Sigma-Aldrich, Massachusetts, U.S.) was chosen to increase the oxygen content inside the crucible. This assemble set was loaded into a multi-zones tube furnace (Lenton, UK) equipped with a Crystalox CRT4000 Crucible Rotation/Translation Unit. To obtain a temperature gradient of 2 K/mm at the solid-liquid interface, two upper zones of 1638 K and a lower zone of 1433 K were achieved at a heating rate of ≈ 90 K/h. After the charged compounds were melted in the hot zones, the crucible was lowered down at a rate of 0.5 mm/h through the interface to crystallize PMN. After growth, the crystal was cooled down to ambient temperature with a cooling rate of 60 K/h. The PMN single crystal was oriented by X-ray Laue camera, and cut along (001) plane. An image of the as-received crystal obtained with an optical microscope is shown in Figure 2.1(a).

PMN-B

Crystal PMN-B was grown via flux method with $\text{PbO}-\text{B}_2\text{O}_3$ mixture as solvent.¹¹² The mixed raw powders, i.e., PbO , MgO , Nb_2O_5 , and solvent, were placed in a Pt-Rh crucible before it was closed and heated to 1353 K. Then, the crucible was cooled with ≈ 0.5 K/h to 1173 K and with ≈ 100 K/h to ambient temperature. The PMN crystal was then gently extracted from the crucible after etching in a hot acetic acid solution. An optical microscope image of the crystal that was used for measurements taken before electroding is presented in Fig. 2.1(b).

PMN ceramics

PMN ceramics were synthesized using PbO (99.9 %), MgO (98 %), and Nb_2O_5 (99.9 %) powders.⁵⁷ A mixture of PbO , MgO , and Nb_2O_5 in the molar ratio corresponding to the stoichiometric $\text{Pb}(\text{Mg}_{1/3}\text{Nb}_{2/3})\text{O}_3$ was high-energy milled in a planetary mill. The ceramics were prepared by pressing isostatically with 300 MPa and sintering in a double alumina vessel in PMN packing powder at 1473 K for 2 h. The heating and cooling rates were 2 K/min. The density of the ceramics measured by Archimedes' method was ≈ 96 % of the theoretical density. The median grain diameter was $d_{50} = (1.98 \pm 1.05) \mu\text{m}$.

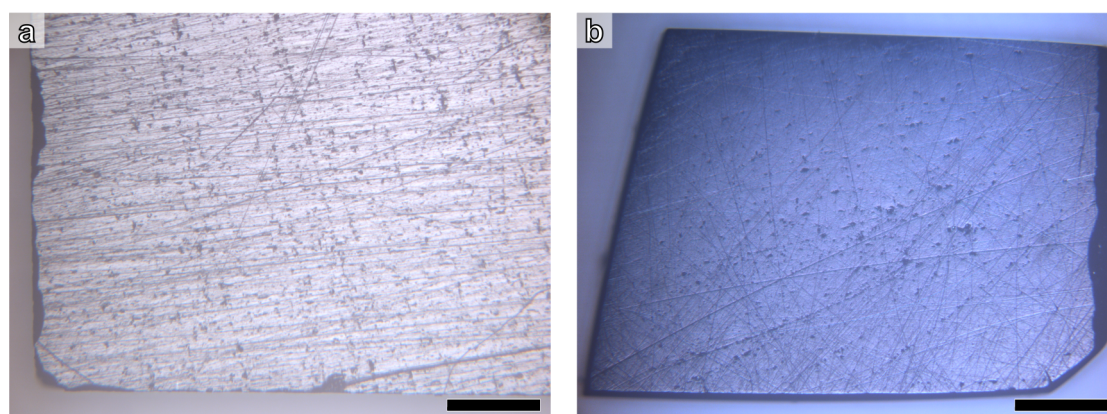


Figure 2.1. Optical microscopy images of lead magnesium niobate, PMN, crystals in as-received conditions. Both scale bars represent 500 μm . (a) Crystal [001]-PMN-A, and (b) crystal [001]-PMN-B.

2.1.3 Lead magnesium niobate lead titanate

Single crystals of lead magnesium niobate lead titanate with dimensions of $(10 \times 10 \times 0.5) \text{ mm}^3$ were purchased from TRS Technologies, Inc. (Zone melting, Pennsylvania, U.S.) and MSE Supplies LLC (Bridgman method, Arizona, U.S.). The optical microscope images of crystals in as-received conditions are shown in Figure 2.2. Samples were attached to a substrate with double-sided tape and cut with a diamond wire saw (Model 3032-4, Well, CH) into pieces of equal size before electroding. In addition, samples obtained from HC materials (Illinois, U.S.) and Microfine (Singapore, SG) used in Ref.[113] were investigated. A summary of the available compositions is given in Table 2.1.

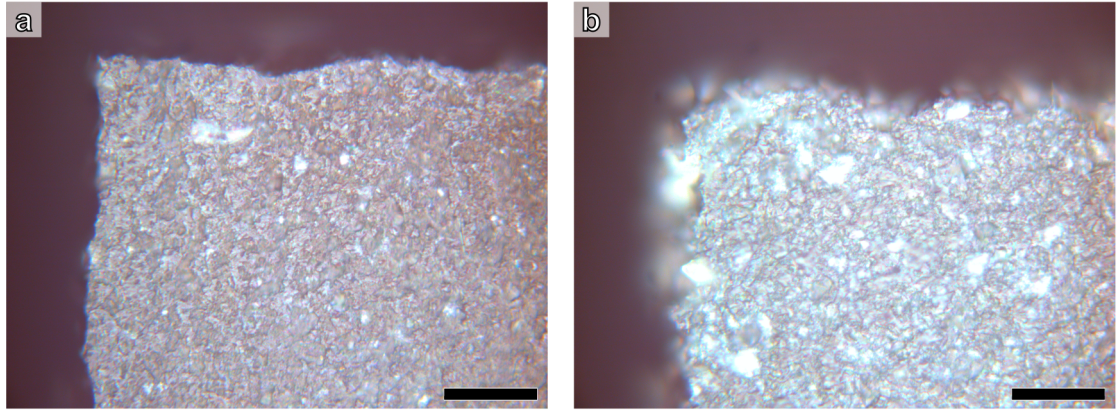


Figure 2.2. Optical microscopy images of PMN- x PT crystals in as received conditions. Both scale bars represent $500 \mu\text{m}$. Crystal obtained from (a) TRS Technologies, and (b) MSE Supplies.

Table 2.1. Investigated PMN- x PT crystals by manufacturer.

Company	Composition	Orientation	Comments
TRS Technologies, Inc	PMN- x PT	[001]	X2B
MSE Supplies TLLC	PMN- x PT	[001], [011], [111]	Type1 & Type2
HC Materials	PMN- x PT	[001], [011], [111]	$x = 29 \text{ \& } 32$
Microfine Materials Technologeis Pte Ltd	PZN-7PT	[001], [011], [111]	–

2.1.4 Electroding

Gold or platinum electrodes were sputter-coated with a sputter coater (EMS 575XD Turbo Sputter Coater, Electron Microscopy Sciences, Hatfield, U.S.). Before the deposition, all samples were immersed in analytical reagent grade propanol-2 (Fischer Scientific U.K. Limited, Loughborough, UK) and cleaned in an ultrasonic cleaner. The sputter chamber was evacuated to pressures of $5 \times 10^{-3} \text{ mbar}$ or less before argon gas with a purity of 99.9999 % was bled into the chamber. Electrodes were deposited under a pressure of $7 \times 10^{-3} \text{ mbar}$ in four cycles of 4 min duration each, with a deposition current of 40 mA. Based on the user manual of the sputter coater, a deposition rate between 10 and 30 nm/min was estimated for these parameters.

2.1.5 Cutting

Samples were cut with a diamond wire saw (Model 3032-4, Well Diamond Wire Saw SA, Switzerland) using a wire with a diameter of 0.3 mm and 60 μm particle size. Beforehand, a randomly chosen side was marked with a pencil to track the orientation of the samples with respect to each other. The samples were fixed on a substrate with double-sided tape. To protect the edges from chipping, the top surfaces were covered with tape too. After cutting, the tape was dissolved in acetone and the samples were cleaned in acetone and isopropanol in an ultrasonic cleaner.

2.1.6 Poling

Samples were immersed in silicone oil and fixed with a spring contact. Voltage was applied with a high voltage amplifier (Model 609D-6, Trek, Inc., U.S.). If not stated otherwise, samples were poled at ambient temperatures for 20 min. Alternating current poling was performed with ten cycles of a bipolar triangular electric field with an amplitude of 10 kV/cm and frequency of 1 Hz.

2.2 Characterization

2.2.1 Temperature-dependent dielectric permittivity

The complex relative dielectric permittivity, ε , was calculated from capacitance measurements of parallel plate-shaped samples using a precision LCR meter (HP4244A, Hewlett Packard, Palo Alto, California, U.S.) according to

$$\varepsilon = \frac{Ct}{A\varepsilon_0}, \quad (2.1)$$

where C is the capacitance, t the thickness of the sample, A is the electroded area, and ε_0 the vacuum permittivity. The loss tangent $\tan \delta$ was acquired simultaneously with the same device. The amplitude of the probing field was 0.02 kV/cm at maximum. Frequencies between 0.1 kHz and 10 kHz were measured with a temperature rate of 2 K/min.

A switch control unit (HP 3488 A, Hewlett Packard, Palo Alto, California, U.S.) allowed to

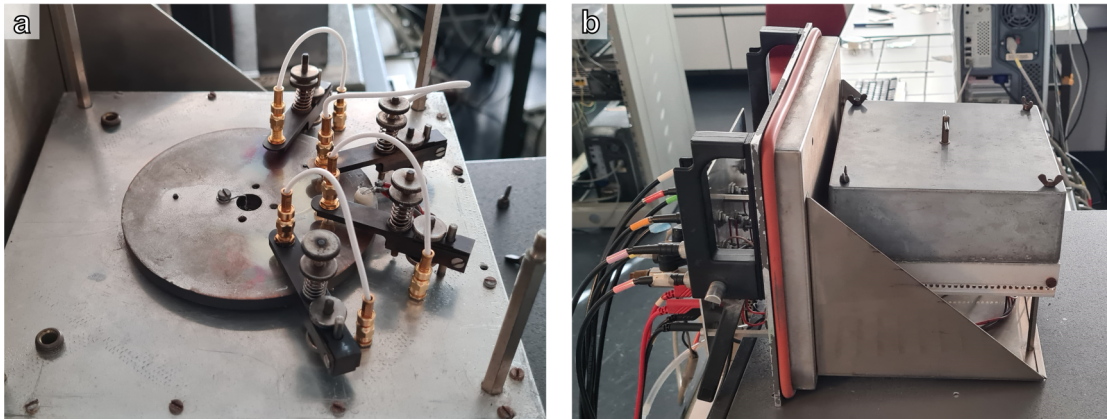


Figure 2.3. Experimental setup for measurements of the dielectric permittivity. (a) Probe stage with four-spring loaded contacts mounted on a (b) removable stage of an environmental test chamber. The probe stage is enclosed by a metal shield during measurements.

measure up to four samples during the same temperature-time program. Samples were mounted on a ≈ 5 mm thick metal plate with spring-loaded contacts, as presented in Figure 2.3(a). The sample stage was enclosed in a metal shield [Fig. 2.3(b)] and placed in an environmental test chamber (Delta9023, Delta Design Inc., San Diego, California, U.S.). Polytetrafluoroethylene (PTFE) shielded coaxial cables were used inside the test chamber.

The temperature was calculated from four-point resistance measurements of a Pt100 resistance temperature detector (RTD) using a multimeter (HP34401, Hewlett Packard, Palo Alto, California, U.S.). Active cooling was achieved by bleeding liquid nitrogen into the chamber through an electrically controlled valve. A LabVIEW program collected all data and regulated the temperature of the environmental chamber using a proportional-integral-derivative (PID) algorithm.

2.2.2 Dynamic pyroelectric current measurements

Dynamic pyroelectric currents, i_p , were measured with a custom-made device that combines an electrometer, an analog PID temperature controller, and a power supply. The essential circuit schematics are provided in Appendix A. The bias voltage feature was not used during any measurements of this study. Measurements were performed with a triangular temperature modulation with an amplitude between 2 - 4 K and a frequency of 10 mHz.

Samples were placed on a copper sample stage with concentric knife edges, as shown in Figure 2.4(a), to avoid secondary pyroelectric contributions that may arise in the case of sample clamping.¹¹⁴ The top surfaces of the samples were electrically contacted with a cantilever probe fixed on a micropositioner (XYZ 300TR, Quater Research & Development, Oregon, U.S.). Potential artifacts due to contact forces were evaluated by systematically changing the latter. In addition, a flexible tungsten wire probe with a radius of $0.5 \mu\text{m}$ (Model 72F, American Probe & Technologies, Inc., California, U.S.) was used instead of the cantilever probe depicted in Figure 2.4(a). No correlation between the contact forces used during this work and i_p could be established for both scenarios. During all measurements, samples were enclosed in a PTFE housing [Fig. 2.4(b)].

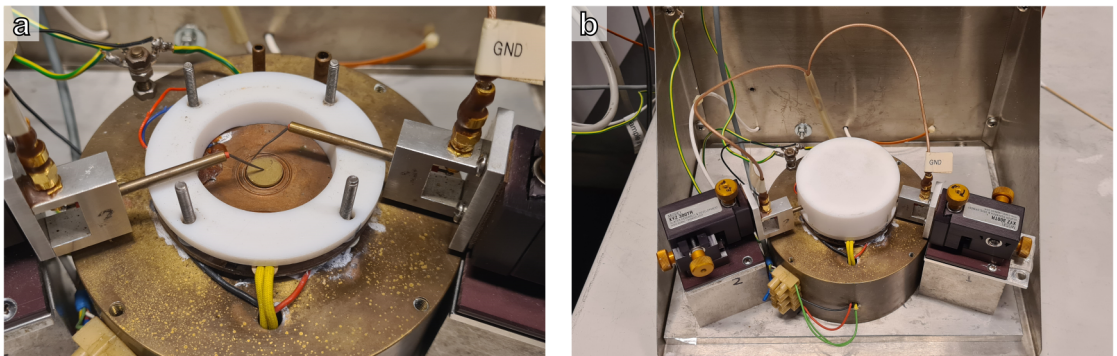


Figure 2.4. Experimental setup for measurements of dynamic pyroelectric currents. (a) A disk-shaped specimen is located in the center of a copper sample stage with concentric knife-edges. The temperature is modulated with a thermoelectric element located between the sample stage and a copper block that acts as a thermal sink. The top electrode of the sample is electrically contacted with a cantilever probe that is fixed to an XYZ-manipulator. (b) The sample stage is mounted on a removable stage of an environmental chamber. A PTFE shield covers the samples stage during measurements.

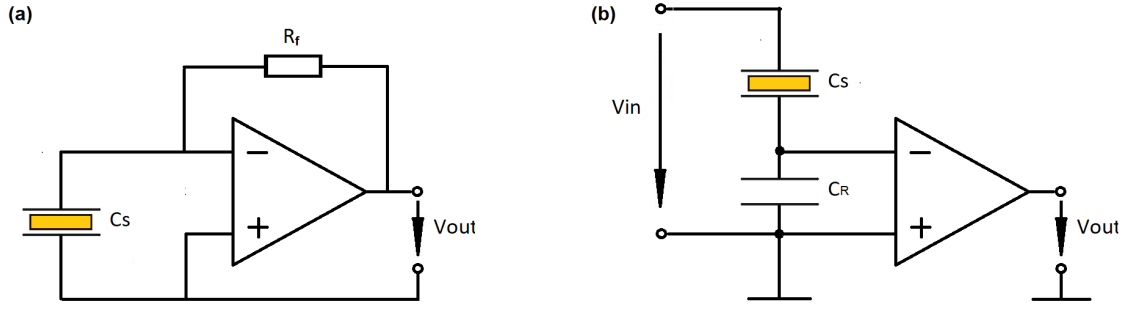


Figure 2.5. Diagrams of basic electronic measurement circuits. (a) Transimpedance amplifier, and (b) modified Sawyer-Tower circuit. ¹¹⁵

The sample stage temperature was periodically modulated with a thermoelectric element (Peltier-element). A Type T thermocouple provided a feedback voltage to the analog PID temperature controller. An external reference voltage signal, provided by an arbitrary waveform generator (HP33120A, Hewlett Packard, Palo Alto, California, U.S.), defined the setpoint of the temperature modulation. A Pt100 RTD located at the edge of the sample stage was measured in a four-point configuration with a multimeter (HP3478A, Hewlett Packard, Palo Alto, California, U.S.) to evaluate the temperature of the sample.

For current measurements, an electrometer as detailed in Appendix A was used. Its central electronic circuit is a transimpedance amplifier as depicted in Figure 2.5(a). In this configuration, the sample is connected between an operational amplifier's inverting and non-inverting input. The non-inverting input is connected to ground so that the operational amplifier will adjust its output voltage V_{OUT} to maintain the same (ground) potential, a *virtual ground*, at the inverting input. Under ideal conditions, the current through the sample and the feedback resistor R_f will be numerically identical so that

$$i_p = \frac{V_{OUT}}{R_f}. \quad (2.2)$$

The output voltage of the electrometer was measured with a multimeter (HP3478, Hewlett Packard, Palo Alto, California, U.S.) and recorded with a LabVIEW program that calculated i_p with a conversion factor of 945 pA/V. The theoretical cut-off frequency f_0 of the transimpedance amplifier was ≈ 16 mHz.

Theoretically, both electrodes of the sample are at the same potential and thus current measurements are performed in the absence of an electric field across its thickness. Due to non-ideal properties of operational amplifiers, however, such as the offset voltage V_{OS} and the input bias current I_B , small burden voltages may be present. I_B of the inverting input will flow through R_f and result in a voltage offset at the output. ¹¹⁶ This error does not affect the sample itself and might be neglectable. On the other hand, V_{OS} is present as a burden voltage across the sample. ¹¹⁶ In addition, any shunt resistance R_{shunt} between the non-inverting input and ground will cause a potential difference ΔV between the non-inverting input and ground of

$$\Delta V = I_B R_{shunt}, \quad (2.3)$$

that may cause an additional burden voltage across the sample. The used OPA627 operational amplifier has a maximum $|V_{OS}|$ of $500\ \mu\text{V}$ at $298\ \text{K}$ and a maximum $|I_B|$ of $10\ \text{pA}$.¹¹⁷ For a sample thickness of $1\ \text{mm}$, this V_{OS} results in a maximum electric field of $5\ \text{mV/cm}$ ($\approx 5 \times 10^{-6}\ \text{kV/cm}$). This is arguably a small field strength in comparison to common coercive fields.^{84,118,119} A burden voltage of similar magnitude due to I_B would require a R_{shunt} of $50\ \text{G}\Omega$ which is highly unlikely to be the case.

V_{OS} results primarily from geometrical differences and doping level variations of the internal architecture of the operational amplifier.¹²⁰ For the experimental conditions met during this work, the temperature and long-term drift of V_{OS} is considered to be minute¹²⁰ and V_{OS} is treated as constant.

2.2.3 Thermally stimulated current measurements

Thermally stimulated current measurements were performed with a variety of devices. The central part of this experiment was the custom-made furnace shown in Figure 2.6(a). A sample was placed inside a cylindrical metal shield and located on a ceramic disc in the center of the furnace [Fig. 2.6(b)]. To calculate the temperature, the voltage of a Type K thermocouple, the tip of which was located approximately $3\ \text{mm}$ below the sample, was measured with a multimeter (HP 3478A, Hewlett Packard, Palo Alto, California, U.S.). The phase transition temperature of a barium titanate single crystal was used to calibrate the system. All measurements were performed with $2\ \text{K/min}$.

Several sample fixtures and sample positions were explored during this thesis. A symmetrical configuration was desired to avoid thermal gradients. These may arise, for example, when a specimen is clamped on a surface that is not in thermal equilibrium with its surrounding gas phase or if the thermal transport is not symmetric across sample faces. Furthermore, it was noted that joining different Pt components through mechanical contact or welding significantly increased leakage currents at high temperatures. To address both issues, the sample was clamped between two Pt wires that were cut from the same wire and oriented in a vertical position. The

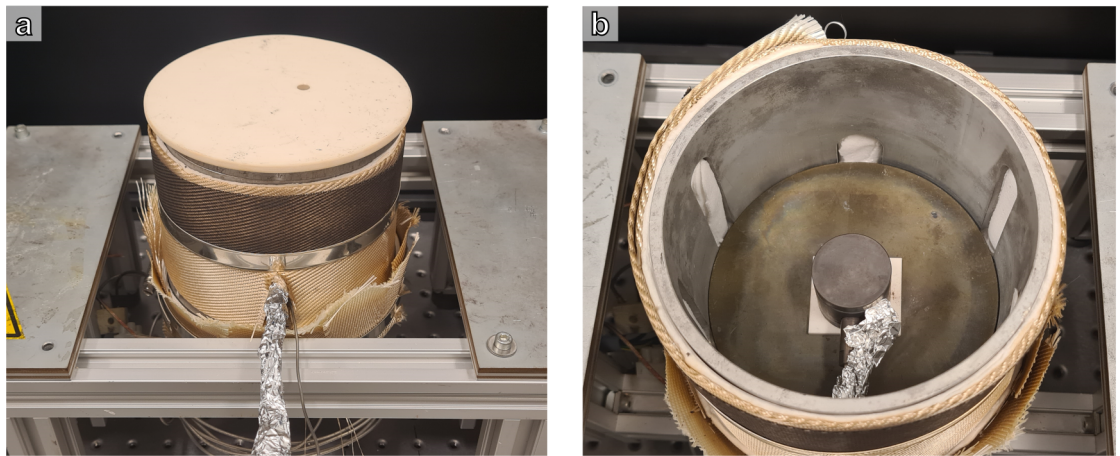


Figure 2.6. Custom-made furnace for thermally simulated current measurements. (a) Outside view, and (b) inside view.

underlying assumption is that thermal gradients, if any, parallel to the electrodes are less crucial than gradients through the thickness.

The temperature of the furnace was regulated with a PID controller (Model 2416, Eurotherm Limited, UK) and a Type K thermocouple for feedback. A power thyristor unit (A425, Eurotherm Limited, UK) operating in a pulsed mode was used for resistive heating of the furnace initially. This pulsed mode considerably contributed to noise, and the thyristor unit was, therefore, replaced with a 600 W constant voltage + constant current LED driver (HLG-600H-54B, Mean Well Enterprise Co., LTD., Taiwan). A drawback of this power supply is its minimum current output. To ensure complete cooling to ambient temperatures, it was, therefore, necessary to disconnect it from the line voltage with a mechanical timer (Typ12, Brennstuhl, GER) at the very end of experiments at temperatures between approximately 350 and 450 K. No correlation between this sudden power cuts and measured currents were noted.

Thermally stimulated currents were measured with three devices; a low-noise current preamplifier (Model SR570, Stanford Research Systems, Inc, California, U.S.), a picoammeter (Keithly 486, Keithley Instruments, Inc., Ohio, U.S.) and a custom-made device. Qualitatively similar results were obtained for all devices. The SR560 current preamplifier was operated with a gain of 100 pA/V without filters, bias, or offset, and its output measured with a multimeter (HP 3478A, Hewlett Packard, Palo Alto, California, U.S.). The picoammeter was used without filters in auto-range mode.

The custom-made device is based on a transimpedance amplifier circuit with an electrometer amplifier (ADA4530-1, Analog Devices, Inc., Massachusetts, U.S.) and an ultra-high resistance high stability hermetically sealed 10 G Ω feedback resistor (RX-1M1008FE, Ohmite Manufacturing Company LLC, Illinois, U.S.). 9V batteries powered ultralow noise linear regulators (LT3093 and LT3401, Analog Devices, Inc., Massachusetts, U.S.), which supplied stabilized voltages to the operational amplifier. V_{OUT} of the transimpedance amplifier was measured with a digital multimeter (34401A, Agilent, California, U.S.) and the current calculated with a conversion factor of 100 pA/V. The ADA4530-1 has a maximum $|V_{OS}|$ of 50 μ V and a maximum $|I_B|$ of 20 fA.

Samples were poled inside the setup up to voltages of 600 V with a high voltage power supply (Model PS350, Stanford Research Systems, Inc, California, U.S.), and in an external oil bath for voltages above 600 V with a high voltage amplifier (Model 609D-6, Trek, Inc., U.S.). Before measurements, samples poled in the oil bath were cleaned with acetone and isopropanol.

2.2.4 Direct piezoelectric measurements

Longitudinal direct piezoelectric coefficients, d_{33} , were measured with the custom-made Berlincourt meter shown in Figure 2.7. A small oscillatory force is applied to a sample and a piezoelectric reference material which are mechanically connected in series. d_{33} was calculated from the voltage drop across capacitors that were electrically connected in parallel to the sample, C_S , and to the reference material, C_R .

For measurements, the sample is clamped with a micrometer screw (Mitoyoto, JPN) on a stainless steel piston that acts simultaneously as a mechanical and electrical contact. The reference sample is located between the sample and a piezoelectric actuator, as depicted in Fig. 2.7(c). Both the sample and the reference material experience the same force. The force is modulated with an actuator that is driven by a high voltage amplifier (P-268, Physik Instrumente GmbH & Co.KG, GER). A sinusoidal driving signal with a frequency of 200 Hz was generated with

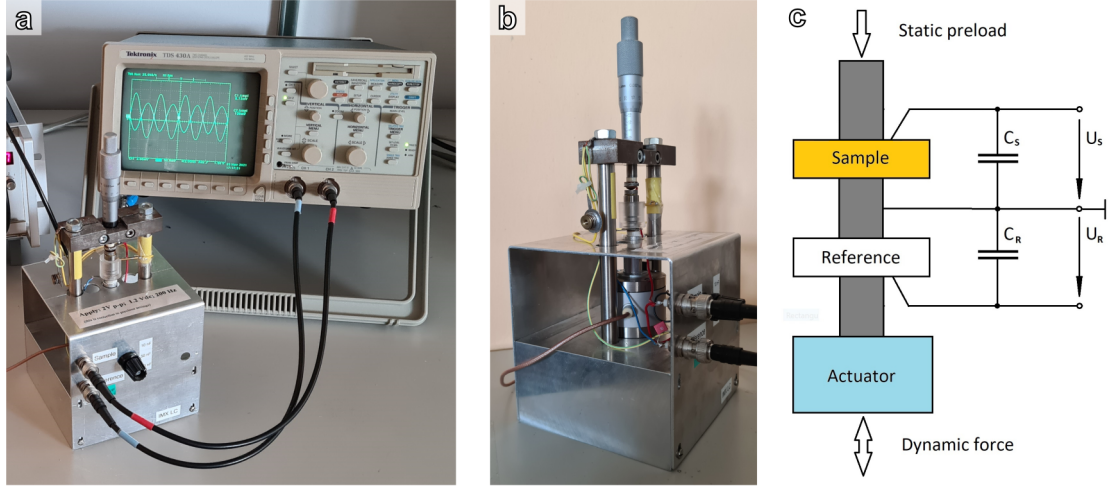


Figure 2.7. Custom-made Berlincourt d_{33} -meter. (a) Berlincourt-meter connected to an oscilloscope, (b) side-view with an actuator at the base, and (c) mechanical and electrical schematic.

an arbitrary waveform generator (33120A, Agilent, California, U.S.). The voltages across C_S and C_R were measured with a two-channel digitizing oscilloscope (TDS 430A, Tektronix, Oregon, U.S.). From the ratio of the voltage amplitudes, d_{33} was calculated according to

$$d_{33} = d_{33,R} \frac{C_S}{C_R} \frac{V_S}{V_R}, \quad (2.4)$$

with $d_{33,R} = 17.5 \text{ pm/V}$ and $C_S = C_R = 10 \text{ nF}$.

2.2.5 Ferroelectric hysteresis measurements

Polarization and strain electric field hysteresis loops were measured with a modified Sawyer-Tower circuit as described in Appendix B. The principle electronic circuit is described in Fig. 2.5(b). A sample is connected in series with a reference capacitor and a high voltage signal is applied. The polarization of the sample is calculated from the voltage drop across the reference capacitor. The experimental setup was connected to a data acquisition card that was controlled by a LabVIEW program. Samples were immersed in silicone oil and electrically contacted. The LabVIEW program generated a voltage signal that was amplified with a high voltage amplifier (Model 609D-6, Trek, Inc., U.S.). The voltage drop across the reference capacitor and the monitor output of the amplifier was recorded simultaneously with the data acquisition card.

For strain measurements, samples were mounted between two metallic pins with a radius of 0.25 mm. The lower pin was part of a brass cup filled with silicone oil. The upper pin was mounted to a notch type double compound rectilinear spring¹²¹ that ensured straight-line, *rectilinear*, motion along the axis of the pin (Figure 2.8). Technical drawings of the fixture can be found in Appendix C. The displacement of the sample was transmitted to a gold-coated mirror and measured with a fiber-optic displacement sensor (MTI-2100 Photonic Sensor, MTI Instruments, Inc., New York, U.S.) equipped with a high-resolution probe (MTI-2032RX, MTI Instruments, Inc., New York, U.S.). An oscilloscope (LC564, LeCroy, New York, U.S.) was used to measure the output of the displacement sensor and the output of the voltage amplifier. Data were recorded

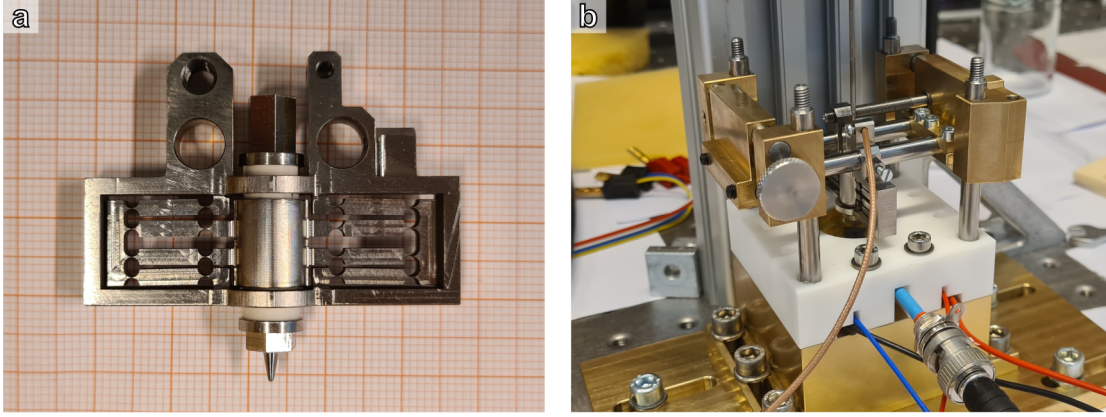


Figure 2.8. Sample fixture for strain and polarization measurements. (a) Notch type double compound rectilinear spring¹²¹ with electric contact at the bottom and mirror at the top, and (b) positioning mechanism.

with a LabVIEW program that calculated the strain with calibrated conversion factors provided by the manufacturer. The conversion factors were verified with quartz (Kistler, CH) and high-temperature PZT (Pz46, Meggit A/S, DK).

The temperature of the oil bath was controlled with two thermoelectric elements located between the brass cub and a brass block heat sink. A programmable power supply (PS2510G, Tektronix, Oregon, U.S.) and a system power supply (HP 6063A, Hewlett Packard, Palo Alto, California, U.S.) powered the thermoelectric elements. The resistance of a Pt100 RTD that was attached to a sapphire substrate at the bottom of the oil bath was measured in a four-point configuration with a multimeter (HP34401A, Hewlett Packard, Palo Alto, California, U.S.). The temperature was calculated with a LabVIEW-based PID algorithm.

2.2.6 Dynamic nonlinear polarization and strain measurements

The dynamic nonlinear polarization measurements were performed with the sample with digital lock-in amplifiers (SR830 DSP, Stanford Research Systems, Inc, California, U.S.). The sinusoidal voltage signal from the internal low-noise function generator of the lock-in amplifier was amplified with either a wideband power amplifier (7602M, Krohn-Hite, Massachusetts, U.S.) or a voltage amplifier (Type400, aixACCT Systems GmbH, GER) and applied to the sample. The voltage V_{OUT} across a resistor R connected in series with the sample was analyzed with a lock-in amplifier, and the data recorded with a LabVIEW program.

The harmonic components of the real and imaginary part of the output signal, $V_{OUT}^{(n)}$ and $V_{OUT}^{\prime(n)}$, were measured with the lock-in amplifier, and the coefficients of the Fourier series

$$P(t) = P_{\text{const}} + \sum_{n=1}^{\infty} [P^{(n)} \sin(n\omega t) + P^{\prime(n)} \cos(n\omega t)], \quad (2.5)$$

were calculated according to

$$P^{(n)} = \frac{V_{OUT}^{(n)}}{An\omega R}, \quad (2.6)$$

and

$$P''^{(n)} = \frac{V_{OUT}''^{(n)}}{An\omega R}, \quad (2.7)$$

where $P^{(n)}$ and $P''^{(n)}$ are the real and imaginary part of polarization and n the order of the harmonic. Equation (2.6) and Eq. (2.7) are derived in Appendix D. To ensure that most of the voltage is applied to the sample R was chosen to satisfy

$$R \ll \omega C, \quad (2.8)$$

where ω is the angular frequency of the driving voltage signal.

Strain measurements may have been performed simultaneously with a fiber optic displacement sensor (MTI-2100 Photonic Sensor, MTI Instruments, Inc., New York, U.S.) as described in Section 2.2.5. The temperature was regulated within ± 0.1 K during experiments. The output of the photonic sensor, V_{OUT} , was analyzed with a lock-in amplifier that was synchronized to the lock-in amplifier performing polarization measurements. The coefficients of the Fourier series of the displacement

$$u(t) = u_{\text{const}} + \sum_{n=1}^{\infty} [u'^{(n)} \sin(n\omega t) + u''^{(n)} \cos(n\omega t)], \quad (2.9)$$

were calculated according to

$$u'^{(n)} = V'^{(n)} S_u, \quad (2.10)$$

and

$$u''^{(n)} = V''^{(n)} S_u, \quad (2.11)$$

where $u'^{(n)}$ and $u''^{(n)}$ are the real and imaginary part of the displacement, n the order of the harmonic, and S_u the sensitivity of the photonic sensor.

The measurement was controlled and recorded with a LabVIEW program. Polarization and strain data were acquired simultaneously. Harmonic components were measured sequentially in ascending order for a given driving voltage.

3 Dielectric and electro-mechanical nonlinearities in ferroelectric materials

3.1 Motivation

In this chapter, the harmonic analysis of dielectric and electro-mechanical nonlinearities in ferroelectric materials is discussed. Nonlinearities are the consequence of material-specific properties and processes and can thus be used to study microscopic processes (such as nanointerfaces or nano-sized polar regions) by measurements of macroscopic properties. At the same time, this method has advantages over microscopic methods (such as piezoresponse force microscopy) because it directly measures the effect of nanoscale processes on the macroscopic scale, i.e., the scale relevant for most devices. In materials that can be sufficiently described by their lattice response, small nonlinearities are usually found. Strong nonlinearities governed by complex relationships are often observed in ferroelectrics and ferroelectric relaxors, in contrast, where several mechanisms can act simultaneously. These mechanisms are reflected in characteristic polarization- and strain-electric field hysteresis loops, the non-analytic form of which can make systematic studies of underlying processes difficult, however. In the following, the harmonic analysis of sub-coercive polarization- and strain-electric field hysteresis loops is presented as an approach to overcome this limitation.

This chapter contains previously published data from the following publication:

- L. M. Riemer, L. Jin, H. Uršič, M. Otoničar, T. Rojac, and D. Damjanovic, “Dielectric and electro-mechanic nonlinearities in perovskite oxide ferroelectrics, relaxors, and relaxor ferroelectrics”, [Journal of Applied Physics](#) **129**, 054101 (2021).

3.2 Dielectric and electro-mechanical nonlinearities

In dielectric materials that can be sufficiently well described by intrinsic lattice response (e.g., movement of atoms around equilibrium positions), rather weak nonlinearities are observed at not too large fields.¹²³ For most practical purposes, such materials are considered linear. Examples are sapphire or strontium titanate at room temperature and piezoelectric materials like quartz or aluminum nitride. However, when defects, dipolar clusters, domains, or other features in a material can readily respond to the field, their response is often nonlinear. With appropriate analysis, these nonlinearities may become visible even at weak fields where the linear lattice response is dominant. Rather strong nonlinearities may appear in ferroelectrics, relaxors, or relaxor ferroelectric solid solutions and are usually correlated to the motion of ferroic domain walls and mesoscopic polar structures.¹²⁴ Nonlinearities in dielectrics and ferroelectrics have

been studied intensively,^{125–127} while the interest in the nonlinear behavior of relaxors and relaxor ferroelectrics is more recent.^{65,112,128,129}

In the following, a large spectrum of different experimentally observed nonlinear behaviors in ferroelectric and relaxor-based materials is discussed and, when possible, a physical interpretation of the nonlinear data in terms of microscopic mechanisms is given. A simple formalism is presented, which permits us to draw some conclusions on dynamic processes taking place in the material even when underlying physical mechanisms are not well understood.

3.3 Nonlinear description

The most fundamental periodic time-dependent signals and a common excitation signal for physical experiments is a single sinusoidal,

$$F(t) = F_0 \sin(\omega t), \quad (3.1)$$

where F is the excitation signal (a driving field), t is the time, F_0 is the excitation signal amplitude, and ω is the angular frequency. A linear system will respond to this type of excitation with a sinusoidal response of the same frequency and may be shifted in time by a phase angle θ with respect to the excitation signal,

$$R(t) = R_0 \sin(\omega t) = m F_0 \sin(\omega t + \theta), \quad (3.2)$$

where R is the response, R_0 is the response amplitude, and m is a system-characteristic coefficient that quantifies the nonlinear response which may be frequency-dependent.¹³⁰ In the present work, F may represent the electric field, E , R the electric polarization, P , or strain, x , and m the dielectric permittivity, ϵ , or piezoelectric coefficient, d . For a linear system, m and θ are independent of F_0 . In general, however, the relationship between the excitation signal and the response is more complex than Eq. (3.2), and m and θ can depend on F_0 , i.e., E_0 . The material is then said to be nonlinear with respect to E_0 , or to be *field-dependent*. Often, F_0 is not only field-dependent but also dependent on history, i.e. *hysteretic*.¹³¹

In principle, the function $R(F)$ contains all field-dependent information of the system and can be conveniently displayed on an oscilloscope, either in the form of two separate time-dependent functions, $F(t)$ and $R(t)$ or in the form of a so-called *hysteresis loop* $R(F)$. Hysteresis loops present multiple values of R for most excitation values F and can come in many forms and shapes.¹³² This nonlinear, nonanalytical, and arbitrary nature of hysteresis loops makes analysis, comparison, and quantitative evaluation of data cumbersome. An approach to overcome these limitations is to analyze data in the frequency domain, where they can be represented with analytical functions.

Fourier's theorem states that arbitrary periodic functions can be represented as a series of weighted sinusoids and cosinusoids that are equidistantly spaced in the frequency domain by $\Delta\omega = 2\pi/T_\omega$, where T_ω is the period of the function.¹³³ The sinusoidal with $\omega = 2\pi/T_\omega$ is called the *fundamental* or first harmonic component. Waveforms with angular frequency $\omega_n = n\omega$ with $n > 1$ are called the n^{th} or *higher harmonic* components, and n the order of the latter. A general response function R can be derived in form of a Fourier series,^{134,135}

$$R(t) = R_{\text{const}} + \sum_{n=1}^{\infty} [R^{(n)} \sin(n\omega t + \theta^{(n)})] \quad (3.3)$$

$$= R_{\text{const}} + \sum_{n=1}^{\infty} [R'^{(n)} \sin(n\omega t) + R''^{(n)} \cos(n\omega t)], \quad (3.4)$$

with

$$R^{(n)} = \sqrt{(R'^{(n)})^2 + (R''^{(n)})^2}, \quad (3.5)$$

$$\tan(\theta^{(n)}) = \frac{R''^{(n)}}{R'^{(n)}}, R'^{(n)} = R^{(n)} \sin(\theta^{(n)}), R''^{(n)} = R^{(n)} \cos(\theta^{(n)}), \quad (3.6)$$

and

$$m'^{(n)} = \frac{R'^{(n)}}{F_0}, m''^{(n)} = \frac{R''^{(n)}}{F_0}, \quad (3.7)$$

where R_{const} is a constant (a "dc" term), $R^{(n)}$ is the amplitude, $\theta^{(n)}$ the phase angle, $R'^{(n)}$ is the amplitude of the in-phase component or real part, $R''^{(n)}$ is the amplitude of the out-of-phase component (quadrature) or the imaginary part, $m'^{(n)}$ is the real part of the material coefficient, $m''^{(n)}$ is the imaginary part (or loss) of the material coefficient, and superscript (n) indicates the order of the harmonic component respectively. In general, m is known as the material's susceptibility (here, dielectric susceptibility or piezoelectric coefficient). Note that the sign of the phase angle is determined by choice of the sign in the argument of the sinusoidal function in Eq. (3.3); in our case, it is a plus sign. Note that $R'^{(n)}$ and $R''^{(n)}$ (and thus also $\theta^{(n)}$) are, in general, functions of E_0 .¹²⁷ According to Eq. (3.7), we define the dielectric permittivity, $\varepsilon^{(n)}$, and the piezoelectric coefficient, $d^{(n)}$, of the n^{th} harmonic as

$$\varepsilon^{(n)} = \frac{P^{(n)}}{E_0}, \quad (3.8)$$

and

$$d^{(n)} = \frac{x^{(n)}}{E_0}, \quad (3.9)$$

where $P^{(n)}$ and $x^{(n)}$ are amplitudes of the n^{th} polarization and strain harmonic, respectively. Note that a simplified notation that emphasizes only the order of the harmonic is used, and matrix or tensor notation is omitted.¹³⁶ The last two would be redundant for this work since only the longitudinal measurement mode, for which polarization and strain are measured in the direction of the electric field, is discussed. The phase angle of the n^{th} polarization, $\delta^{(n)}$, and strain, $\phi^{(n)}$, harmonic are defined following Eq. (3.6) as

$$\delta^{(n)} = \tan^{-1} \left(\frac{P''^{(n)}}{P'^{(n)}} \right), \quad (3.10)$$

and

$$\phi^{(n)} = \tan^{-1} \left(\frac{x''^{(n)}}{x'^{(n)}} \right). \quad (3.11)$$

Through-out this work δ and ϕ will be used whenever discrimination between polarization and strain response is necessary, while θ will be used for general mathematically derived statements and definitions.

Only non-centrosymmetric materials may be piezoelectric; therefore, the first harmonic and all odd number higher harmonics should not appear in strain in centrosymmetric materials (for example, unpoled ceramics). For the present purpose, we shall not discuss separately the electrostrictive effect,¹³⁷ $x(E) = ME^2$, where M is the electrostrictive coefficient, which appears in all dielectric materials and will consider it only within the total strain response, together with the piezoelectric effect. Similarly, it is usually assumed that the induced polarization should not exhibit even number harmonics in centrosymmetric materials.^{130,138,139} However, materials of interest for this study are rarely ideal and both odd and even harmonics, in general, appear in the Fourier expansion of both polarization and strain response.

In principle, it is possible to measure the time-dependent response of a system, $R(t)$, and mathematically perform a Fourier transform to obtain harmonic components. An elegant experimental alternative is the use of lock-in techniques. Lock-in techniques can filter small signals of a specific frequency out of large background noise. Tunable bandpass filters with quality factors above 10^8 and a noise bandwidth below 0.001 Hz can be achieved by taking advantage of the orthogonality of sine and cosine functions.¹⁴⁰ This makes lock-in amplifiers effective tools to extract harmonic components directly.

A word of caution may be necessary at this point. Electronic instruments (such as signal generators and amplifiers) can add distortions and a parasitic direct current, dc, bias to driving signals. A distorted alternate current, ac, driving signal necessarily adds higher harmonics to the effective material output signal, even for perfectly linear materials. A dc-bias field will cause a first harmonic (piezoelectric-like) strain response even if the material is centrosymmetric in the unbiased condition.¹⁴¹ While instrumental distortions may appear small when looking at the instrument specifications, they can be significant when investigating thin films, where small signals translate into large electric fields, and in bulk materials, which require considerable amplification of driving signals. Also, amplifiers may act as filters and attenuate dynamic signals at high frequencies, distorting both phase and amplitude of driving fields.

3.4 Harmonic analysis of ferroelectrics

As mentioned previously, lock-in techniques can directly measure fundamental and harmonic components of signals. When applied to polarization or strain measurements, they can thus be used to obtain Fourier expansions of polarization- or strain-electric field hysteresis loops. A single hysteresis loop in the polarization or strain vs electric field plane is thereby represented by a set of amplitudes and phase angles (Figure 3.1). In this representation, the shape of hysteresis loops can be fully quantified if a sufficient number of harmonics is used. The first three harmonics ($n = 1, 2, 3$) are usually sufficient for the basic analysis of hysteresis loops at sub-coercive driving fields. More complex hysteresis loops, however, may require additional terms.¹⁴²

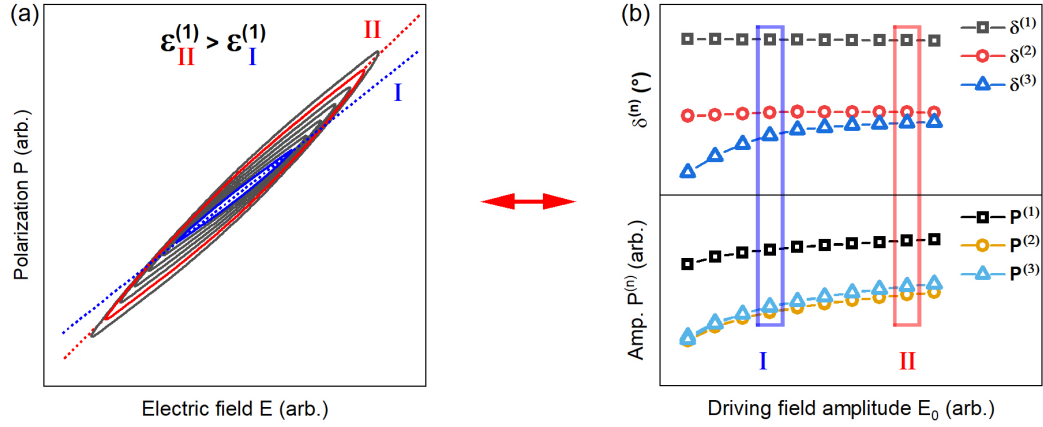


Figure 3.1. Polarization, P , electric field, E , hysteresis loops, and Fourier expansion, $P(t)$, measured for a commercially available PIC151 lead zirconate titanate, PZT, sample. (a) Polarization hysteresis loops in polarization vs. electric field space for different maximum electric field amplitudes, E_0 . (b) Amplitudes, $P^{(n)}$, and phase angles, $\delta^{(n)}$, of the first three harmonic sinusoids of the corresponding Fourier expansion of the hysteresis loops shown in (a). The components of the Fourier series are determined experimentally using a lock-in technique. The red and blue hysteresis loops in (a) are represented by the set of coefficients framed in red and blue in (b). Only the first three out of an infinite number of harmonics are given. For the two hysteresis loops highlighted in (a), the dotted lines illustrate the linear polarization response, which is contained in the amplitude of the first harmonic of polarization, $P^{(1)}$.

Being able to determine and track slight changes in the shape of hysteresis loops to varying excitation levels enables detailed studies of electric field-dependent nonlinearities and the underlying mechanisms. To correlate specific nonlinear patterns to mechanisms such as the motion of domain walls and nano-sized polar entities, a phenomenological model is needed, which makes a definitive prediction of nonlinear behavior. The model can then be verified experimentally by measuring harmonic components. The best-known example is the Rayleigh-Néel model^{143,144} for domain wall motion in a random potential, which will be discussed in some detail in Sections 3.5 to 3.7. This model predicts that only odd harmonics are present in the Fourier expansion of the polarization response and that the phase angle of all higher harmonics is -90° . Therefore, a Fourier analysis of experimental data allows for a relatively straightforward verification of this model. However, even if a model is not available, which is most often the case, especially when the nature of mesoscopic objects is not well understood, at least some details of the dynamic behavior of the hypothetical mesoscopic objects can be deduced from the nonlinear experimental data. Such examples will be discussed in Sections 3.5 to 3.7 for acceptor-doped, so-called *hard* ferroelectrics, and ferroelectric relaxors.

In general, the results of Fourier analysis can be interpreted in three ways. The first is based on the geometric description of harmonic components, which is always possible. The second is the interpretation based on the existing models and theories that apply to that particular system. The theory predicts a definite nonlinear response, which can then be verified experimentally. While such theoretical background exists for some types of motion of ferroic domains (for example motion of domain walls in donor-doped, so-called *soft* ferroelectrics), it is missing or is insufficiently developed for other polar objects (nano-sized polar regions or defect clusters) and their interaction with ferroic domains. The third way is a phenomenological interpretation, where

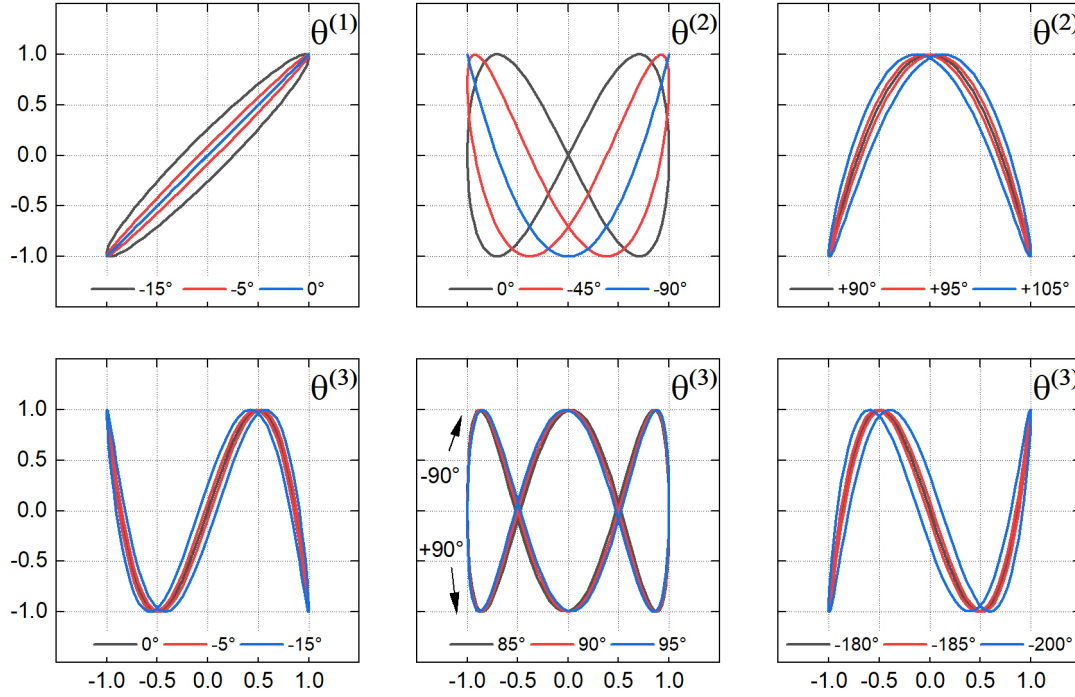


Figure 3.2. Representation of the first three harmonic vs. the fundamental sinusoids for various values of the phase angles, $\theta^{(n)}$. The vertical axis represents $P_n \sin(\omega t)$ and the horizontal $E_0 \sin(\omega t + \theta^{(n)})$.

materials under investigation and their response are compared to well-understood systems.

3.5 Geometric interpretation

To understand how different harmonics can be correlated to the response of materials, we start with a purely formal, geometric approach, which may reveal important details of nonlinear processes. It is illustrative to plot fundamental ($n = 1$) and higher harmonic components ($n > 1$) as a function of a sinusoidal driving field, as shown in Figure 3.2. The resulting curves represent *Lissajous* curves with frequency ratios $1:n$, where n is the order of the harmonic. In general, odd harmonics represent anti-symmetric and even harmonics symmetric responses. Due to the orthogonality of sinusoids and cosinusoids, only the out-of-phase component of the first harmonic contributes to the area of hysteresis, whose physical meaning may be related to energy loss.^{131,145,146} All other harmonics merely change the shape of the overall hysteresis loop. In particular, the in-phase component of odd harmonics ($\theta^{(2k+1)} = 0^\circ$) and components with $\theta^{(2k+1)} = 180^\circ$ for $k > 1$ bend hysteresis loops (most notably the tips of the loops), while out-of-phase components redistribute the hysteresis area. For even harmonics, the opposite is true. Out-of-phase components ($\theta^{(2k)} = 90^\circ$ and -90°) bend hysteresis loops, while in-phase components redistribute hysteresis area.

As mentioned before, the obtained Lissajous curves have symmetry relations that depend on the parity of the harmonic component. It is seen in Fig. 3.2 that curves of odd harmonics are symmetric with respect to the origin, while curves for even harmonics are symmetric with respect to the ordinate. Some $\theta^{(n)}$ values, for example, $\theta^{(3)} = \pm 90^\circ$, can result in curves that differ only in the sense of rotation. This rotation will define which part of the total hysteresis loop is

expanded and which part is contracted by a given harmonic. As will be seen later, a contraction in the central part of a hysteresis loop is a defining feature of hard (acceptor-doped) perovskite oxide ferroelectrics.¹⁴² Even though it is mathematically possible to obtain a clockwise rotation of (first harmonic) strain- and polarization-electric field hysteresis loops (for phase angle $0^\circ < \theta^{(1)} < 180^\circ$), it is thermodynamically forbidden for polarization, as it would represent a net gain of energy.¹⁴⁶ This limitation does not apply for electro-mechanical hysteresis loops with mixed mechanical and electrical functions, such as $x(E)$, where the area of the hysteresis does not have units of energy.¹⁴⁶ In the following, the first three harmonic components are discussed in more detail.

The first harmonic or fundamental component contains the linear response of a system (and possesses, in general, a nonlinear response as well). In the case of the data presented in Fig. 3.1, $\varepsilon^{(1)}$ can be calculated using Eq. (3.8) as the quotient of $P^{(1)}$ and E_0 , while $d^{(1)}$ could be calculated from the corresponding strain measurements. It is seen that the dielectric permittivity increase with increasing E_0 , as one would expect for a nonlinear material. Mechanisms contributing to hysteresis can be of various origins, including conductivity, displacement of ferroelectric and ferroelectric-ferroelastic domain walls, and dipole reorientation. In the case of the data in Fig. 3.1, the hysteresis loops are dominated by irreversible domain wall motion.¹⁴⁷ The phase angle of the first harmonic respects the symmetry relations of the corresponding tensor property. This implies that the phase angle of the first harmonic in polarization for a dielectric without loss has to be zero, while the phase angle of the first harmonic in strain for a material without loss can be either 0° or 180° . The actual observed value will depend on the crystallographic orientation or, in the case of ferroelectric materials, on the poling direction.

The second harmonic represents responses that are invariant to the sign of the applied excitation field (cf. Fig. 3.2). Switching of 180° domains and other polar dipoles can contribute to the second harmonic response.¹³⁷ In this case, the amplitude of the second harmonic in strain is directly related to the electrostrictive response, while the second harmonic in polarization leads to asymmetry of polarization hysteresis loops. Switching of 180° domains and the piezoelectric effect together may lead to the so-called *butterfly loops* in strain, which are sometimes interpreted as the electrostrictive effect.¹⁴⁸ Incidentally, it has been shown that the displacement of 180° domain walls may contribute to the piezoelectric effect if the polarization on both sides of domain walls are not equal.¹²⁸ This is a reasonable assumption in thin films and polycrystalline materials due to the complex internal field distribution.

As the second harmonic in strain represents electrostriction, it is always present regardless of the material's symmetry. The ideal case of pure intrinsic electrostriction results in $\phi^{(2)} = -90^\circ$ for positive or $\phi^{(2)} = +90^\circ$ for negative¹⁴⁹ electrostrictive coefficients, independent of the orientation of the sample or the poling direction. It can be shown that in perfect centrosymmetric materials, the second and all higher even harmonics in polarization (but not in strain) should vanish.¹⁵⁰ In experimental physics, perfect symmetry may be considered an idealization. Asymmetry may arise on different length scales of materials, reflecting physical processes or be induced artificially by constant external field or other boundary conditions. Therefore, the presence of a second harmonic component itself may not serve as a robust indicator of a given mechanism or material's true symmetry, especially for thin specimens where weak external forces can generate huge fields. However, variations and anomalies of the second harmonic may yield valuable insights. An example of intentionally induced asymmetry is the alignment of ferroelectric domains by the application of electric fields larger than the coercive field, E_c , so-called *poling*. Experimentally po-

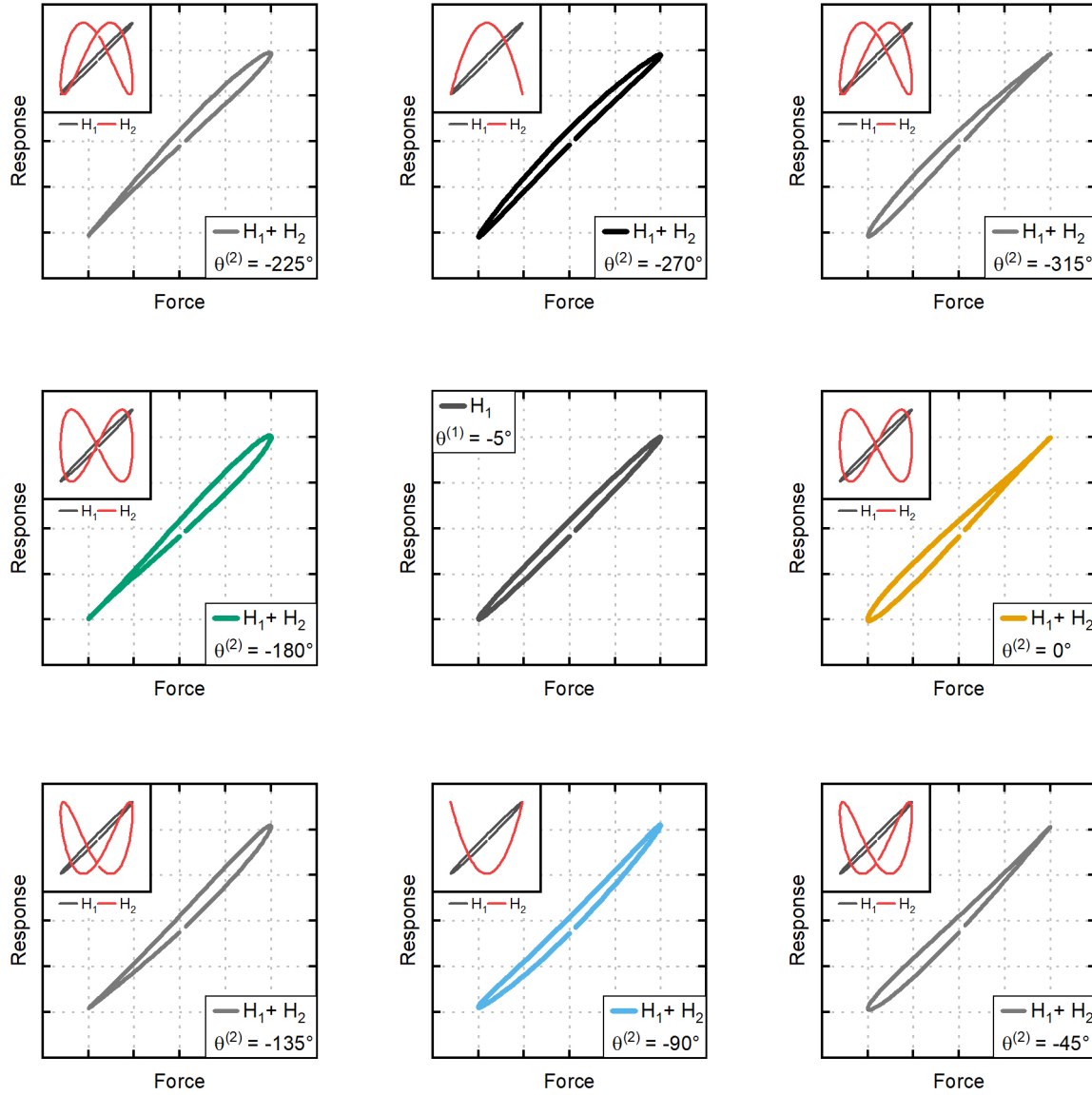


Figure 3.3. Geometric description of the combination between first and second harmonic components. Insets depict the first and second harmonic components individually. The central graph presents the first harmonic component with a phase angle $\theta^{(1)} = -5^\circ$.

larized samples show a $\delta^{(2)}$ around $+90^\circ$ or -90° dependent on the orientation of the polarization with respect to the driving field. The superposition of first and second harmonic components for different $\theta^{(2)}$ can be found in Figure 3.3.

The third harmonic phase angle of polarization, $\delta^{(3)}$, has been proven to be a sensitive indicator for different processes operating in ferroic materials. Phase angles between 0° and -240° (negative angles measured clockwise) have been observed experimentally and related to different underlying mechanisms. Polarization saturation in lead magnesium niobate (PMN) and barium strontium titanate (BST) have been correlated to $\delta^{(3)} \approx 0^\circ$.^{133,151} The displacement of ferroelectric and ferroelectric-ferroelastic domain walls in soft ferroelectric materials as described by the Rayleigh-Néel model has been correlated to $\delta^{(3)} \approx -90^\circ$.^{144,151,152} For materials with absent or

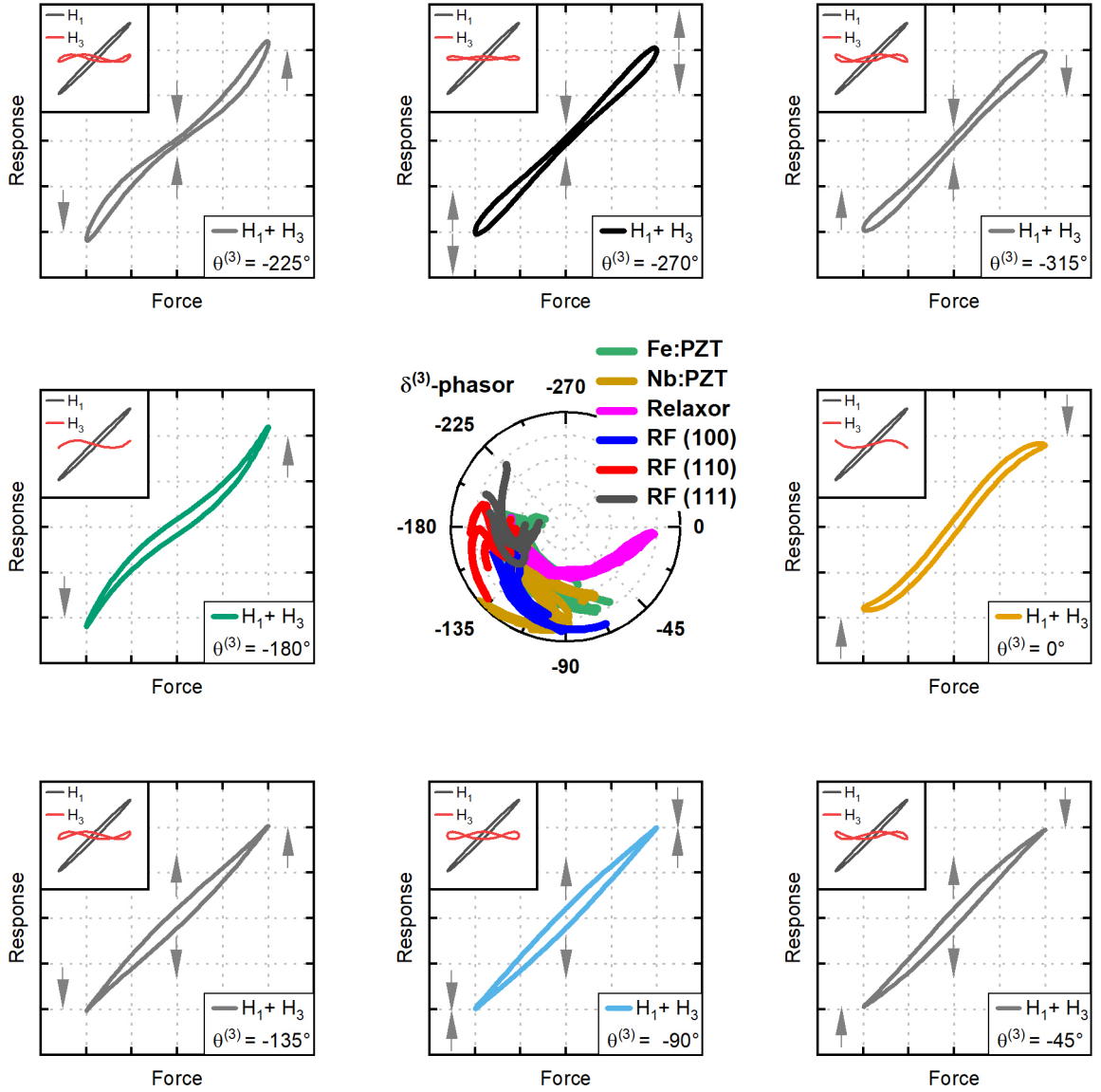


Figure 3.4. Geometric description of the combination between first and third harmonic components, and phasor diagram for commonly observed phase angles of the third harmonic of polarization $\delta^{(3)}$: 0° , indicating response saturation; -90° , indicating Rayleigh behavior; -180° , indicating polarization response similar to most non-ferroelectric dielectrics and hard ferroelectrics, -270° , indicating polarization loop pinching as seen for hard ferroelectrics (experimentally only -240° are usually observed because of competing contribution from a dynamic component with $\delta^{(3)} = -180^\circ$). The phasor diagram in the middle is constructed using more than 40 individual measurements as illustrated in Figure E.1 in Appendix E. RF stands for relaxor ferroelectrics: PZN-4.5PT, PZN-7PT, PMN-28PT, PMN-33PT. Relaxor: PMN ceramics, PMN crystal with $[100]_{pc}$ orientation. Nb:PZT stands for 1 at.% Nb-doped PZT ceramics with Zr/Ti ratio: 42/58, 52/48, and 58/42. Fe:PZT stands for 1 at.% Fe-doped PZT with Zr/Ti ratio: 42/58, 52/48, and 58/42.

weak extrinsic contributions such as dielectric or piezoelectric materials like sapphire, strontium titanate at room temperature or quartz, hard ferroelectrics, or in many materials for weak driving fields, $\delta^{(3)} \approx -180^\circ$. For hard-doped lead zirconate titanate, $\text{Pb}(\text{Zr}_{1-x}\text{Ti}_x)\text{O}_3$ (PZT), under high driving fields, where pinching of the polarization electric field loops becomes apparent,¹⁴² and for

some lead-based relaxor-ferroelectric solid solutions when poled along $\langle 111 \rangle_{\text{pc}}$ $\delta^{(3)} \approx -240^\circ$ has been measured. The third harmonic phase angle of strain $\phi^{(3)}$ has been studied less extensively and will be explored in this work. The general influence of $\theta^{(3)}$ on the shape of hysteresis loops is illustrated in Figure 3.4.

An overview of commonly measured values for $\delta^{(3)}$ and their evolution with E_0 are presented in the phasor diagram in the centre of Fig. 3.4. An example of a detailed analysis of the nonlinear polarization in lead magnesium niobate lead titanate PMN-*x*PT solid solutions in terms of $\delta^{(3)}$ can be found in Ref. [65]. Evolution of $\delta^{(3)}(E)$ across the phase diagram together with microscopic scanning transmission electron microscopy studies aided in the identification and discovery of a new microscopic mechanism contributing to the macroscopic properties.

3.6 Theoretical interpretation

One example of a definite theoretical prediction of nonlinear behavior is the well-known Rayleigh model. It describes the interaction of moving interfaces with pinning centers in a general framework that has attracted broad interest in various fields of science. It was described empirically first for magnetic systems by Rayleigh,¹⁵³ derived theoretically by Néel,¹⁴³ and later by Kronmüller,¹⁵⁴ introduced to ferroelectric systems by Turik,¹⁵⁵ and discussed for the piezoelectric effect in ferroelectrics by Damjanovic and Demartin.¹⁵⁶ Presently, there is no firm experimental evidence that the Rayleigh model is valid for strain-stress measurements in ferroelectric materials with ferroelectric-ferroelastic domains. In the only available study known to the authors, the Young modulus as a function of stress amplitude is not a strictly linear function,¹⁵⁷ as required by the Rayleigh model. On the contrary, the available evidence (dependence of friction on stress amplitude) indicates that the model may not be valid for strain-stress relation in purely ferroelastic materials. This raises interesting questions on the mechanisms behind the model's validity for ferroelectric-ferroelastic domain walls contributing to mixed electro-mechanic phenomena in ferroelectric and its purported absence for purely ferroelastic walls in ferroelastic materials.¹⁵⁸

The interaction of ferroelectric domain walls with pinning centers was investigated from the early days of ferroelectricity. Its detailed understanding may allow for the effective tailoring of properties. It was shown that domain wall movement in soft ferroelectrics results in polarization- and piezoelectric strain-electric field hysteresis loops that can be described by the Rayleigh equations for polarization,^{124,125,159}

$$P(E) = (\epsilon_{\text{init}} + \alpha_\epsilon E_0)E \mp \frac{\alpha_\epsilon}{2}(E_0^2 - E^2), \quad (3.12)$$

and strain

$$x(E) = (d_{\text{init}} + \alpha_d E_0)E \mp \frac{\alpha_d}{2}(E_0^2 - E^2), \quad (3.13)$$

where E is an electric field value smaller or equal to the electric field amplitude E_0 , ϵ_{init} is the intrinsic relative dielectric permittivity, α_ϵ is the Rayleigh coefficient of dielectric permittivity, d_{init} is the intrinsic piezoelectric coefficient, and α_d is the Rayleigh coefficient of the piezoelectric coefficient. The "-" sign in Eqs. (3.12) and (3.13) corresponds to increasing and the "+" sign to the decreasing electric field values. The polarization and strain at zero electric field are given as $\mp \frac{\alpha}{2} E_0^2$. Nonlinearity and hysteresis are directly coupled and completely described by the corresponding

Rayleigh coefficient α . The Rayleigh model does not take into account rate-dependent loss mechanisms, the only contribution to hysteresis in Eqs. (3.12) and (3.13) come from irreversible jumps of domain walls.¹³¹ Note that $\varepsilon_{\text{init}}$ and d_{init} may contain linear contributions from domain wall motion.

Eqs. (3.12) and (3.13) cannot *a priori* identify the underlying microscopic mechanism. These may be revealed by the theoretical models^{144,154} that derive these equations and that have been subsequently confirmed in numerous, more or less direct experiments.^{94,125} Some information about the dynamics of the unknown objects can be reached by considering purely formal predictions of the empirical equation along the lines discussed in Section 3.5. For example, the Fourier transform of Eq. (3.12), given in Eq. (3.14), indicated that the contributing objects might move reversibly (the linear component of the first harmonic) and irreversibly (all other terms) and that every irreversible, hysteretic motion is at the same time nonlinear (all term containing α_ε). Such insights pose a number of requirements on the model, which Néel has demonstrated in his derivation of the Rayleigh relations. Another purely formal insight, can be reached by taking the Preisach approach^{160–163} that identifies the distribution of hypothetical internal and coercive fields associated with the units responsible for the Rayleigh behavior. There is little doubt that the objects that dominate Rayleigh's behavior in ferroelectric materials are domains walls. The nature of the pinning centers that define the energy potential is less certain but essential for the understanding of microscopic mechanisms of nonlinearity and hysteresis.

Kronmüller has related dislocation density in magnetic materials (pinning defects in that case) with the Rayleigh parameters¹⁵⁴ showing that the model predicts $\alpha \sim 1/\rho_d$, where ρ_d is the dislocation density. It is interesting to compare this prediction with the experimental data in ferroelectric materials.^{135,164} Hagemann reports data for acceptor-doped barium titanate, BT, for which the Rayleigh model is not valid, but the slope of $\varepsilon(E)$ indeed decreases with increasing concentration of the dopant. Morozov *et al.* presented data for both soft and hard PZT¹³⁵. The soft PZT exhibits $\alpha \sim C_{\text{Nb}}$ where C_{Nb} is the niobium concentration, which seems to contradict the theoretical prediction. In fact, this may not be the case, and the actual situation is more subtle than that. As the higher concentration of $\text{Nb}_{\text{Ti}}^{+1}$ most likely leads to a lower concentration of oxygen vacancies, V_{O}^{+2} , this behavior, in fact, may reveal that the actual pinning centers in both hard and soft PZT are oxygen vacancies. This illustrates how modeling nonlinear properties in combination with experimental data can help identification of details of atomistic mechanisms operating in ferroelectrics.

The Rayleigh model assumes the motion of domain walls in a perfectly random energy potential, which may be difficult to achieve in real systems. Thus, deviations from the predicted behavior are often observed, especially at very weak and strong fields. There are two approaches to explain this behavior. It is useful here to recall the results of the Preisach model. Put simply, it says that the Rayleigh model arises in a system that consists of units that can be described by internal bias and coercive fields which have equal distribution (probability). So, a (small) departure from this ideal distribution would lead to a different dependence of the response on the field, but that does not mean that the mechanism is completely different if the distribution was ideal.^{165,166} In the author's opinion, it is justified to speak of Rayleigh-like systems as long as hysteresis and nonlinearities are closely related, i.e., one can be calculated from the other¹⁵⁹ using Eqs. (3.12) and (3.13) or alternative representations that preserve this link between nonlinearity and hysteresis. If this is not the case, other processes in which nonlinearity and hysteresis emerge

from different mechanisms may dominate.¹³⁵ It would be interesting to see which of these cases is valid for strain-stress relations in ferroelectric materials. The deviation from the Rayleigh model may thus contain information on the distribution of pinning centers in a material, their strength, the presence of non-domain related processes such as charge transport, etc.¹³⁵

The Rayleigh coefficient is often used as a measure to quantify extrinsic domain wall-related contributions to dielectric and piezoelectric properties. To justify this approach, it has to be verified that the material under investigation obeys the Rayleigh equations. To obtain objective criteria for this it is convenient to convert Eq. (3.12) or Eq. (3.13) to an analytical form via expansion into Fourier series,

$$P(t) = (\varepsilon_{\text{init}} + \alpha_{\varepsilon} E_0) E_0 \sin(\omega t) + \sum_{1,3,5,\dots} \frac{4\alpha_{\varepsilon} E_0^2 \sin\left(\frac{\pi n}{2}\right)}{\pi n(n^2 - 4)} \cos(n\omega t), \quad (3.14)$$

and

$$d(t) = (d_{\text{init}} + \alpha_d E_0) E_0 \sin(\omega t) + \sum_{1,3,5,\dots} \frac{4\alpha_d E_0^2 \sin\left(\frac{\pi n}{2}\right)}{\pi n(n^2 - 4)} \cos(n\omega t). \quad (3.15)$$

In this form, several criteria for the justification of the use of Rayleigh equations for the interpretation of data are given. First, the in-phase components of the piezoelectric coefficient of the first harmonic are linear functions of the driving field amplitude,

$$\varepsilon'^{(1)}(E_0) = \varepsilon_{\text{init}} + \alpha_{\varepsilon} E_0, \quad (3.16)$$

and

$$d'^{(1)}(E_0) = d_{\text{init}} + \alpha_d E_0. \quad (3.17)$$

Second, the amplitudes of higher harmonics are quadratic functions of E_0 , decreasing with increasing n according to specific ratios. Third, all higher harmonic components are constituted by cosine functions, meaning that $\delta^{(n)}$ and $\phi^{(n)}$ are equal to -90° with respect to the driving field for $n > 1$.

In practice, the linear field-dependence of $\varepsilon'^{(1)}(E_0)$ and $d'^{(1)}(E_0)$, and in-particular the value of the third harmonic phase angles ($\delta^{(3)}$ and $\phi^{(3)}$) should be verified first. From Fig. 3.4, it is seen that the condition of $\delta^{(3)} = -90^\circ$ and $\phi^{(3)} = -90^\circ$ results in sharp tips of the corresponding hysteresis loops. Linear field-dependence of $\varepsilon'^{(1)}(E_0)$ and $d'^{(1)}(E_0)$ [nonlinearity in $P(E)$ and $x(E)$] can be evaluated by comparing the slope of subsequent loops with increasing E_0 as shown for the dotted lines in Fig. 3.1. When $\varepsilon'^{(1)}(E_0)$ and $d'^{(1)}(E_0)$ are nonlinear functions of E_0 and $\delta^{(3)} \neq -90^\circ$ and $\phi^{(3)} \neq -90^\circ$, this does not mean that the response is not related to domain wall motion. It could indicate an overlap with other mechanisms, but also merely that domain walls move in a potential that is not random.¹⁶⁵

3.7 Phenomenological interpretation

A phenomenological approach for the higher harmonic analysis will be illustrated on representative ferroelectric and relaxor ferroelectric materials. PZT is perhaps the most studied ferroelectric

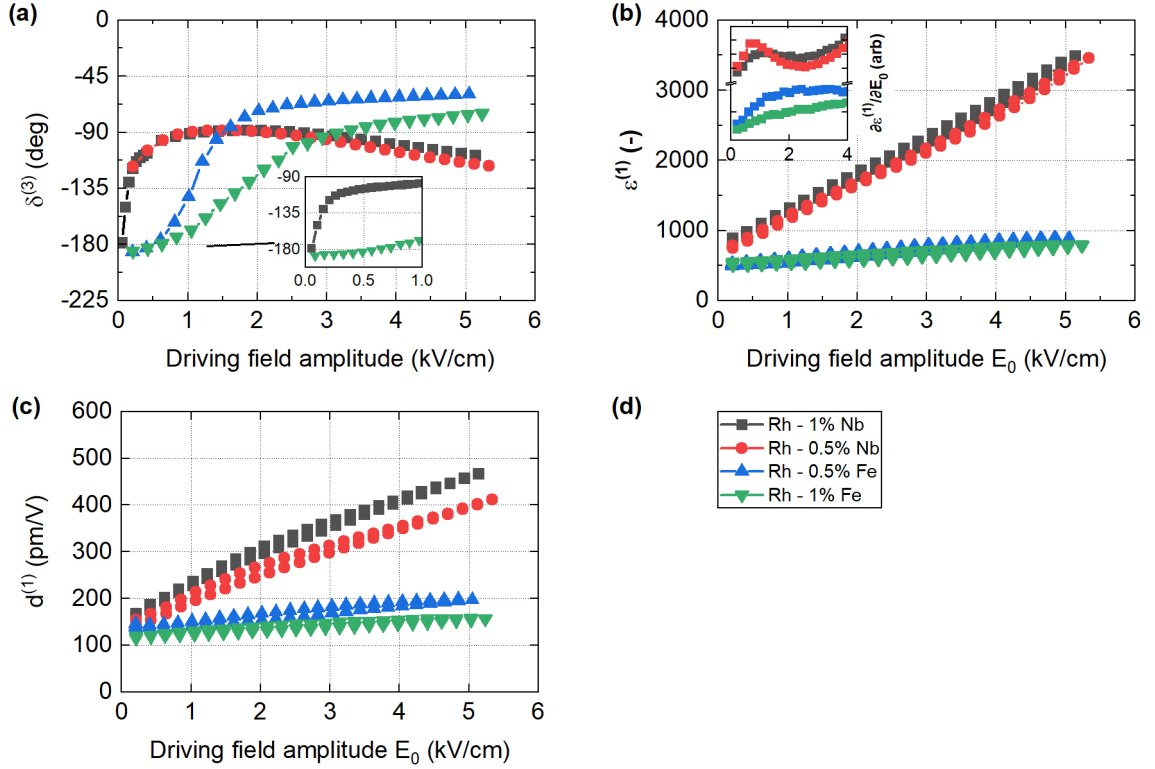


Figure 3.5. Dielectric and electro-mechanical nonlinearities of poled Nb- and Fe-doped rhombohedral PZT, [PZT(58/42)]. Dielectric and piezoelectric data were simultaneously acquired. (a) Third harmonic phase angle of polarization, $\delta^{(3)}$, (b) first harmonic permittivity, $\epsilon^{(1)}$, and (c) first harmonic piezoelectric coefficient, $d^{(1)}$. Each curve in (b) and (c) shows data for ascending and descending electric-field amplitudes, E_0 . (d) Legend for (a), (b), and (c).

material with arguably a rather good understanding of various contributions to polarization and strain.^{167–170} Based on this knowledge and having in mind soft materials as a reference system for which a theoretical description exists (i.e., Rayleigh model), we can attempt to interpret the case where the Rayleigh model does not hold. Pronounced nonlinearities are often related to the reconfiguration of domain structures.^{142,171} Domain wall motion can contribute to strain, polarization, or both depending on the domain wall type and the symmetry property. Therefore, dielectric and electro-mechanic nonlinearities can carry different information.

In Figure 3.5, the field-dependent third harmonic phase angle of polarization, $\delta^{(3)}$, of Nb- (soft) and Fe-doped (hard) rhombohedral PZT is compared with the field-dependent dielectric permittivity and piezoelectric coefficient.^{135,169} Polarization and strain response were measured simultaneously as hysteretic nonlinear mechanisms may alter the state of the sample during measurements.¹⁴² For soft and hard compositions, $\delta^{(3)}$ is approximately -180° at weak fields, as expected for weakly active extrinsic contributions. The rise of $\delta^{(3)}$ for the 1 at.% Nb-doped PZT composition, presented in the inset of Fig. 3.5(a), indicates the onset of domain wall motion for an electric field strength of about 0.2 kV/cm, as generally observed for soft-doped PZT ceramics.^{167,168,172} The $\delta^{(3)}$ of Nb-doped PZT approached -90° (the Rayleigh case) at electric field amplitudes of about 1 kV/cm before it is reduced to approximately -135° at around 5 kV/cm, resulting in a broad peak around 1.5 kV/cm. Only marginal differences in $\delta^{(3)}$ are seen between

the two soft-doped compositions. The field-dependent dielectric permittivity [Fig. 3.5(b)] and piezoelectric coefficient [Fig. 3.5(c)] show a linear increase up to approximately 1.5 kV/cm, which could be considered an upper limit of Rayleigh behavior. Note that linear polarization and strain response would be represented by constant permittivity and piezoelectric coefficient. For Fe-doped PZT, $\delta^{(3)}$ approaches -60° to -70° .

Comparing dielectric permittivity and piezoelectric coefficient of soft- and hard-doped PZT in Fig. 3.5, larger extrinsic contributions for the soft-doped samples become apparent. Moreover, it is seen that doping causes a larger variation in the absolute values of piezoelectric coefficients than in the dielectric permittivity. This indicates that doping affects extrinsic mechanisms that can have relatively stronger contributions to strain than to polarization, for example, non- 180° domain walls. A deviation from Rayleigh behavior and discrepancies between dielectric and piezoelectric nonlinearities is clearly seen for rhombohedral soft-doped PZT around 2 kV/cm. Such anomalies were previously reported in ceramics¹⁵⁶ and films¹⁷³. Studies of PZT films with different crystallographic orientations correlated such deviations in dielectric and piezoelectric nonlinearities to different contributions of ferroelectric and ferroelastic domains.¹⁷⁴ Rhombohedral (100)-oriented films, where 71° and 109° domain walls are not ferroelastically active, show stronger deviations between dielectric and piezoelectric nonlinearities as compared to (111)-oriented films, where 71° and 109° domain walls are ferroelastically active.

The deviation of permittivity and piezoelectric coefficient from linear electric-field dependence (nonlinear strain and polarization) between 1 kV/cm and 2 kV/cm in Fig. 3.5(a) and Fig. 3.5(b) could consequently be correlated to the pronounced onset of non- 180° switching. These anomalies are more visible in the derivative of the dielectric permittivity shown in the inset of Fig. 3.5(b). A pronounced onset of non- 180° switching may result in two competing effects: an increase in macroscopic polarization aligned with the field vector during each half cycle and a reduction of domain wall density. Considering the relatively small hysteresis between increasing and decreasing field subcycle in dielectric permittivity and piezoelectric coefficient, the change due to modifications of the macroscopic polarization state appears to be small. In the framework

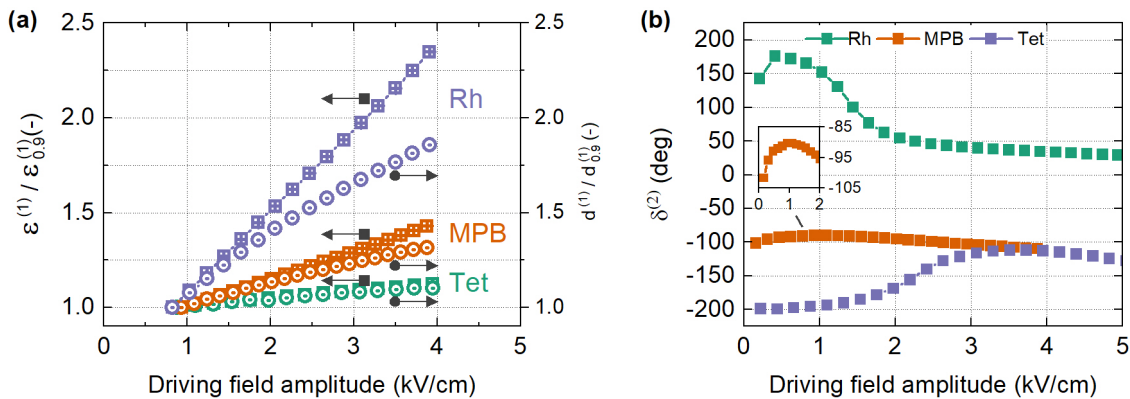


Figure 3.6. Dielectric and piezoelectric nonlinearities for Nb-doped PZT ceramics with rhombohedral, tetragonal and morphotropic phase boundary composition. (a) Normalized dielectric permittivity and piezoelectric coefficient of Nb:PZT. The data are normalized to the measurement point at a driving field amplitude of ≈ 0.9 kV/cm. (b) Second harmonic phase angle of polarization for tetragonal (42/58) morphotropic (52/48), and rhombohedral (58/42) PZT ceramics with 1 at. % Nb.

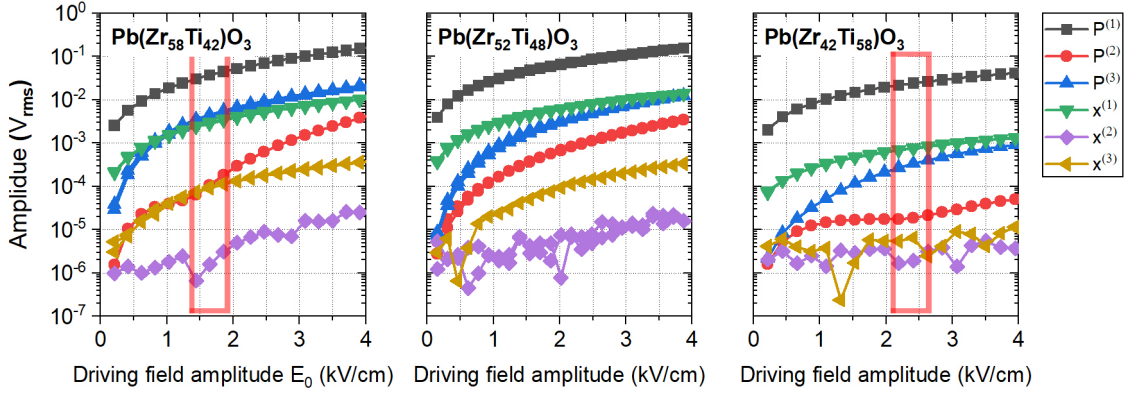


Figure 3.7. Amplitudes of the first three harmonic sinusoids of strain and polarization for different PZT compositions with 1 at.% Nb-doping. The V_{rms} values on the ordinate indicate the output of the lock-in amplifier, used to measure strain and polarization. The red rectangle marks the field region where the amplitude of the second harmonic in polarization exhibits a sharp increase.

of Rayleigh equations, the reduction of slope could be interpreted as the reduction of extrinsic contributions.¹⁶⁴ However, the onset of switching would effectively transfer response from the first to the second harmonic as domains can switch twice per bipolar cycle.

The normalized permittivity and piezoelectric coefficient presented in Figure 3.6(a) show that the relative deviation between nonlinear polarization and strain response increases toward rhombohedral compositions. These findings are consistent with the experimentally determined increase of extrinsic and non-180° switching contribution towards rhombohedral compositions.¹⁷⁵ Assuming the onset of pronounced non-180° domain wall switching as the origin for the observed anomalies and discrepancies between dielectric and piezoelectric nonlinearities, simultaneously occurring anomalies in the second harmonic components of polarization and strain can be expected. Note that the second harmonic is not expected from Rayleigh equations [Eqs. (3.14) and (3.15)]; however, in poled ceramics, the symmetry is broken, and the second harmonic may appear. It may be manifested by different Rayleigh parameter α for increasing and decreasing field branches of the hysteresis loop (different irreversible behavior for increasing and decreasing field). In Fig. 3.6(b), $\delta^{(2)}$ of PZT compositions doped with 1 at.% Nb is presented. An anomaly in $\delta^{(2)}$ is seen between 1 kV/cm and 2 kV/cm for the rhombohedral composition. A similar anomaly in the phase angle of polarization could be measured between 2 kV/cm and 4 kV/cm for the tetragonal composition. This shift could be explained by the higher coercive field and a larger difference in spontaneous strain for non-180° switching of tetragonal compositions.

Consistent with the observed anomalies in $\delta^{(2)}$, a marked increase in the amplitude of the second harmonic in polarization, $P^{(2)}$, is observed at the corresponding fields as depicted in Figure 3.7. For the compositions in the vicinity of the morphotropic phase boundary (MPB), such clear anomalies could not be detected even though a subtle peak in the $\delta^{(2)}$ around 1 kV/cm can be revealed as shown in the inst of Fig. 3.6(a). It is assumed that a relatively stronger contribution of different origins prevents more pronounced changes in $\delta^{(2)}$. Analyzing the real and imaginary parts of the second harmonic in polarization in more detail, it can be shown that observed anomalies in $\delta^{(2)}$ are related to local maxima in the real part of the second harmonic component (Fig. E.2). In contrast to rhombohedral and tetragonal samples, the MPB composition shows a

local minimum followed by a strong increase. It appears that other contributions (e.g., interphase motion and electrostriction) indeed dominate the second harmonic response. While the discussed observations are ascribed to domain wall movement, similar results might be obtained for mechanisms of other origins.

As mentioned before, the reported anomalies of $\delta^{(2)}$ and $P^{(2)}$ are not expected from Eq. (3.14) and Eq. (3.15). From experimental experience of polarization hysteresis loops of polarized ferroelectrics, those anomalies are not surprising, however.^{176,177} In polarized samples most ferroelectric domains are usually closely aligned along the direction of the previously applied electric poling field. Such domain configurations have a unidirectional $\infty \cdot m$ symmetry that may require annealing above Curie temperature, T_C , or electric-field cycling above E_C , to approach the $\infty/\infty \cdot m$ symmetry of a perfectly randomized domain state.

In the sub-coercive field regime, where only small parts of the volume may switch in response to applied electric fields, the poling induced domain state will persist and dominate the macroscopic symmetry. Sub-coercive driving fields applied along or against the macroscopic symmetry will cause different amounts of domain switching, resulting in asymmetric response as presented in Figure 3.8(a) for example. Asymmetric hysteresis loops are not only limited to the sub-coercive regime, however, as shown in Fig. 3.8(b). An insufficient number of field cycles for the randomization of domains, stable internal bias-fields caused by defects or strain gradients, or external origins such as asymmetric electrodes and unfavorable electric and mechanical boundary conditions could cause such asymmetric response.

To verify that domain switching can affect the second harmonic response as proposed, a PMN-20PT ceramic sample was polarized, and the ac-field-dependent polarization and strain response measured with applied electric dc-bias field (E_{dc}) to ensure macroscopic polarization reversal during the measurement. The results obtained can be seen in Figure 3.9(a). A super-linear

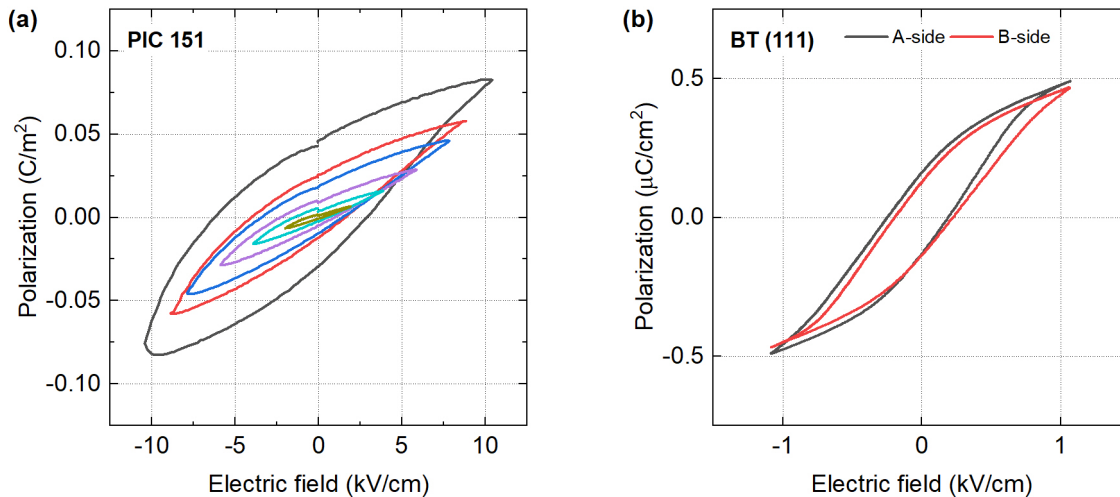


Figure 3.8. Asymmetry of polarization electric-field hysteresis loops of poled ferroelectric samples. (a) Commercially available poled PIC151 PZT sample measured at 1 Hz with a Sawyer-Tower setup. (b) [111]-barium titanate crystal obtained from FEE measured at 1 Hz with a charge amplifier. Both sample orientations were measured to verify that boundary conditions do not dominate the asymmetric polarization response.

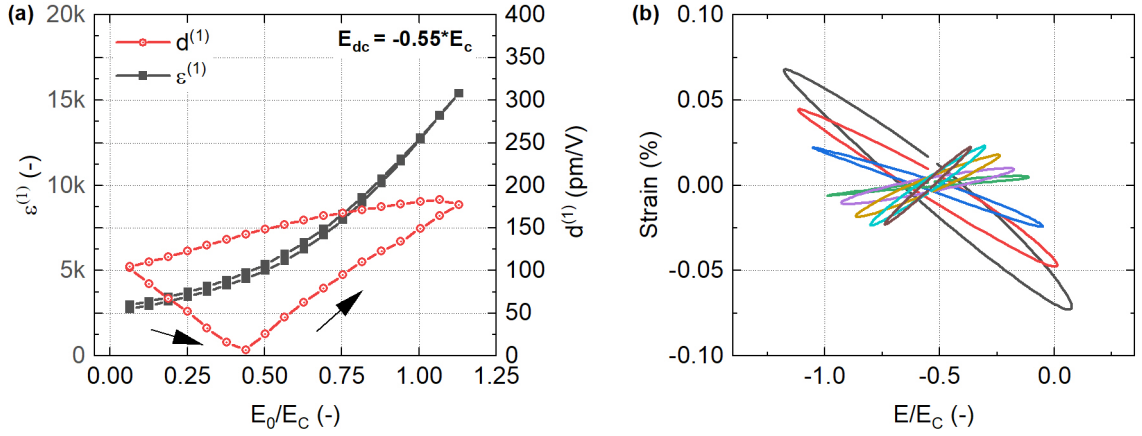


Figure 3.9. Dielectric and piezoelectric response of poled a PMN-20PT ceramic measured with an applied electric dc-bias field, E_{dc} , equal to 55 % of its coercive field, E_c . E_{dc} was chosen to ensure macroscopic switching during the experiment. (a) Dielectric permittivity and piezoelectric coefficient. (b) Reconstructed strain electric-field hysteresis loops using the data from (a) and Figure 3.10. The smallest loop corresponds to $E_0/E_c \approx 0.2$, the green loop to $E_0/E_c \approx 0.4$, and the black loop to $E_0/E_c \approx 1.1$.

nearly anhysteretic increase in permittivity is contrasted by a strong initial drop of the piezoelectric coefficient with significant hysteresis between the ascending and descending branches. The reconstructed strain hysteresis loops in Fig. 3.9(b) demonstrate that the sample switched macroscopically, signaled by the change from a positive to a negative slope of the strain hysteresis loops when $-E_c$ is surpassed.

Knowing that the sample switches macroscopically when $E_0 \approx 0.45E_c$ is reached, the phase angles of polarization $\delta^{(n)}$ in Figure 3.10(a) are compared with the phase angles of strain $\phi^{(n)}$ in Fig. 3.10(b). The absolute value of $\delta^{(1)}$ increases continuously with E_0 , reflecting an increase in energy dissipation which may be ascribed to the switching of domain walls or other polar dipoles. $\delta^{(1)}$ displays a peak centered around $0.6E_c$ with a baseline of 0° for the ascending branch and a monotonous increase from 0° to 90° for the descending branch. $\delta^{(3)}$ is almost constant around 0° signaling polarization saturation. This is unexpected, in particular, at weak fields, for which some evolution of $\delta^{(3)}$ starting from around -180° or -90° would be expected. However, no indication of saturation in $\epsilon^{(1)}$ or $P^{(1)}$ is present. The applied dc-bias field could be responsible for this observation.

It is speculated that E_{dc} is sufficiently high to break a random distribution of the strength of pinning centers into a different distribution, which is heavily biased. In this configuration, the energy landscape is distorted, and since it is relatively close to E_c , every ac field will saturate the response. This is somewhat different from polarization saturation, where all dipoles are aligned. Interestingly, poled ceramics and dc-biased ceramics do not behave alike. It is assumed that after poling, a part of the polarization will switch back to its initial orientation very quickly, while under persistent E_{dc} the polarized state will be maintained as long as E_{dc} is applied. The experimental manifestation of this *backswitching* is observed as the difference between saturation and remnant polarization in polarization electric field hysteresis loops. A quite different response is obtained for $\phi^{(n)}$. For $\phi^{(1)}$ and $\phi^{(3)}$ a jump of $\Delta\phi \approx 180^\circ$ around $0.45E_c$ occurs. This jump in $\phi^{(1)}$ describes the change of slope of strain electric-field hysteresis loops as discussed for Fig. 3.9(b).

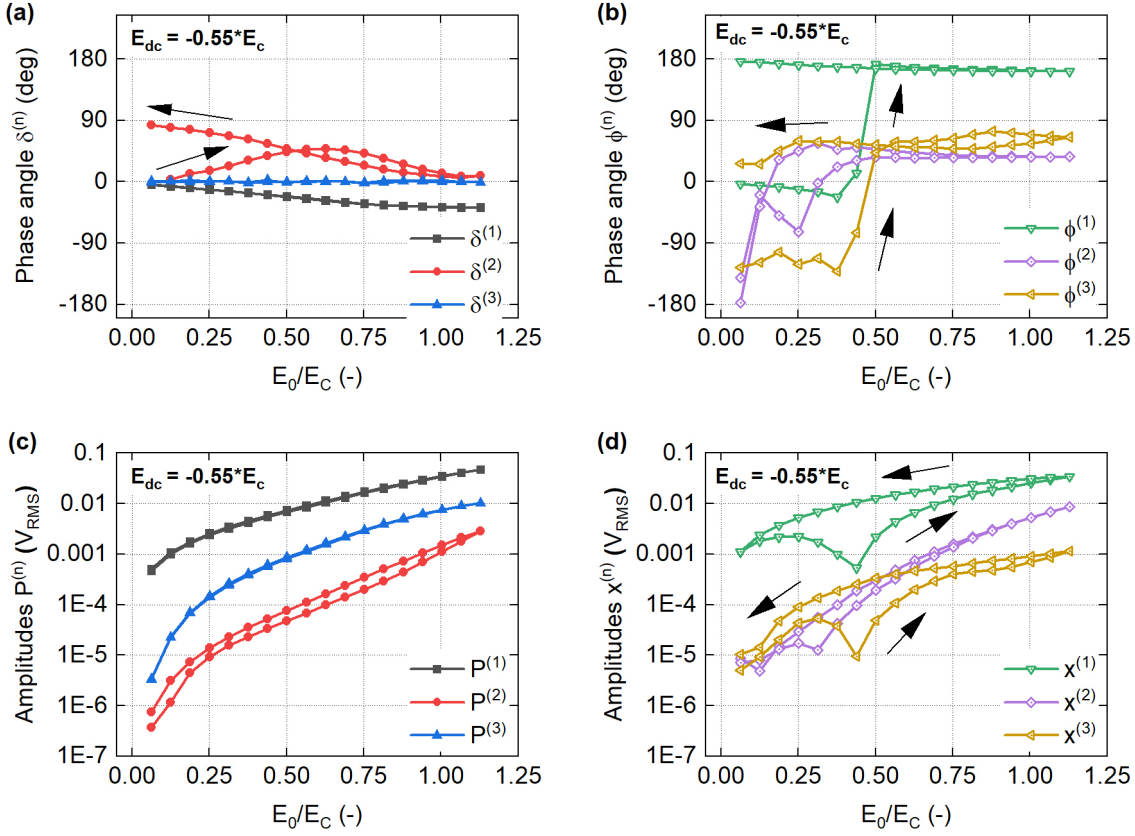


Figure 3.10. Harmonic components of polarization and strain response of a poled PMN-20PT ceramic measured with an applied electric dc-bias field, E_{dc} , equal to 55 % of its coercive field, E_c . (a) Phase angles of polarization, $\delta^{(n)}$, (b) phase angles of strain, $\phi^{(n)}$, (c) amplitudes of polarization, $P^{(n)}$, and (d) amplitudes of strain, $x^{(n)}$.

Interestingly, $\phi^{(2)}$ shows an anomaly at lower E_0 as compared to $\phi^{(1)}$ and $\phi^{(3)}$. For the amplitudes of the harmonic components in Fig. 3.10(c) and (d), anomalies are most notably observed in $P^{(2)}$, $x^{(1)}$, and $x^{(3)}$. These experiments show that anomalies in the harmonic components can be observed when the sum of E_0 and E_{dc} exceed E_c . E_c is correlated to substantial onset of switching. Hence, the correlation proposed previously in this chapter between anomalies in $\delta^{(2)}$ and $P^{(2)}$ and domain switching can be confirmed. The question of whether this holds for nano-sized polar regions in ferroelectric relaxor will be addressed in the next chapter.

It must be mentioned that data obtained from harmonic measurements can differ significantly from measurements obtained from single hysteresis loop measurements with a Sawyer-Tower setup. Results obtained for PMN ceramics measured at 200 K with a lock-in amplifier and a Sawyer-Tower setup are compared in Figure 3.11. In Fig. 3.11(a), $\epsilon(E)$ data measured for different driving field frequencies are seen. $\epsilon(E)$ increases sharply around 2 kV/cm and 3 kV/cm for 10 kHz and 1 kHz, respectively. This sharp increase in $\epsilon(E)$ signalizes a sudden change in the slope of $P(E)$ hysteresis loops as seen for the reconstructed curves in Fig. 3.11(b). While these data could be interpreted in the form of a frequency-dependent anomaly, single $P(E)$ hysteresis loops obtained from Sawyer-Tower measurements in Fig. 3.11(c) do not show any anomaly of the like. Therefore, it is suggested that the anomalies observed for harmonic measurements are

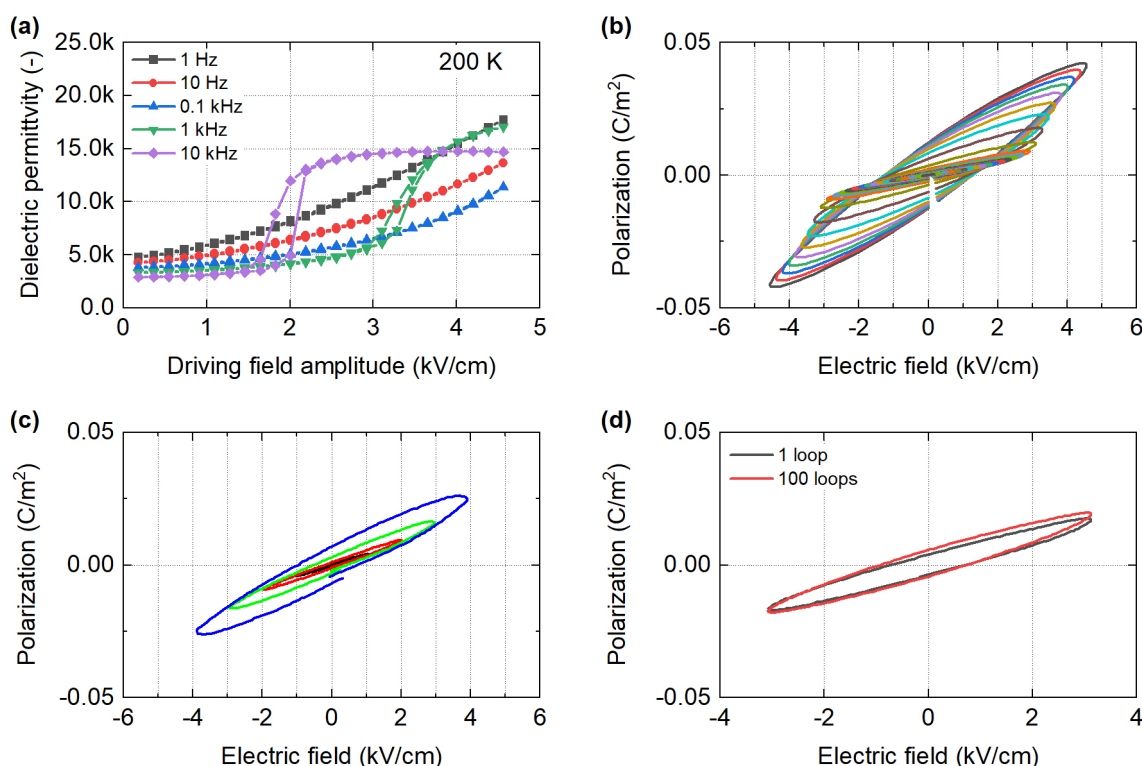


Figure 3.11. Comparison between harmonic measurements and polarisation electric-field hysteresis loops, $P(E)$, obtained with the Sawyer-Tower method for a PMN ceramic measured at 200 K. Anomalies in harmonic measurements are related to fatigue. (a) Electric field-dependent dielectric permittivity for various driving field frequencies. (b) Reconstructed $P(E)$ hysteresis loops from 1 kHz data presented in (a). (c) Single loop measurements obtained with Sawyer-Tower method at 1 kHz. (d) First and hundredth $P(E)$ hysteresis loop obtained with Sawyer-Tower method at 1 kHz.

related to electric field cycling. During measurements of harmonic components with lock-in amplifiers, a substantial number of field cycles is often applied, especially for high frequencies and when several components (first, second, third) are measured for each driving field amplitude. The comparison between the first and the hundredth $P(E)$ loop obtained with Sawyer-Tower measurements seen in Fig. 3.11(c) supports this suggestion.

3.8 Summary

In this chapter, the theoretical foundations of the harmonic analysis of sub-coercive polarization- and strain-electric field hysteresis loops of ferroelectric materials have been discussed. A geometrical, theoretical, and phenomenological interpretation of the first three harmonic components is given. The first harmonic components describe the linear response of materials and may be related to loss. The second harmonic components are related to responses that are invariant with respect to the polarity of the electric driving field. It has also been shown that anomalies in the second harmonic response can indicate switching processes in ferroelectric materials. The question is raised whether similar anomalies can be seen in relaxor ferroelectrics. The third harmonic components may be used to distinguish processes operating in ferroic materials and the third harmonic phase angle of polarization to identify polarization saturation, Rayleigh behavior,

and loop pinching as observed in hard ferroelectrics. Particular values of the second and third harmonic phase angle have been correlated to distinct shapes of polarization hysteresis loops.

4 Macroscopic polarization in lead magnesium niobate

4.1 Motivation

In the previous chapter, the harmonic analysis of dielectric and electro-mechanical nonlinearities was introduced, using lead zirconate titanate (PZT) and solid solutions of lead magnesium niobate lead titanate (PMN-20PT) as an example. It has been shown that the third harmonic of polarization is a sensitive indicator to distinguish mechanisms that contribute to permittivity and that anomalies in the second harmonic of polarization may indicate polarization reversal processes. The question was raised whether similar anomalies can be found in relaxor ferroelectrics, which do not show classic ferroelectric behavior. To address this question, dielectric and electro-mechanical nonlinearities of the most-studied relaxor ferroelectric, lead magnesium niobate (PMN), will be discussed in this chapter. Additional dynamic pyroelectric measurement will be used to study the ground state and the electric field-induced polar state with respect to characteristic temperatures of PMN.

This chapter contains previously published data from the following publication:

- L. M. Riemer, K. Chu, Y. Li, H. Uršič, A. J. Bell, B. Dkhil, and D. Damjanovic, “Macroscopic polarization in the nominally ergodic relaxor state of lead magnesium niobate”, [Applied Physics Letters](#) **117**, 102901 (2020),
- L. M. Riemer, L. Jin, H. Uršič, M. Otoničar, T. Rojac, and D. Damjanovic, “Dielectric and electro-mechanic nonlinearities in perovskite oxide ferroelectrics, relaxors, and relaxor ferroelectrics”, [Journal of Applied Physics](#) **129**, 054101 (2021).

4.2 Introduction

Despite sixty years of ever-growing experimental and theoretical research, the ground state of relaxor ferroelectric still sparks controversial discussion in the field of ferroelectrics and solid-state physics.^{10,18,33,40,50,110} In particular, the dynamics and correlation between macro-, meso-, and nanoscopic-scale polarization and its impact on functional properties remains an enigma.^{11,39,83,90,178} Common characteristics of relaxors are a broad maximum in the dielectric permittivity measured as a function of temperature and dielectric dispersion below the temperature of maximum permittivity (T_m).^{49,77} Most theoretical models correlate these characteristic features to the relaxation of polar dipoles.^{18,49,74,110,179} In the mesoscopic description, the coexistence of static and dynamic nano-sized regions of correlated polarization is commonly

accepted.^{18,45,81} It should be noted that no consensus exists in the literature about the geometric interpretation or the terminology used to describe the aforementioned regions.^{82,101} To emphasize this unresolved debate, the generic term "nano-sized polar regions" is used in this manuscript, even when quoting references that use different terminologies.

Several characteristic temperatures were introduced to describe different states of PMN: the Burns temperature, $T_B \approx 600\text{--}650\text{ K}$, the coherence temperature, $T^* \approx 400\text{--}500\text{ K}$, and the freezing temperature, $T_f \approx 220\text{ K}$.^{45,81–83} At T_B , a transition from the paraelectric state to the ergodic relaxor state takes place. This transition is explained as the first appearance of dynamic nano-sized polar regions.^{11,45,83} At T^* , static regions of correlated polarization emerge.^{11,45,83} Below T_f , the system is said to be in the non-ergodic relaxor state in which the polar structure is frozen in an out-of-equilibrium state that depends on the thermal and field history, as opposed to the ergodic state.⁷⁴ While the onset of non-ergodic behavior in the vicinity and below T_f was investigated intensively in the early 1990s,^{74,75,180} PMN was still referred to as paraelectric at temperatures above T_f .^{73,181} Later on, the term ergodic relaxor was introduced to distinguish the temperature region between T_f and T_B from the paraelectric state above T_B .^{77,118}

At ambient temperature, the structure of PMN is usually described as macroscopically cubic and centrosymmetric with locally broken symmetry within nano-sized polar regions.^{3,26,77} In contrast, measurements of functional properties indicate a macroscopically broken symmetry.^{182,183} Piezoelectric response measured between 300 and 770 K, well above T_B , was attributed to the orientation of nano-sized polar regions within strain gradients of chemically ordered regions.¹⁸² In another study, the presence of a second harmonic polarization response and pyroelectric current peaks around T_f were attributed to a non-zero average polarization of nano-sized polar regions.¹⁸³ Second harmonic response in strontium barium niobate (SBN), on the other hand, was correlated to deep trapping of mobile charges during the application of the first half cycle of the probing field.¹³⁹

Dynamic pyroelectric currents have been proven to be a convenient, non-destructive way to verify whether materials possess macroscopic polarization P_M .^{114,184} When measured under dynamic thermal conditions, pyroelectric current densities, j_p , result dominantly from the temperature dependence of P_M :

$$j_p = \frac{\partial P_M}{\partial T} \frac{\partial T}{\partial t} = p \frac{\partial T}{\partial t}, \quad (4.1)$$

where T is the temperature, t is time, and p is the pyroelectric coefficient.¹¹⁴ According to Eq. (4.1), a temperature modulation with a triangular waveform of a polar material is expected to result in a square wave current response if P_M changes sufficiently quickly with temperature.¹¹⁴ Moreover, a direct correlation between the sign of the pyroelectric response and the orientation of P_M is given, i.e., the sign of the pyroelectric current obtained for a positive temperature rate changes if the spontaneous polarization vector is reversed (e.g., if the sample is flipped over). In the case of a non-polar dielectric material, a change in temperature does not result in a pyroelectric current, unless the sample is biased by a dc electric field during the measurement.

Macroscopic polarization in nominally cubic systems was studied intensively in the paraelectric phase of strontium barium titanate and barium titanate.^{185–189} Two components were identified, a stable *built-in* polarization and a volatile compensating component that is trapped

around the build-in polarization.¹⁸⁵ Atomic-resolution chemical analysis revealed that the material is chemically homogeneous on the nanometer scale, and thus the built-in polarization was attributed to local strains originating from host ions, impurities, and vacancies.¹⁸⁹ The volatile component was assigned to oxygen vacancies or nano-sized polar regions.¹⁸⁵ It was furthermore shown that this local polarization results in distinct nonlinearities in the dielectric permittivity¹⁵¹ and that similar nonlinearities are observed in PMN.^{151,190} Dielectric tunability and the reorientation of polar nano-entities have been considered viable mechanisms to explain this response, but some inconsistencies in the proposed models and experimental results are still unresolved.^{110,151,190,191}

4.3 Nonlinearities of lead magnesium niobate

The first harmonic permittivity, $\epsilon^{(1)}$, and the third harmonic phase angle of polarization, $\delta^{(3)}$, as a function of driving field amplitude, E_0 , measured for a PMN ceramic are presented in Figure 4.1(a). A maximum in $\epsilon^{(1)}$ and a sharp step-like increase of $\delta^{(3)}$ from -180° to 0° is observed. The driving field amplitude of maximum permittivity, $E_{0,m}$, is approximately 1.4 kV/cm. The data are in good agreement with previous studies¹⁵¹. The real and imaginary parts of the second harmonic of polarization, $P^{(2)}$ and $P''^{(2)}$, are presented in Fig. 4.1(b). Both components show a peak in the vicinity of $E_{0,m}$, whereby the peak in $P^{(2)}$ is relatively stronger. A similar anomaly in the second harmonic has been observed for Nb-doped PZT ceramics in the previous chapter (Fig. E.2) and was related to polarization reversal.

Given the general nature of polarization reversal, additional information are required to analyze underlying mechanisms in more detail. Comparing $\delta^{(3)}$ of PMN in Fig. 4.1(a) with the examples given in Figure 3.2 in Chapter 3, a saturation of polarization can be deduced ($\delta^{(3)} = 0$). The fact that the permittivity drops after its maximum also suggests that the contribution of nano-sized polar regions at field amplitude above 1.4 kV/cm to the permittivity has qualitatively changed. This is an interesting point that deserves additional discussion. A classical model of relaxors is the *superparaelectric model*,⁴⁹ which assumes the reorientation of nano-sized polar regions in an electric field. An alternative model, the so-called *breathing model*, is based on the displacement of boundaries of nano-sized polar regions in an electric field.¹⁹² The breathing

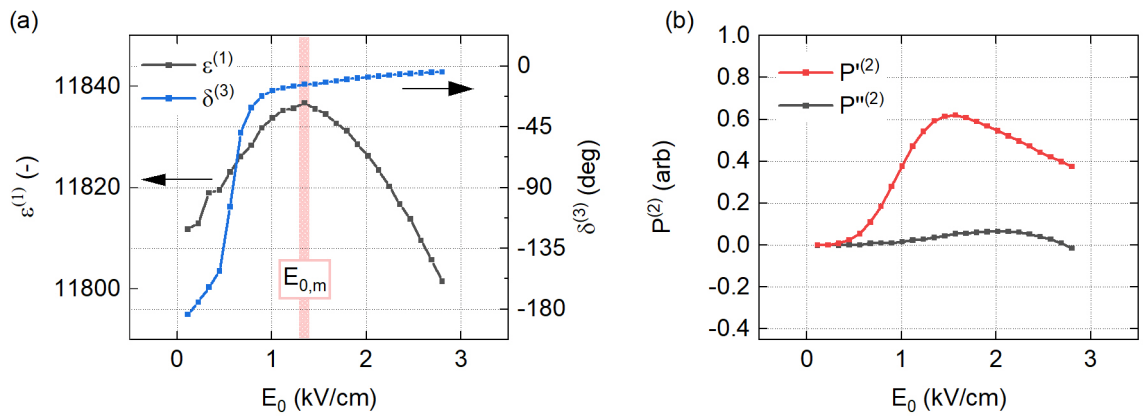


Figure 4.1. Dielectric nonlinearities of lead magnesium niobate, PMN, ceramics. (a) First harmonic permittivity, $\epsilon^{(1)}$, and third harmonic phase angle, $\delta^{(3)}$, of polarization.

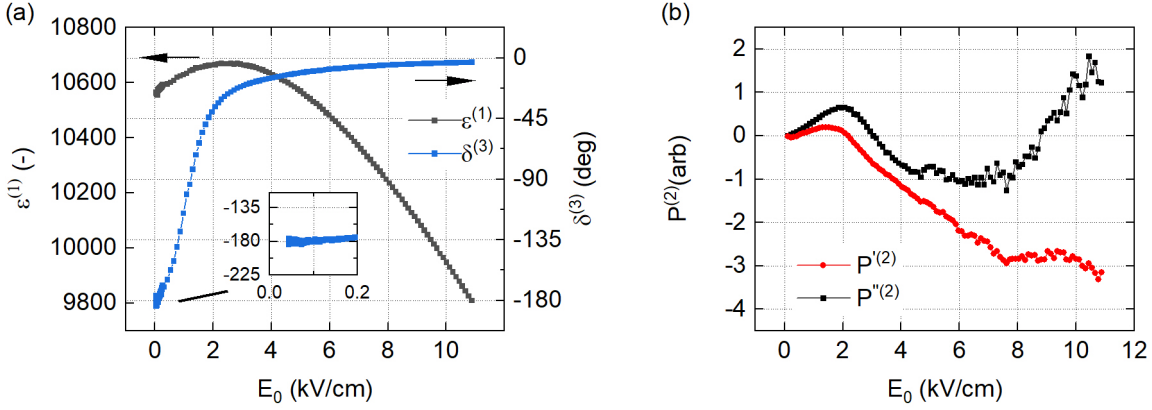


Figure 4.2. Dielectric nonlinearities of [001]-PMN-A crystal. (a) First harmonic permittivity, $\epsilon^{(1)}$, and third harmonic phase angle of polarization, $\delta^{(3)}$. (b) Real, $P'^{(2)}$, and imaginary part, $P''^{(2)}$, of the second harmonic of polarization, $P^{(2)}$.

model makes a definite prediction about the phase angle of the third harmonic: it should be -180° , as has been experimentally observed¹⁹² for fields of about 0.04 kV/cm.¹⁹³ However, for larger fields $\delta^{(3)}$ approaches -0° indicating saturation of the underlying mechanism. This suggests that either the displacement of the interfaces breathing saturates at high fields, or it might mean that at higher fields, nano-sized polar regions start flipping, and it is this flipping mode that eventually saturates (once flipped, the further increase of the field might only cause extension of the dipole). Thus, both breathing and flipping of nano-sized polar regions may take place but at different field levels.¹⁹³

For comparison, the nonlinear dielectric properties of a [001]-PMN crystal are presented in Figure 4.2. A similar behavior as for ceramics is obtained for $\epsilon^{(1)}$ and $\delta^{(3)}$, as can be seen in Fig. 4.2(a). The weak-field response of $\delta^{(3)}$, for which breathing of nano-sized polar regions may be the dominant mechanism, is shown in the inset. The small discontinuity observed around 0.4 kV/cm originates from a two-step measurement procedure. At weak fields, only the internal function generator of a lock-in amplifier was used to apply voltage to the sample. Above 0.4 kV/cm, a voltage amplifier was used in addition to the lock-in to perform measurements. Note that the center of the peak in $\epsilon^{(1)}$ for the PMN crystal in Fig. 4.2(a), with $E_{0,m} = 2.2$ kV/cm, is at larger field amplitudes than for the PMN ceramic in Fig. 4.1(a). Two possible reasons for this variation were identified, a sample thickness- and a history-dependence. In the present case, it is most likely due to the difference in sample thickness, h , between the crystal ($h = 0.23$ mm) and ceramic ($h = 1.03$ mm). A history-dependence of the $E_{0,m}$ has been reported previously.^{151,186} The second harmonic polarization response is presented in Fig. 4.2(b). As for PMN ceramics, peaks in $P'^{(2)}$ and $P''^{(2)}$ can be observed for the [001]-PMN crystal. However, this time, the peak in $P''^{(2)}$ is relatively stronger. The anisotropic dielectric and ferroelectric properties of PMN^{78,194,195} or ceramic-specific processes^{196–198} may explain this finding.

The nonlinear dielectric response was measured for different sample orientations to study the second harmonic response in more detail. Since the second harmonic phase angle of polarization, $\delta^{(2)}$, is sensitive to polarization orientation, intrinsic response is expected to depend on the sample orientation while artificial response induced by boundary conditions should be independent

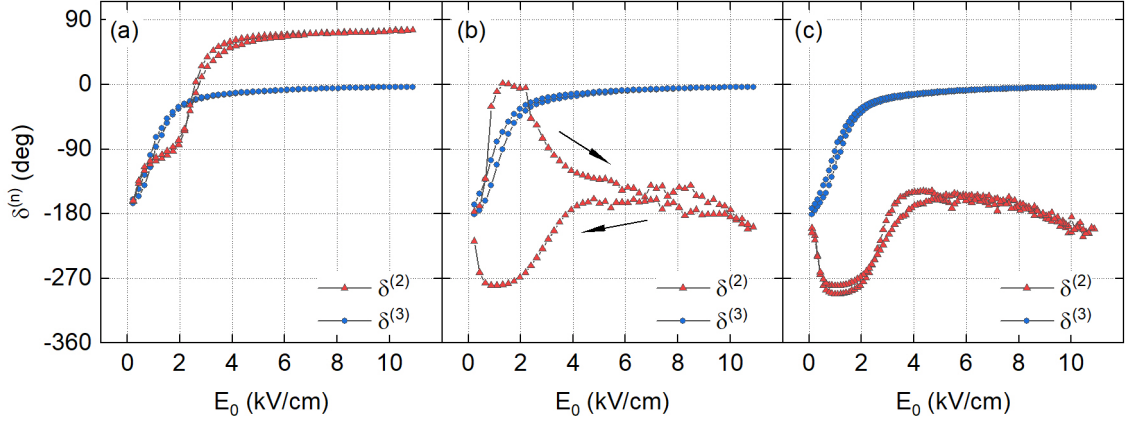


Figure 4.3. Subsequent measurements of harmonic phase angles of polarization, $\delta^{(n)}$, for different sample orientations of a [001]-PMN-A crystal. (a) Up orientation, (b) down orientation, and (c) down orientation.

of the sample orientation. $\delta^{(2)}$ and $\delta^{(3)}$ for a [001]-PMN crystal are presented in Figure 4.3 for a sequence of three measurements. Measurements were performed by first increasing and then decreasing E_0 resulting in an *ascending* and a *descending branch* in each figure. Dielectric nonlinearities were first measured for an arbitrarily selected orientation [Fig. 4.3(a)] before the sample was flipped and measured two more times [Fig. 4.3(b) and Fig. 4.3(c)].

For all measurements, the characteristic step-like response of $\delta^{(3)}$ is obtained. $\delta^{(2)}$, on the other hand, shows an individual behavior for each measurement. For the first measurement, depicted in Fig. 4.3(a), $\delta^{(2)}$ is congruent to $\delta^{(3)}$ up to $E_0 \approx 1$ kV/cm above which a shoulder forms at $\delta^{(2)} \approx -90^\circ$. Then a step-like increase to $\delta^{(2)} \approx 90^\circ$ at $E_0 \approx 2.5$ kV/cm occurs. Little hysteresis is present between the ascending and descending branches for $\delta^{(2)}$ and $\delta^{(3)}$. After the sample is flipped, Fig. 4.3(a), a different behavior is observed. In the ascending branch $\delta^{(2)}$ changes from -180° to 0° at around 1 kV/cm and stays approximately constant up to 2 kV/cm. Above 2 kV/cm $\delta^{(2)}$ approaches -180° . The descending branch looks similar to the ascending branch mirrored along 180° . Not only is a marked hysteresis present in $\delta^{(2)}$ after the sample was flipped, but also is the hysteresis in $\delta^{(3)}$ increased as compared to the previous measurement in Fig. 4.3(a). The sample was subsequently measured again without mechanically manipulating the sample [Fig. 4.3(c)]. For $\delta^{(2)}$, a similar response as observed for the descending branch of the previous measurement is obtained. However, the hysteresis between ascending and descending branches of $\delta^{(2)}$ and $\delta^{(3)}$ is substantially reduced compared to the previous measurement. Qualitatively similar results were obtained for a PMN crystal obtained from a different source [Fig. F3], showing that the response is not sample-specific.

There are a few interesting points to note about the second harmonic response obtained for the PMN crystal. First, the observed anomaly occurs at the same field amplitude as the maximum in permittivity. Second, a clear dependence on the sample orientation suggests that the behavior is inherent to the sample. Third, a hysteretic behavior is seen at temperatures where PMN is thought to be anhysteretic. Fourth, $\delta^{(2)}$ is not just mirrored, i.e. a change in phase by 180° (see Figure 3.3), when the sample orientation is flipped. This is seen at fields above 6 kV/cm where the difference in $\delta^{(2)}$ between sample orientations is 90° or 270° . Differences in response for

flipped samples have been attributed to external boundary conditions¹⁸⁵. It is not clear, however, how external boundary conditions would result in asymmetric behavior with respect to the sample orientation if a sample is centrosymmetric. Therefore to explain the obtained results, it is necessary to consider external boundary conditions together with non-centrosymmetric sample properties. Symmetry breaking in nominally centrosymmetric materials has been observed before and was attributed to local strain.^{187–189}

Asymmetric boundary conditions could arise from thermal gradients, clamping of the sample, or small burden voltages of the measurement equipment. Given that the experiments were conducted in an oil bath with temperature regulation better than ± 0.1 K, with a spring contact that applies at maximum a force of 3 N, and high-precision and low-noise measurement equipment, the possible external bias is considered to be small with respect to the applied electric fields. Even if the external bias may be small, it could still break the symmetry and favor one direction over the other. It is therefore suggested that external boundary conditions may facilitate the orientation of nano-sized polar regions in one direction. It is noted that no anomalies in $\delta^{(2)}$ or $\delta^{(3)}$ are observed for strontium titanate in Figure F.1 in Appendix F at ambient temperatures.

An alternative explanation for the asymmetry in $\delta^{(2)}$ could be the presence of two mechanisms with different symmetry properties. As observed for a polarized lead magnesium niobate lead titanate, PMN-0.28PT, crystal in Figure F.2, the second harmonic phase angle of strain, $\phi^{(2)}$, can change by 180° when the sample is flipped. Since $\phi^{(2)}$ is related to electrostriction, which does not depend on sample orientation, there must also be a component that does not change phase. Consequently, the superposition of such two effects may cause an asymmetric response for different sample orientations. Even though for PMN-0.28PT the asymmetry in $\phi^{(2)}$ is not as pronounced as for $\delta^{(2)}$ in PMN, it is hypothesized that a similar yet unexplored effect may, in principle, be possible for the polarization response.

Nevertheless, that nano-sized polar regions can be flipped in PMN is widely accepted.^{18,33} Therefore, it is suggested that anomalies in the second harmonic polarization response are a common signature for polarization reversal of ferroelectric domains and other polar entities. This is not unexpected, knowing that polarization reversal also contributes to the second harmonic of strain.¹⁹⁹ The hysteresis observed here at ambient temperature is unexpected, however. PMN is not only considered anhysteretic for applied electric fields,^{78,200} but time-dependent, *aging* processes,^{49,201} and electric field-induced *fatigue*²⁰² are also considered negligible in stoichiometric compositions. As a matter of fact, the flipping of polar regions together with hysteresis implies at least some sort of short-term stability of polar states. In other words, it should be possible to polarize PMN and measure piezoelectric properties.

To test whether PMN can be polarized at ambient temperature, a poling study has been conducted. Ceramic samples that had been used for small signal measurements only⁵⁷ and a crystal that had seen several bipolar electric field cycles and dc poling procedures were investigated. A field-cycled crystal was used due to the scarcity of PMN crystals, which were not commercially available during the period of this work. The results obtained for direct and converse measurements are compared in Figure 4.4. A sequential poling procedure without intermediate annealing was applied. For *dc-poling*, a constant poling field, E_p , was applied for 20 min. In addition, an *ac-poling* procedure was adapted, originally reported for PMN-*x*PT crystals.¹⁰⁷ During *ac-poling*, ten bipolar cycles with an amplitude equivalent to E_p were applied with a frequency of 1 Hz. For both measurements, the response was measured immediately after poling. The measurement

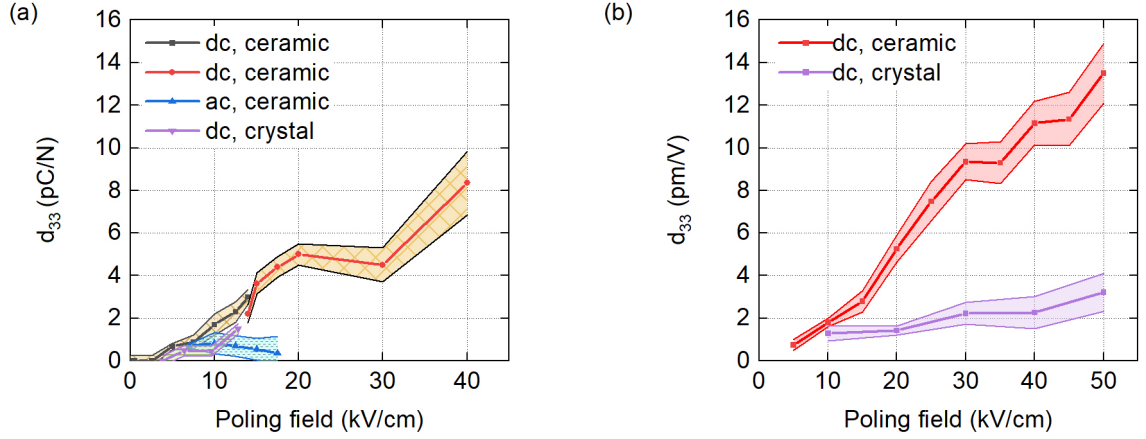


Figure 4.4. Longitudinal piezoelectric coefficient, d_{33} , obtained for PMN ceramics and [001]-crystals for different poling fields, E_p . Samples were poled for 20 min for dc-poling and with 10 bipolar triangular cycles at 1 Hz for ac-poling. All experiments were performed at ambient temperatures. (a) Direct measurements performed at 200 Hz and with a dynamic force of ≈ 6 N, and (b) converse measurements taken at 80 Hz and driving field amplitudes of 0.2 kV/cm.

series represented by a black and red line in Fig. 4.4(a) was interrupted and continued during the next day.

For direct measurements of the longitudinal piezoelectric coefficient, d_{33} , of dc-poled PMN a non-zero d_{33} value could be measured starting at $E_p = 5$ kV/cm as presented in Fig. 4.4(a). d_{33} increases approximately linearly up to $E_p = 20$ kV/cm, forms a shoulder at $d_{33} = 5$ pC/N, and then increases above 30 kV/cm to the maximum measured value of $d_{33} \approx 8$ pC/N at $E_p = 40$ kV/cm. These coefficients are rather small compared to values reported for measurements under applied dc-bias ($d_{33} \approx 240$ pm/V at 10 kV/cm)²⁰³ or for fatigue-induced piezoelectricity in PMN ceramics (250 pC/N for field-cycling of 100 μ m thick ceramic samples up to 100 kV/cm).¹⁹⁶ For ac-poling, a weak maximum around 10 kV/cm was obtained. This procedure did not enhance d_{33} as compared to ac-poling as observed for PMN-xPT crystals. The ac-poling procedure is not well understood, however, and its enhancement has not been demonstrated for ceramics so far.²⁰⁴ Therefore, it might be that a different ac-poling protocol could enhance d_{33} of PMN. As compared to ceramics, the crystal shows a relatively weaker response. This could be due to ceramic-specific processes that might enhance d_{33} , such as the suggested pile-up of oxygen vacancies at grain boundaries,¹⁹⁶ or due to anisotropic properties of PMN.¹⁹⁴ It would be interesting to perform comparative studies with [111]-PMN crystals to see whether poling along the polar $\langle 111 \rangle$ direction increases or decreases d_{33} .

An overall similar behavior is seen for the converse measurements of d_{33} presented in Fig. 4.4(b). For ceramics, d_{33} increases approximately linearly with increasing poling field up to $E_p \approx 30$ kV/cm before the slope changes slightly. As for direct measurements, poling is less efficient for crystals. It is noted that relatively larger values are obtained for converse as compared to direct measurements. It is suggested that the clamping between two flat jaws during the measurements is responsible for this observation.²⁰⁵

To gain insight into the dynamic response of the induced polar state of PMN, dynamic nonlinear polarization and strain measurements of unpoled and poled PMN crystal were performed.

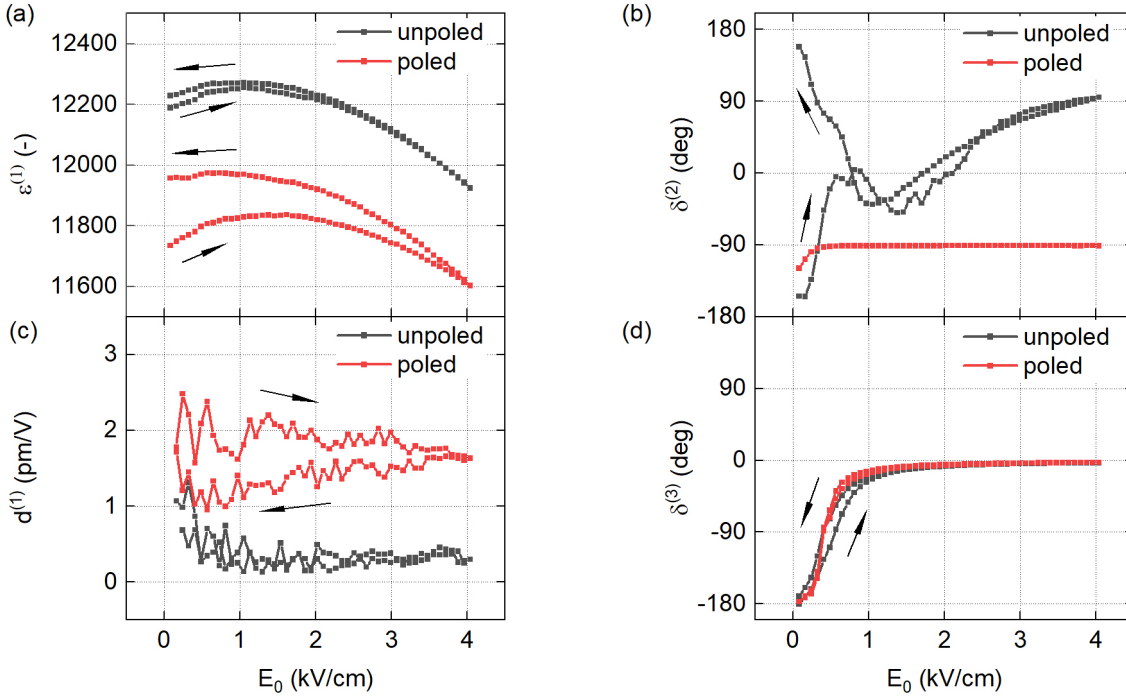


Figure 4.5. Dielectric and electro-mechanical nonlinearities of unpoled and poled [001]-PMN-B crystal.

The sample was polarized sequentially up to 50 kV/cm without intermediate annealing in 10 kV/cm increments for 20 min each. Poling was performed in the same experimental setup as the measurements, and the sample was not mechanically manipulated during the experiment. The sample was immersed in silicone oil during measurements with a temperature of $T = (296.0 \pm 0.1)$ K. (a) First harmonic permittivity, $\epsilon^{(1)}$, (b) first harmonic piezoelectric coefficient, $d^{(1)}$, (c) second harmonic phase angle of polarization, $\delta^{(2)}$, and (d) third harmonic phase angle of polarization, $\delta^{(3)}$.

As pointed out previously, the used crystal had been polarized, and electric field cycled several times before this measurement. For the unpoled case in Figure 4.5(a), a peak in $\epsilon^{(1)}$ with $E_{0,m} \approx 1.0$ kV/cm, and weak hysteresis between the ascending and descending branches is observed. After cumulative poling of the sample up to 50 kV/cm, the weak-field permittivity is reduced by approximately 4 %. This reduction of $\epsilon^{(1)}$ after poling along the non-polar $\langle 001 \rangle$ -direction is in contrast to PMN- x PT compositions in the vicinity of the morphotropic phase boundary. For these PMN- x PT compositions, $\epsilon^{(1)}$ increases when it is poled along non-polar $\langle 001 \rangle$ -directions. For the ascending branch $E_{0,m}$ increases to around 1.5 kV/cm. A clear hysteresis is seen in the form of a continuously increasing $\epsilon^{(1)}$ that makes the maximum less apparent in the descending branch. A weak maximum or an immediate saturation of $\epsilon^{(1)}$ for some specimen have been noted previously.¹⁵¹

The measured d_{33} values are presented Fig. 4.5(b). For the unpoled case, the response is small up to 4 kV/cm, compared to the reference measurements of strontium titanate provided in Fig. E.1 non-zero after all. Upon poling, d_{33} increases to around 2 pm/V at weak fields and is slightly reduced with increasing E_0 . It further decreases in the descending branch, which might be related to electric-field induced depolarization or a time-dependent decay. For $\delta^{(2)}$ in Fig. 4.5(c), market anomalies and hysteresis between the ascending and descending branches are observed for the unpoled state. In contrast, a primarily flat response is observed for $\delta^{(2)}$ for the poled state. It is

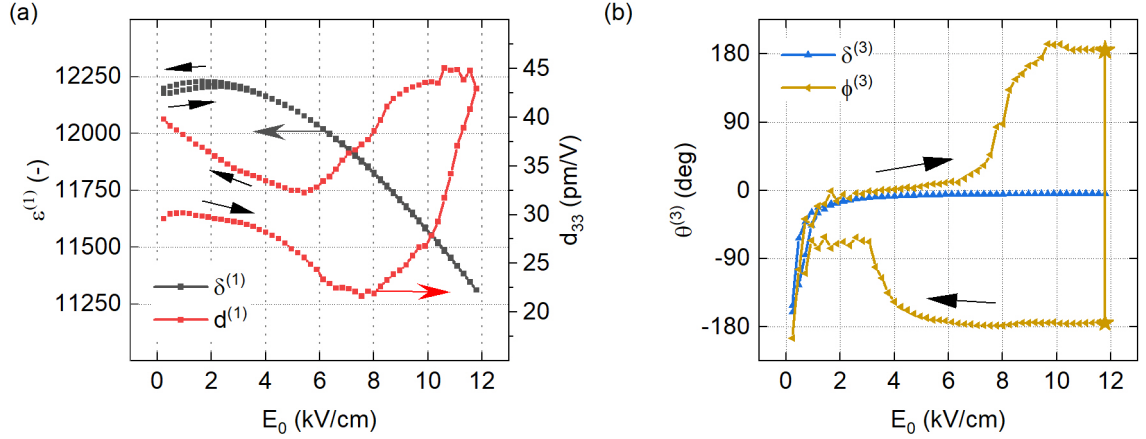


Figure 4.6. Dielectric and electro-mechanical nonlinearities of electric field-trained PMN ceramics. (a) First harmonic permittivity, $\epsilon^{(1)}$, and first harmonic piezoelectric coefficient, $d^{(1)}$, as a function of driving field amplitude, E_0 . (b) Third harmonic phase angle of polarization, $\delta^{(3)}$, and strain, $\phi^{(3)}$. The direction of measurement is indicated by arrows. The descending branch of $\phi^{(3)}$ was shifted by 360° for a better comparison. The phase angles marked by stars are equivalent representations of the same data point.

speculated that the mechanism or mechanisms responsible for the anomalies observed in the unpoled state are either reduced or dominated by a relatively stronger mechanism in the poled state.

The characteristic step-like response of $\delta^{(3)}$ is present for the unpoled and poled state, as seen in Fig. 4.5(d). For the unpoled state, the curve is more hysteretic, and the transition between -180° and 0° seems to take place more gradually. For the poled state, a sharp and almost anhysteretic step is observed, indicating that polarization saturation sets in earlier as compared to the unpoled state. A reduced density of mobile nano-sized polar regions could be a reason for this. It is interesting to note that the hysteretic behavior of different nonlinear components changes between the unpoled and the poled state. For the unpoled state, mostly the higher harmonic components ($n > 1$) are hysteretic, while for the poled state, the first harmonic components show strong hysteresis. Unfortunately, no meaningful response could be measured for the third harmonic phase angle of strain, $\phi^{(3)}$, for polarized PMN crystals due to the overall relatively small electro-mechanical response.

For PMN ceramics that were *trained* with repeated application of electric field cycles, in part during the work of [186], $\phi^{(3)}$ could, however, be measured. It has to be pointed out that the obtained results have been obtained for more than one sample, but the trained state could not be reproduced on demand. However, the trained state was not permanent and could be removed by annealing at 773 K. In this framework, the measurements on trained samples should be considered for illustrative purpose, for which they are considered valuable as they initially motivated significant parts of the work presented in this chapter.

$\epsilon^{(1)}$ and d_{33} of such a trained PMN ceramic sample are presented in Figure 4.6(a). A maximum in $\epsilon^{(1)}$ is present that shifts from $E_{0,m} \approx 2.4$ kV/cm in the ascending to $E_{0,m} \approx 1.7$ kV/cm in the descending branch. For d_{33} a three-fold increase as compared to the poled ceramic in Fig. 4.4 could be measured. A minimum of about 20 pm/V is obtained at around 8 kV/cm before d_{33}

increases to 42 pm/V at the highest applied E_0 of 12 kV/cm. In the descending branch, d_{33} increases first slightly to 45 pm/V before a minimum appears at 6 kV/cm. After the measurement, d_{33} increases to 40 pm/V. $\delta^{(3)}$ and $\phi^{(3)}$ are compared in Fig. 4.6(b). For $\delta^{(3)}$ the characteristic step-like response with slight hysteresis is seen. $\phi^{(3)}$ shows a similar behavior up to 6 kV/cm in the ascending branch before a second step-like change between 0° and 180° takes place. This increase coincides with the minimum in d_{33} in Fig. 4.6(b). The descending branch is shifted by -360° to an equivalent representation within the $\pm 180^\circ$ range for a better comparison. The two phase angles highlighted by stars are identical representations of the same data point. At high fields, $\phi^{(3)}$ shows a flat response around -180° . Below 6 kV/cm a plateau in $\phi^{(3)}$ around -70° gradually evolves in the field range of the minimum obtained for d_{33} . According to Figure 3.5, this data can be interpreted as strain saturation followed by a regime in which the tips of strain electric field hysteresis loops bend upwards, in agreement with the response obtained for d_{33} in Fig. 4.6(b).

However, $\phi^{(3)}$ has to be interpreted with respect to $\phi^{(1)}$, which depends on the polarization orientation. In the present case, $\phi^{(1)}$ is around -180° at all investigated E_0 . In that sense, $\phi^{(3)} = \pm 180^\circ$ would suggest saturation of the strain response above 8 kV/cm in the ascending and above 6 kV/cm in the descending branch. This interpretation conflicts with the observed behavior of d_{33} . An explanation for this finding could be that different mechanisms dominate d_{33} and $\phi^{(3)}$. This idea is supported by the fact that after repeated measurements $\delta^{(2)}$ of the same sample flipped by 180° . As the second harmonic is sensitive to the polarization orientation, these results suggest that the direction of polarization changed. In that case, also $\phi^{(1)}$ should change, which was not observed, however (cf. Figure F.4).

4.4 Dynamic pyroelectric measurements of lead magnesium niobate

To investigate the polarization reversal suggested by the 180° change in $\delta^{(2)}$ by an independent method, the dynamic pyroelectric response of trained PMN ceramics was measured. A selection of the obtained results is presented in Figure 4.7. For the applied triangular temperature modulation represented by the grey lines, a square wave current response is expected for polar

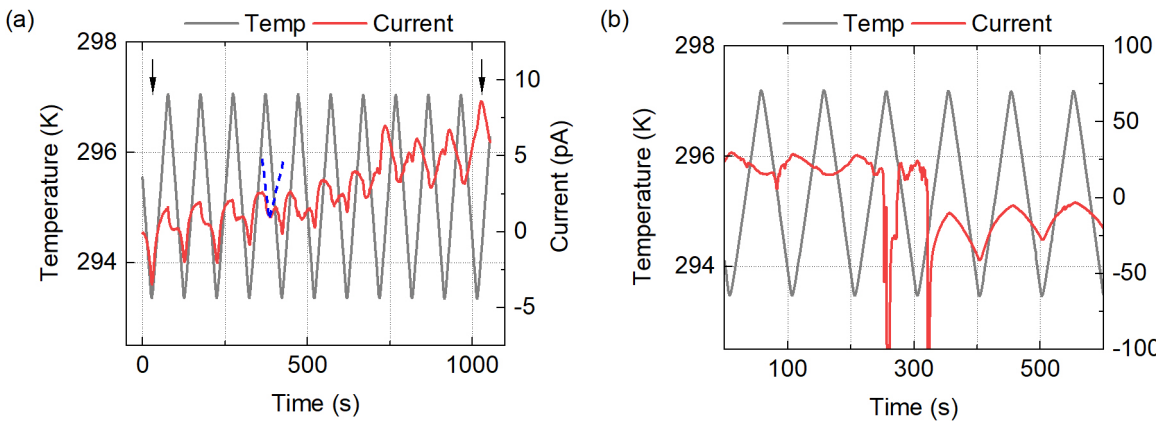


Figure 4.7. Dynamic pyroelectric measurements of trained PMN ceramics. (a) Measurement sequence in which the phase of the pyroelectric current, j_p , with respect to the triangular temperature profile is reversed. (b) Pyroelectric measurements in which the phase reversal of j_p takes place abruptly involving relatively large peaks in j_p at a time of about $t = 300$ s.

materials.¹¹⁴ However, in Fig. 4.7(a), a complex current response is seen that evolves over time, t . At the beginning of the measurement, at $t = 0$ s, a triangular current response is observed that follows the temperature profile; it is in phase with the temperature modulation. It appears that a triangular signal of opposite polarity is superimposed and increases in magnitude over time, as indicated by the blue dashed line in Fig. 4.7(a). Finally, around $t = 1000$ s, the pyroelectric response is out of phase with T . It is speculated that this response represents a gradual polarization reversal process that potentially involves more than one mechanism. In contrast to the continuous process observed in Fig. 4.7(a), a rather quick phase reversal that involves relatively large current spikes is presented in Fig. 4.7(b). Such abrupt changes in polarization state could be due to Barkhausen jumps⁷⁵ or the breakdown of percolated nano-sized polar regions²⁰⁶. Another possible explanation could be space charges that were induced by the electric fields applied during dynamic nonlinear measurements.¹³⁹ Space charges have been correlated to saw-tooth-like pyroelectric response without experimental proof, however.¹¹⁴ To rule out electric field-induced trapped charges, the pyroelectric response of pristine PMN crystals was investigated.

Pyroelectric current measurements of a pristine PMN crystal performed at around 295 K are presented in Figure 4.8(a). The crystal had not been subjected to any electric fields before those measurements. At this temperature, approximately 75 K above T_f and 25 K above the temperature of maximum permittivity, T_m , the material is supposed to be in the nominally macroscopically non-polar ergodic relaxor state. Contrary to expectations, a clear pyroelectric square wave response is evident. To exclude pyroelectric response artifacts, that might arise in the case of a burden voltage of the measurement device²⁰⁷ or from temperature gradients across the sample¹¹⁴, the sample was flipped over. As expected for a material with persistent macroscopic polarisation, the pyroelectric response changes its phase by 180° when the sample is flipped over. This is a

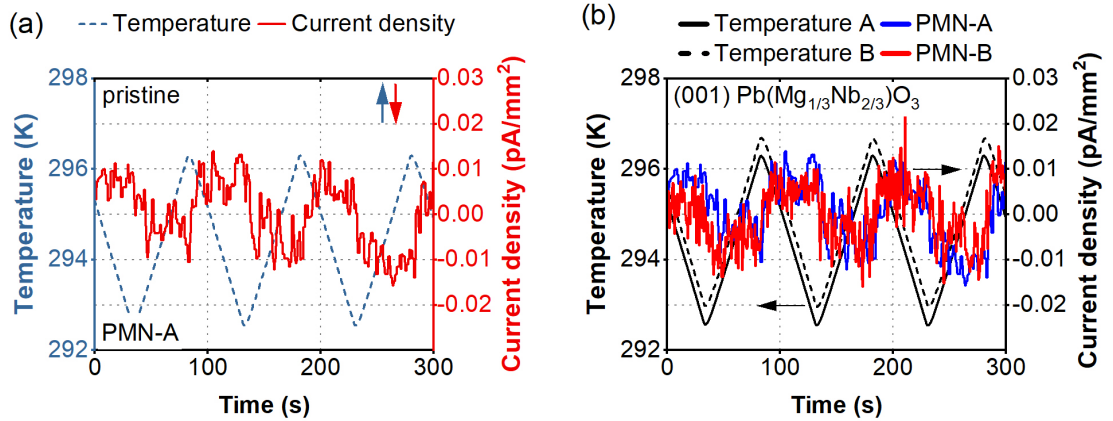


Figure 4.8. Proof of persistent macroscopic polarization in the ergodic phase of ferroelectric relaxor lead magnesium niobate (PMN) by pyroelectric measurements of pristine [001]-crystals obtained from different sources. A qualitatively similar response is obtained after annealing at 773 K, for samples with Au and Pt electrodes, and for ceramic samples. (a) A triangular temperature modulation of crystal PMN-A results in a square wave current response as expected for materials with persistent macroscopic polarization, see Eq. (4.1). A pyroelectric coefficient of $p = (0.073 \pm 0.010) \text{ C/m}^2\text{K}$ was determined. (b) Comparison between crystals PMN-A and PMN-B. The striking similarity obtained for crystals of different sources provides evidence that the observed behavior is not sample-specific. For crystal PMN-B, data were shifted by 180° to be in phase with the data of crystal PMN-A.

direct proof of persistent macroscopic polarity in the ergodic phase of pristine PMN. The striking similarity obtained for crystals of different sources [Fig. 4.8(b)] furthermore provides compelling evidence that the observed behavior is not sample-specific.

Similar pyroelectric experiments were performed for crystals with different electrodes, thicknesses, and surface finishing (see Figure E.5), and for ceramic samples in pristine and annealed conditions, respectively (Figure E.6). In all cases, a periodically modulated response was obtained. For pristine PMN crystals an average pyroelectric current densities of $j_p = (0.005 \pm 0.001) \text{ pA/mm}^2$ could be measured, resulting in a pyroelectric coefficient of $p = (0.073 \pm 0.010) \text{ C/m}^2\text{K}$. For PMN ceramics, $p = (0.063 \pm 0.027) \text{ C/m}^2\text{K}$ was obtained. The difference, which is within the experimental error, might be explained by long-range symmetry breaking strain fields of grain boundaries¹⁹⁷ or differences in homogeneity, stoichiometry, or defect concentration between different grains, which to some degree, are present in any material.⁴⁷ The calculated pyroelectric coefficients of PMN are approximately two orders of magnitude smaller than the pyroelectric coefficient of polyvinylidene fluoride (PVDF)¹⁸⁴ and approximately four orders of magnitude smaller than the pyroelectric coefficients of lead magnesium niobate lead titanate (PMN-*x*PT) single crystals with morphotropic phase boundary composition.⁸⁴

Pyroelectric and piezoelectric effects have been reported for approximately 500 nm thick PMN films in the past.²⁰⁸ However, all thin films are inherently asymmetrical, and the origin of the polarization cannot be unequivocally assigned to the properties of relaxors. For example, the pyroelectric coefficient was two orders of magnitude higher than in single crystals and ceramics examined in this study, suggesting contributions of thin film-related processes such as electrode asymmetry and clamping from the substrate.²⁰⁹ Symmetry breaking in nominally centrosymmetric oxides has also been reported for amorphous strontium titanate films,²¹⁰ barium titanate,²¹¹ lead zirconate,²¹¹ and barium strontium titanate.¹⁸⁸ Potential mechanisms involve *inter alia*, octahedral rotation,²¹⁰ polar entities,^{188,211} defects,¹⁸⁸ and strain gradients.¹⁸⁸

In agreement with the current results, previous studies demonstrated piezoelectric response in the ergodic state of PMN using resonant piezoelectric spectroscopy (RPS) and resonant electrostriction spectroscopy (RES).¹⁸² A breaking of macroscopic centrosymmetry was hypothesized to result from the alignment of dynamic polar nano-entities in stress gradients of chemically ordered regions.¹⁸² In contrast to pyroelectric measurements, RPS and RES cannot prove macroscopic polarity however, since electrostriction is a general property of dielectric solids^{149,212} and piezoelectricity merely requires breaking of centrosymmetry.^{149,213}

The thermal stability of the observed pyroelectric response was investigated by *in-situ* pyroelectric measurements of a [001]-PMN crystal at different temperatures. All measurements were recorded sequentially in a single run. In total, more than ten measurements were performed at different temperatures with dwell times around 1000 s or more each. The obtained results are summarized in Figure 4.9. The averages of j_p calculated for sections of constant heating rate are indicated as black curves. At ambient temperatures, Fig. 4.9(a), the previously discussed response is obtained. With increasing temperature, the pyroelectric response is reduced. This reduction is not necessarily related to a reduction in macroscopic polarization itself since pyroelectric response results from a change in polarization. A reduction of the magnitude of spontaneous polarization or enhanced stability of spontaneous polarization, both, can therefore reduce pyroelectric response. This means that a large but stable polarization and weak polarization that responds readily to changes in temperature may yield a comparable pyroelectric response. The

4.4. Dynamic pyroelectric measurements of lead magnesium niobate

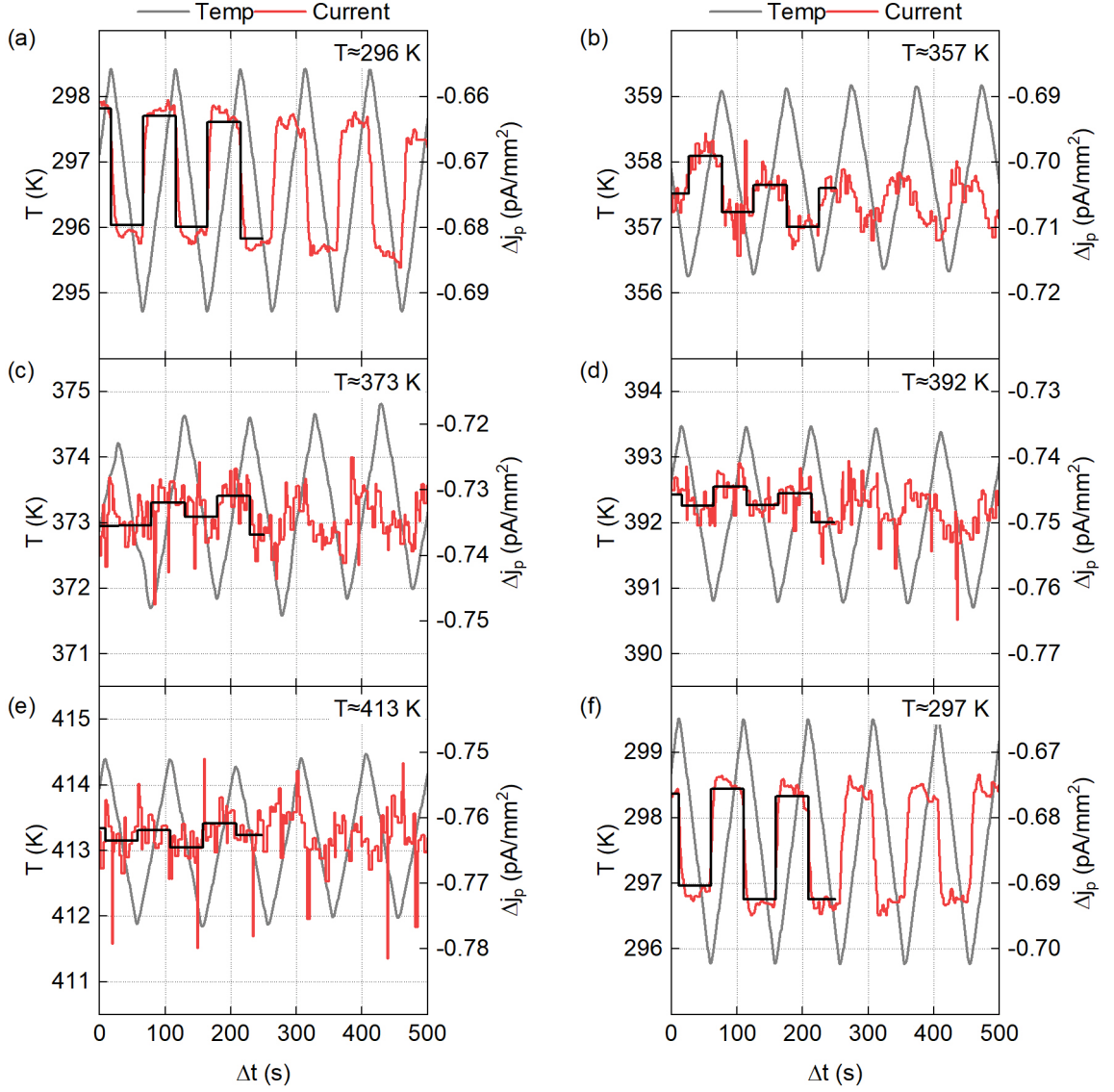


Figure 4.9. Dynamic pyroelectric current density, j_p , of a pristine [001]-PMN crystal measured sequentially at different temperatures, T . The black curves indicate averaged values of j_p calculated for time intervals Δt of constant heating rate. (a) $T \approx 296$ K, (b) $T \approx 357$ K, (c) $T \approx 373$ K, (d) $T \approx 392$ K, (e) $T \approx 413$ K, and (f) $T \approx 297$ K.

obtained results may therefore only be interpreted as a reduction in macroscopic polarization under the reasonable assumption that the underlying polarization mechanism can respond more readily at elevated temperatures. At the maximum temperature at which experiments were performed, $T = 413$ K, small modulations in j_p can still be observed. Due to the relatively low signal-to-noise ratio, it is difficult to determine the shape of the current modulations properly, however. The indicated square wave current response is, therefore, an assumption. The amplitude of the temperature modulation also changes slightly with temperature. This is due to the nonlinear characteristics of the used thermocouple in combination with an analog temperature controller.

A noteworthy aspect of the data is that the magnitude and phase of the pyroelectric response before [Fig. 4.9(a)] and after [Fig. 4.9(f)] the temperature cycle are almost the same. This immediate reappearance of pyroelectric response suggests that mostly reversible changes of the polar structure take place between 297 and 413 K. The influence of thermal quenching^{214–217} was not tested, however. Unfortunately, dynamic pyroelectric measurements at higher temperatures were not possible due to the limitations of the used equipment. It would be interesting to see whether any anomalies of the pyroelectric response, indicative for a first- or second-order phase transition,²¹⁸ could be found at any of the characteristic temperatures.

The stability of the polarized state above 413 K in PMN crystals was investigated instead indirectly by annealing experiments. A polarized sample was therefore annealed at different temperatures, and the pyroelectric response was measured after cooling to ambient temperatures. Pyroelectric measurements obtained before and after a direct current (dc) electric field of 10 kV/cm was applied against the initial polarization orientation of the pristine PMN-A sample are compared in Figure 4.10(a) and Fig. 4.10(b). When compared to the same crystal in its pristine condition, two significant changes are seen after applying a dc field. First, the relation between the sign of temperature rate and the sign of j_p changed, implying the reversal of macroscopic polarization. The minimal dc field strength for this polarization reversal was determined to be $E_M = (1.35 \pm 0.05)$ kV/cm in both crystals and ceramic samples. Second, the amplitude of j_p increased by more than an order of magnitude with respect to the pristine sample.

The polarized sample was then annealed above and below T_B , and the remaining pyroelectric response measured at ambient temperature. An interesting result highlighted by this experiment is that the direction of macroscopic polarization does not return to its initial, pristine orientation if the sample is annealed below T_B [Fig. 4.10(c)]. The initial orientation [Fig. 4.10(a)] is only recovered after annealing above T_B as shown in [Fig. 4.10(d)]. Such a *memory effect* has been previously observed in relaxor ferroelectric solid solutions.²¹⁹ The correlation between the direction of macroscopic polarization and T_B indicates that at least a part of the induced polarity is directly related to nano-sized polar regions as they are assumed to disappear above T_B . After both annealing temperatures, the amplitude of j_p is around 0.006 pA/mm² but of the opposite sign, as shown in Fig. 4.10(d). Therefore, it is likely that the majority of the induced polarity decays during annealing while a smaller fraction is more persistent. Several reports have mentioned hierarchical relaxation processes with different activation energies.^{47,220,221} It would be interesting to investigate the evolution of polarization at high temperatures in more detail, for example, with continuous thermally stimulated current measurements.

To study the temporal stability of the electric field-induced state at ambient temperature, the dynamic pyroelectric response of a newly poled sample was measured over several days as depicted in Figure E8. In contrast to the slower stretched exponential decay of dielectric permittivity observed below T_f ²²², the decay of the pyroelectric response can be fit by the Curie von Schweidler (CvS) law [$f(t) = f_0 + (t/\tau)^{n_{CvS}}$],²²³ where f_0 defines the offset, t is time, τ is the time constant, and n_{CvS} is the power exponent. A power exponent of $n_{CvS} = -0.235 \pm 0.001$ was derived, in good agreement with previous reports, in which the decay of meta-stable piezoresponse was studied locally with piezoresponse force microscopy (PFM) in PMN crystals.²²³ The induced piezoelectric response was attributed to the realignment and subsequent relaxation of dynamic nano-sized polar regions.²²³ Relaxation mechanisms following the CvS law were previously assigned to the motion of phase boundaries of nano-sized polar regions,²²⁰ which can become

4.4. Dynamic pyroelectric measurements of lead magnesium niobate

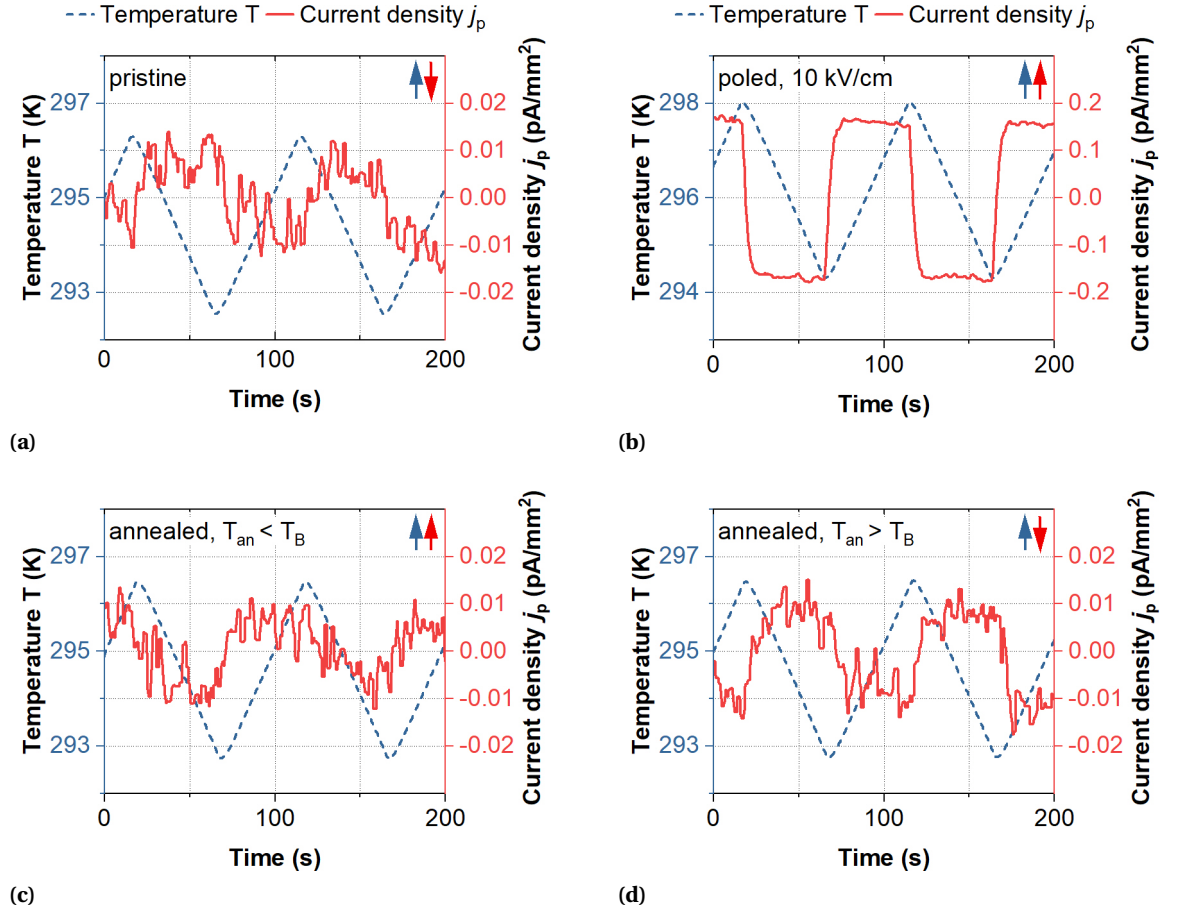


Figure 4.10. Dynamic pyroelectric response of a pristine, poled, and annealed [001]-PMN-A crystal. Blue and red arrows indicate the relation between the sign of temperature rate and the sign of current density, j_p . Poling against the initial orientation of polarization results in persistent macroscopic polarization of the opposite direction. A minimum dc electric poling field of $E_M = (1.35 \pm 0.05)$ kV/cm is required for this polarization reversal. Annealing above Burns temperature, $T_B \approx 600$ -650 K,^{45,81-83} restores the initial orientation of polarization. The ordinate of the pyroelectric current density in Fig. 4.10(b) is stretched by a factor of ten in relation to Fig. 4.10(a),(c),&(d). All measurements were performed with identical sample orientation. The sample was poled for 20 minutes at ambient temperature. (a) Pristine sample, (b) poled at 10 kV/cm, (c) poled at 10 kV/cm and annealed at 573 K, and (d) poled at 10 kV/cm and annealed at 673 K.

significant under large electric fields.²²⁴

To investigate the dynamic nature of P_M in more detail, the dielectric permittivity ϵ_r of PMN was measured as a function of driving field amplitude E_0 and frequency f , assuming that the response is sensitive to the dynamic properties of nano-sized polar-entities.^{68,151,183,190,225} As can be seen in Figure 4.11, neither the field nor the frequency dependence of $\epsilon_r(E_0)$ between 1 Hz and 1 kHz allow for any further conclusion beyond the discussion in Chapter 3 or Ref.[151]. However, a striking similarity between the electric field needed for macroscopic polarization reversal, E_M , and the electric field amplitude of maximum $\epsilon_r(E_0)$ was found. Similar results were obtained for crystals and ceramics as summarized in Figure F.9. In all samples, the driving field amplitude of maximum dynamic dielectric permittivity ($E_{0,m}$) depends weakly on the sample

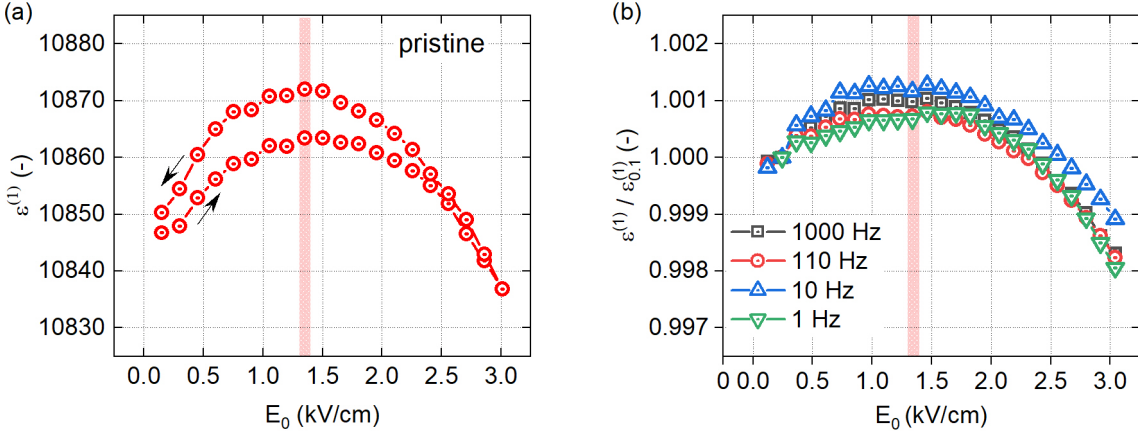


Figure 4.11. First harmonic permittivity of a [001]-PMN-A crystal as a function of driving field amplitude, $\varepsilon^{(1)}(E_0)$, for various frequencies. Arrows indicate the direction of field cycling, starting with increasing amplitude. The exact value of the electric field amplitude of maximum permittivity, $E_{0,m}$, depends weakly on sample history and measurement conditions indicating non-ergodic behavior (see Fig. F.10). It can be estimated to $E_{0,m} = (1.50 \pm 0.05)$ kV/cm with little frequency dependence between 1 Hz and 1 kHz. This value matches well with the experimentally determined field for polarization reversal $E_M = (1.35 \pm 0.05)$ kV/cm indicated by the red hatched area. The coincidence between these two characteristic electric fields and the presence of dielectric hysteresis strongly suggests that the underlying mechanism is related to the switching of nano-sized polar regions. Similar results were obtained for ceramic samples (see Fig. F.9 in Appendix F). (a) Very first measurement of a PMN-A crystal. (b) $\varepsilon_r(E_0)$ for various frequencies normalized to the first measurement point, $\varepsilon_{0.1}^{(1)}$, i.e., the value at $E_0 \approx 0.1$ kV/cm.

history and measurement setting, e.g., the time taken at each driving field amplitude level and the field amplitude increment, as presented in Figure F.10. Nevertheless, the maximum of $\varepsilon_r(E_0)$ can be estimated to occur around $E_{0,m} = (1.50 \pm 0.25)$ kV/cm. It was speculated previously that this maximum could be attributed to either intrinsic lattice tunability or the flipping of nano-sized polar regions.^{151,190,191} Intrinsic electric tunability is a reversible process^{226,227} that cannot explain the reversal of persistent polarization. The fact that the polarization reversal field E_M coincides with the field at which $\varepsilon_r(E_0)$ reaches its maximum thus, strongly suggests that the underlying mechanism is related to the switching of nano-sized polar regions and not to lattice tunability. This conclusion agrees with the analysis of the nonlinear behavior of $\delta^{(3)}$ presented in Chapter 3.

Furthermore, it can be shown that the fields used in this study do not induce a ferroelectric state in PMN samples. In principle, a ferroelectric phase can be induced in PMN by field-cooling or by the application of bipolar electric fields under isothermal conditions. The smallest threshold field required to induce a ferroelectric state by field-cooling below T_f with dc bias applied along $\langle 111 \rangle$ or $\langle 100 \rangle$ -directions are reported in the literature to be around 1.8 kV/cm and 2.9 kV/cm, respectively. At ambient temperatures, the threshold fields increase to more than 25 kV/cm⁷⁸. For bipolar driving fields under isothermal conditions, the threshold fields are comparable or greater than that.^{78,194} The characteristic electric fields found in this study (1.35 kV/cm and 1.50 kV/cm) and the poling field used (10 kV/cm) are significantly smaller and thus cannot enable percolation of nano-sized polar regions into a ferroelectric state at ambient temperature.

It is interesting to note that $\delta^{(3)}$ of STO below ≈ 100 K shows similarities to the response of PMN as seen in Figure E11. Around this temperature, STO undergoes an antiferrodistortive phase transition into a tetragonal phase^{228,229} and develops scattering characteristics as observed for PMN.²³⁰ Static disordered regions^{231,232} or defects^{233–235} have been suggested to explain these findings.

4.5 Summary and conclusions

Experimental evidence for macroscopic polarity in the nominally ergodic relaxor phase of pristine PMN is presented. The orientation of macroscopic polarization can be switched with the application of an electric dc field and requires subsequent annealing above Burns temperature (T_B) to return to its initial orientation. The dc electric field strength required to change the orientation of polarization macroscopically is similar in magnitude to the ac field amplitude of maximum permittivity. This strongly suggests that the aforementioned maximum is related to the reorientation of nano-sized polar regions and not to the intrinsic electric tunability of dielectric permittivity.

Longitudinal piezoelectric coefficients, d_{33} , of poled PMN ceramics and crystals were measured with direct and converse methods. For cumulative poling up to 50 kV/cm, moderate values of $d_{33} \approx 12$ pm/V and $d_{33} \approx 3$ pm/V were obtained for ceramics and a crystal, respectively. A hysteretic and orientation-dependent anomaly in the second harmonic phase angle of polarization, $\delta^{(2)}$, was attributed to a polarization reversal process. It is suggested that these anomalies in $\delta^{(2)}$ are a common signature for polarization reversal of ferroelectric domains and other polar entities.

These results question not only the commonly accepted narrative of a non-polar ground state^{46,49,77,82} but also the existence of an ergodic relaxor state^{77,118} in PMN below T_B . It is speculated that strain gradients,¹⁸² static nano-sized polar regions,²²⁴ charge disorder,⁷⁵ chemical ordered regions,²⁰ or other mesoscopic inhomogeneities result in a separation of phase space into at least two parts, which individually act ergodically.²³⁶

5 Thermally stimulated depolarization currents in lead magnesium niobate

5.1 Motivation

In the previous chapter, macroscopic polarization in the nominally ergodic relaxor state of lead magnesium niobate, PMN, has been revealed with the aid of dynamic pyroelectric measurements. It has been shown that the macroscopic polarization can be reversed with the application of an electric poling field and that, under isothermal conditions, the polarization decays according to the Curie von Schweidler, CvS, law over several days. Annealing experiments in combination with dynamic pyroelectric measurements have been performed to investigate the depolarization of polarized PMN *ex-situ*. It has been found that the sample has to be annealed above Burns temperature, $T_B \approx 600\text{-}650\text{ K}$,⁸¹⁻⁸³ to recover the initial orientation of macroscopic polarization. These results are surprising since it is widely believed that polarization is dynamic above the coherence temperature, $T^* \approx 400\text{-}500\text{ K}$,⁸¹⁻⁸³ at which depolarization would therefore typically be expected. In this chapter, thermally stimulated depolarization currents, TSDC, of PMN are used to investigate the depolarization process *in-situ* in more detail.

5.2 Introduction

During TSDC measurements, the thermally-activated relaxation of out-of-equilibrium polar states is studied. Therefore, a sample is first polarized before the current released during a subsequent heating cycle is measured under zero-field conditions. Appropriate heating cycles will considerably shorten the lifetime of the induced polarized state and may yield distinct current peaks that can be analyzed to attribute them to individual relaxation processes of dipoles and space charges. The experimental time can thus be considerably shortened and a larger number of processes resolved, as compared to isothermal measurements.²³⁷ In addition, TSDC measurements often have a better sensitivity and resolving power as compared to conventional dielectric permittivity measurements, in part owing to the relatively low equivalent measurement frequency of $f \approx 10^{-3}\text{ Hz}$.^{238,239} In contrast to the previously discussed dynamic pyroelectric method, for which the intrinsic response of polarization is predominately investigated, extrinsic contributions are of major importance for TSDC measurements.^{238,239} The theory of thermally stimulated depolarization currents arising from dipolar and space charge relaxation will be discussed below.

5.2.1 Dipolar relaxation

Dielectric dipoles describe a displacement of positive and negative charge centers by a finite distance. In other words, the charges are intimately linked to each other, determined by physical or chemical interactions and the local electric field.²⁴⁰ For the simplest case, dipolar relaxation is described by a single relaxation time, τ_0 , and activation energy, E_a . The expected current density, j_D , can then be derived as shown in Appendix G to

$$j_D(T) = \frac{P_e(T_p)}{\tau_0} \exp\left(-\frac{E_a}{k_B T}\right) \exp\left[-\frac{1}{q\tau_0} \int_{T_0}^T \exp\left(-\frac{E_a}{k_B T'}\right) dT'\right], \quad (5.1)$$

where P_e is the equilibrium polarization, T_p the poling temperature, k_B Boltzmann's constant, q the heating rate, and T_0 the initial temperature. Equation (5.1) describes an asymmetric peak for which the first exponential function increases j_D at the low-temperature side of the peak, while the second exponential function decreases and finally suppresses it. In the initial rise of a peak described by Eq. (5.1), the integral in the second exponential is small so that j_D can be approximated with an Arrhenius-type function and E_a obtained from^{241,242}

$$\ln j_D(T) = \text{const.} - \frac{E_a}{k_B T}. \quad (5.2)$$

To study the influence of the individual parameters on j_D , Eq. (5.1) is differentiated with respect to temperature to obtain an expression for the maximum temperature, T_m , of the current density peak

$$T_m = \left[\frac{E_a}{k_B} q \tau_0 \exp\left(\frac{E_a}{k_B T_m}\right) \right]^{1/2}. \quad (5.3)$$

It can be seen that the peak position increases with q , τ_0 , and E_a , and that it is approximately proportional to E_a .²⁴³ Moreover, for a fixed heating rate, T_m will have a constant value since all other parameters in Equation (5.3) are material constants. On condition that P_e respects the Langevin function and that it can be obtained and maintained until the TSDC experiment begins, the peak amplitude j_{\max} is characterized by a linear increase with increasing electric poling field, E_p .^{244,245} Taken together, for dipolar relaxation with single activation energy and relaxation frequency, a peak with fixed position and a linear increase in amplitude with increasing poling fields is expected for a TSDC experiment with a constant heating rate.

It must be emphasized that several assumptions and simplifications were made to derive Eq. (5.1). To clarify the limitations of the following TSDC analysis, the most important shortcomings shall be discussed. For the temperature dependence of the relaxation frequency, an Arrhenius-type relation was assumed. In practice, this may not be justified for relaxor ferroelectrics, for which the empirical distribution of relaxation times of Williams, Landel and Ferry,²⁴⁶ the so-called WLF equation, maybe more accurate.^{57,63} In the field of relaxor ferroelectrics, the WLF equation is better known as Vogel-Fulcher relationship.⁷² Consequently, Eq. (5.2) would need to be reformulated to account for the actual distribution. Another assumption is that the Langevin equation describes the equilibrium polarization [see Eq. (G.2)], which is achieved and maintained until the experiment has begun. However, in the vicinity of glass transitions in polymers the former may not hold true.²³⁸

It is also frequently found in experimental practice that the obtained polarization is larger than expected when the sample is polarized at elevated temperatures due to the continuation of the poling procedure during cooling.^{238,239} Similarly, changes in polarization during storage of samples may influence the obtained results.²³⁸ Accordingly, results may depend on cooling rates and storage times. A possible deviation from a linear $j_D(E_p)$ relation may therefore have several causes. The last simplification discussed here is the assumption of a single activation energy and relaxation frequency. This can hardly be justified in disordered systems, in which dipole-dipole interactions, variation in dipole size and shape, and inhomogeneous internal fields can cause distributions of the former.²⁴⁷ This may not only alter the appearance of TSDC peaks,^{239,248} but may also result in similar relations for dipoles and space charges with distributed relaxation parameters.^{238,239} It is remarkable that, nonetheless, some disordered systems follow the relations derived here.^{249,250}

5.2.2 Space charge relaxation

The theoretical description of space charge relaxation is much more complex than the case of dipolar relaxation. Processes such as the creation, migration by drift and diffusion, trapping, and the recombination of charge carriers, as well as the blocking effect of the electrode-dielectric interface must be considered.²³⁸ The underlying processes are space and time-dependent, governed by a set of nonlinear partial differential equations. Existing models rely on a substantial number of simplifications to derive general trends, some of which will be introduced shortly following Ref.²³⁹.

The term space charge refers to a spatially inhomogeneous distribution of charge carriers in a dielectric medium, causing the material to be locally non-neutral. In general, these charges can be classified as hetero and homo charges. The polarity of hetero charges has the opposite polarity to the adjacent electrode, while homo charges have the same. Hetero charges are the consequence of electric field-induced transport and the generation of mobile charge carriers. Homo charges, on the other hand, are often the result of charge injection at high electric fields. Furthermore, there is a significant difference between space charges stemming from the migration of mobile ions and those due to charges bound to localized states, the so-called trap charges. Before discussing them separately, it is useful to clarify the difference between polarization and conduction. Polarization is the result of a finite displacement of positive and negative charge centers, while conduction relates to a finite average velocity of charge carriers.²⁴⁰ Both phenomena can involve the same species, causing internal recombination and reduced detection efficiency for space charge relaxation processes as compared to dipolar relaxation.²⁴⁰

Relaxation due to ion migration

Ionic polarization relaxation can be described by drift and diffusion motion under the influence of space charge fields.²⁴¹ Drift is a result of local fields that force charge carriers to move towards the opposite charge, whereby neutrality is restored. This mechanism is often referred to as space charge limited drift (SCLD). Diffusion will result from concentration gradients and will act to reduce them. While diffusion is often neglectable in TSDC measurements, it can be considerable in dielectrics with high polarization and after poling at high temperatures.²³⁹ In hetero electrets, SCLD and diffusion will act together, whereas, in homo electrets, diffusion may cause a current reversal. Diffusion will, in any case, only be visible for blocking electrodes, i.e., electrodes that do

not permit mass transport through the dielectric electrode interface for the migrating ion under consideration. Otherwise, the diffusion current will be compensated by intrinsic conduction. As mentioned earlier, mobile ions or the dissociation of defect clusters can provide charge carriers for ion migration mechanisms. The resulting TSDC peaks can therefore be expected to be larger and appear at higher temperatures with respect to peaks originating from dipolar reorientation,²³⁹ and to saturate as one of the last processes. This is due to the relatively larger separation of charge carriers, which can involve macroscopic motion within the sample. The temperature dependence of current caused by ion migration will often follow closely that of ohmic conduction in dielectrics, as both processes can involve the same charge carriers. It is interesting that the release of space charges is often associated with a glass transition in polymers.²⁴⁵ The measured current resulting from the migration of a single ionic species under the influence of a poling field can be approximated to

$$Q_D \approx P = 2avNqt_p \exp\left(-\frac{E_a}{k_B T}\right) \sinh\left(\frac{qaE_p}{2kT_p}\right) = Q_0 \sinh\left(\frac{qaE_p}{2kT_p}\right), \quad (5.4)$$

where P is polarization, a jump distance, v is the attempt to escape frequency, N is the ion density, q is the ionic charge, H is the potential barrier height. The equation predicts a parabolic increase in released charge with increasing poling fields and a decrease for increasing poling temperatures.²⁵¹ In practice, a peak shift to higher temperatures with increasing poling temperatures is usually observed.^{244,245} Other interpretations can be found that predict different outcomes.^{238,239,241}

Trap charge relaxation

Trap charges are electrons and holes that are bound to localized electronic states.²⁴¹ Chemical disorder in the form of dopants, impurities, vacancies, interstitials, and their associations often cause strong or deep trap states.^{237,252} Structural disorder, on the other hand, is more likely to result in weak or shallow traps states.^{237,252} Both trap states can result in thermally activated conduction mechanisms, such as charge hopping or multiple-trapping.²³⁷ For a discrete set of initially filled trap states without retrapping, the I_D takes the form of

$$I_D(T) = n_0 \tau e \mu v \exp\left(-\frac{E_a}{k_B T}\right) \exp\left[-\frac{s}{q} \int_{T_0}^T \exp\left(-\frac{E}{k_B T'}\right) dT'\right], \quad (5.5)$$

where n_0 is the initial density of filled trap states μ is the electron mobility. Current peaks resulting from trap charges may shift to lower temperature with increasing poling fields,²⁵³ while different results can be obtained for varying the sample thickness.^{241,254,255}

Despite severe limitations in the mathematical description of depolarization processes, especially for systems with distributed parameters, an close correlation between TSDC peaks and the dipolar polarization and defect structure of materials is present. Having in mind theses limitations, the following discussion will be guided by relations derived for basic models, nonetheless, since similar relations have also been observed in complex materials.^{249,250}

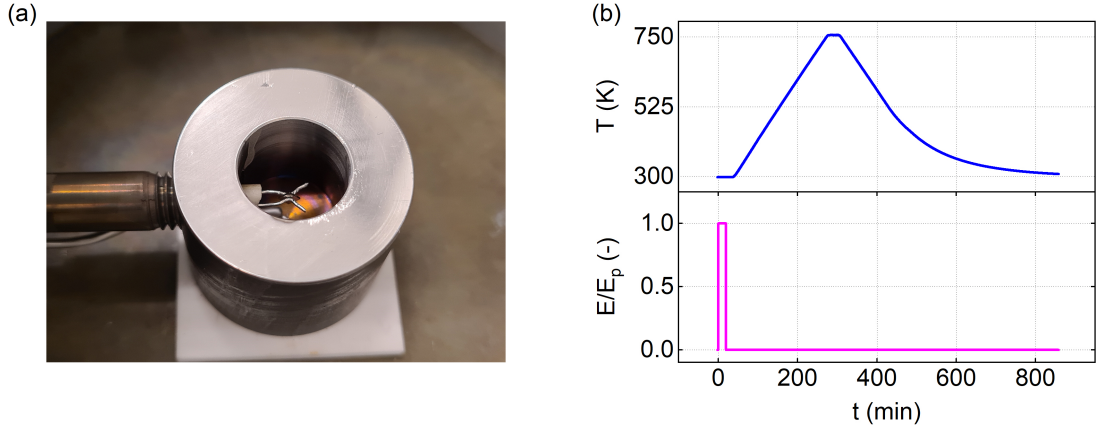


Figure 5.1. Thermally stimulated depolarization current, TSDC, experimental setup and procedure. (a) Thermal and electrical shield with sample fixture. The sample is clamped between two platinum wires that act as leaf springs. The thermocouple is located approximately 3 mm below the sample. (b) Visualization of the usually applied temperature and poling procedure. The heating rate was 2 K/min and the isothermal holding time at 750 K lasted ≈ 30 min.

5.3 Thermally stimulated depolarization currents of lead magnesium niobate

For this study, samples in parallel plate capacitor geometry were electrically or mechanically polarized, and the relaxation of the induced states were subsequently measured without delay, if not stated otherwise. Electric fields were applied along the thickness direction while stress was applied perpendicular thereof. The setup was optimized throughout this work to minimize noise and parasitic voltages. Inherent to this procedure are variations in noise level, temperature, and current readings. The optimized setup is shown in Figure 5.1(a). A scheme of the most frequently applied electrical poling procedure and the subsequent heating cycle is depicted in Fig. 5.1(b). In addition, four other poling procedures were applied: isothermal poling (IP), continuous field-cooling (FC), fractional-poling (FP), and pulse poling (PP). For IP, the sample was heated to a given temperature and polarized for 20 min. After that, the sample was cooled to ambient temperature with the electric field applied. During the FC procedure, the sample was annealed at 750 K for 30 minutes and subsequently cooled to ambient temperature. At a given poling temperature, the poling field was applied and maintained during cooling back to ambient temperature. FP follows a similar protocol, but the electric field is removed before reaching ambient temperature, and the top and bottom electrode are connected electrically to form a short-circuit before the cooling cycle ends. During PP, short pulses of 0.5 kV/cm were applied during cooling from elevated temperature, followed by a constant poling field applied at a lower temperature and maintained until ambient temperature was reached. After poling, the current was measured during subsequent zero-field heating/cooling cycles.

Figure 5.2 compares TSDC measurements of electrically polarized PMN ceramics and crystals ($T_p = 300$ K). As seen for the ceramic sample in Fig. 5.2(a), a systematic variation of current density, j_D , between 600 K and 700 K is obtained for different poling fields (E_p). Polarizing the sample at 393 K causes two notable changes. A relative stronger j_D increase in the high-temperature part of the spectrum and a smaller peak around the polarization temperature, T_p . While both peaks

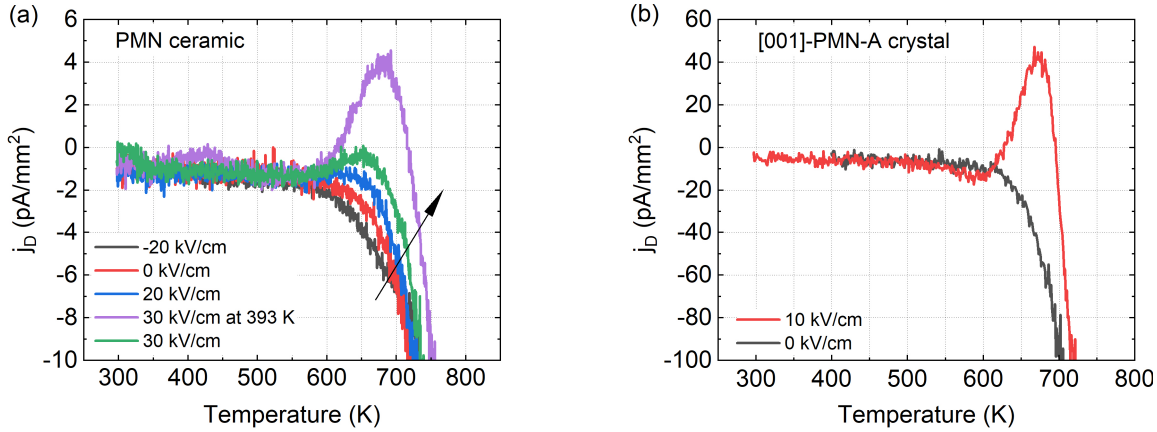


Figure 5.2. Comparison of TSDC spectra of lead magnesium niobate, PMN, ceramics and crystal. (a) Ceramic samples polarized at ambient temperature and 393 K with different electric fields. (b) Comparison between TSDC measurements obtained for annealed and at ambient temperature poled [001]-PMN-A crystal.

appear in characteristic temperature regions of relaxor ferroelectrics, namely Burns temperature, $T_B \approx 600\text{--}650\text{ K}$,^{82,83} and the coherence temperature, $T^* \approx 400\text{--}500\text{ K}$,^{82,83} the peak around T^* may also be explained by a polarization mechanism with distributed relaxation parameters. A similar response around T_B is obtained for a [001]-PMN crystal as presented in Fig. 5.2(b). Note that the ordinate is stretched by a factor of ten and that the maximum of j_D is more than an order of magnitude larger as compared to the ceramic sample. For PMN ceramic and crystal samples, noise in the order of a few pA, and a strong increase in the absolute value of j_D above 700 K is observed. The noise was related to the action of the thyristor heating unit, insufficient shielding, and noise inherent to the measurement device. The strong increase is likely due to the onset of conduction²⁵⁶ caused by a parasitic offset voltage or similar.

Results obtained for an unpoled and poled PMN crystal of similar quality and dimensions after optimization of the experimental setup are shown in Figure 5.3. The old and new setups are compared in Fig. 5.3(a). As readily seen in the inset, the magnitude of j_D increases exponentially between approximately 400 K and 700 K without detectable anomalies for the new setup. A slight hysteresis between heating and cooling cycle is observed that could be due to many reasons, including measurement artifacts. This hysteresis was not further investigated, and the current response of the unpoled state will be used as a reference state in the following for a series of subsequent measurements with increasing E_p .

In the following, the evolution of TSDC spectra with increasing direct current, dc, electric poling field up to 6 kV/cm is discussed. During this measurement series, the sample was polarized inside the setup to avoid any uncertainties that may arise from sample handling. The three generic TSDC curves obtained are contrasted in Fig. 5.3(b): (i) The unpoled reference curve, in which heating and cooling cycles approximately coincide. (ii) A curve in which only the heating cycle is significantly different from the reference curve. (iii) And a curve in which both the heating and the cycle deviate from the reference curve. A strong decay of j_D around 300 K is observed for all polarized samples, as depicted for $E_p = 6\text{ kV/cm}$ in the inset. This decay reflects the immediate polarization relaxation after the poling field is removed, which results in a current opposite of the

5.3. Thermally stimulated depolarization currents of lead magnesium niobate

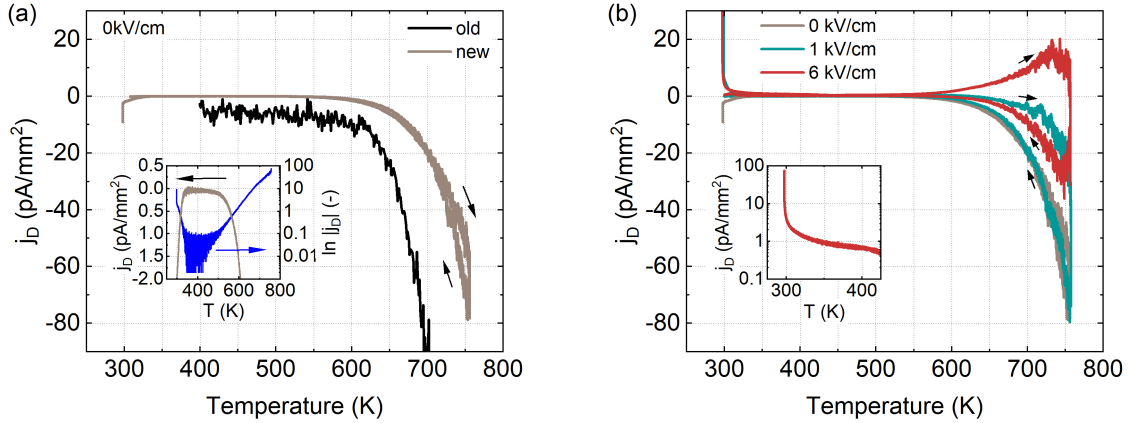


Figure 5.3. TSDC spectra as a function of electric poling field, E_p , of a [001]-PMN crystal. (a) Unpoled reference state. (b) Polarized state. E_p is indicated in the legend. The sample was polarized for 20 min at ambient temperature. Measurements were taken under zero-bias conditions. The vertical section at 750 K appears during a 30 min period of constant temperature before the heating rate is reversed.

poling current, and intrinsic pyroelectric. Usually, we also expect TSDC peaks to have currents opposite to the poling current.²³⁹

Taking a closer look now at TSDC result in the temperature range between 600 K and 750 K in Figure 5.4(a), four distinct behaviors can be resolved: State o), the unpoled state; State i), the weakly polarized state, with poling fields up to 1.5 kV/cm; State ii), the intermediate polarized state, with poling fields ranging between 2.0 kV/cm and 5.0 kV/cm; State iii), the strongly polarized state, with poling fields starting from 6.0 kV/cm. The term weakly and strongly polarized are here arbitrarily defined based on the chosen electric field range. While the reference curve falls below -20 pA/mm² at around 700 K, a weak poling field of 0.5 kV/cm is already sufficient to notably change the current response. The current intensity decreases before it strongly increases at around 750 K. It is assumed that this behavior results from the superposition of the negative current obtained for the unpoled reference state and a positive current resulting from a relaxation process. An alternative explanation could be an overall reduction in conductivity after poling. For intermediate poling fields between 2.0 and 4.5 kV/cm, the current intensity is further decreased with respect to states o) and i). At $E_p = 6.0$ kV/cm, the current response changes sign above 600 K, followed by a peak with a maximum of approximately 15 pA/mm².

On a lower scale, two distinct peaks can be associated with Stage i) and Stage ii), as shown in Fig. 5.4(b). First, Peak A emerges around 600 K, followed by Peak B around 700 K. Above 2.5 kV/cm the two peaks merge. Taking into account that TSDC peaks are often located at lower temperatures as compared to peaks in dielectric measurements²³⁹ and uncertainty in the temperature reading of $\approx \pm 10$ K due to a distance of 3 mm between the thermocouple and the sample, the position of Peak A corresponds well to Burns temperature T_B and the position of Peak B to the first appearance of piezoelectric response in PMN crystals.¹⁸² It is intriguing that Peak A and Peak B appear in sequential order with increasing poling field. An important question to ask is whether individual or sequential mechanisms are present. Sequential mechanisms could be the orientation and dissociation of dipoles,^{251,253} or sequential phase transitions. It is also interesting to note that the response does not change gradually with increasing poling field but incremental between the

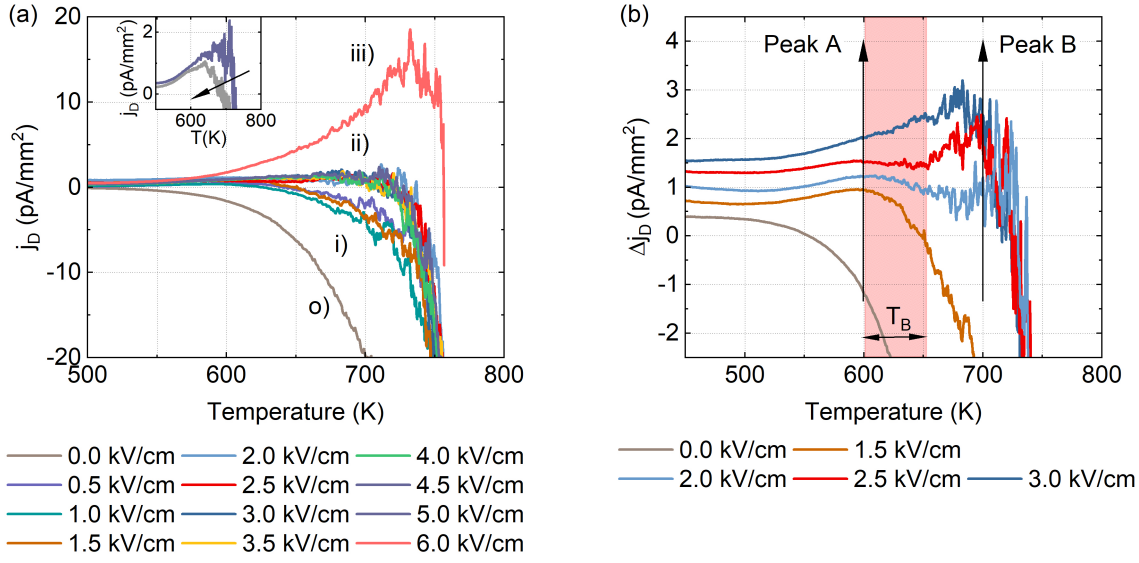


Figure 5.4. TSDC spectra of [001]-PMN-A crystal in the vicinity of Burns temperature. $T_B \approx 600 - 650 \text{ K}$ ^{81,83}. The electric poling field, E_p , is indicated in the legend. (a) Four stages can be identified for E_p between 0 kV/cm and 6 kV/cm. Reference state o), weakly polarized state i), intermediate polarized state ii), and strongly polarized state iii). (b) Two peaks sequentially emerge with increasing poling field. Peak A in the vicinity of T_B and Peak B around 700 K. The TSDC spectrum for $E_p = 5.0 \text{ kV/cm}$ is only presented in the inset.

stages. However, between Stage ii) and Stage iii), at around 5.0 kV/cm, j_D is first reduced before a strong rise follows, as indicated by an arrow in the inset of Fig. 5.4(a).

Two remarkable observations can be made. First, the transition between Stage i) and Stage ii), i.e., the first appearance of Peak B occurs at an electric fields strength for which macroscopic polarization reversal can be induced, and a peak in the electric field-dependent dynamic dielectric permittivity is observed.¹²² Second, the most obvious TSDC response is obtained at temperatures around T_B . That is unexpected since it is widely accepted that local polarization in PMN is fundamentally dynamic in nature above T^* .^{45,82,83} In other words, it could be expected that a polarized state becomes unstable in this temperature regime, resulting in a distinguishable anomaly in the TSDC spectra. However, most theories try to predict the evolution of the ground state and do not consider the induced non-equilibrium states under investigation.

Inspecting the temperature region around T^* more closely in Figure 5.5(a), indeed, a third peak can be identified, Peak C. It appears at $E_p \approx 2.5 \text{ kV/cm}$, and its strength increases approximately linearly with increasing E_p before it is reduced above $E_p = 5.0 \text{ kV/cm}$. It is interesting to compare this evolution with the behavior of Peak B in Fig. 5.5(b) and Fig. 5.4(b). Above 2.5 kV/cm the intensity of Peak B saturates with respect to E_p until approximately 5 kV/cm, above which Peak C starts to diminish. A linear increase of peak amplitude as observed for Peak C together with a nearly invariant peak maximum temperature is often assigned to dipolar relaxation. To investigate the evolution of the third peak, Peak C, in more detail, its background is fit with two exponential functions [$y = A_1 \exp(-x) + A_2 \exp(+x)$] and subtracted from the measurement data. These fits are detailed in Figure H.1 in Appendix H, and extracted peaks and Gaussian fits to the latter are presented in Figure 5.6(a)&(b). The obtained peak amplitudes, j_{\max} , and peak positions, T_{\max} ,

5.3. Thermally stimulated depolarization currents of lead magnesium niobate

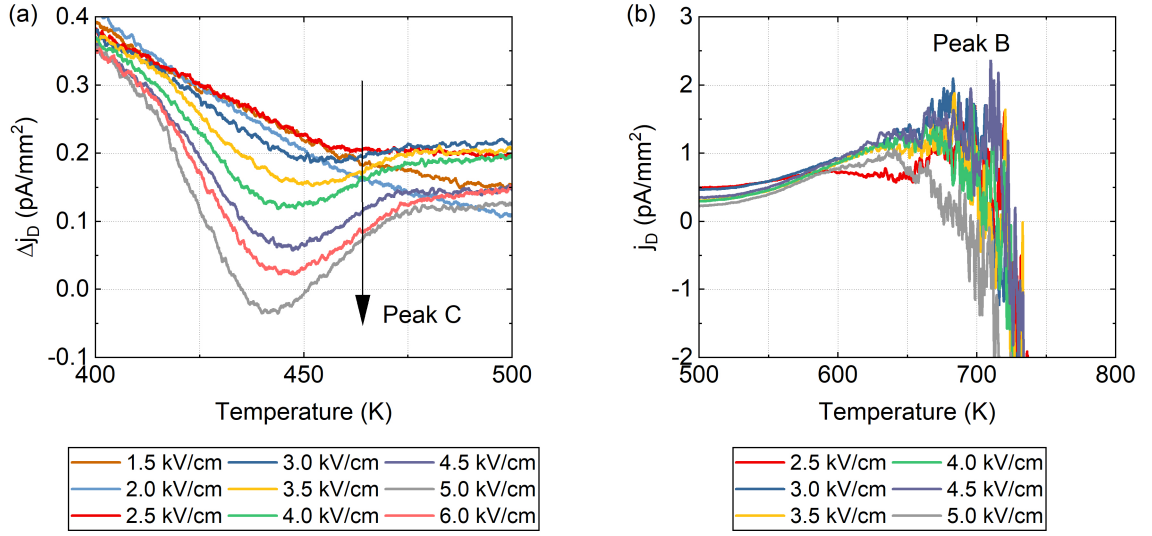


Figure 5.5. TSDC spectra in the vicinity of characteristic temperatures for a polarized [001]-PMN-A crystal. E_p is indicated in the legend. TSDC spectra in the vicinity of (a) the coherence temperature T^* and (b) T_B . The data in (a) are vertically shifted for a better comparison.

are illustrated in Fig. 5.6(c). It is seen that i_{\max} increases quasi-linearly with E_p up to 4.5 kV/cm before it is reduced above 5.0 kV/cm, while the peak centers shift slightly to lower temperatures with E_p , and the shift saturates at higher temperatures. Such a shift to lower temperatures could be interpreted in favor of trapped charges as the underlying mechanism.²⁵³ Since the origin of the background is not identified, the arbitrarily chosen fit function may cause a systematic error that may result in the observed change of peak temperature. If a tolerance of ± 2.5 K is accepted, the temperature of the peak position can be considered constant. In that case, the data would suggest dipolar relaxation as the origin of the peak around T^* .

A peculiar feature of Peak C is that it has an opposite direction as compared to the peaks at T_B and above. As mentioned previously, a positive j_D is expected for processes that result in a current opposite of the poling current. That means the depolarization current of Peak C has the same direction as the current during poling. This is a rather exceptional observation that has been observed for specimens with charge injection at the electrodes in combination with other mechanisms. In particular, space charge limited drift and dipolar relaxation, or space charge limited drift and diffusion, often observed just in the vicinity of glass transitions in polymers.²⁴⁵ It is noted that injection of ionic charge carriers into the material is not expected for the applied sputter-coated platinum electrodes. Another occurrence of current reversal has been observed for phase transitions,²⁵⁷ e.g., for relaxor ferroelectric solid solutions.²⁵⁸

For $E_p = 6$ kV/cm, a strong increase of j_D above 700 K has been found, Fig. 5.2. It is not clear if this is a continuation of Peak B after a hypothetical intermediate process or an additional contribution. It has been previously shown in Fig. 5.3(b) that the cooling curve deviates from the unpoled reference measurement for this poling field. This could be either attributed to incomplete depolarization or a persistent change in conductivity. Studies on degraded iron-doped barium titanate suggest that persistent changes in conductivity may be attributed to alterations of the defect structures that cannot be fully recovered even after annealing at around 673 K.²⁵⁹

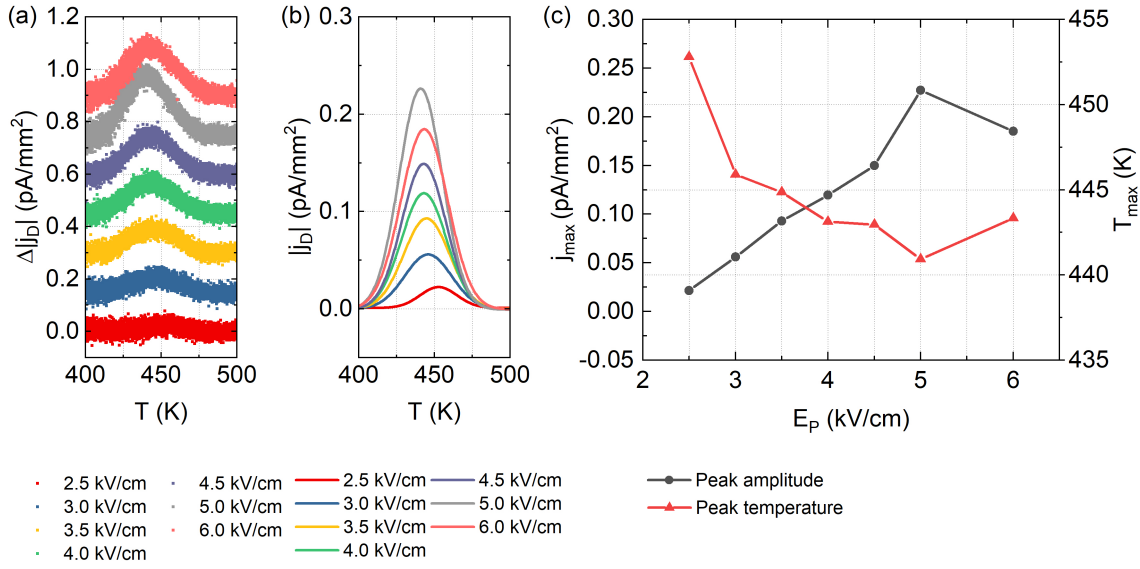


Figure 5.6. Results of peak fitting of TSDC peak in the vicinity of T^* . (a) Peaks extracted via the peak fitting procedure depicted in Fig. H.1 in Appendix H. Data are vertically shifted for comparison. (b) Gaussian fits to data presented in (a). (c) Current density maximum, j_{max} , and temperature of current density maximum, T_{max} , as a function of poling field, E_p , obtained from (b).

To gain further insight into the underlying depolarization mechanisms the effect of the variation of the isothermal poling temperature was investigated. The obtained results are compared in Figure 5.7. For $T_p = 393$ K, the TSDC spectrum is dominated by Peak C at T^* . For poling temperatures above T^* , various peaks and a strong increase of j_D are present. For $T_p = 513$ K, a weak additional peak below T_p and a single strong peak around 680 K were measured. For $T_p = 554$ K, four peaks were obtained. A peak around 400 K, a peak just below T_p , a weak peak around 675 K, and a strong peak at around 700 K. Peak C could not be detected, either because it is absent or due to an overlap with the peak below T_p . For the maximum poling temperature, $T_p = 750$ K, it was not possible to apply $E_p = 2$ kV/cm due to a strong increase in poling current. A pulse poling (PP) approach was therefore applied with $E_p = 0.5$ kV/cm. For PP, a peak around 400 K and a broad asymmetric peak around 680 K were observed. The appearance of peaks just below the T_p suggests that either a distribution of dipoles or ions is present. A major finding of these experiments is the appearance of a peak around 400 K for poling temperatures above 550 K. Several authors proposed a phase transition at around $T_C \approx 400$ K,^{45,48,83,260} and the TSDC peak obtained around this temperature will be referred to as Peak E.

To gain further insight into the nature of the underlying mechanisms for TSDC a mechanical poling approach was used. A constant stress was applied perpendicular to the electrode faces of the PMN crystal under open-circuit conditions. Note that even in ferroelastic materials, a constant unidirectional normal stress is ideally not expected to result in a polarized state of the sample. While ferroelastic-ferroelectric domains may be reoriented in principle,^{261,262} in theory, there always exists an energetically equivalent state with opposite polarization and the same strain, resulting in a zero net polarization. An exception to this would be a single domain state,^{263,264} which we do not anticipate in the present case. For stress gradients²⁶⁵ or uniaxial stress in the presence of a bias that lifts the degeneracy of domain variants,^{266,267} however, a

5.3. Thermally stimulated depolarization currents of lead magnesium niobate

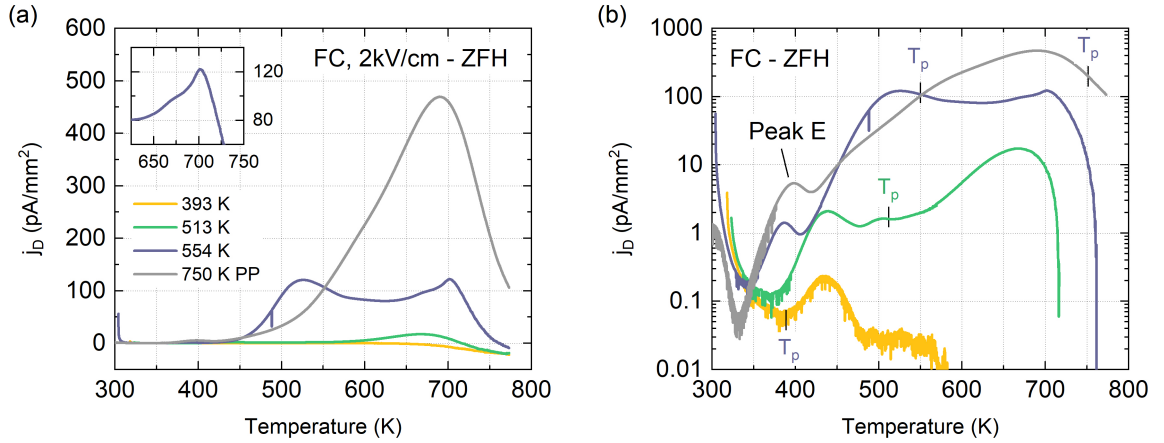


Figure 5.7. TSDC spectra for electric field-cooled (FC) [001]-PMN-A crystal. (a) The sample was poled with an electric field of 2 kV/cm for 20 min at the temperatures indicated in the legend and subsequently cooled to ambient temperature with the applied field before the data presented were recorded under zero-field conditions. (b) Same data as (a) in logarithmic scale. The individually poling temperatures, T_p , are indicated. Peaks around T_C and T^* are seen. For measurements above ≈ 500 K, a peak just below T_p is observed, indicative of processes with distributed relaxation parameters.

polarized state may be obtained by uniaxial stress. The mechanical poling procedure was inspired by observations of subtle changes in dynamic pyroelectric response for samples subjected to mechanical shock.

TSDC measurements for mechanically poled samples are shown in Figure 5.8. It is seen that two peaks can be induced, which are not present in the unpoled state (see Fig. 5.3). A relatively weaker peak around 600 K, Peak A' and a relatively stronger peak around 700 K, Peak B'. Comparing these stress-induced peaks with the electrically induced peaks of similar current intensity in Fig. 5.4, it can be observed that for the electrical poling induced case, only one peak, while in the mechanically poling two peaks are present. It is not trivial to compare electrically and mechanically induced polarization states since the underlying tensor properties are of different ranks.⁴⁷ To compare the two poling procedures, the energy stored in electrically polarized and a mechanically strained PMN crystal are estimated in Appendix I. The results show that an applied stress field of -3 MPa (used here) is energetically equivalent to an electric field of approximately 0.25 kV/cm which is relatively low. Therefore, it may be more accurate to compare the stress-induced current response in Fig. 5.8 to the current of weakly and intermediately electrically polarized state in Fig. 5.4. Based on the observed similarities in peak temperatures, the electrically induced Peak A and Peak B are assigned to the stress induced Peak A' and Peak B', respectively.

It is interesting to note that stress seems to be more efficient in polarizing PMN crystals if the linear elastically stored energy is compared to the resulting TSDC response. Different electrical and mechanical activation energies for the reorientation of nano-sized polar regions is a disputed topic.^{57,268} To estimate whether the mechanically polarized state could have been induced by a slight asymmetry of the sample, the polarization induced by the flexoelectric effect was compared to polarization induced by an electric dc bias field in Appendix J. Approximating the sample as a truncated pyramid, the maximum applied compressive stress in this study would result in polarization that would be expected from an applied dc electric bias field of approximately

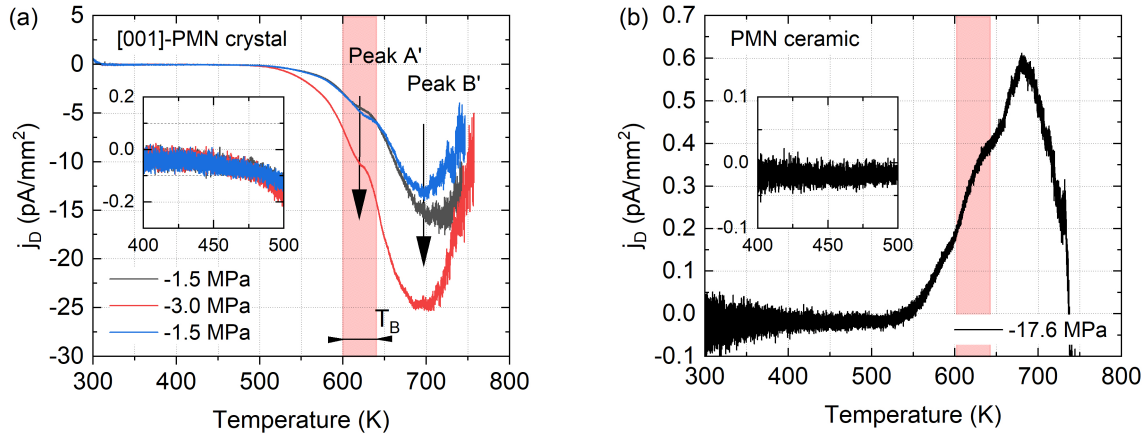


Figure 5.8. TSDC spectra of mechanically poled PMN. A constant compressive stress, as indicated in the legend, was applied perpendicular to the electroded faces for 20 min at ambient temperature. (a) TSDC spectra for different applied stresses for [001]-PMN-A crystal. Two peaks, Peak A' and Peak B', can be observed. T_B is indicated as a red hatched area. No peak can be observed around T^* , as shown in the inset. (b) TSDC spectra for PMN ceramic.

0.04 kV/cm. This field strength appears to be too small to sufficiently polarize the sample; see TSDC response for samples polarized at $E_p = 0.5$ kV/cm in Fig. 5.8(b). This suggests that the applied stress is insufficient to induce a polarized state via the flexoelectric effect. It is thus more probable that the stress lifts the degeneracy of domain variants and directs ferroelastic switching towards a macroscopically polar state.²⁶⁶

The same arguments hold true for an internal pre-existing electrical bias. The hypothesis of an internal electric bias is supported by the existence of macroscopic polarization that has been previously reported¹¹² and the obtained negative j_D . For electrical poling, the poling field was applied against the pre-existing polarization, and the sample was mounted so that positive j_D values are expected. For mechanical poling, the sample was compressed and then mounted in the same orientation as for electrical poling resulting in reversed TSDC peaks. In other words, stress polarizes the sample in the same direction as the pre-existing polarization, the origin of which is still unclear. Therefore, it is suggested that mechanical poling is due to ferroelastic-like switching in the presence of an internal electric bias field that could be accompanied by pre-existing strain gradients¹⁸² or similar. A pressure-induced phase transition would require hydrostatic pressures above 4 GPa and is therefore not considered viable.^{269,270}

It is beyond any doubt that nano-sized polar regions in PMN are elastically active.^{47,57} What is rather surprising is that stress-induced TSDC peaks are stable up and above T_B , and the absence of any detectable anomaly around T^* . This could be the case because the mechanism responsible for Peak C is not elastically active or cannot be sufficiently activated with the applied stress field. An unfavorable orientation of the strain tensor of the underlying entity with respect to the applied stress could explain this. The former seems to be unlikely given that PMN is considered mechanically active below T^* , based on structural and acoustic techniques.^{45,81} To probe a variety of crystallographic directions simultaneously, TSDC experiments with a ceramic PMN sample were performed. The results are shown in Fig. 5.8(b). Up to a transversal load of -17.6 MPa, no detectable peak could be induced at T^* while Peak A and Peak B appear. However,

5.3. Thermally stimulated depolarization currents of lead magnesium niobate

the relatively low peak intensities raise the question of whether the experimental sensitivity is sufficient, keeping in mind that Peak C is expected to be the weakest peak to observe. It would be interesting to perform similar experiments with crystals of different orientations, which were not available at the time of writing.

Electrical and mechanical poling induce peaks in TSDC spectra at T_B and above. The stability of the induced states up to T_B and the absence of a peak at T^* for mechanically poled samples raise questions about the meaning of T^* in models based on a single type of continuously evolving polar entities.^{18,47,179} TSDC measurements as a function of T_p , on the other hand, show a strong increase in j_D and peaks intensities below T_p . Following the literature on TSDC in polymers, this could be interpreted as an equivalent of a glass transition at T^* and a distribution of dipoles or ionic defects. An approach to distinguish between distributed dipoles and ionic defects is fractional-poling. For this, the sample is polarized during continuous cooling from a temperature where dipoles are assumed to be mobile, followed by a period of short-circuiting. In case of a distribution of dipoles, a fraction of the available dipoles will be oriented and frozen- in during cooling, while subsequent shorting will remove the part of the distribution with shorter relaxation times. As a result, during subsequent heating, a peak should only be observed in the temperature range where poling took place.

For this experiment, it is assumed that dipoles exist and are mobile between T_B and T^* . The poling parameters were adjusted accordingly, as indicated in the top panels of Figure 5.9. Before poling, the PMN crystal was annealed at approximately 750 K for 30 min and then continuously cooled as indicated in Fig. 5.1(b). For this field-cooling approach, no isothermal holding time was applied in contrast to the previously discussed isothermal poling experiments in Fig. 5.7. For fractional-poling, the electric field was applied only between 575-550 K. The cooling procedure was stopped at around 400 K to avoid depolarization during the extended time required to cool to 300 K.

For electric field-cooling in Fig. 5.9(a), four peaks located at T_C , at T^* , around T_B , and around 720 K have been obtained. In contrast to the previous isothermal poling experiments, no peak could be resolved at T_p . Instead, strong peaks around T_B and 720 K are present. For fractional-poling, a peak slightly below T_B and around 710 K are observed. Again, no peak can be observed around T_p . The absence of a peak around T_p for the fractional-poled case would support the picture of purely dynamic polarization mechanisms active above T^* . However, the strong peaks at T_B and 720 K show that persistent polarization can be induced. An issue open to argument is whether dipolar relaxation can be expected above T_p . While some theories predict that peaks can only be obtained below T_p ,^{238,239} it is a well-known fact that some ferroelectric materials can be polarized at ambient temperature and subsequently depolarized at significantly high temperatures.

It is interesting to compare the peak position between field-cooling and fractional-poling. Under the assumption that the peaks obtained above 600 K have the same origin, a shift to higher temperatures can be observed for field-cooling. Since, for both poling procedures, the same electric field was initially applied at the same poling temperature, it is suggested that different poling and short-circuiting times or the field-cooling through T^* cause this shift. The fact that there is no peak around T_p for field-cooling experiments while it is present for isothermal poling may indicate the presence of a time-dependent process. A time-dependent process that operates at elevated temperatures is ionic migration.

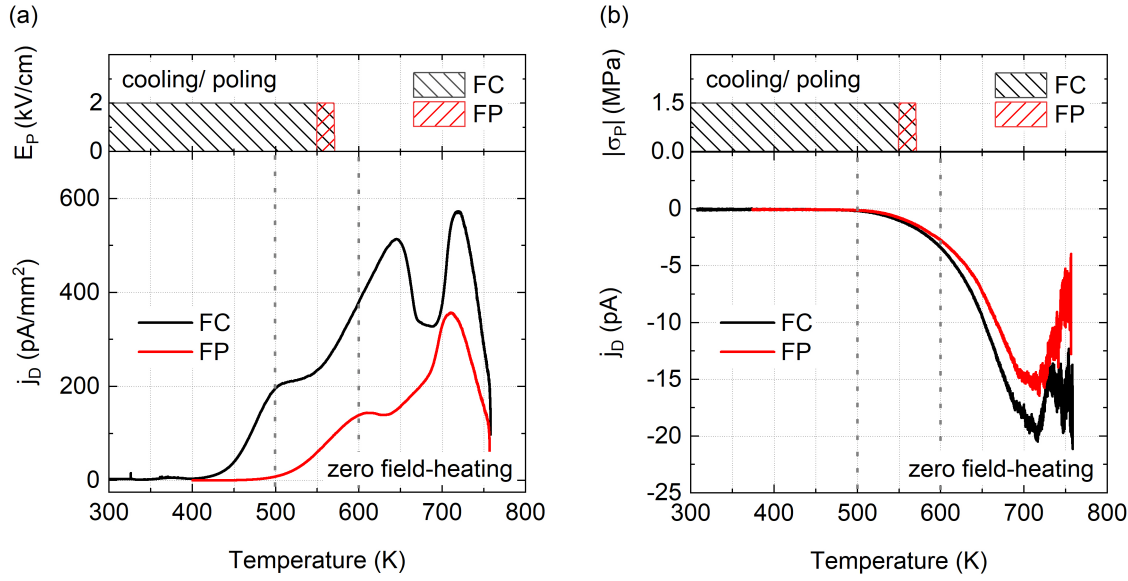


Figure 5.9. TSDC spectra for electrical and mechanical field-cooled, FC, and fractional-poled, FP, [001]-PMN-A crystal. Each panel, (a) and (b), consist of two parts. The upper part describes the poling condition during cooling, and the bottom part describes the TSDC spectra recorded during heating without applied poling field, i.e., zero-field heating. For FC, the electric poling field, E_p , and compressive stress, σ_p , were applied from 575-300 K. For FP, E_p and σ_p were applied only between 575-550 K. The dashed lines indicate the approximate lower and upper bound of T_B and T^* , respectively. (a) Electrical poling with $E_p = 2$ kV/cm, and (b) mechanical poling with $\sigma_p = -1.5$ MPa.

For mechanically field-cooled samples, the TSDC spectra in Fig. 5.9(b) features only a single peak around 700 K that is slightly larger for field-cooling. The absence of a peak around T_B is intriguing. It is speculated that, in principle, a peak around T_B is either due to dipole reorientation or ionic motion. If there were mechanically active dipoles present above T^* , one could expect that these are more readily aligned as compared to mechanical poling at ambient temperatures. This is obviously not true for the peak at T_B . A reason for this could be that dipoles only exist below T^* and that their formation can be avoided by uniaxial stress. An alternative explanation could be the absence of the electrical bias above T^* that lifts the degeneracy of equivalent symmetry variants. In that case, a symmetric, i.e., a non-polar state could be expected. Finally, the mechanical boundary conditions used for the mechanical poling approach could be different at elevated and ambient temperatures.

5.4 Aging in lead magnesium niobate

While several peaks can be observed during the heating cycle for mechanically or electrically poled samples, only one peak around ambient temperature was observed during the cooling cycle, as seen in Figure 5.10. Since the sample is not polarized anymore and the response is measured during cooling, it is referred to as thermally stimulated current, TSC, measurement only. Its peak position weakly depends on the poling field, but it can be of either polarity dependent on the poling conditions as presented in Fig. 5.10(b). For mechanical poling, a relatively weak peak was measured [see Fig. 5.10(c)], especially if compared to the strong peaks at T_B and above. It must be pointed out that for temperatures below approximately 500 K, the cooling rate cannot be

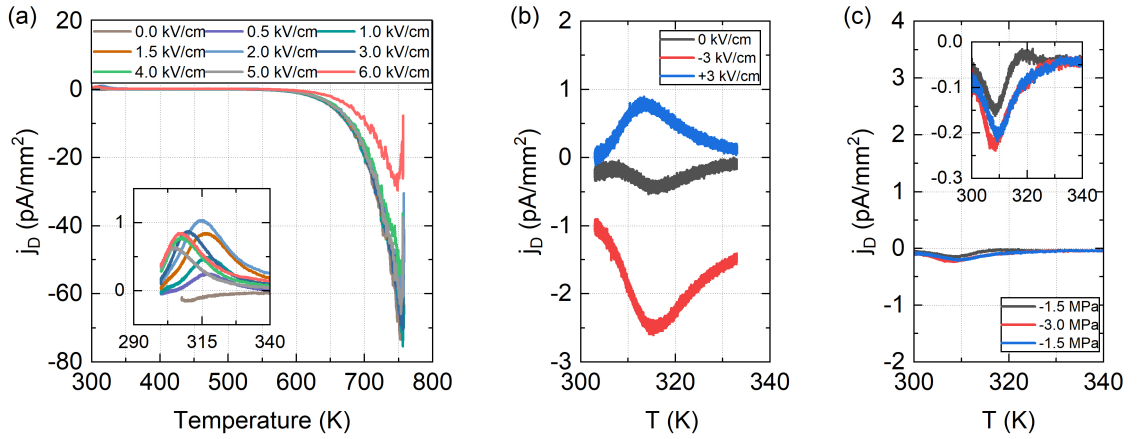


Figure 5.10. Thermally stimulated current response of [001]-PMN-A crystal recorded during cooling. (a) A single peak located around 310 K can be observed. The peak intensity and position depend on the previously applied electric poling field. (b) The polarity of the aforementioned peak can be reversed. (c) Its intensity is relatively weak for mechanical poling.

sufficiently regulated and deviates from the heating curve, as seen in Fig. 5.1(b). This results in an exponential decay of temperature and considerably more time spend between 500 K and ambient temperature as for higher temperatures. It would be interesting to see if the same peak can be observed if the cooling rate is kept constant until ambient temperature.

It is interesting to note that for the peak in Fig. 5.10 positive currents are obtained. One assumption made for TSC measurements is that the processes activated during poling the sample are reversed during depolarization. That means a peak that results in a positive depolarization current should be caused by a negative poling current and vice versa. The only peak with negative j_D that, thus, could be related to the positive currents obtained here is Peak C at T^* . The large temperature difference between these two peaks raises questions about the time dependence of the underlying process.

To investigate the time-dependent response of PMN after the completion of a TSC measurement, the sample was removed from the setup and the evolution of its dynamic pyroelectric response was investigated over several days. As shown in Figure 5.11, directly after the TSC measurement, an unexpected triangular current response following the temperature profile was observed. The amplitude of this current response decreases first before the phase of the signal is reversed after around 45 min of measurement, and the amplitude increases. After 4 hours, the current response disappears completely before a square wave current response (expected for pyroelectric current under triangular temperature change) is obtained 4 days later. Its amplitude increases over time and reaches values similar to previously published results.¹¹² While the physical reason for this response evolution is unclear, it demonstrates a complex time dependence of properties that may involve different mechanisms.

Finally, to investigate aging of PMN, a pristine ceramic sample was annealed and then aged for 1 year before TSDC measurements were performed without applying any poling fields to the sample. Figure 5.12(a) depicts the obtained results. Two peaks around T_B and at 700 K have been observed. In addition, a weak anomaly is indicated around 400 K in the inset. Directly after this measurement, a second measurement was performed. As can be seen in Fig. 5.12(b), the response

is considerably flattened out as compared to the aged state, with a weak minimum at around 650 K. For comparison, the data of Fig. 5.12(a) are included in the inset. For the annealed state, the previously observed anomaly at lower temperatures can not be resolved. The direct comparison between the annealed and aged state suggests that the polarity of the TSDC peak around 400 K of the annealed state is of opposite polarity as compared to its peaks at higher temperatures. This is analogous to the observations made for the electric field poled crystal in Fig. 5.6. After this measurement, the sample was aged for 3 weeks before the data presented in Fig. 5.12(c) were recorded. During this measurement, the sample orientation was flipped to exclude measurement artifacts simultaneously. A clear minimum at around 600 K is observed, with opposite polarity with respect to the anomalies observed above 550 K in Fig. 5.12(a). The TSDC response below 450 K seems to be mirrored with respect to j_D values of $\approx 0.02 \text{ pA/mm}^2$, which would be consistent with a reversal of intrinsic pyroelectric response due to the sample rotation. It is assumed that the offset is related to the device and not related to the sample, which was not determined exactly. Nevertheless, clear aging phenomena could be demonstrated. Moreover, the observation of TSDC peaks in pristine ceramic samples excludes charge injection as contributing mechanism. It is therefore suggested that the polarity reversal between TSDC peaks around T^* and T_B is related to the interaction of mechanisms that are intrinsic to the material.

5.5 Summary and Conclusions

Thermally stimulated current measurements of electrically polarized PMN crystals and ceramics could lead to several distinct peaks in the vicinity of temperatures characteristic for ferroelectric relaxors. The first four peaks appear sequentially with increasing electric poling field, and their intensity saturates or declines before the next peak appears. The fifth peak only appears upon poling at temperatures above 550 K and is located at $T_C \approx 400 \text{ K}$. The unexpected stability of the induced polarized state up to T_B questions the meaning of $T^* \approx 500 \text{ K}$, at which only a weak depolarization peak was observed. The peak at T^* has the peculiar feature of a reversed current,

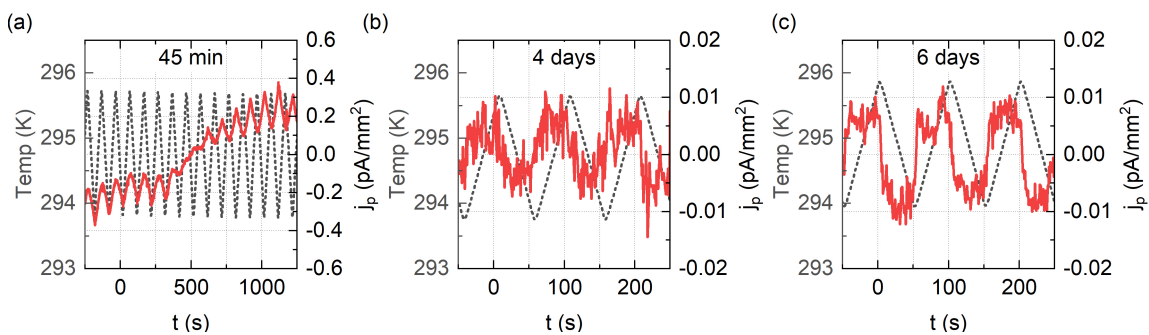


Figure 5.11. Dynamic pyroelectric response of [001]-PMN-A crystal measured after thermally stimulated current measurements. (a) An unexpected triangular current response is observed directly after the TSC experiment. Its phase changes by 180° after 45 min. After approximately 1 day and 2 days a pyroelectric signal can no longer be detected (not shown). Changing the measurement conditions, such as the contact force, could not induce a detectable pyroelectric response. (b) 4 days after the TSC experiment, a square wave current response was detected as expected for a sample with macroscopic polarization. (c) 6 days after the TSC experiment, the amplitude of the square wave current response increased slightly, matching the values previously reported.

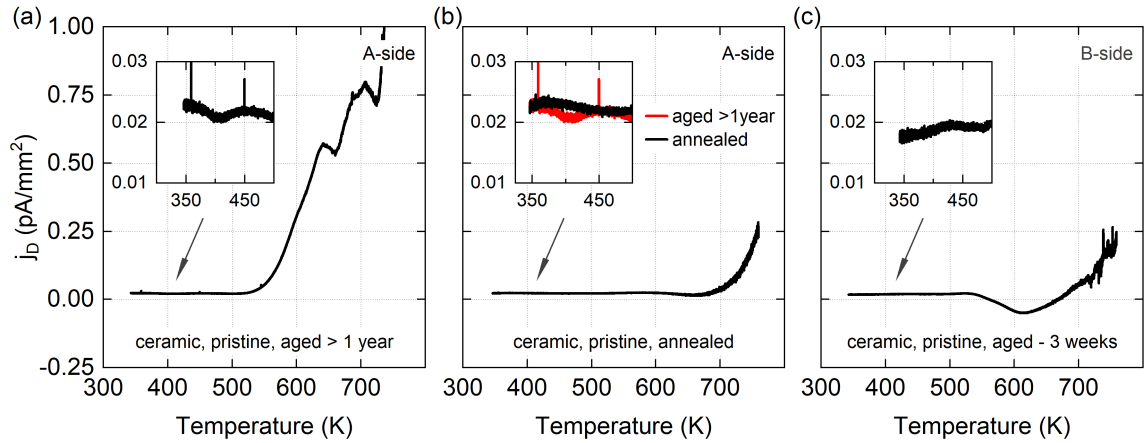


Figure 5.12. TSDC spectra of pristine aged PMN ceramic. The sample was not subjected to a poling field. Sample measured (a) after over 1 year of aging, (b) directly after the measurement presented in (a), and (c) three weeks after the measurement presented in (b).

i.e., it has the same direction as the previously applied poling current. Such a reversal is rare and often correlated to the interaction of polarization relaxation mechanisms in the presence of charge injection. Specifically, the interaction between space charge limited currents, SCLD, and dipolar relaxation, and between SCLD and diffusion has been pointed out in the literature.^{238,239} It has to be mentioned that a variety of perovskite oxide dielectrics (non-relaxors) feature a TSDC peak in the temperature region of T^* in PMN, which is often related to the migration of oxygen vacancies.^{250,271–273} In particular, TSDC peaks around T^* have been observed and attributed to oxygen vacancy migration in PMN-30PT and BT, two systems for which nano-sized polar entities have been identified.^{250,274} Other cases of current peaks of both polarities have been reported for phase transitions,²⁵⁷ e.g., for relaxor ferroelectric solid solutions.²⁵⁸ Several authors have outlined the close link between changes in orientational polarization and the release of screening or trapping charges.^{238,239,275,276} In addition, it has been recently shown that chemical and structural heterogeneity are located around nano-sized polar regions in PMN.²⁰ Another notable feature of the peak around T^* is the linear increase of its amplitude followed by decay with increasing poling fields. For iron-doped strontium titanate, the formation of modulated oxygen vacancy structures, as observed for reduced barium titanate,²⁷⁷ has been considered to explain a time-dependent decay in TSDC response.²⁵³ A mechanical transversal poling procedure was able to induce distinct peaks at T_B and at around 720 K. This procedure appeared to be more efficient than electrical poling, while no peak could be observed around T^* . Since T^* in PMN was identified based on structural or mechanical techniques,^{45,81,83} its mechanical activity origin is undoubted. It is noted that the strain tensor of a single point defect theoretically has the highest possible symmetry,²⁷⁸ interaction mostly with hydrostatic stress fields. A charged point defect could therefore be able to screen polarization efficiently while being sluggish with respect to stress. Another explanation could be the absence of charge injection for mechanically poled samples. At the same time, this argument can be used to relate the stress-induced peaks observed at T_B and 720 K to pre-existing polar entities exclusively. To test ergodicity, electrical and mechanical field-cooling and fractional-poling procedures were applied between T^* and T_B . Strong TSDP peaks around T_B and around 720 K have been found for both electrical

poling procedures. On the other hand, only one peak around 720 K has been identified for the mechanical poling procedures. These results clearly indicate broken ergodicity in PMN above T^* . Furthermore, differences between isothermal poling and field-cooling suggested a timed dependent behavior above T^* . A complex temporal evolution was also observed for the dynamic pyroelectric response of PMN samples, which was measured directly after TSDC measurements. In summary, it has been shown that thermally stimulated depolarisation current measurements are capable of resolving all so far identified characteristic relaxor temperatures above 300 K. These are the phase transition temperature, $T_C \approx 400$ K, the coherence temperature, $T^* \approx 400$ -500 K, Burns temperature, $T^* \approx 620$ K, and the onset of piezoelectricity at $T \approx 720$ K. The combination of electrical and mechanical poling procedures revealed a selective activation of peaks, i.e. some peaks are significantly more pronounced for one of the of the procedures. For poling temperatures above T^* , this selective activation of peaks changes systematically. The unexpected stability of all induced polar states up to T_B and the relatively weak or absent anomalies around T^* are not consistent with a continuous evolution of a single polar mechanism during cooling, as proposed by many present models.^{11,18,179} It is speculated that local polarization is screened by point defects that cause time-dependent properties of the relaxor ferroelectric PMN even at ambient temperatures. The existence of an ergodic relaxor state is not consistent with our results.

6 Aging and alternate current poling in relaxor ferroelectric solid solutions

6.1 Motivation

In the previous chapter, unexpected anomalies around characteristic temperatures of the canonical ferroelectric relaxor lead magnesium niobate, PMN, have been revealed with the aid of thermally stimulated current, TSC, measurements. These anomalies have been in part related to time-dependent *aging* processes, which were commonly considered to be neglectable for stoichiometric compositions.^{49,201} Interestingly, studies on related relaxor ferroelectric solid solutions, conducted by master student Fabiano Romano and bachelor student Lise Kretz, suggest that 25 % larger piezoelectric coefficients are obtained when experiments are performed on a daily instead of a weekly basis. It is therefore hypothesized that aging effects have severe practical implications for state-of-the-art high-performance piezoelectric single crystals. The goal of the following chapter is thus to investigate the influence of aging on the piezoelectric properties of lead magnesium niobate lead titanate solid solutions, $(100-x)\text{Pb}(\text{Mg}_{1/3}\text{Nb}_{2/3})-x\text{PbTiO}_3$ PMN- x PT.

This chapter contains previously published data from the following publication:

- L. M. Riemer, L. Jin, H. Uršič, M. Otoničar, T. Rojac, and D. Damjanovic, “Dielectric and electro-mechanic nonlinearities in perovskite oxide ferroelectrics, relaxors, and relaxor ferroelectrics”, [Journal of Applied Physics](#) **129**, 054101 (2021),

and is inspired by the master thesis work of Fabiano Romano and the bachelor semester project of Lise Kretz conducted under the supervision of Prof. Dragan Damjanovic and the author:

- Fabiano Romano, Nonlinear dielectric and piezoelectric properties of relaxor ferroelectrics, master thesis, EPFL, Switzerland, 2021,
- Lise Kretz, Dielectric anomalies above Curie temperature in relaxor ferroelectrics, bachelor semester project, EPFL, Switzerland, 2021.

6.2 Introduction

PMN- x PT solid solutions are state-of-the-art materials for transducer and sensor applications.¹⁰³ The system has a complex phase diagram with morphotropic phase boundary, MPB, between $x \approx 31 - 38$ (see Fig. 1.6), at which ultrahigh piezoelectric coefficients ($d_{33}^* = 1500 - 2500$ pC/N) and electro-mechanical coupling factors ($k_{33} > 0.9$) can be obtained for single crystals.^{103,281}

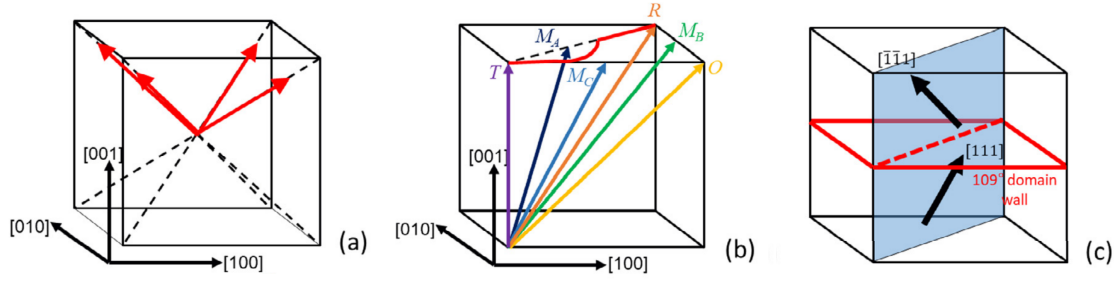


Figure 6.1. Domain states for different poling conditions and symmetries in pseudocubic coordinates, modified from [279]. (a) 4R-configuration of rhombohedral crystals poled along [001]-direction with polarization orientation indicated by red arrows. (b) Polar directions for rhombohedral, R, orthogonal, O, tetragonal, T, and monoclinic, (M_A , M_B , M_C), phases. Experimentally observed polarization rotation path for rhombohedral PMN- x PT is indicated as a red line.²⁸⁰ (c) 2R-configuration with 109° domain wall indicated by full lines.

These outstanding piezoelectric characteristics are related to a polarization rotation mechanism facilitated by specific domain configurations obtained for samples polarized along certain non-polar crystallographic directions.⁸⁷ The exact domain configuration will thereby not only depend on the composition and poling procedure but also on the history of the sample. Despite this complex nature, models are often based on simplified domain structures with rhombohedral $R3c$ and tetragonal $P4mm$ symmetry.^{107,108,279}

In the *polarization rotation model*,^{87,107,108,279} the unpoled state, UNP, of PMN- x PT for $x < 31$ is described by a mixture of eight domain variants with rhombohedral, R, symmetry (8R-configuration).^{108,282} When a direct current, dc, electric poling field is applied along a $\langle 001 \rangle$ -direction, for example, along the [001]-direction, a *domain-engineered* 4R-state is induced. Four domain variants are aligned along the [001]-direction in this state, as illustrated by the red arrows in Figure 6.1(a). When an electric driving field is subsequently applied along the same direction, the polar vectors rotate towards a tetragonal, T, symmetry via an intermediate monoclinic, M_A , phase²⁸⁰ as depicted by the red line in Fig. 6.1(b). Other intermediate monoclinic phases, M_B and M_C , bridging orthogonal, O-, and R-phase, and T- and O-phase, respectively, are possible.

However, this polarization rotation mechanism is not limited to PMN- x PT or relaxor ferroelectric solid solutions, and can therefore not explain their superior performance as compared to other systems. For example, moderate enhancements of piezoelectric properties by domain engineering have been reported for barium titanate and potassium niobate single crystals.^{283,284} Recently, the origin of ultrahigh piezoelectricity in domain-engineered crystals of relaxor ferroelectric solid solutions was attributed to the presence of nano-sized polar regions embedded in ferroelectric domains.^{90,105} It has been suggested that the presence of local structural heterogeneity destabilize surrounding ferroelectric domains resulting in high dielectric permittivity values.^{90,105} Given that the electrostrictive coefficient and the spontaneous polarization of PMN- x PT is relatively small as compared to other materials, the enhancement of the piezoelectric coefficient has been attributed to this increase in dielectric permittivity according to

$$d_{33} = 2\varepsilon_{33}Q_{33}P_r, \quad (6.1)$$

where d_{33} is the longitudinal piezoelectric coefficient, Q_{33} is the electrostrictive coefficient, P_r the

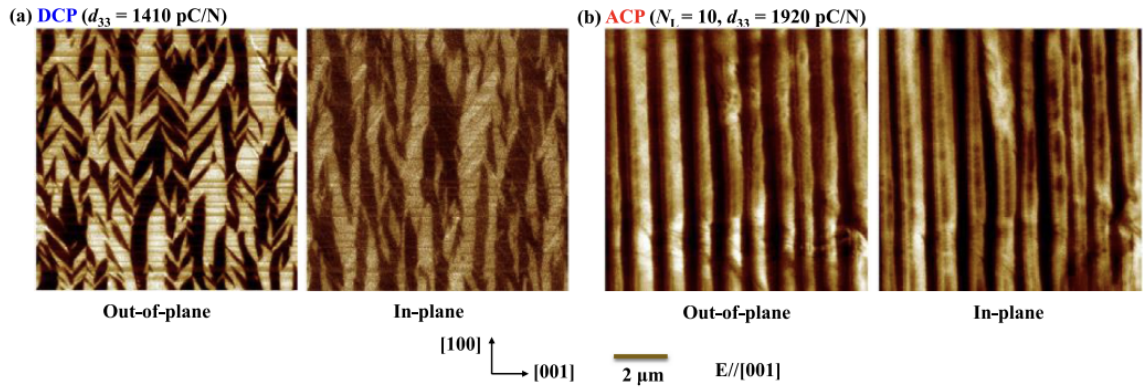


Figure 6.2. Piezoresponse fore microscopy, PFM, images of direct current, DCP, and alternate current (electric field) poled, ACP, PMN-0.27PT crystal with [001]-orientation, modified from [288]. Out-of-phase and in-phase responses obtained for (a) DCP with 4R configuration containing both 71°- and 109°-domain walls, and (b) ACP with 2R configuration containing mostly 109° domain walls. Note that the direction of the poling field is rotated by 90° with respect to Fig. 6.1.

remnant polarization, and ϵ_{33} is the dielectric permittivity.⁹⁰

An alternative model suggests that ultrahigh piezoelectricity is related to the formation of Néel-type domain walls in which polar vectors rotate in the [110]-plane with only small variations of their magnitude.²⁷⁹ Consequently, these domain walls break the macroscopic symmetry locally and feature a complex structural phase sequence (R-M_B-O-M_B-R and R-M_A-T-M_A-R for 71°- and 109°-domain walls, respectively). It has been argued that these complex domain walls and their widening can significantly contribute to piezoelectric activity.

A considerable enhancement of the piezoelectric performance of domain-engineered PMN-xPT crystals has been recently achieved by a simple variation of the poling procedure. It has been demonstrated that alternating current (electric field) poling, ACP, can increase the piezoelectric coefficient and dielectric permittivity by about 40 % as compared to conventional direct current (electric field) poling, DCP.¹⁰⁷ During ACP, the sample is polarized with several bipolar electric field cycles. The physical origin of the enhancement is not yet conclusively clarified. An increase in 71°-domain wall density and a reduction in domain width,^{107,285,286} a reduction of 71°-domain wall density and an enhanced domain width^{108,287}, a reduction of domain wall intersections,²⁸⁸ as well as electric field-induced phases mixtures between R,²⁸⁷ M_A¹⁰⁷-, or M_B- and M_C-phases¹⁰⁶ have been suggested. Note that a large variety of initial annealing procedures has been reported, with set temperatures between 523 - 873 K and dwell times between 30 min to 60 hrs.^{107,108,204,282,288,289}

Domain structures obtained for ACP are often described to be more homogeneous as compared to DCP. Lamella domain structures perpendicular to the applied poling field, as presented in Figure 6.2, have been reported by several authors.^{107,282,288} This particular domain structure is attributed to a 2R-configuration in which two domain variants form 109°-domain walls as depicted in Fig. 6.1(c) and Figure 6.3. Note that the direction of the poling field in Fig. 6.2 is rotated clockwise by 90° with respect to Fig. 6.1. Enhancements of the piezoelectric performance have also been observed for the related Pb(In_{1/2}Nb_{1/2})O₃ - Pb(Mg_{1/3}Nb_{2/3})O₃ - PbTiO₃, PIN-PMN-PT, system.^{289,290} Comparably shorter domain length for acceptor-doped as compared

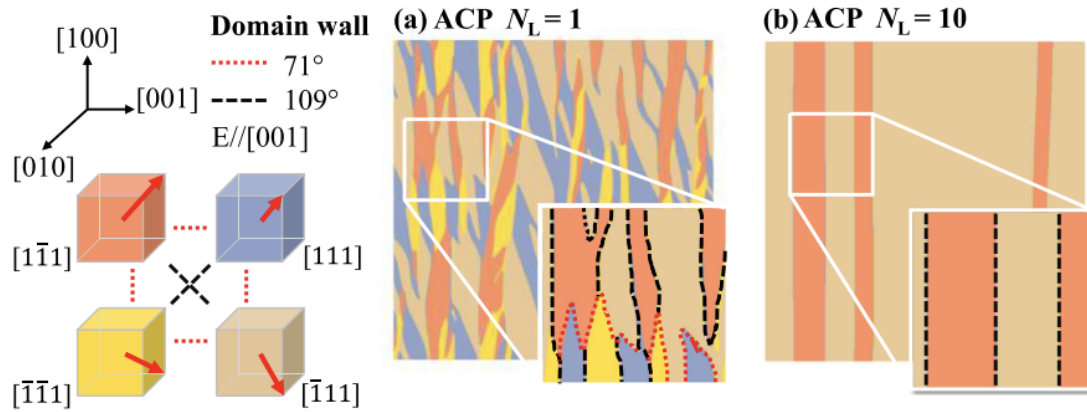


Figure 6.3. Evolution of domain structure during ACP according to phase-field simulations, modified from [288]. The polarization orientations of the different rhombohedral variants aligned with the [001]-poling direction are indicated by different colors. 71°- and 109°-domain walls are indicated by red dotted, and black dashed lines. Domain configuration (a) after the first bipolar poling cycle (4R), and (b) after the tenth bipolar poling cycle (2R).

to undoped compositions have been attributed to domain wall clamping and the introduction of local heterogeneity by defect dipoles.²⁸⁹

In its most basic sense, aging can be defined as the spontaneous change of properties in the absence of external driving forces.²⁹¹ It often results in a gradual reduction of weak-field dielectric and piezoelectric properties.^{291,292} In some cases, a contraction of polarization hysteresis loops at the origin, often referred to as *loop pinching*,^{293,294} or a horizontal shift of hysteresis loops^{294,295} is observed. Aging effects are generally attributed to the stabilization or *pinning* of domain patterns by mobile charged defects.²⁹² The governing mechanisms have been classified as interface, domain wall, or volume effect, according to the length scale on which they act.²⁹² The interface effect is related to the macroscopic diffusion of ions, vacancies, or electrons to interfaces like grain boundaries or electrodes and the formation of space charges.²⁹² Similarly, the domain wall effect is described by the diffusion and pinning of these charged defects to domain walls.²⁹² The volume effect, on the other hand, can act locally on a short-range, stabilizing domains by the formation of defect dipoles throughout the volume, often involving oxygen vacancies.^{292,296,297} For all cases, the driving force is the minimization of the elastic and electrostatic energy.^{292,298}

Aging is often considered minor for stoichiometric compositions of relaxor ferroelectrics and their solid solutions.^{201,291,299} Over short time periods, relatively fast nonlinear aging on a logarithmic time scale is observed, however.^{299,300} A 4 % reduction of the dielectric constant of PMN-31PT ceramics measured at ambient temperature within 60 minutes after annealing at 393 K has been reported.²⁹⁹ For polarized PMN-30PT crystals, a 4 % reduction of d_{33} within 7 days followed by stable response has been observed.³⁰¹ An aging phenomenon specific to relaxor ferroelectric solid solutions is the dampening of the dielectric dispersion around the temperature of aging, when the material was aged below the temperature of maximum permittivity, T_m .^{201,300,302} A large variety in aging phenomena and aging rates have been correlated to variations in stoichiometry and defect chemistry, mostly defined by the preparation conditions.^{201,301,303}

The defect chemistry of PMN- x PT has been described by oxygen and lead vacancies, and

their dipoles,^{201,250,303,304} thermal ionization of electrons across the band gap,²⁰¹, single³⁰³ and double ionization of oxygen,^{303,304} interactions of electrons with Ti^{4+} , Mg^{2+} , and Nb^{5+} ,³⁰³ electron hopping from deeply localized Ti^{3+} centers and p-type conduction related to lead vacancy concentration.²⁵⁰ While *Eichel* suggests that cation diffusion may only be observed above 1073 K²⁹⁷, *Wu* proposes lead diffusion above 573 K.³⁰⁴

6.3 Results

For the investigation of aging in PMN- x PT four samples of approximately equal dimensions cut from a $10 \times 10 \times 0.5 \text{ mm}^3$ crystal were prepared. The dielectric permittivity, ϵ , and dielectric loss tangent, $\tan \delta$, of a pristine sample is presented in Figure 6.4(a) and (b). A shoulder in ϵ around $T_{\text{RT}} \approx 375 \text{ K}$ signalizes the rhombohedral to tetragonal phase transition.^{305,306} The sharp increase at the Curie temperature $T_{\text{C}} = 395.2 \text{ K}$ is the consequence of a tetragonal to cubic phase transition.^{305,306} In addition, a transition from a ferroelectric to relaxor state takes place at T_{C} , indicated by the appearance of significant dielectric dispersion.⁷⁷ A comparison of the dielectric response on heating and cooling of the four investigated samples can be found in Figure K.1 in Appendix K. The composition, x , of the samples was estimated based on the empirical formula^{113,307}

$$x \approx \frac{T_{\text{C}} + 59^\circ\text{C}}{630^\circ\text{C}} (x > 45.7), \quad (6.2)$$

to be between $x \approx 28.7$ and 29.0 . After the permittivity measurements, the sample was annealed at 750 K for 30 min and subsequently aged for four months at ambient temperatures. The TSC spectra obtained for this unpoled and aged state, aged-UNP, are depicted by the grey curve in Fig. 6.4(a). Two peaks in the current density, j_{D} , of opposite polarity are obtained. A broad positive peak around T_{RT} and a sharp negative peak around T_{C} . The red curve in the same figure presents the data collected for a second measurement, which started approximately 8 hrs after the end of the previous, i.e., 8 hrs after the sample was cooled back to ambient temperatures. Note that each TSC experiment was performed up to 750 K . In between the measurements, the sample was not manipulated in any way to avoid any artifacts. Assuming that the sample depolarized during the measurement, it is referred to as UNP. For the second measurement, two overlapping peaks of the same, positive, polarity are obtained for j_{D} . As compared to aged-UNP, the peaks are broader and closer together. The polarization, P , presented in Fig. 6.4(c), was calculated for both states by integrating j_{D} . It was assumed that the temperature of zero polarization is $T_{\text{0P}} = 423 \text{ K}$. For aged-UNP, the polarization at 300 K , $P_{300\text{K}}$, is approximately three times lower than for UNP. A reduction of dielectric properties with time is a typical aging phenomenon,^{142,292,293,308} It is speculated that it could be related to a change in the domain structure, a depolarization process, or the stabilization of polarization to higher temperatures. With increasing temperature, P decays continuously with kinks around 365 and 370 K for aged-UNP and UNP, respectively. For both conditions, P is approximately two orders of magnitude lower than the remnant polarization, $P_{\text{r}} \approx 0.24 \text{ C/m}^2$, obtained from polarization electric field hysteresis loops.^{258,286}

Fig. 6.4(d)&(e) compare the TSC response of aged-UNP and UNP up to 650 K . For aged-UNP a shoulder in j_{D} around 500 K and a broad peak at 600 K is observed. In contrast, for UNP these anomalies are mostly absent. Note that a weak peak in j_{D} is still present around 500 K , as indicated in the inset. The anomaly found around 500 K is interesting for two reasons. First, anomalies in

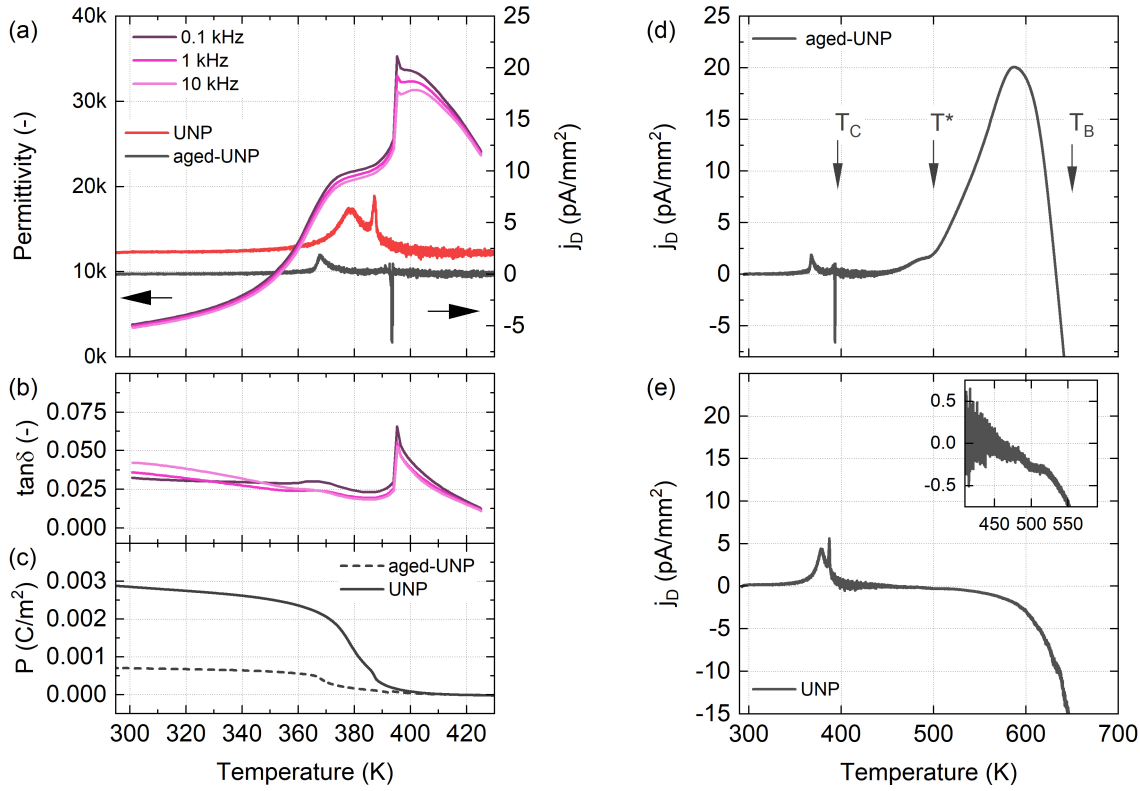


Figure 6.4. Dielectric permittivity and thermally stimulated currents of unpoled and aged [001]-PMN-29PT crystal; Sample MSE(i). (a) Comparison between dielectric permittivity, ϵ , and depolarization current, j_D , in unpoled, UNP, and unpoled and then aged, aged-UNP, condition. (b) Loss tangent, $\tan \delta$, for UNP. (c) Polarization, P , calculated by integration of j_D given in (a) with the assumption that P is equal to zero at 423 K. TSC spectra for (d) unpoled and aged state and (e) unpoled state. The inset illustrates a weak anomaly around 500 K. UNP: annealed at 750 K for 30 min. Aged-UNP: annealed at 750 K for 30 min and then aged for four months at ambient temperatures.

PMN- x PT around 500 K have been previously investigated by impedance spectroscopy,^{250,303} low-frequency dielectric,³⁰³ TSC,²⁵⁰ and highly accelerated lifetime test²⁵⁰ measurements. They have been related to oxygen vacancy migration²⁵⁰ or the relaxation of defect dipoles formed by oxygen and lead vacancies³⁰³. Second, structural investigations suggest a local phase transition^{11,83} common for lead-based relaxor ferroelectric solid solutions around the coherence temperature, $T^* \approx 500$ K.⁸¹ While other studies relate T^* to changes in the dynamic properties of complex domain structures,¹⁸ it is generally accepted that at T^* static local polarization emerges.^{11,18,83} These findings suggest that local polarization in PMN- x PT is related to oxygen vacancies or that at least some kind of interaction between the former and the latter exists.

An interesting finding is that if T_{0P} is chosen to be T^* , similar values of P for the aged-UNP and UNP are found at ambient temperatures [Figure K.2(a)]. The relative strong peak in j_D observed for aged-UNP in Fig. 6.4(d), on the other hand, results in a depolarization peak around the Burns temperature, $T_B \approx 600$ -650 K,^{81,83} that is an order of magnitude larger as compared to the peak at T^* [Figure K.2(b)]. (T_B is commonly regarded as the first emergence of correlated dynamic polarization.^{18,81,83}) Corresponding anomalies around T^* and T_B have been found for

polarized PMN in Chapter 5, for aged crystals with similar composition obtained from a different provider, and for $\text{Pb}(\text{In}_{0.5}\text{Nb}_{0.5})\text{O}_3 - \text{Pb}(\text{Mg}_{1/3}\text{Nb}_{2/3})\text{O}_3 - \text{PbTiO}_3$ (PIN-PMN-PT), as depicted in Figure K.3. (The anomaly around T^* was not apparent in PIN-PMN-PT however.) In general, the observation of a depolarization peak around T_B is unexpected since polarization is believed to be dynamically disordered above T^* ,^{18,81,83} as discussed previously in Chapter 5. It is intriguing that strong anomalies in j_D above T_C can only be found in the aged state. Consequently, it is suggested that these anomalies are of extrinsic nature and are not related to intrinsic lattice response like phase transitions.

Before the influence of aging on subsequent poling procedures is investigated, samples that were annealed before poling are characterized. For DCP the sample was polarized with 10 kV/cm for 20 min and for ACP with ten bipolar triangular electric field cycles with an amplitude of 10 kV/cm and a frequency of 1 Hz. For both procedures, the samples were annealed at 750 K for 30 min and polarized within the following 8 hours. Measurements for ACP and DCP were performed with individual samples. The obtained results are compared in Figure 6.5. Two sharp peaks in ϵ are seen for DCP in Fig. 6.5(a). One peak at $T_{RT} = 363.5$ K and another peak at $T_C = 396.9$ K. $\tan \delta$ presented in Fig. 6.5(b) features an additional shoulder just above T_{RT} . For j_D , two sharp peaks around the phase transitions are observed in Fig. 6.5(c). A negative peak around T_{RT} and a positive peak at T_C , as has been observed before.²⁵⁸ The negative peak around T_{RT} implies an enhancement of P_r . It has been related to an alignment of domains and polarization rotation from the $\langle 111 \rangle$ - to $\langle 001 \rangle$ -direction between the R- and T-phase.²⁵⁸ The concomitant increase in P_r has been experimentally demonstrated with temperature-dependent polarization electric field hysteresis loops.²⁵⁸ The inset in Fig. 6.5(c) illustrates that more than two peaks are present, as already indicated in $\tan \delta$. P of DCP in Fig. 6.5(d) shows two sharp changes. An increase around T_{RT} , attributed to an alignment process,²⁵⁸ and an almost vertical drop at T_C due to depolarization at the phase transition to macroscopic cubic symmetry. The slope of P changes notably after T_{RT} . P_{300K} is in good agreement with reported values of P_r .^{258,286}

For ACP three, possibly four peaks in ϵ are seen in Fig. 6.5(e). It has been speculated that up to the first peak at $T_1 = 360.7$ K a mixture between R- and M-phases coexist, while at higher temperatures, up to the second peak at $T_2 = 360.7$ K, only the R-phase is present.^{106,107} Other studies modeled X-ray diffraction data obtained at ambient temperatures with different R-phase variants only.²⁸⁷ A fourth peak just above T_2 is indicated in ϵ and $\tan \delta$ in Fig. 6.5(e)&(f). For j_D of ACP, depicted in Fig. 6.5(g), a series of multiple peaks is obtained at each of the aforementioned temperatures. First, a series of negative peaks around T_1 , followed by a series of negative and positive peaks at T_2 , and finally, a series of positive peaks around T_C is seen. The inset demonstrates the complex response obtained around T_C . This complex response is reflected in ϵ by a round peak at T_C for ACP as compared to a sharp spike in ϵ for DCP. For P of ACP in Fig. 6.5(g), a similar initial decay with temperature as for DCP is observed. P_{300K} of ACP is about 0.3 C/m^2 smaller, however, which could be related to sample or poling specific property variations. An increase in P occurs at T_1 , followed by a small second anomaly around T_2 . As for DCP, the most significant change in P happens during the depolarization around T_C , which is slightly broader for ACP. The longitudinal piezoelectric coefficients, d_{33} , obtained before the individual measurements are indicated in Fig. 6.5(a),(c),(e) & (g). The error is given as the standard deviation of three subsequent measurements. In agreement with previously reported results, ACP enhances d_{33} up to 40 % as compared to DCP.^{285,286,309} It is noted that up to 50 % larger values of d_{33} have

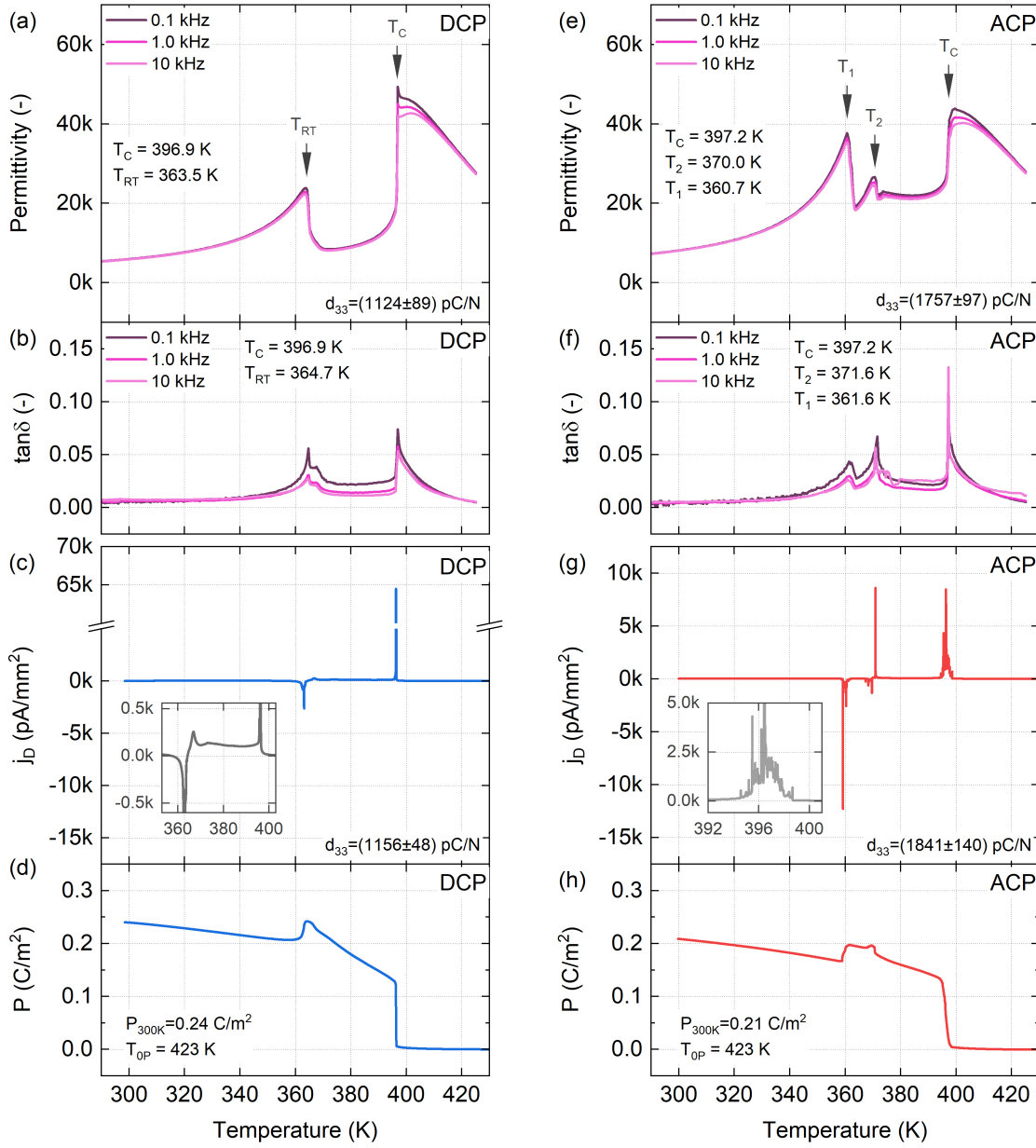


Figure 6.5. Comparison between temperature dependent dielectric permittivity and thermally stimulated currents for direct current and alternate current (electric field) poled, (DCP and ACP respectively), [001]-PMN-29PT crystals. (a)-(d), DCP for sample MSE(i), ACP for PMN-xPT sample MSE(ii). (a)&(e) Dielectric permittivity for (a) DCP and (e) ACP. (b)&(d) Loss tangent $\tan \delta$ for (b) DCP and (d) ACP. (c)&(f) Current density, j_D , for (c) DCP and (f) ACP. Insets illustrate the detailed structure of the depolarization peaks for different temperature regions. (d)&(g) Polarization, P , calculated as the integral of j_D from (c)&(f) with the assumption of $P = 0$ at 423 K for (d) DCP and (h) ACP. The mean values and standard deviations of the longitudinal piezoelectric coefficient, d_{33} , measured before the start of the individual experiments are indicated in (a), (c), (e) & (g). Samples were annealed at 750 K for 30 min before the poling procedure. DCP: 10 kV/cm, 20 min. ACP: 10 kV/cm, 1 Hz, 10 bipolar triangular cycles.

been measured for the same crystals and poling states with a converse method. It is suggested that clamping of the samples between the two flat jars used during direct measurements of this work caused this discrepancy.²⁰⁵

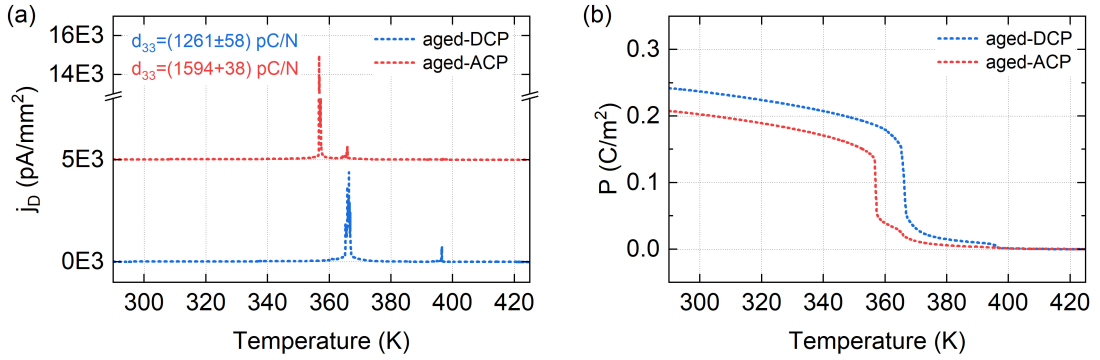


Figure 6.6. TSDC spectra and polarization for aged and then polarized [001]-PMN-29PT crystals. (a) Measured current density, j_D , and (b) calculated polarization, P . Aged-DCP: annealed at 750 K for 30 min, then aged for four months at ambient temperatures, and polarized with 10 kV/cm for 20 min; Sample MSE(iii). Aged-ACP: annealed at 750 K for 30 min, aged for four months at ambient temperatures, and then polarized with 10 bipolar triangular cycles with amplitude of 10 kV/cm and frequency of 1 Hz; Sample MSE(iv).

The influence of aging was investigated by storing samples for four months (end of July to end of November) at ambient temperatures before poling them according to the previously described DCP and ACP procedures. This time, the samples were not annealed before poling, while all other poling parameters were set identical. The obtained TSC spectra for these aged-DCP and aged-ACP samples are presented in Figure 6.6(a). Surprisingly, only positive peaks in j_D are notable, suggesting the absence of the previously cited domain orientation mechanism.²⁵⁸ For both aged states, the low-temperature peaks around 360 K are dominant, and only for DCP a weak peak at T_C is seen. Note that for aged-ACP, both peaks are shifted to lower temperatures, and T_2 is similar to T_{RT} in DCP. Piezoelectric coefficients of $d_{33} = (1261 \pm 58)$ pC/N and $d_{33} = (1594 \pm 38)$ pC/N were obtained for aged-DCP and aged-ACP, respectively. The slight increase for aged-DCP as compared to DCP is within the experimental error. For aged ACP, on the other hand, a reduction of around 15 % as compared to regular ACP is observed. This reduction is smaller as suggested by the previously mentioned master and bachelor projects but nonetheless significant.

The temperature dependence of P for the aged-DCP and aged-ACP is presented in Fig. 6.6(b). For both states, P resembles theoretically predictions for first-order phase transitions³¹⁰ with additional tails above the transition temperatures as has been observed before.⁴⁹ Moreover, a second depolarization process is present around T_C and 365 K for aged-DCP and aged-ACP, respectively. Note that both aged samples depolarize at significantly lower temperatures than samples that were annealed before the poling procedures. P_{300K} , on the other hand, follows the previously observed trend of relatively lower values for ACP as compared to DCP. This is unexpected since, according to Equation (6.1), a lower value of P_{300K} should result in lower d_{33} values. The opposite trend is observed for d_{33} , however, suggesting that the enhancement in d_{33} for ACP is mostly related to an increase in ϵ , analogous to considerations concerning local heterogeneity.¹⁰⁵

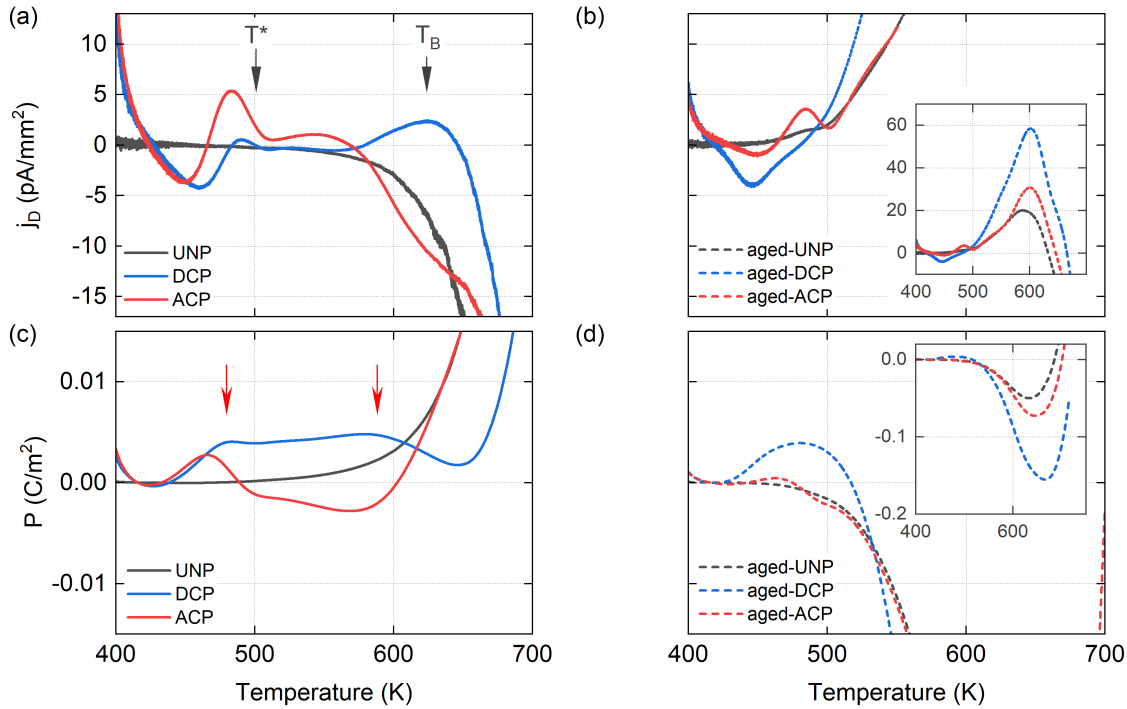


Figure 6.7. TSDC spectra and polarization for annealed and aged samples. (a) Measured current density, j_D , for samples that were annealed (a), and for samples that were aged (b) and then measured in unpolarized, UNP, direct current poled, DCP, and alternating current poled, ACP, state. Calculated polarization, P , for annealed and aged samples.

To correlate these findings with the previously observed anomalies in j_D around T^* and T_B (see Fig. 6.4), samples that were annealed and samples that were aged before poling are compared next. j_D and P for samples that were annealed before the poling procedure are compared in Figure 6.7(a)&(b). For UNP, the absolute values of j_D and P increase monotonously without significant anomalies. j_D of DCP, however, shows a local minimum around 450 K followed by a maximum around T^* and T_B . A similar response is obtained for ACP, for which the maximum at T^* is relatively stronger, while the maximum at T_B appears to be reversed with respect to DCP. This circumstance is better seen for P presented in Fig. 6.7(b). For DCP, two peaks with positive polarity indicated by red arrows are obtained, while for ACP, two peaks of opposite polarity with respect to each other are observed. It is interesting to note that the high-temperature tail, presumably related to conductivity, is shifted to higher temperatures for DCP.

The results obtained for aged samples are contrasted in Fig. 6.7(c)&(d). For aged-UNP, anomalies in j_D around T^* and T_B are present, as discussed for Fig. 6.4(d) and (e). Aged-DCP exhibits a minimum at around 450 K, followed by a relatively large maximum around T_B . In comparison, aged-ACP has a weaker minimum and maximum at around 450 K and T_B , respectively. In addition, an intermediate maximum at around 480 K is present. Overall, it appears that the peaks in j_D around T^* for aged samples have similar or reduced absolute magnitudes as compared to annealed samples. , On the other hand, the peaks around T_B are relative stronger as compared to samples that were annealed before poling, as evident from the insets in Fig. 6.7(c)&(d).

From the comparison in Fig. 6.4, it is clearly seen that not only the poling procedure²⁵⁰ but

also the aging state considerably affects the TSC spectra of PMN- x PT. It is remarkable that independent of the poling procedure and aging state, an intermediate enhancement of polarization is found around T^* . A peculiarity for samples that were poled after annealing is that the peak around T_B is of opposite polarity for ACP and DCP even though the orientation of macroscopic polarization after poling and with respect to the measurement electrodes was the same. It is therefore hypothesized that these two poling procedures result in significantly different polar, possibly, defect structures. For samples that were aged before poling, the dominant feature in the TSC spectra is the anomaly around T_B . For aged-ACP and aged-DCP, the magnitude of this anomaly is enhanced with respect to aged-UNP.

Calling to attention that aged samples lack an intermediate polarization enhancement around 360 K and depolarize at comparable lower temperatures as compared to annealed and then polarized samples [see Fig. 6.6(d)&(h)], it is speculated that the applied electric poling fields are not sufficient to overwrite the aged state. Therefore, the defect structure for aged samples is relatively random. For samples that were annealed, however, defects can align to the local polarization resulting in a stabilizing effect and intermediate polarization enhancement around T_{RT} and T_I , respectively. The obtained results, therefore, not only confirm the hypothesis of aging but also suggest a hardening effect that affects the piezoelectric performance of PMN- x PT.

To verify that the observed behavior is related to aging and reproducible, a sample was first

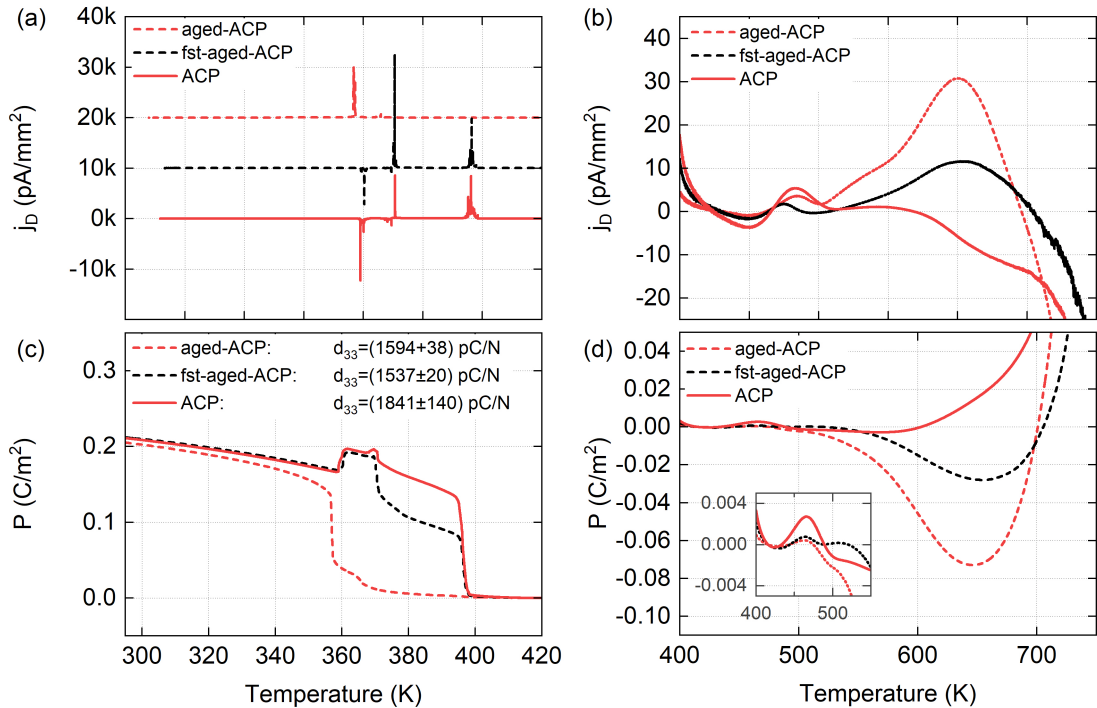


Figure 6.8. TSDC spectra and derived polarization for ACP [001]-PMN-29PT crystals. (a-b) Current density, j_D , and (c-d) calculated polarization, P . The mean values and their standard deviations of the longitudinal piezoelectric coefficient, d_{33} , measured before the start of the individual experiments are indicated in (c). Fst-aged-ACP: annealed at 750 K for 30 min, aged for approximately 4 hrs at 318 K, and then polarized with 10 bipolar triangular cycles with amplitude of 10 kV/cm and frequency of 1 Hz; Sample MSE(ii). ACP: Sample MSE(ii). Aged-ACP: Sample MSE(iv).

annealed as described before, then cooled back to ambient temperature, and finally aged at 318 K for approximately 4 hours. This accelerated, *fast-aged* (fst-aged) sample was then ac-poled before the TSC data depicted by the black dashed lines in Figure 6.8 were recorded. For comparison, the results obtained for ACP and aged-ACP are provided. j_D of fst-aged-ACP in Fig. 6.8(a) resembles the response obtained for ACP with several sequences of peaks mostly confined into the three temperature regions around $T_1 \approx 360$ K, $T_2 \approx 370$ K, and $T_C \approx 397$ K. The differences between the states become more apparent for P in Fig. 6.8(b). The response of fst-aged-ACP and ACP is virtually the same up to around 370 K, at which temperature P of fst-aged-ACP drops by about 0.05 C/m² while P for ACP only shows a weak anomaly. The slope of P above this temperature is approximately the same for fst-aged-ACP and ACP up to T_C , where both states depolarize in a similar manner. It is useful to recall that for calculating the data presented in Fig. 6.8(b), it was assumed that the polarization is equal to zero at $T_{0P} = 423$ K. The data could therefore be vertically shifted. For aged-ACP, polarization takes place at the lowest temperature. Even though the $P(T)$ curves look quite different for aged-ACP and fst-aged-ACP, similar d_{33} values were obtained before the TSC measurements. It is noted that these two samples were not identical even if they were cut from the same crystal. Fig. 6.8(c) shows j_D data above 400 K. The peak around T_B follows a similar trend for both aged samples, while the peak for ACP is of opposite polarity. The trend of j_D around 500 K is less clear. The data for aged-ACP indicate a third peak at around 550 K, which could be related to the trapping of electrons around B-side ions.^{250,303} From the P data in Fig. 6.8(c), in particular from the data presented in the inset, it is evident that the enhancement of polarization around 450 K is strongest for the ACP state. Note that aging of the poled state has also been confirmed (Figure K.4).

To further examine the reproducibility of the present study, the ACP procedure was verified for a PMN- x PT sample of a similar composition obtained from a different provider. An interesting finding of this experiment is that the anomalies observed in j_D and the obtained d_{33} values weakly depend on the sample orientation, as depicted in Figure 6.9. For this experiment, two poling cycles followed by TSC measurements each were performed. For the first cycle, an arbitrarily chosen side was selected as the *A-side*. The sample was then annealed and ac-poled with the A-side up before TSC measurements were performed. For the second cycle, the sample orientation was flipped by 180° during poling and the measurement. In other words, the orientation of polarization was reversed with respect to the sample coordinate system but was identical with respect to the measurement electrodes for the two measurements. As can be seen in Fig. 6.9(a) for the A-side, a similar response as previously discussed was obtained. In contrast, P for the B-side is reduced with respect to P of the A-side starting between $T_1 \approx 360$ K and T_C . The drop in P in the vicinity to T_2 is relatively stronger and occurs at lower temperatures for the B-side as compared to the A-side.

Another striking difference between the A- and B-side is presented in Fig. 6.9(b). The peaks in j_D around 500 K obtained for the A- and B-side are of opposite polarity. In addition, for the B-side, a weak shoulder around 475 K possibly indicates the presence of two mechanisms. It is speculated that one mechanism may be related to built-in polarization as observed for PMN in Chapter 4, and the other mechanism to the orientation of the poling field with respect to the sample coordinate system. To test the first hypothesis, the dynamic dielectric response was measured. A weak initial polarization has been found with orientation so that it was aligned with the poling field for the A-side. Subsequent dynamic dielectric measurements of the samples

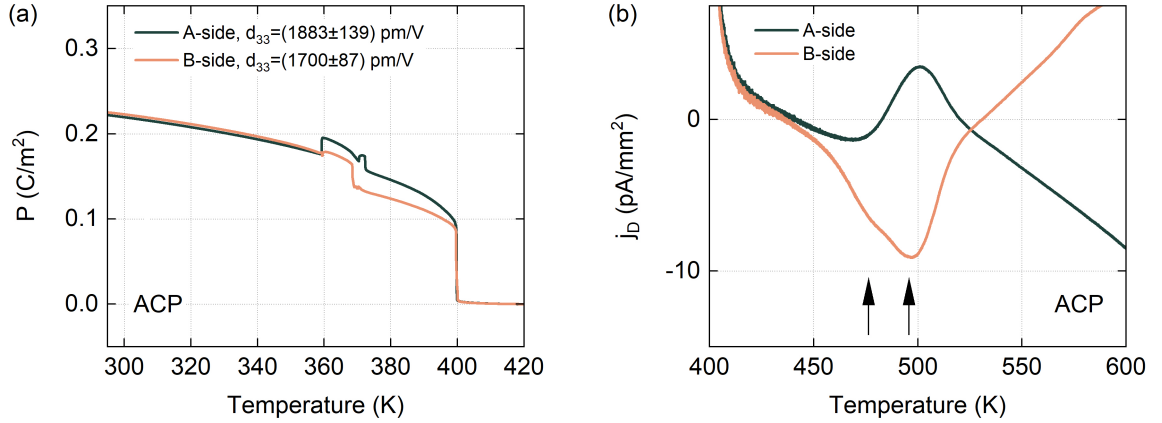


Figure 6.9. Polarization and thermally stimulated currents for different sample orientations of ACP [001]-PMN-30PT; Sample HC28. The polarized state was aligned with an initial polarization detected with dynamic pyroelectric measurements for the A-side. For the B-side, the polarized state was antiparallel with respect to this initial polarization. The polarization orientation with respect to the measurement electrodes was identical for both measurements. (a) Polarization, P , and (b) current density, j_D . Longitudinal piezoelectric coefficient, d_{33} , measured before the start of the individual experiments are indicated in (a).

previously investigated in this chapter revealed a weak initial polarization too, which was aligned to the poling field during experiments. Thus, only for the B-side in Fig. 6.9, this initial polarization and poling field were antiparallel. It is interesting to note that approximately 10 % lower d_{33} values were measured for the B-side. However, it has to be pointed out that this experiment was only conducted once and that its statistical significance has to be confirmed. Nevertheless, a clear correlation between the sample orientation and the TSC spectra is present.

So far, the initial hypothesis that aging is present in PMN- x PT and that it affects the macroscopic piezoelectric properties could be confirmed. In addition to aging phenomena, hardening of the polar structure has been indicated. One of the typical indications of hardening is an increase in the coercive field E_c resulting in a horizontal shift of polarization electric field hysteresis loops.^{294,295} To verify the presence of hardening, the polarization hysteresis loops for three samples of similar composition obtained from three different provider were thus measured. In addition to the ten cycles applied during ACP it was necessary to measure an additional eleventh cycle which is expected to be close to the tenth cycle. The second and eleventh cycles of these experiments are compared in Figure 6.10. It is evident that the centers of all second hysteresis loops are shifted towards higher electric fields. The differences between the positive and negative coercive fields, the *internal bias-field* $\Delta E_c = E_c^+ - E_c^-$, are indicated for each measurement. Values between $\Delta E_c = 0.7$ - 1.4 kV/cm have been obtained for the second cycles. During the eleventh cycles, the shifts of the hysteresis loops are considerably reduced with $\Delta E_c = 0.0$ - 0.2 kV/cm. It is noted that these measurements were taken shortly after the samples were annealed, indicating that the underlying process acts on the time scale of hours. Alternatively, ΔE_c could already be defined at elevated temperatures, for example in temperature regions starting below T_B or T^* . The relatively faster aging for ceramics as compared for crystals^{299,301} could therefore be a reason why ACP is not efficient for ceramics.^{204,311} Several authors have observed internal bias fields and

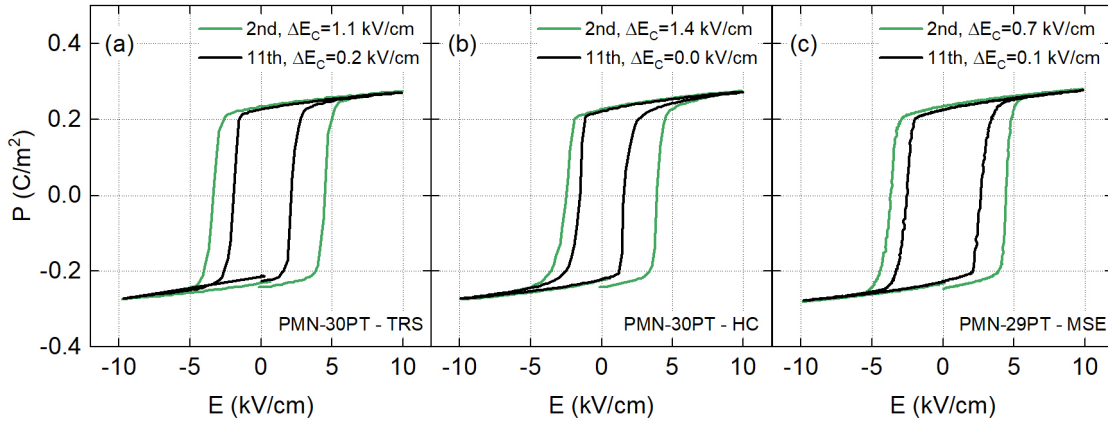


Figure 6.10. Change of polarization electric field hysteresis loops, $P(E)$, during ACP of [001]-PMN- x PT crystals obtained from different providers. The differences between the positive and negative coercive fields, ΔE_c , for the second and an additional eleventh cycle are indicated. (a) TRS Technologies: Sample X2B, (b) H.C. Materials: Sample HC28, and (c) MSE Supplies: Sample MSE(iv).

a reduction of E_c during ac-poling without critical discussion of its physical origin.^{286,312} One model relates the decrease in E_c to a reduction of domain wall intersections, or *joints*, which are thought to act as pinning centers.²⁸⁸ According to this model, the reduction of joints would result in an overall softening of the material.

Hardening and (de-)aging have been previously studied in acceptor-doped lead zirconate titanate, PZT, with the help of nonlinear dielectric measurements.¹⁴² It has been found that the third harmonic phase angle of polarization, $\delta^{(3)}$, is a sensitive indicator for the aging state, shifting to lower phase angles with increasing domain stability. Before $\delta^{(3)}$ is investigated, the first harmonic permittivity, $\epsilon^{(1)}$, and first harmonic piezoelectric coefficient, $d^{(1)}$, for DCP and ACP are compared in Figure 6.11. $\epsilon^{(1)}$ for DCP in Fig. 6.11(a) shows a superlinear, upwards bending, trend that was assigned to a relaxor-specific softening due to atomistic-scale disorder.⁶⁵ A marked hysteresis between measurements obtained for increasing and decreasing electric field amplitudes, E_0 , is seen. $d^{(1)}$, on the other hand, exhibits linear response with little hysteresis. Assuming that Eq. (6.1) holds true, the differences between $\epsilon^{(1)}$ and $d^{(1)}$ are attributed to electric field-induced depolarization. The difference between the first and the last measurement point, at $E_0 \approx 0.03$ kV/cm, for $\epsilon^{(1)}$ and $d^{(1)}$ amounts to approximately 2.1 % and 0.4 %, respectively.

For ACP in Fig. 6.11(b) the response obtained for $\epsilon^{(1)}$ and $d^{(1)}$ is relatively similar. In contrast to DCP, a sublinear, downwards bending, trend is present that was related to classic ferroelectric behavior and moderate piezoelectric coefficients.⁶⁵ Nevertheless, a strong increase of about 35 % as compared to DCP is obtained with almost no hysteresis. The difference between the first and the last measurement point for $\epsilon^{(1)}$ and $d^{(1)}$ is 0.2 % and 0.1 %. Surprisingly, these results suggest that the polarization for ACP is more stable than the polarization in DCP, even though $\epsilon^{(1)}$ and $d^{(1)}$ are significantly larger. These observations are not consistent with the proposed softening due to a reduction of joint density.²⁸⁸

Figure 6.12 directly compares the normalized nonlinear dielectric and electro-mechanical response of ACP and DCP. ACP does not only feature higher coefficients and lower hysteresis but also a relatively stronger increase of $\epsilon^{(1)}$ and $d^{(1)}$ with increasing E_0 up to ≈ 0.5 kV/cm. $\delta^{(3)}$ in

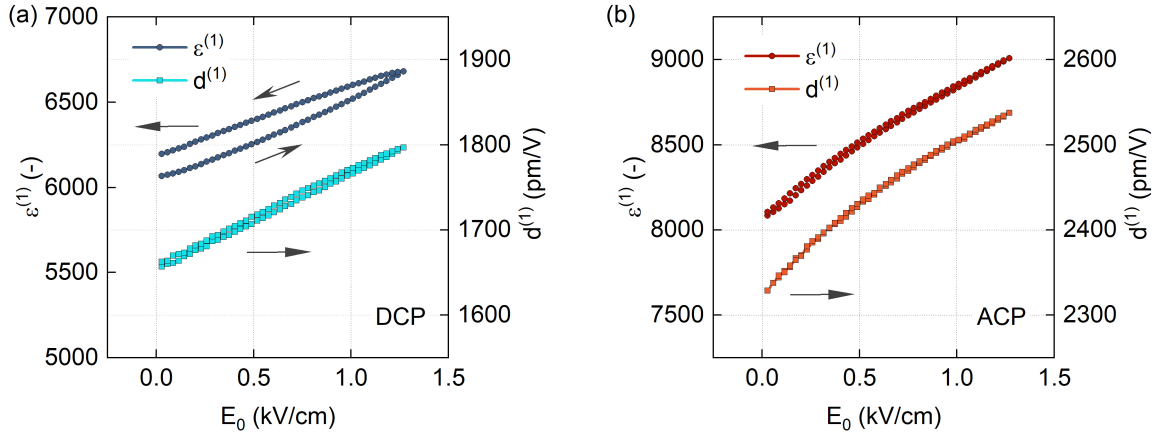


Figure 6.11. Comparison of subcoercive dielectric and electro-mechanical nonlinearities for DCP and ACP of [001]-PMN-29PT. First harmonic permittivity, $\epsilon^{(1)}$, and first harmonic piezoelectric coefficient, $d^{(1)}$, for (a) direct current polarized, DCP, MSE(iii), and (b) alternating current polarized, ACP, MSE(ii) samples.

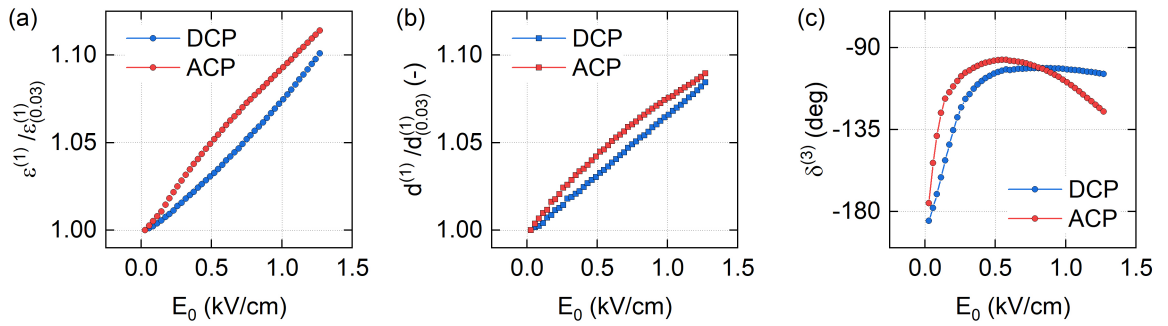


Figure 6.12. Normalized dielectric and electro-mechanical nonlinearities and third harmonic phase angle of polarization for DCP and ACP of [001]-PMN-29PT. (a) First harmonic permittivity, $\epsilon^{(1)}$, and (b) first harmonic piezoelectric coefficient, $d^{(1)}$, normalized to the first measurement points, i.e., the data obtained at electric field amplitudes, $E_0 \approx 0.03$ kV/cm. (c) Third harmonic phase angle of polarization, $\delta^{(3)}$. DCP: Sample MSE(iii). ACP: Sample MSE(ii).

Fig. 6.12(c), however, indicates an underlying hardening effect for ACP compared to DCP. For DCP, $\delta^{(3)}$ changes from around -180° to about -70° in the investigated range of E_0 , forming a maximum at around 0.75 kV/cm. For ACP a similar but more pronounced increase and decrease below and above the maximum is seen. Similar tendencies have been observed for acceptor-doped PZT.¹⁴² Thus, the nonlinear dielectric and electro-mechanical response of ACP combines two, at first glance, opposing characteristics. The pattern and magnitude of its weak-field response are characteristic for mobile or *soft* polarization, while the absence of hysteresis in $\epsilon^{(1)}$ and $d^{(1)}$ together with the downward bending $\delta^{(3)}$ suggests stable or *hard* polarization.

It is speculated that differences in the defect structures between ACP and DCP could be responsible for these observations. For DCP, defects migrate over macroscopic distances, potentially piling up at interfaces and electrodes, resulting mostly in an interface pinning effect. For ACP on the other hand, the bipolar poling field should result in a net-zero migration of defects, for ideal symmetric conditions. In that case, only the last half-cycle of the poling procedure would

result in a net displacement of defects. Therefore, defects should be more evenly distributed through out the volume of the material, assuming a random initial distribution. It is therefore suggested that a volume stabilization of polarization is dominant for ACP while interface stabilization is dominant in DCP. Moreover, in the presence of defects of different polarities, such as lead and oxygen vacancies, one would expect that the density of defect dipoles is higher for ACP since, for DCP, these species would be located at different ends of the sample in the extreme case. Consequently, not only a different distribution but also a completely different defect structure could be present ACP and DCP.

The origin of the suggested hardening was studied in more detail, with measurements of the nonlinear response of different relaxor ferroelectric solid solutions. Dielectric nonlinearities of various compositions and crystallographic directions of poled crystals of three different relaxor ferroelectric solid solutions are presented in Figure 6.13. Strong anisotropy in the nonlinear response is apparent. For samples poled along $[001]_{pc}$, a linear increase in first harmonic permittivity and $\delta^{(3)}$ of polarization approaching -90° characteristic for Rayleigh behavior are observed. In contrast, the nonlinear dielectric permittivity of samples poled along the $[111]$ direction is described by a higher-order polynomial and a $\delta^{(3)}$ of polarization that features a peak around 0.4 kV/cm. The relatively slow increase of permittivity at low fields as compared to $[001]$ -poled samples and the drop of $\delta^{(3)}$ of polarization below -180° at higher fields indicate hardening and an unexpected tendency toward loop pinching in $[111]$ -poled samples (see Fig. 3.4). Samples poled along the $[011]$ -direction show intermediate behavior. With increasing measurement frequency, $\delta^{(3)}$ generally shifts to lower phase angles for $[001]$ - and $[111]$ -poled PMN-0.28PT as observed in Figure K.5. In addition, the peak in $\delta^{(3)}$ shifts to higher E_0 for $[111]$ -poled PMN-0.28PT, as may be expected for the reorientation of domains or defect dipoles.^{295,313,314}

To correlate the observed nonlinearities with microscopic features, a $[111]$ -PMN-28PT was polished to 200 μm thickness and coated with transparent indium tin oxide electrodes. The sample was then electrically contacted to the top and bottom electrodes and mounted on a stage of a polarized light microscope, PLM. Dielectric nonlinearities were first measured in the unpoled state before the picture presented in Figure 6.14a was taken. The corresponding $\delta^{(3)}$ is shown as an inset. A complex domain pattern and Rayleigh-like behavior are observed. The sample was then thermally depolarized and subsequently poled at room temperature. Dielectric nonlinearities of the poled state were measured, and a PLM image was taken again after the experiment (Fig. 6.14a). A clear contrast in the PLM image and a peak in the third harmonic phase angle (see inset) can be observed for the $[111]$ -poled PMN-28PT crystal, as previously described in Fig. 6.13(d). A transparent appearance of polarized crystals has been observed before.^{108,315}

Clear differences in the polar/domain structure are observed optically for unpoled and poled PMN-28PT $[111]$ -crystals after measurements of dielectric nonlinearities. The absence of contrast under the PLM for the poled case suggests that the mechanisms responsible for the peak in $\delta^{(3)}$ (Figs. 6.13 and 6.14) act on a shorter length scale as compared to the dominant mechanism in the unpoled state. In addition, the hardening effect of poling can be confirmed. While complex domain structures are present after field cycling in the case of an unpoled sample, the poled sample appears to be less affected, consistent with the drop in $\delta^{(3)}$ below -180° above 0.4 kV/cm. Note that 180° domain walls cannot be seen in the case of PLM images, but their density should be small in poled samples. Considering the polar features that were recently visualized in PMN- x PT²⁰ it can be assumed that mechanisms on the nano-scale play a key role in the observed

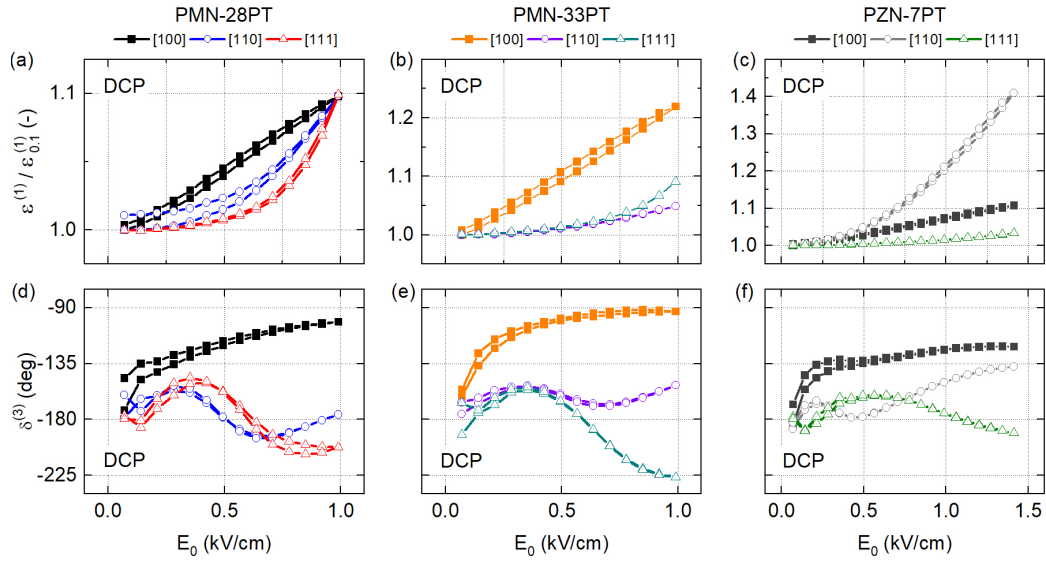


Figure 6.13. Anisotropic electric field-dependent nonlinear polarization response of poled relaxor ferroelectric single crystals. (a)–(c) First harmonic permittivity, $\epsilon^{(1)}$, normalized to the values measured at a driving field amplitude of ≈ 0.1 kV/cm, and (d)–(f) third harmonic phase angle $\delta^{(3)}$ as a function of driving field amplitude of crystals poled along three different pseudo cubic crystallographic directions. Note that the scales of the ordinates of figures (a)–(c) are not identical. (a) and (d): PMN-28PT; (b) and (e): PMN-32PT; and (c) and (f): $0.93\text{Pb}(\text{Zn}_{1/3}\text{Nb}_{2/3})-0.07\text{PbTiO}_3$ (PZN-7PT). [100]-crystals approach Rayleigh behavior. [111]-crystals show a peak in $\delta^{(3)}$ of polarization at relatively weak field levels before dropping below -180° . The latter is reminiscent of pinched hysteresis loops. [110]-crystals show intermediate behavior.

nonlinear dielectric behavior¹¹² of the investigated [111]-poled crystals. This assumption is supported by the strikingly similar nonlinear response obtained for barium titanate single crystals provided in Figure K.6, for which polar nanodomains were also recently visualized at ambient temperatures.³¹⁶

Assuming nano-sized polar regions as the origin of the peak in $\delta^{(3)}$, the second harmonic response of polarization, $P^{(2)}$, and strain, $x^{(2)}$, were analyzed regarding the switching signatures previously discussed in Chapter 3 and Chapter 4. Figure K.7 and Figure K.8 show the second harmonic response for [111]-poled PMN-0.28PT and [111]- and [011]-poled lead zinc niobate lead titanate crystals (PZN- x PT). As previously observed for PZT and PMN, anomalies in the polarization response indicate an underlying switching mechanism. In addition, anomalies in the strain response provide evidence that the underlying mechanism is electro-mechanically active. However, even if the results presented suggest that nano-sized polar regions switch within parent domains, the absence of obvious anomalies in $\epsilon^{(1)}$ in Fig. 6.14 at all electric field levels investigated suggest that the direct contribution of such a dynamic mechanism is relatively weak and that it is rather the presence of nano-sized polar regions that affects the dielectric response by softening the material.^{105,317} This is somewhat analogous to the case where domain walls improve the properties of a ferroelectric material not by their displacement but by their presence. This has been observed, for example, in BT single crystals where stationary charged domain walls improve piezoelectric and dielectric response by destabilizing polarization within domains even if they do not move.^{95,284}

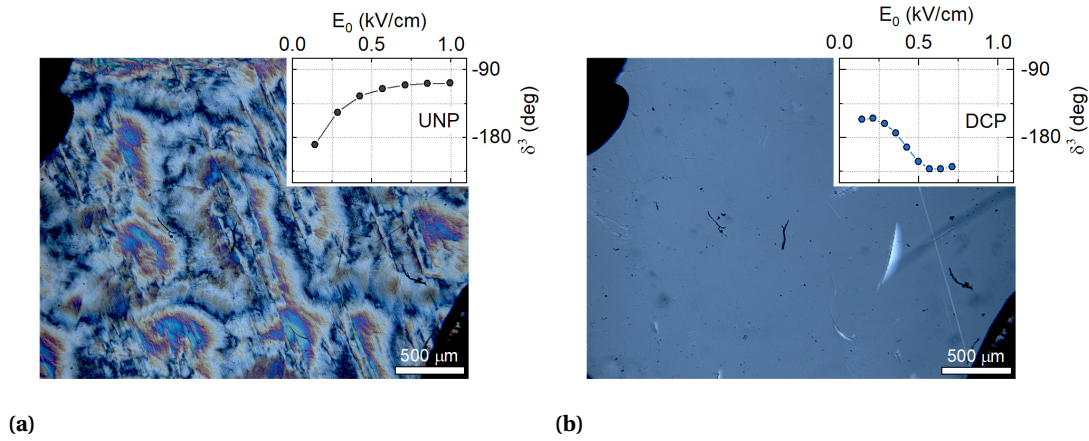


Figure 6.14. Polarized light microscopy, PLM, images and third harmonic phase angle of polarization, $\delta^{(3)}$, of a $\approx 200 \mu\text{m}$ thick [111]-PMN-28PT crystal with transparent indium tin oxide electrodes. The PLM images were taken after the measurements of $\delta^{(3)}$ shown in the insets. The sample was thermally depolarized between measurements. (a) Initially unpoled sample shows Rayleigh behavior of $\delta^{(3)}$ and a complex domain pattern after the measurement. (b) The same sample as in (a) but poled before the measurement of $\delta^{(3)}$. The absence of clear polar features suggests that the mechanism responsible for the peak in $\delta^{(3)}$ has dimensions below the resolution limit of visible light.

It should be mentioned that the characteristics of nano-sized polar regions and defect clusters are remarkably similar. They can be electrically and elastically active, cause dielectric and anelastic relaxation,^{57,318} break local symmetry^{20,319,320}, and may contribute to large reversible strains.^{105,321} Specifically for PMN-30PT, T^* was independently attributed to oxygen vacancy migration²⁵⁰ and the first appearance of static nano-sized polar regions.^{81,83} However, theoretical models consider defects only in the framework of quenched random fields that either result in a broken ferroelectric state or a dipolar glass.

6.4 Summary and conclusions

Aging and its influence on the dielectric and piezoelectric properties of PMN-*x*PT crystals were investigated through thermally stimulated current measurements, polarisation electric field hysteresis loops, and subcoercive dynamic dielectric and piezoelectric measurements. An aging effect has been demonstrated by history- and time-dependent thermally stimulated depolarization peaks for unpolarized samples, internal electric bias fields, and a reduction of the weak-field and subcoercive piezoelectric coefficient and dielectric permittivity with time.

Direct current, DCP, and alternating current poling, ACP, procedures for samples that were either aged for four months or previously annealed were compared. Only minor differences in the longitudinal piezoelectric coefficient, d_{33} , between annealed and aged samples have been found for DCP. For ACP, on the other hand, annealing the sample before poling results in an enhancement of d_{33} of $\approx 15\%$ as compared to the aged-ACP and $\approx 50\%$ as compared to DCP. Independent of the poling procedure, the aged state depolarizes at $\approx 30\text{ K}$ lower temperatures compared to samples that were annealed before poling. In addition, annealed and then poled samples exhibit an intermediate polarization enhancement²⁵⁸ which has been attributed to the presence of aligned defect structures, presumably related to oxygen and lead vacancies.^{24,304}

In addition to aging, an unexpected hardening effect has been suggested. For ACP, hardening seems to be enhanced as compared to DCP, even though the weak-field piezoelectric and dielectric properties for ACP are larger. It has been speculated that different defect configurations are related to these observations. For DCP, oxygen vacancies accumulate at the cathode region,²⁵⁰ while for ACP, defects are more likely homogeneously distributed throughout the volume. Consequently, the distance between defects of opposite charge is shorter for ACP, and defect associates, like defect dipoles, can form more easily. These defect associates could locally break the symmetry,^{20,319,320} enhance reversible polarization rotation and switching locally, and stabilize the domain structure simultaneously.^{105,321}

These findings are not only relevant for the development of high-performance domain-engineered single crystals but also for the design of future experimental guidelines. It is suggested that the variety of sometimes contradicting experimental results, and interpretations available in the literature are in part related to the large variety of applied thermal treatments^{107,108,204,282,288,289} in combination with aging phenomena. Fundamental research conducted in vacuum up to high temperatures^{322–324} and the observed severe discoloration of samples³²³ have to be reconsidered.

7 Summary, conclusions, and perspectives

This work aims to deepen the fundamental understanding of micro- and nano-scale polarization and its correlation to functional properties in the relaxor ferroelectric lead magnesium niobate, $\text{Pb}(\text{Mg}_{1/3}\text{Nb}_{2/3})\text{O}_3$ (PMN), and its solid solutions with lead titanate, $(100-x)\text{Pb}(\text{Mg}_{1/3}\text{Nb}_{2/3})\text{O}_3 - x\text{PbTiO}_3$ (PMN- x PT). In these materials, dielectric and electro-mechanical nonlinearities are of paramount importance for the operation of many electronic devices, and thus a correlation between mechanisms acting on the nano-scale and macroscopic functional properties is desired. For this purpose, two precision experimental setups have been developed to study nonlinear dielectric and electro-mechanical properties, as well as thermally stimulated currents. The main findings of this work and its major implications are discussed in the following.

At first, the well-known ferroelectric $\text{Pb}(\text{Zr}_x\text{Ti}_{1-x})\text{O}_3$, lead zirconate titanate (PZT), was studied in Chapter 3, in order to develop an experimental approach that expands the understanding of the harmonic analysis of sub-coercive nonlinear dielectric and electro-mechanical response in ferroelectric and related materials. Known contributions to the nonlinear polarization response and its influence on the third harmonic phase angle of polarization were discussed in this perspective. Additionally, an anomaly in the second harmonic polarization response in the sub-coercive electric field regime was revealed and attributed to a polarization reversal mechanism. This hypothesis was then verified with experiments during which macroscopic polarization reversal was intentionally induced with an additional direct current, dc, electric bias field superimposed on an alternating, ac, current probing field.

The presented results may contribute to the development of an experimental approach to expand the understanding of the harmonic analysis of sub-coercive nonlinear response in ferroelectric and related materials. For future research, a comparison of obtained results with PZT or tetragonal PMN- x PT crystals would be of interest. However, single crystals of these compositions are rare and commercially not available.

With the established setup, the nonlinear dielectric and electro-mechanical responses were then investigated for the model system PMN in Chapter 4. Based on these measurements, two fundamental aspects could be established: the origin of the maximum in the dynamic dielectric permittivity could be attributed to nano-sized polar regions, and the widely accepted picture of a non-polar and ergodic ground state of PMN at ambient temperatures was questioned.

In PMN, a maximum in the dielectric permittivity together with hysteretic anomalies in the second harmonic polarization response were observed. In analogy to PZT, the anomalies in the

second harmonic response were interpreted as a polarization reorientation mechanism. Poling experiments were conducted in order to confirm the temporal stability of polarization in PMN. Weak piezoelectric coefficients of $d_{33} = 13.5 \pm 1.4$ pm/V and 3.2 ± 0.9 pm/V were measured for ceramics and single crystals, respectively, after cumulative poling procedures up to 50 kV/cm. Subsequently, the isothermal depolarization at ambient temperature was investigated with dynamic pyroelectric measurements. The pyroelectric current decayed according to Curie von Schweidler law with a power exponent $n_{CVS} = 0.235 \pm 0.001$ over several days. To investigate the origin of the underlying polarization and to exclude the contribution of electric field induced trapped charges, the dynamic pyroelectric response of pristine PMN crystals was measured. A modulation of the pyroelectric current for crystals of different origins was revealed, as expected for materials with macroscopic polarization. It was speculated that this initial polarization is related to strain gradients, static nano-sized regions, charge disorder, chemically ordered regions, or other mesoscopic inhomogeneities. The electric field to reverse macroscopic polarization was then determined to be $E_{0,m} = 1.35 \pm 0.05$ kV/cm, approximately coinciding with the electric field of maximum dielectric permittivity of $E_M = 1.5 \pm 0.05$ kV/cm measured for the same crystal. Annealing experiments were subsequently performed to correlate the polarized state with characteristic temperatures of PMN. It was found that the sample had to be annealed above Burns temperature, T_B , to reverse the orientation of polarization to its initial orientation. Since T_B is attributed to the first emergence of nano-sized polar regions, a part of the observed polarization was related to these entities. Consequently, a relation between the observed maximum in the dynamic field-dependent dielectric permittivity and nano-sized polar regions was proposed.

The contribution of the presented results to the fundamental understanding of PMN is twofold. First, the origin of the maximum in the dynamic dielectric permittivity is clarified. This may influence future theoretical models and help to enhance the performance of various related systems and applications, such as high performance piezoelectric PMN-*x*PT crystals,¹⁰⁵ high energy storage density dielectrics,⁹⁰ and electrocaloric cooling.¹⁹⁶ Second, the widely accepted picture of a non-polar and ergodic ground state of PMN at ambient temperatures is questioned. This is an important finding, as it may explain the variety of sometimes contradicting experimental results reported in the literature. Since there is no unified thermal treatment of specimens to be applied before measurements, the here identified nonergodic behavior implies that different states of the systems have been tested. The present findings may therefore help to develop and implement a standardized method for sample treatments, thereby increasing the reproducibility of results.

Future research motivated by the obtained results could explore the anisotropy of the dynamic pyroelectric response and piezoelectric coefficients in PMN crystals. The results of these experiments could be used to estimate the direction of the polar axis in PMN and help to clarify if nano-sized regions facilitate large piezoelectric shear contributions as commonly believed. Moreover, it would be interesting to see whether fundamental thermodynamic relations concerning piezoelectric coefficients hold true when polarization is induced dynamically.

Following the above-mentioned findings, the depolarization of PMN was further investigated *in-situ* by thermally stimulated depolarization current, TSDC, measurements in Chapter 5. These experiments are fundamentally interesting because they contribute to the understanding of T_B and the coherence temperature, T^* , for which a consistent assignment and interpretation remains

a controversial issue in the literature. For electrically poled samples, TSDC peaks around T_B , T^* , and the temperature of the first appearance of piezoelectric response were found. It was observed that the peak at T^* is of opposite polarity as compared to the remaining peaks, a rare observation that may be related to the interaction of polarization mechanisms or to phase transitions. In addition to electrical poling, a mechanical poling procedure was applied for which the peak around T^* was absent. Based on a comparison with results from the literature, it was speculated that the TSDC peak around T^* is related to oxygen vacancies, and its absence for mechanical poling was attributed to the relatively higher symmetry of point defects as compared to defect clusters. To test whether PMN is ergodic between T^* and T_B , different poling procedures were applied. It was found that if a poling field is only applied between T^* and T_B TSDC peaks could still be found above and around T_B .

It was argued that these results are not consistent with the existence of an ergodic relaxor state below T_B , in which case no TSDC peaks would be expected at all for this procedure. During cooling cycles, in general, only one TSDC peak around ambient temperatures was observed, and its magnitude and polarity were related to the previously applied poling field. At the same time, a complex evolution of the dynamic pyroelectric response over several days was observed, which led to the hypothesis that the observed macroscopic polarization is related to aging phenomena. A pristine ceramic sample was aged for over one year, before TSDC measurements were performed to test this hypothesis. This study revealed peaks around T^* and T_B of opposite polarity, as previously observed for the electrically polarized sample. Since charge injection for pristine samples can be excluded, an indirect correlation between oxygen vacancies and nano-sized polar regions was suggested. Furthermore, it was shown that these peaks are not present immediately after previous measurements but reoccurred to some extent after three weeks. Therefore, the TSDC peaks observed could be related to aging phenomena.

These results are fundamentally interesting because they contribute to the understanding of T^* and T_B , two characteristic temperatures that have been extensively investigated by structural methods in previous studies. A common interpretation of T^* is the first appearance of static nano-sized polar regions at which, accordingly, depolarization would be expected. However, the results presented in this work provide evidence that depolarization in polarized and aged samples takes mostly place around T_B . For mechanically poled samples, the peak around T^* was even absent. The latter is not consistent with the widely accepted model of a single polar entity that evolves during cooling below T_B , for which the presence of all characteristic peaks simultaneously would be expected. The results of this work, therefore, suggest that the combination of TSDC measurements with different electric poling procedures can help to resolve different aspects of polarization mechanisms as compared to structural measurements. Another fundamentally and practically relevant result is the observation of an aging effect which is widely considered to be negligible for stoichiometric compositions. In contrast, our results show that aging can induce TSDC peaks at similar temperatures as electric fields and that its effects should not be neglected in theoretical models and fundamental experimental studies.

Further studies could include structural investigations of polarized samples to elucidate the origin of the individual peaks. In particular, the correlation between poling conditions and the absence of certain TSDC peaks would be of interest. Another question that could be addressed is whether aging of pristine PMN single crystals also results in TSDC peaks of opposite polarity around T^* and T_B or if these are related to ceramic-specific processes. Moreover, quenching

experiments could yield insights into the formation of macroscopic polarization in PMN.

Following the observations made for PMN, aging and its effect on macroscopic functional properties of technologically relevant compositions of PMN-*x*PT were investigated in Chapter 6. For this purpose, the response of unpoled, direct current poled, DCP, and alternating current poled, ACP, samples were compared for annealed and aged samples. For PMN-*x*PT samples that were aged for four months, similar TSDC anomalies as for PMN were found, which were only weakly present in annealed samples. Moreover, it was found that aging, in general, reduces the depolarization temperature by about 30 K and results in relatively larger anomalies around T_B . For ACP after annealing, the piezoelectric performance was enhanced by 15% as compared to aged samples and 50% as compared to DCP. In addition, an intermediate polarization enhancement was observed for annealed samples before the depolarization around the Curie temperature. Together with aging, an unexpected hardening effect was observed with polarization electric field hysteresis loops and nonlinear dielectric measurements. An apparent contradicting duality of polarization stabilization and property enhancement was observed for alternating current poling. It was suggested that the applied bipolar poling field leads to a distribution of oriented defect clusters throughout the volume, which could improve dielectric and piezoelectric properties through locally broken symmetry and mediated reversible polarization rotation. Moreover, a weak dependence of the sample orientation on the TSDC and piezoelectric response was observed, requiring further statistical verification.

The obtained results are expected to benefit the scientific community because they demonstrate a correlation between macroscopic functional properties with anomalies around temperatures related to the emergence of dynamic and static nano-scale polarization. Importantly, several characteristics and previous studies relate these anomalies also to defects. However, it is unclear if oxygen vacancies can be assigned to static nano-sized polar regions or if it is rather the interaction, i.e., the screening of their polarization, that is observed. The here reported variations of piezoelectric performance with aging and potentially sample orientation are of practical importance, as they represent relatively cheap ways to improve the piezoelectric performance of domain engineered single crystals. Even though a variation of the depolarization temperature was observed for aged samples, it is not expected that it can be further enhanced above T_C with annealing procedures.

Further work motivated by this research could investigate the optimization of ACP procedures and their potential for ceramic samples. In this context, the influence of pre- and post-poling annealing temperatures could be insightful. Pre-annealing above T^* but below T_B would not only be of interest for the investigation of the hardening mechanisms but potentially also for the cost optimization in the industrial context. Furthermore, it would be interesting to see how ACP samples age and if the coercive field could be enhanced through appropriate post-poling treatments, which would be of practical importance for transducer applications. Moreover, ACP for ceramics could be tried. Since aging has been shown to be faster for ceramics than for single crystals, samples should be poled at elevated temperatures directly after annealing without cooling them to room temperature first. Another insightful aspect would be to understand whether ACP would also be applicable for other relaxor ferroelectric solid solution systems, such as sodium bismuth titanate barium titanate, $(\text{Na}_{1/2}\text{Bi}_{1/2})\text{TiO}_3 - \text{BaTiO}_3$ (NBT-BT).

It must be mentioned that this work also pointed out similarities of the nonlinear response between PMN at ambient and strontium titanate at cryogenic temperatures, as well as between PMN-*x*PT and barium titanate. The former two are characterized by antiferrodistortive characteristics and local disorder. The latter two display hierarchical domain structures with nano-scale polarization within ferroelectric domains, indicating that a variety of material systems with similar polar structures show the same nonlinear response. Therefore, the harmonic analysis of dielectric nonlinearities as presented in this work could become a general approach to investigate nanoscale polarization. Moreover, the macroscopic polarization observed in PMN and the internal bias observed in PMN-*x*PT suggest that macroscopic symmetry breaking, as has been previously reported for barium titanate and its solid solution with strontium titanate,¹⁸⁹ could be a common feature for ferroelectric and relaxor ferroelectric materials.

While open questions remain about the detailed mechanisms involved, this thesis has provided fundamental insights into the dynamics and correlation of micro-, and nanoscale polarization and its impact on functional properties in PMN and PMN-*x*PT. It has been proposed that functional and structural properties of undoped PMN and undoped PMN-*x*PT are considerably affected by defect structures, which depend on the thermal, electric and mechanical field history, and on time. Moreover, questionable aspects of well-established models, characteristic temperatures (T^* and T_B), and their entailing mechanisms have been pointed out. The outcomes of this work are expected to further the fundamental understanding of relaxor ferroelectrics, help to improve their properties and contribute to an enhanced reproducibility of experimental results found in the literature.

A Circuit schematics for pyroelectric measurements

This appendix provides circuit schematics for pyroelectric measurements as discussed in Chapter 2. The attached documents have been retrieved from the archive of Prof. Dragan Damjanovic's Group for Ferroelectrics and Functional Oxides, former part of the Ceramics Laboratory of Prof. Nava Setter. These plans have not been verified. Undocumented modifications may have been performed by manufacturers, technicians, or scientists.

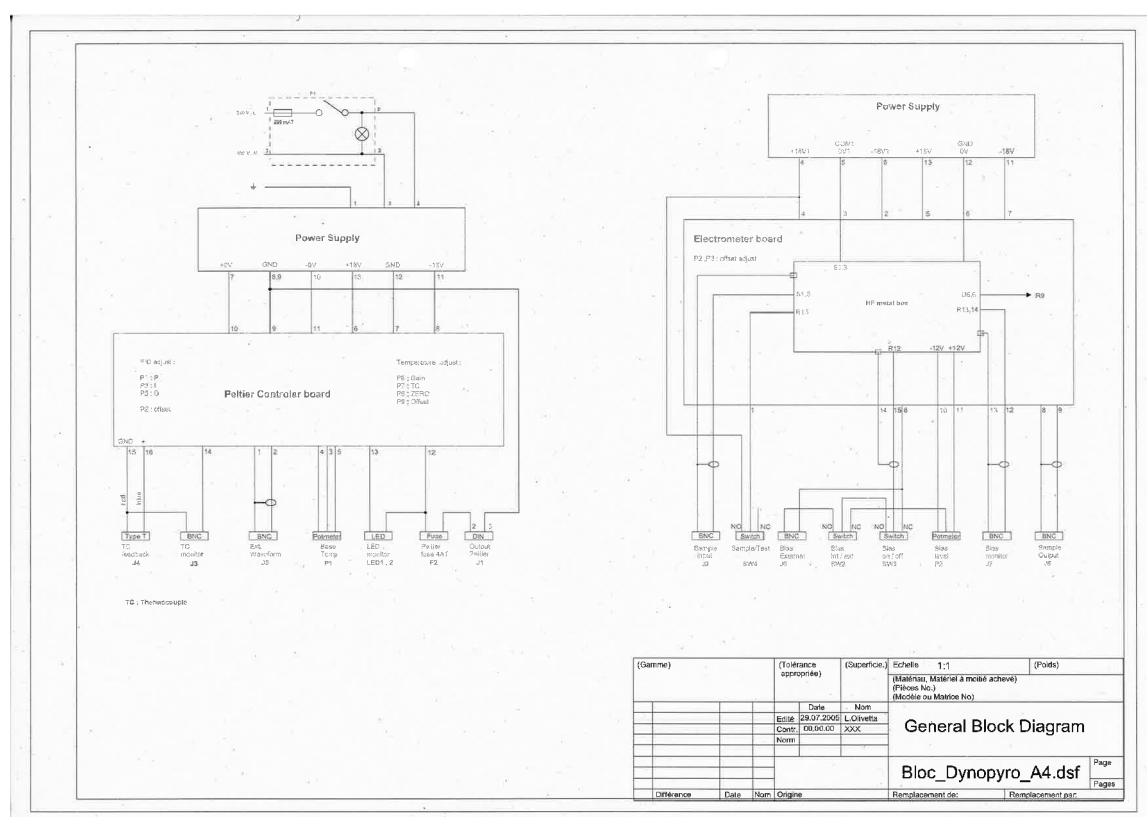
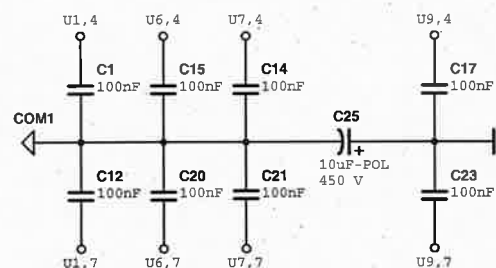
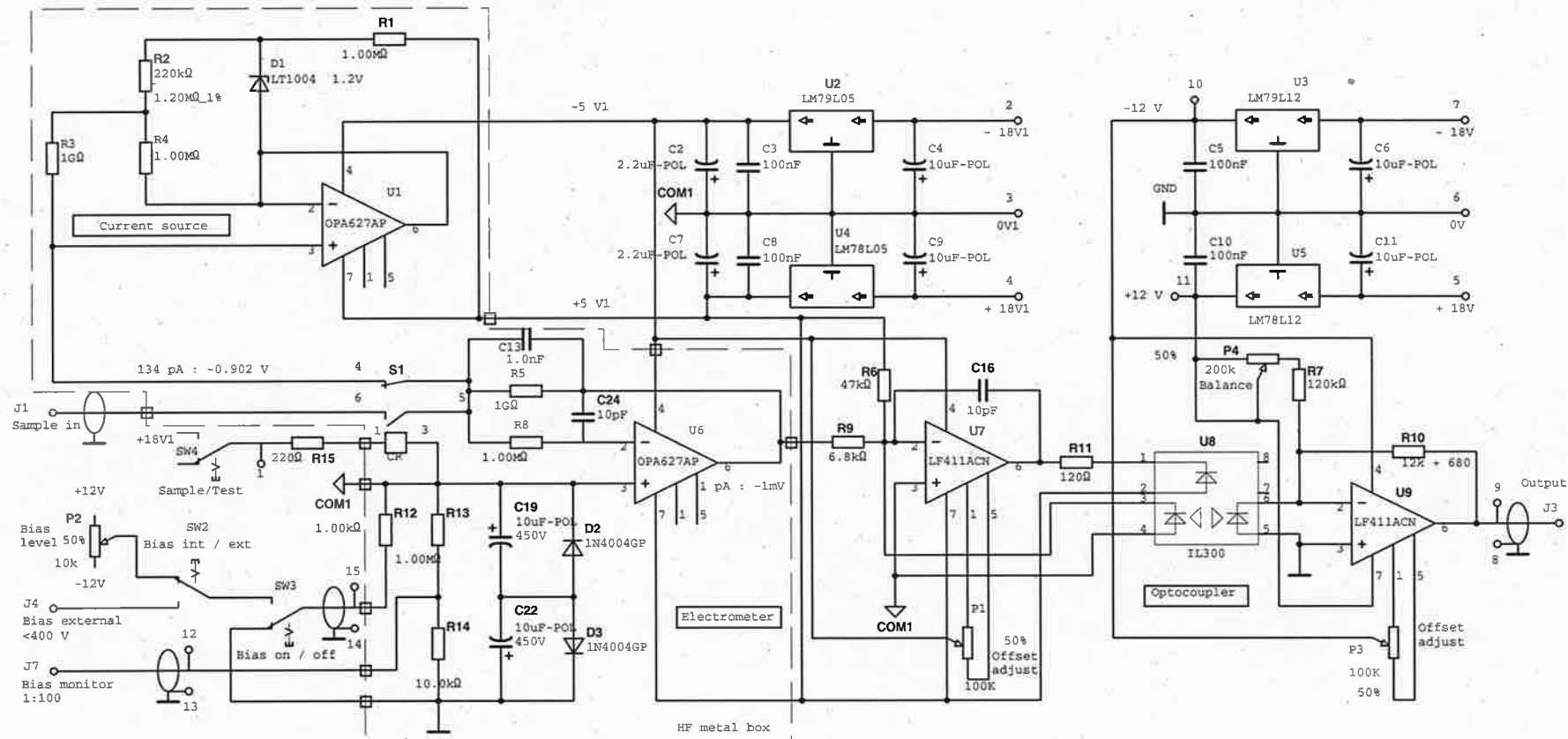


Figure A.1. Block diagram of *Dynopyro*, a device for dynamic pyroelectric measurements.



Title: Electrometer8

Size:
A3

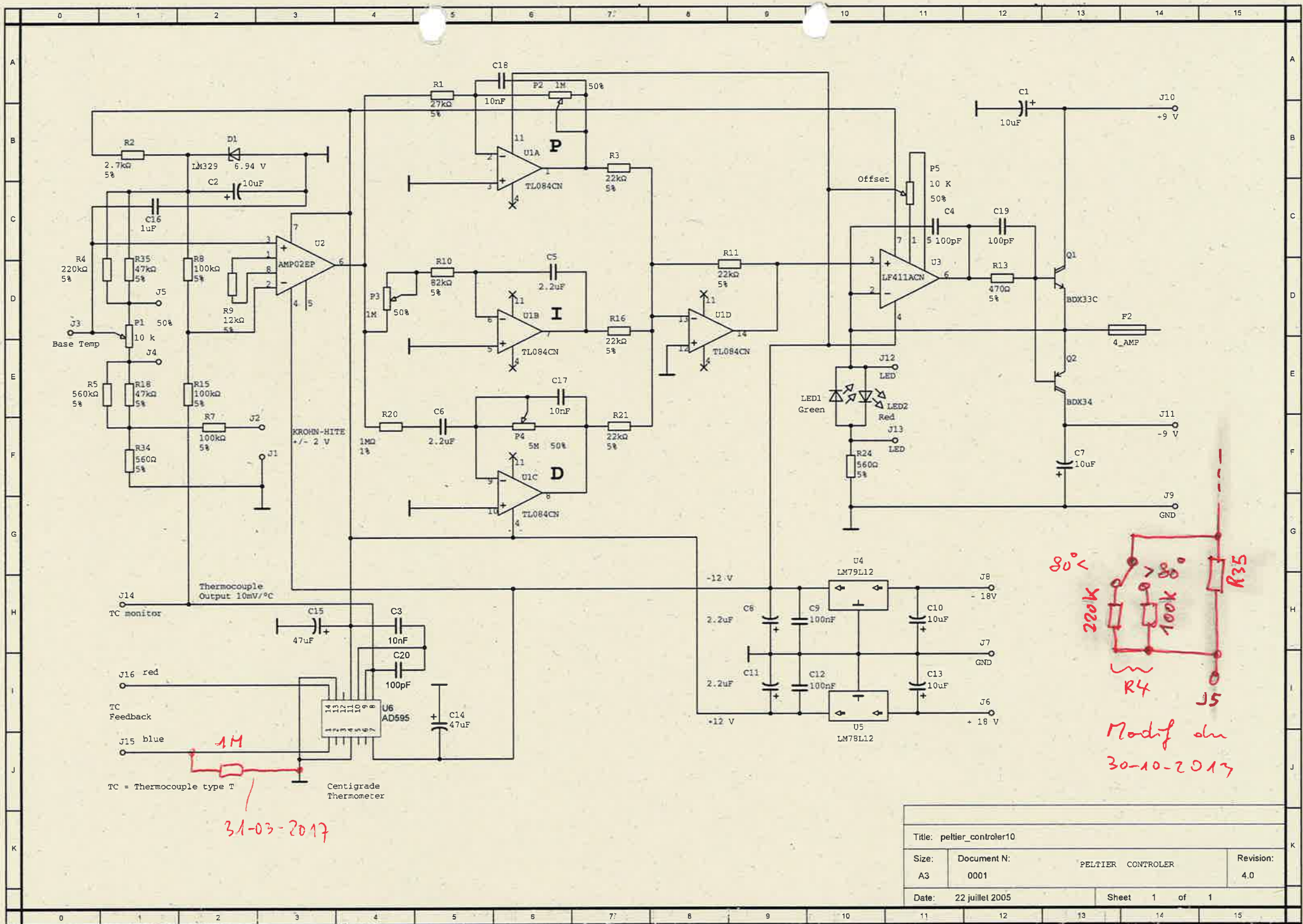
Document N:
0001

Electrometer with bias voltage

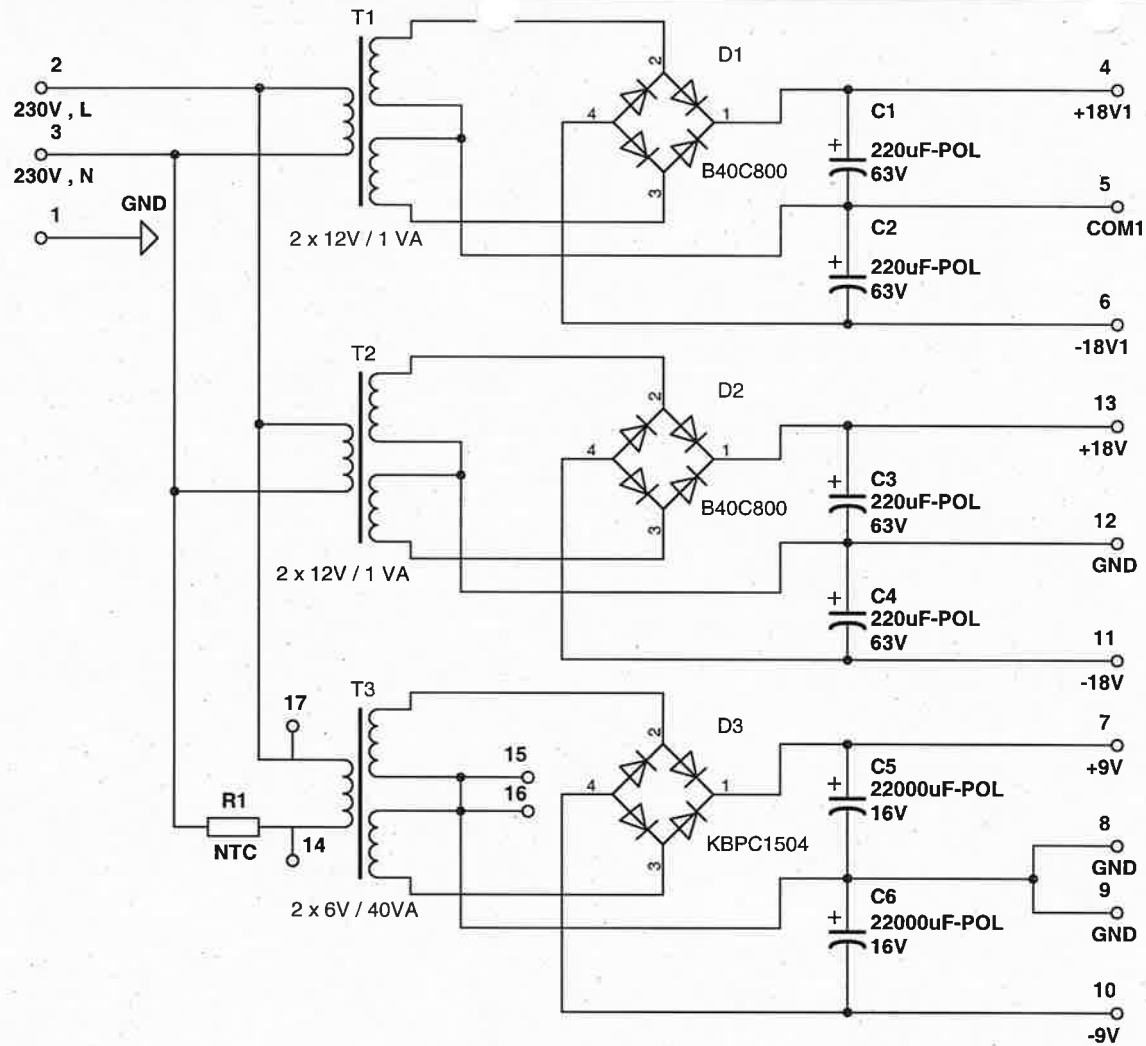
Revision:
1.0

Date: 27 juillet 2005

Sheet 1 of 1



Title: peltier_controller10			
Size: A3	Document N: 0001	PELTIER CONTROLLER	Revision: 4.0
Date: 22 juillet 2005	Sheet 1 of 1		



Title: alim_dynopyro		
Project 1		
Designed by: Lino Olivetta	Document N: 0001	Revision: 2.0
Checked by:	Date: 23 février 2005	Size: A
Approved by:	Sheet 1 of 1	

B Circuit schematics for Sawyer Tower measurements

This appendix provides circuit schematics for a modified Sawyer Tower circuit as discussed in Chapter 2. The attached documents have been retrieved from the archive of Prof. Dragan Damjanovic's Group for Ferroelectrics and Functional Oxides, former part of the Ceramics Laboratory of Prof. Nava Setter. These plans have not been verified. Undocumented modifications may have been performed by manufacturers, technicians, or scientists.

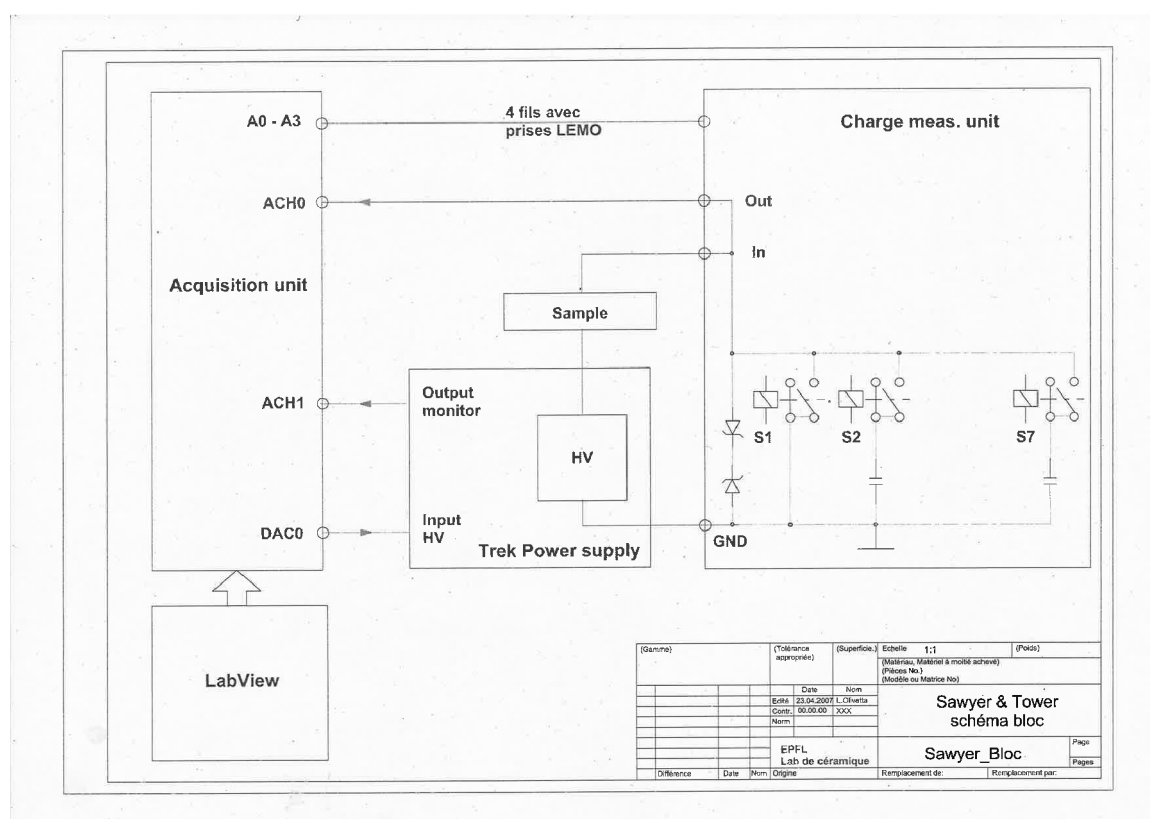
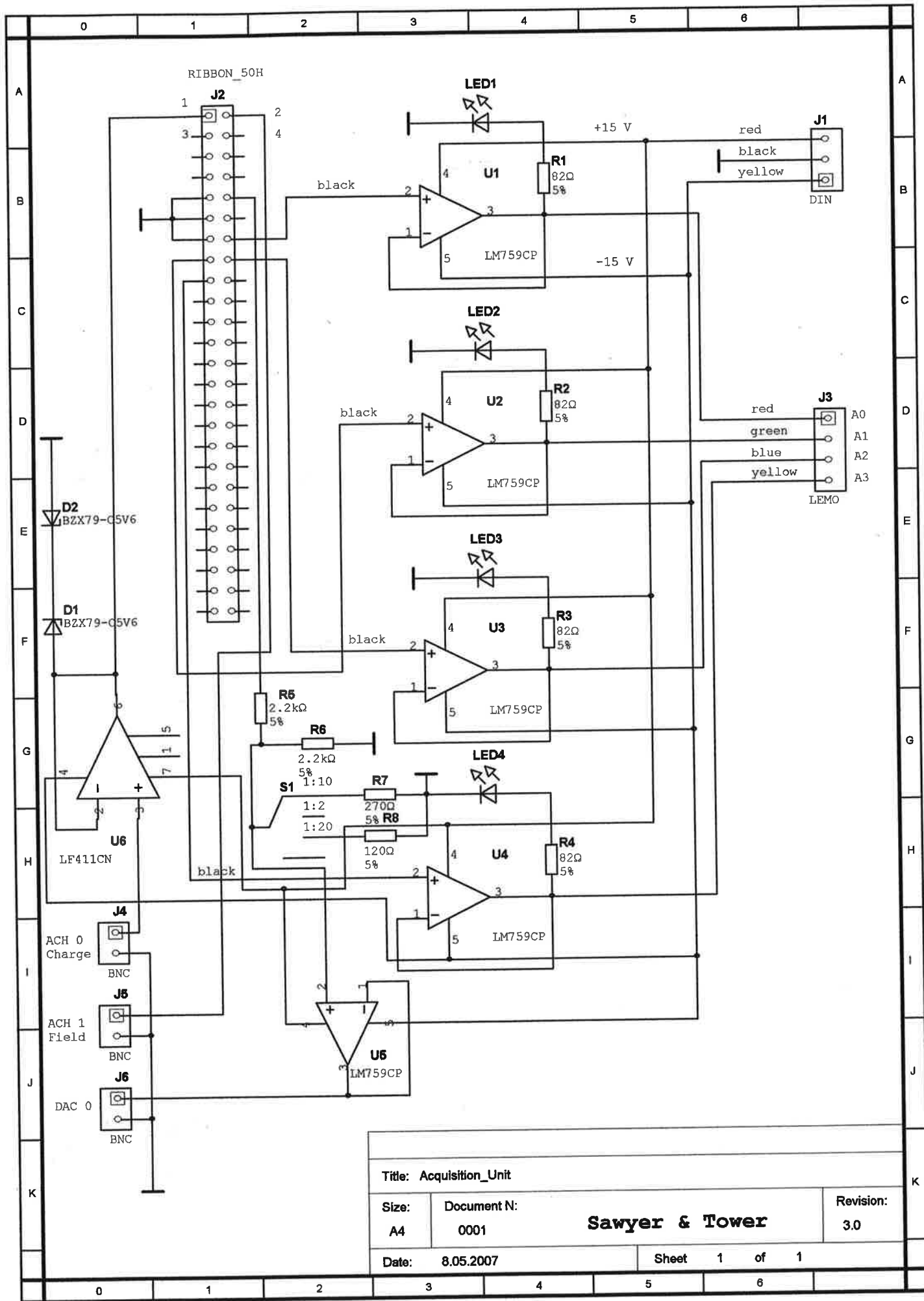


Figure B.1. Block diagram of modified Sawyer Tower circuit.



Title: Acquisition_Unit

Size:

A4

Document N:

0001

Sawyer & Tower

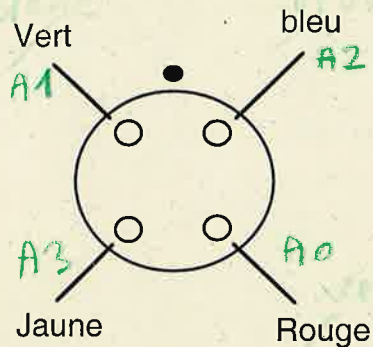
Revision:

3.0

Date: 8.05.2007

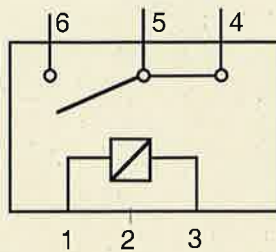
Sheet 1 of 1

SAWYER AND TOWER

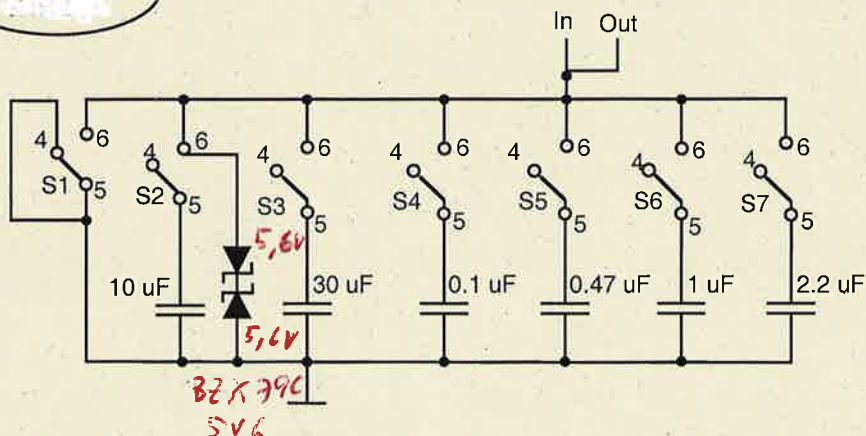
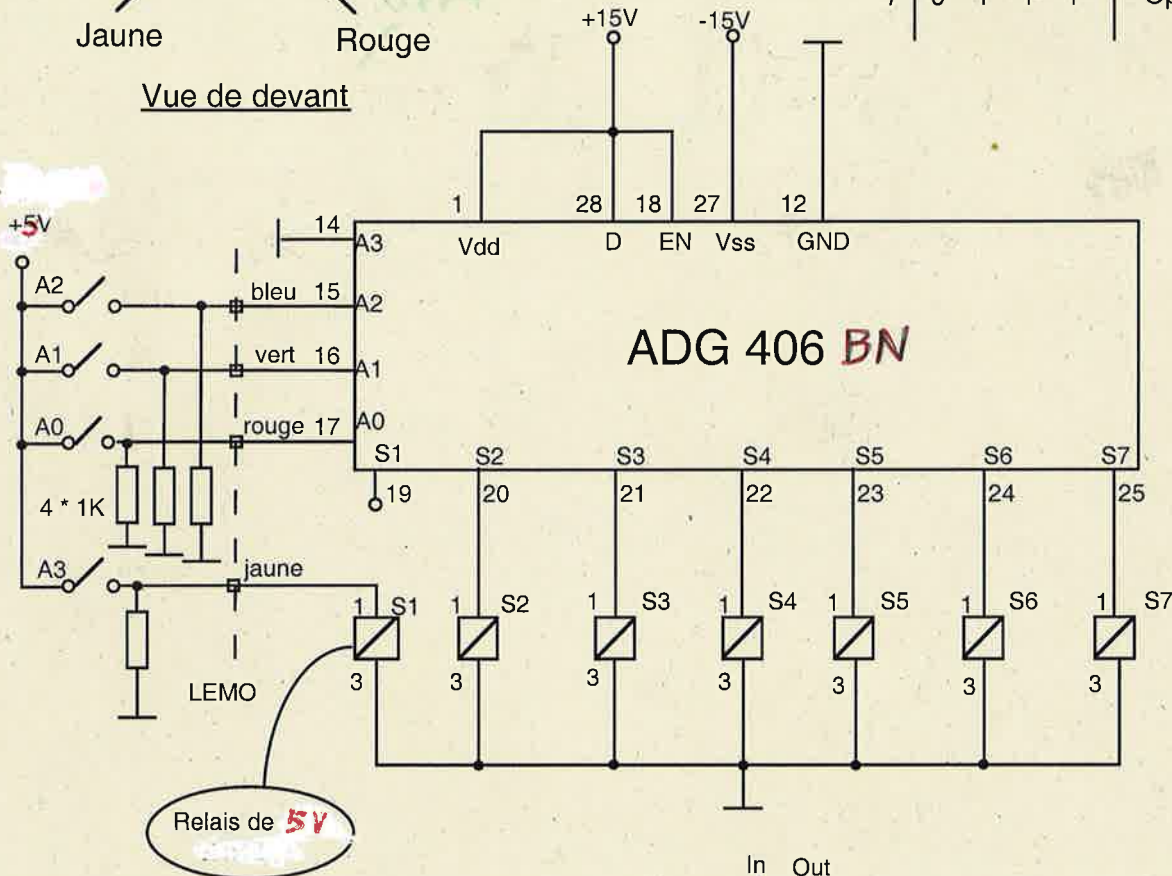


Vue de devant

Relais NAIS
TK1 - 12V



#	A3	A2	A1	A0	OUT	Relais
0	0	0	0	0	Open	—
0	1	0	0	0	Short	S1
1	0	0	0	1	10 uF	S2
2	0	0	1	0	30 uF	S3
3	0	0	1	1	0.086 uF	S4
4	0	1	0	0	0.468 uF	S5
5	0	1	0	1	0.935 uF	S6
6	0	1	1	0	2.27 uF	S7
7	0	1	1	1	Open	—



EPFL
DMX-LC

Title: charge meas. unit
Sawyer and Tower

Date:
28-11-2001

File:
Sawyer_Tower

Page: 1
Rev: 1

C Technical drawings of rectilinear precision spring

This appendix provides technical drawings of a notch type double compound rectilinear spring as discussed in Chapter 2. The design was taken from Ref. [121]. The mechanism presented in Figure C.1 was designed and manufactured as part of this work together with the Atelier de l'Institut des Matériaux at EPFL. The attached technical drawings were the foundation for technical discussions, and modifications may have been implemented without documentation.

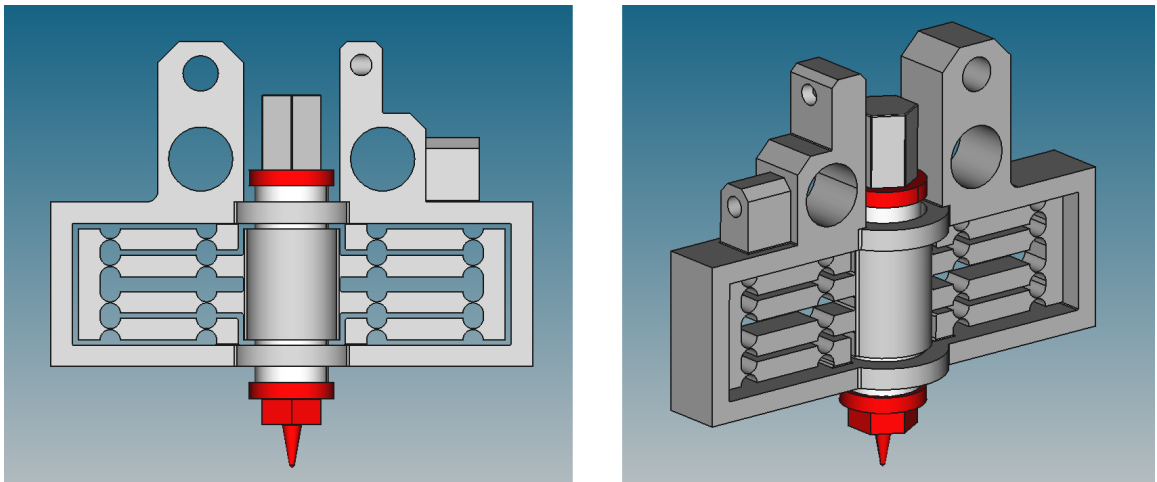
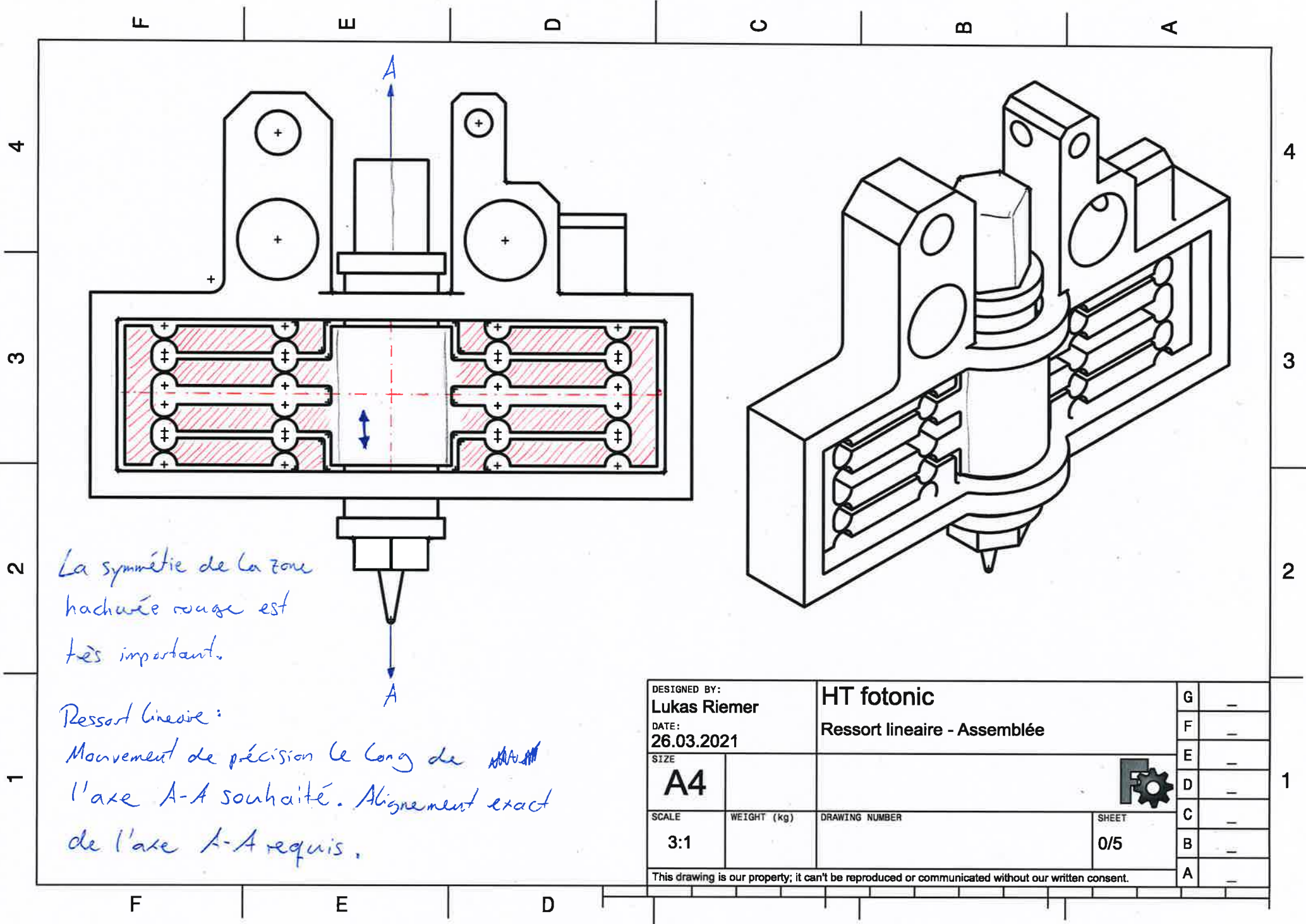



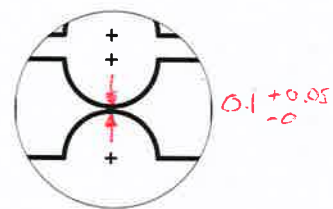
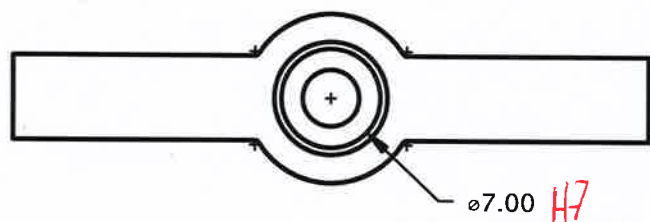
Figure C.1. Rectilinear precision spring for measurements of strain and electrical signals. (a) Front view, and (b) another view.



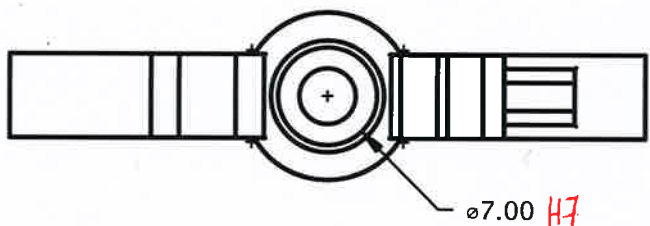
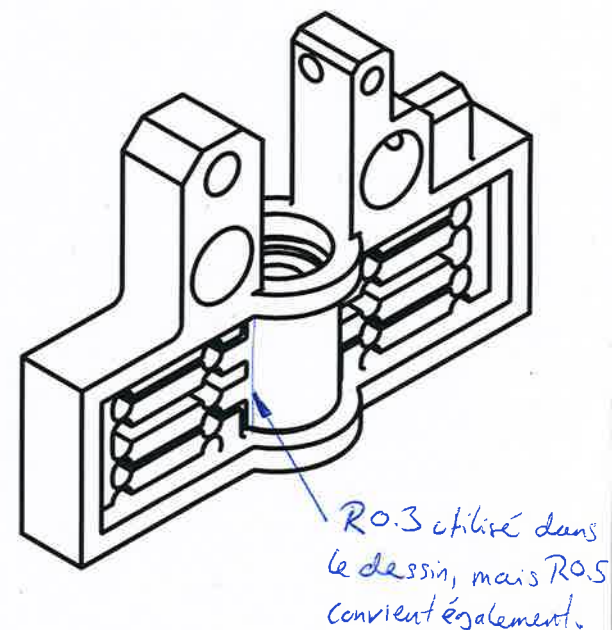
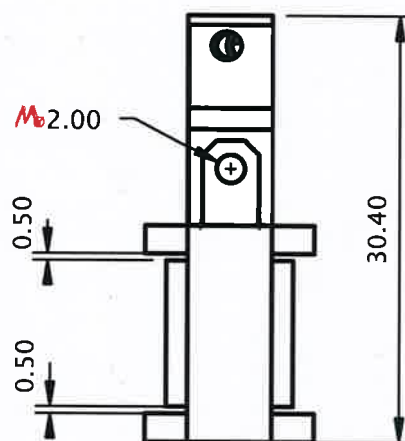
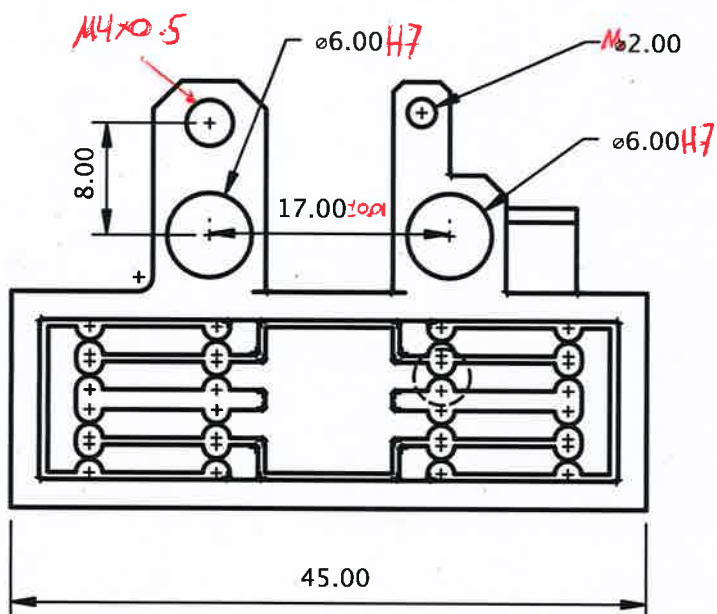
La symétrie de la zone hachurée rouge est très importante.

Ressort linéaire :
Mouvement de précision le long de l'axe A-A souhaité. Alignement exact de l'axe A-A requis.

DESIGNED BY: Lukas Riemer		HT fotonic Ressort lineaire - Assemblée		G	—	
DATE: 26.03.2021				F	—	
SIZE A4				E	—	
				D	—	
SCALE 3:1	WEIGHT (kg)	DRAWING NUMBER		C	—	
				SHEET 0/5	B	—
				This drawing is our property; it can't be reproduced or communicated without our written consent.		A



Dimensions
selon 3D!



DESIGNED BY:
Lukas Riemer
DATE:
26.03.2021

HT fonic
Ressort lineaire - Titan Grade 5

SIZE
A4

SCALE
2:1

WEIGHT (kg)
~ 15.3 g

DRAWING NUMBER
1/1

SHEET
1/5

This drawing is our property; it can't be reproduced or communicated without our written consent.

G	—
F	—
E	—
D	—
C	—
B	—
A	—

F

E

D

C

B

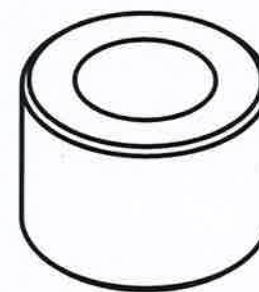
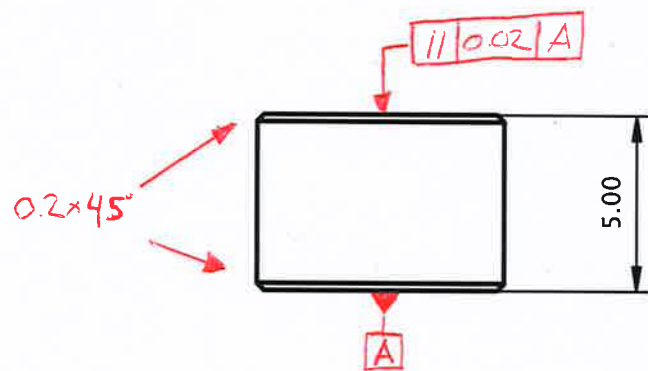
A

4

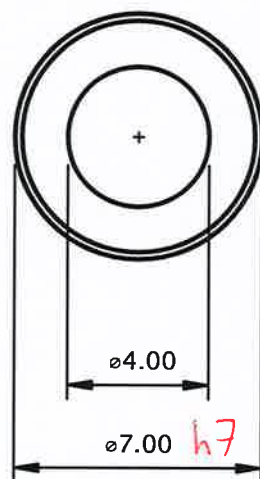
3

2

1



Tube en ceramique rectifie h7
fourni par le laboratoire (sera commandé
et livré plus tard).



DESIGNED BY:

Lukas Riemer

DATE:

23.03.2021

SIZE

A4

2x

SCALE

5:1

WEIGHT (kg)

~ 0.5 g

HT fotonic

Entroise - Alumine/ Al2O3

DRAWING NUMBER

1/1

SHEET

2/5

G

-

F

-

E

-

D

-

C

-

B

-

A

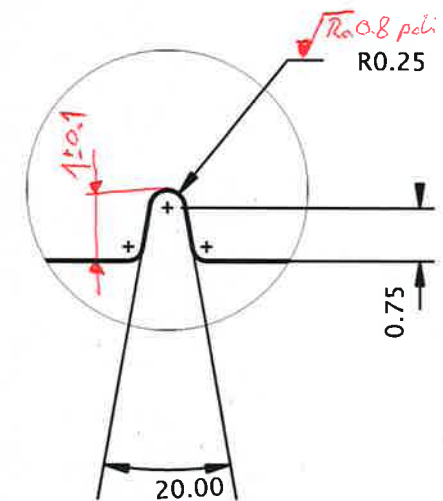
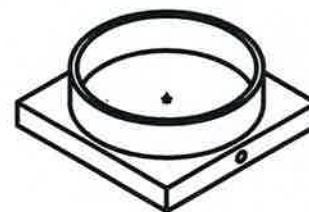
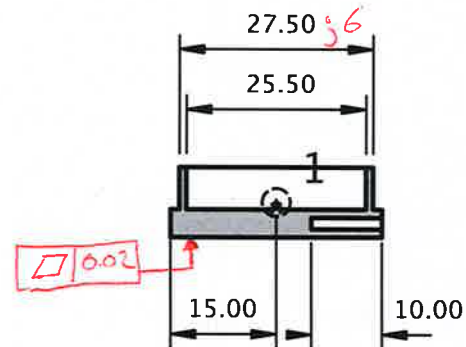
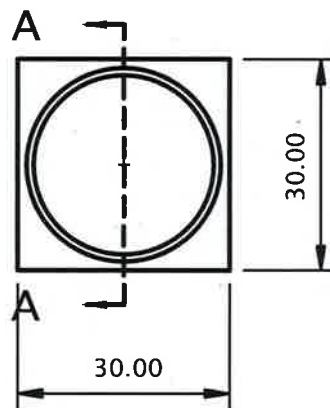
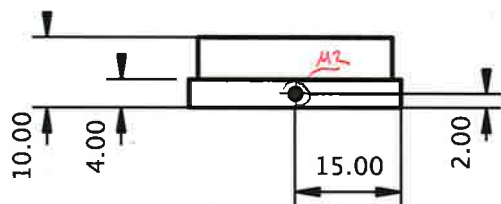
-


This drawing is our property; it can't be reproduced or communicated without our written consent.

F

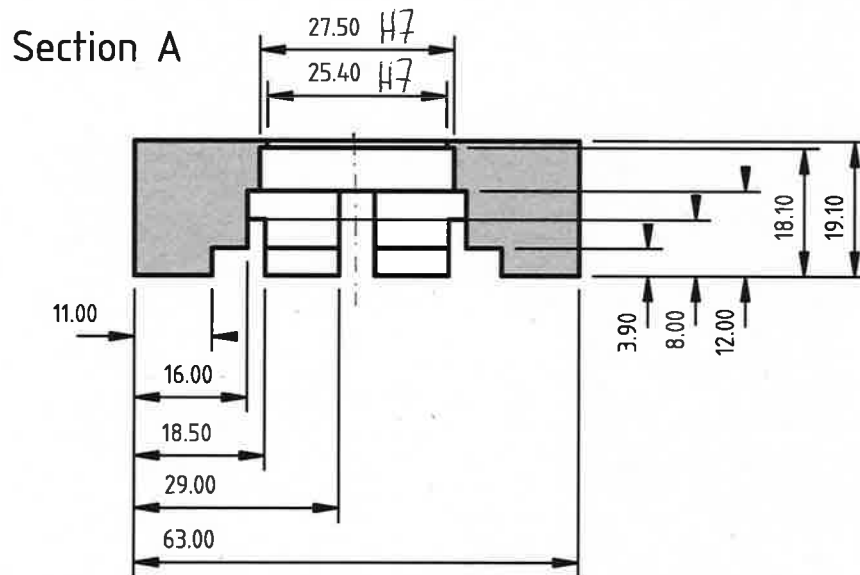
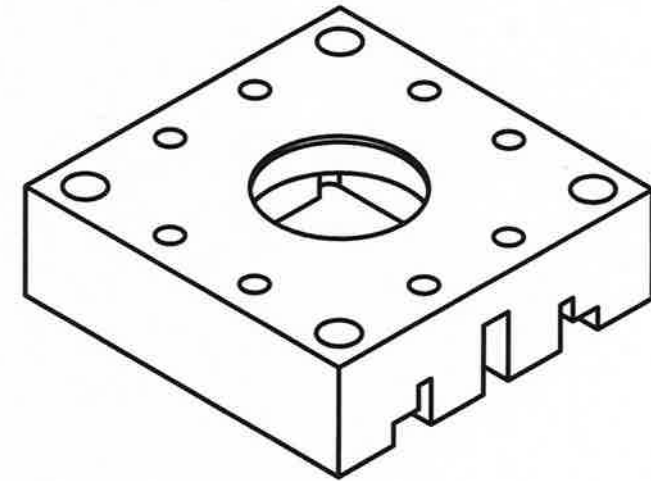
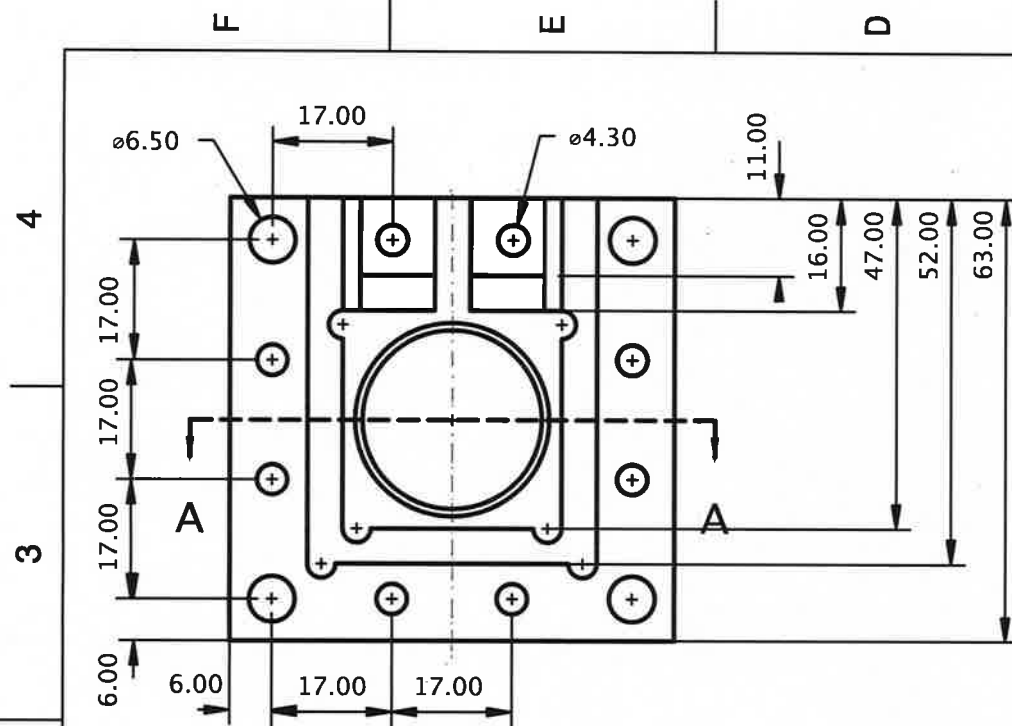
E


D



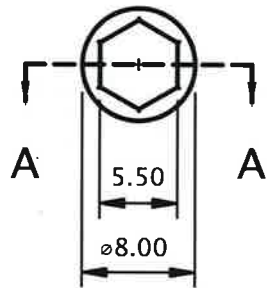
DESIGNED BY: Lukas Riemer		Sample stage HT Fotonic		G	—		
DATE: 16.06.2021				F	—		
SIZE	A4	1x	Loniton		E	—	
SCALE					1:1	D	—
WEIGHT (kg)		DRAWING NUMBER	1/1	SHEET	1/6	C	—
						B	—
This drawing is our property; it can't be reproduced or communicated without our written consent.						A	—

This drawing is our property; it can't be reproduced or communicated without our written consent.

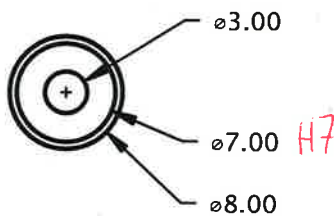
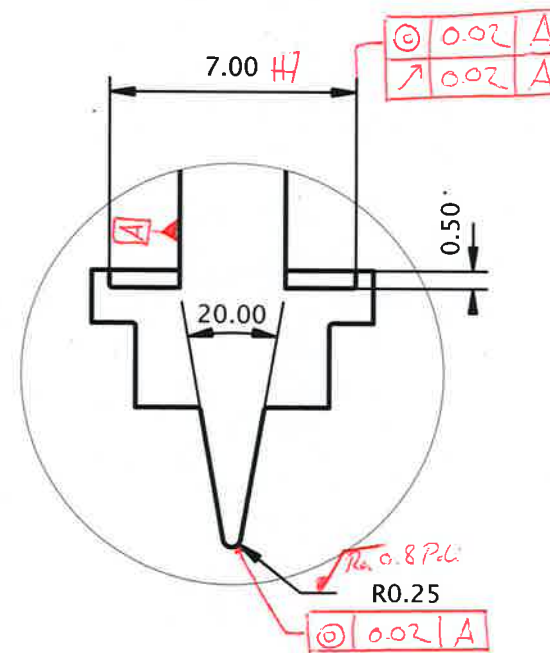
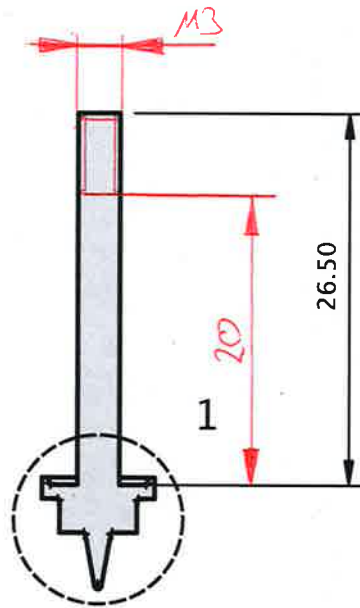
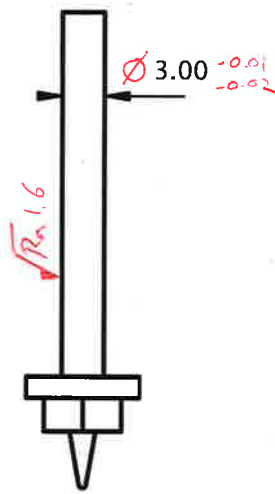


DESIGNED BY: Lukas Riemer		Square flanch HT Fotonic		G	—
DATE: 15 Juin 2021				F	—
SIZE	A4	1x	PEEK	E	—
				D	—
SCALE	WEIGHT (kg)	DRAWING NUMBER		C	—
1:1		1/1		B	—
				A	—
This drawing is our property; it can't be reproduced or communicated without our written consent.					

F E D C B A



Par clé à douille 5.5 mm. (5.5^{±0.05}?).



DESIGNED BY:
Lukas Riemer

DATE:
16.05.2021

SIZE
A4

SCALE
2:1

WEIGHT (kg)

HT fotonic

Contact de mesure

Böckler N700 XSC-M.C.N. 16-4
(fourni par Labo)

DRAWING NUMBER

1/1

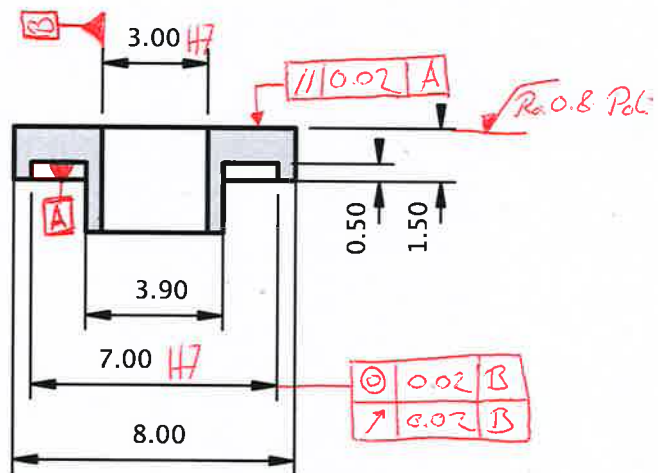
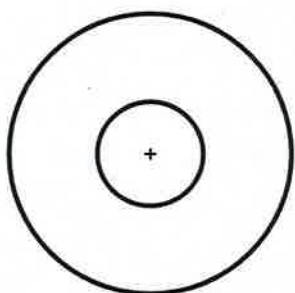
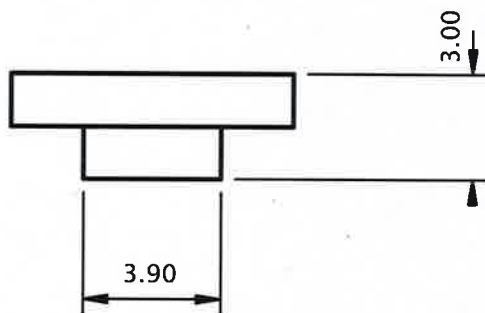
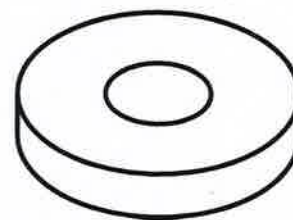
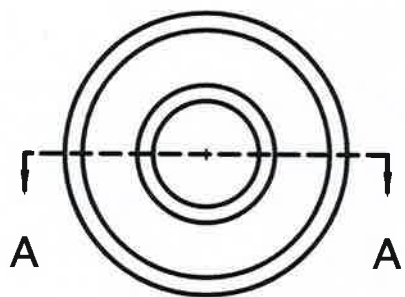
SHEET

3/6

G	—
F	—
E	—
D	—
C	—
B	—
A	—

This drawing is our property; it can't be reproduced or communicated without our written consent.

F E D



DESIGNED BY:
Lukas Riemer
DATE:
16.06.2021

HT fotonic
Disque de centrage

SIZE
A4

1x

Boehler N700 XSC-N: Cu-Nb 16-4
(fourni par Ludo)



SCALE
5:1

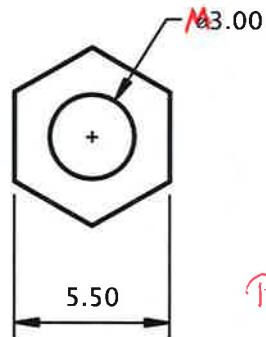
WEIGHT (kg)

DRAWING NUMBER
1/1

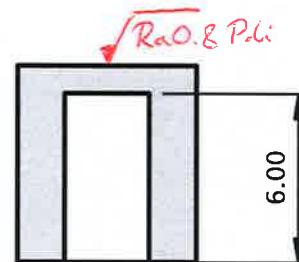
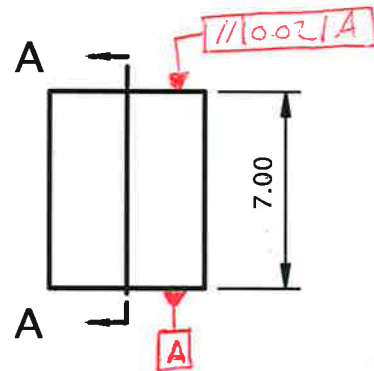
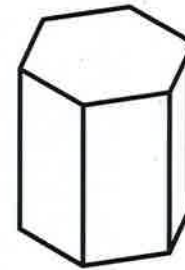
SHEET
4/6

This drawing is our property; it can't be reproduced or communicated without our written consent.

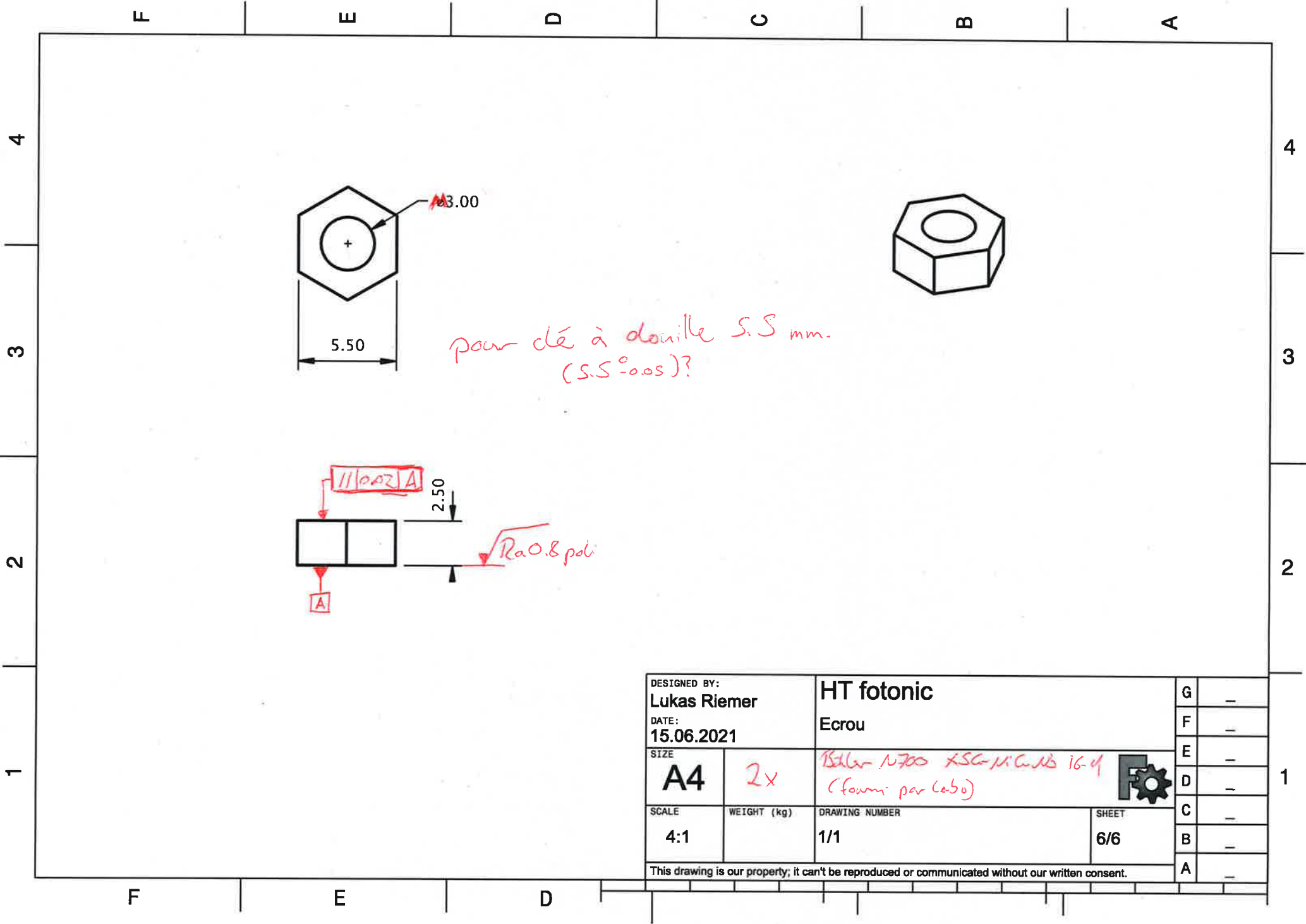
G	—
F	—
E	—
D	—
C	—
B	—
A	—



pour dé à douille 5.5 mm.
(SS 90.05?).



DESIGNED BY: Lukas Riemer		HT fotonic		G	-
DATE: 15.06.2021		Miroir		F	-
SIZE A4	2x	<i>Buchse M700 XSC-Mi CnV 16-4</i> <i>(fourni par Labo)</i>		E	-
				D	-
SCALE 4:1	WEIGHT (kg)	DRAWING NUMBER 1/1	SHEET 5/6	C	-
This drawing is our property; it can't be reproduced or communicated without our written consent.				B	-
				A	-



DESIGNED BY: Lukas Riemer		HT ftonic		G	-
DATE: 15.06.2021		Ecrou		F	-
SIZE A4	2x	Böhrer N700 XSG-MC-MB 16-4 (fourni par Co.50)		E	-
				D	-
SCALE 4:1	WEIGHT (kg)	DRAWING NUMBER 1/1	SHEET 6/6	C	-
This drawing is our property; it can't be reproduced or communicated without our written consent.				B	-
				A	-

D Circuit schematics for nonlinear polarization measurements

In this appendix the calculation of harmonic components of polarization as discussed in Chapter 2 is derived. For the harmonic analysis of the polarization response, a sinusoidal voltage signal is applied to a sample that is connected in series with a resistor. The resulting voltage across the resistor is analyzed and the polarization response is calculated. The equivalent circuit for this measurement is depicted in Figure D.1

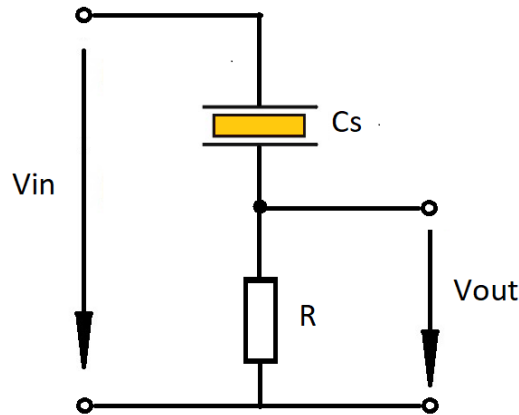


Figure D.1. Equivalent circuit of the experimental configuration for measurements of polarization harmonics.

The displacement current is defined as

$$i(t) = A\epsilon_0 \frac{\partial E}{\partial t} + A \frac{\partial P}{\partial t}. \quad (D.1)$$

Since changes in polarization usually dominate the dielectric response in ferroelectric materials³²⁵ the current through the sample i_S can be written in good approximation to

$$i_S(t) = A \frac{\partial P}{\partial t}. \quad (D.2)$$

Appendix D. Circuit schematics for nonlinear polarization measurements

To perform the partial differentiation the polarization is expressed in the form of a Fourier series

$$P(t) = P_{\text{const}} + \sum_{n=1}^{\infty} [P'^{(n)} \sin(n\omega t) + P''^{(n)} \cos(n\omega t)], \quad (\text{D.3})$$

where P_{const} is a constant, n the order of the harmonic, $P'^{(n)}$ is the real part and $P''^{(n)}$ the imaginary part of polarization. The combination of Equation (D.2) and Equation (D.3) yields

$$i_S(t) = A \sum_{n=1}^{\infty} [n\omega P'^{(n)} \cos(n\omega t) + n\omega P''^{(n)} \sin(n\omega t)]. \quad (\text{D.4})$$

According to Kirchhoff's current law, the current through the resistor i_R and the sample are equal

$$i_S(t) = i_R(t) = \frac{V_{\text{OUT}}(t)}{R}. \quad (\text{D.5})$$

The amplitudes and phase angle θ of the harmonic components of V_{OUT} with respect to the driving field can directly be measured with a lock-in amplifier.

$$V_{\text{OUT}}(t) = \sum_{n=1}^{\infty} [V'^{(n)} \sin(n\omega t) \cos(\theta) + V''^{(n)} \cos(n\omega t) \sin(\theta)]. \quad (\text{D.6})$$

Comparing Equation (D.3) and Equation (D.6) a relation between the polarization harmonics and experimentally measured voltages can be derived

$$P'^{(n)} = \frac{V'^{(n)}_{\text{OUT}}}{An\omega R}, \quad (\text{D.7})$$

and

$$P''^{(n)} = \frac{V''^{(n)}_{\text{OUT}}}{An\omega R}. \quad (\text{D.8})$$

E Supplementary data for Chapter 3

This appendix provides supplementary material for Chapter 3.

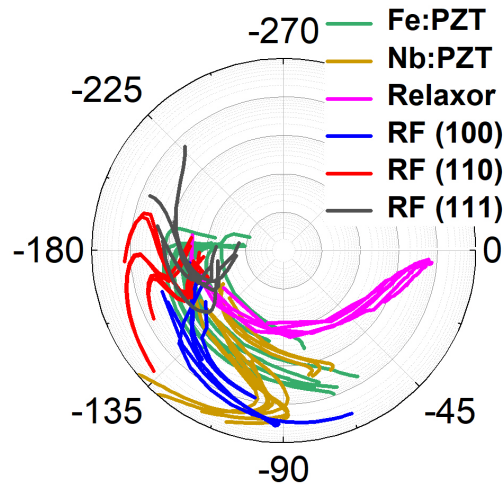


Figure E.1. Phasor diagram for commonly observed phase angles of the third harmonic of polarization, $\delta^{(3)}$: 0° , indicating response saturation; -90° , indicating Rayleigh behavior; -180° , indicating polarization response of most non-ferroelectric dielectrics, hard ferroelectrics, relaxors and many ferroelectrics at very weak fields; -270° , indicating polarization loop pinching and hard ferroelectrics (experimentally one usually observes -240°). RF stands for relaxor ferroelectrics: PZN-4.5PT, PZN-7PT, PMN-28PT, PMN-33PT. Relaxor: PMN ceramic, PMN crystal with [100]pc orientation. Nb:PZT stands for 1 at.% Nb doped PZT ceramics with Zr/Ti ratio: 42/58, 52/48, 58/42. Fe:PZT stands for 1 at.% Fe-doped PZT with Zr/Ti ratio: 42/58, 52/48, 58/42.

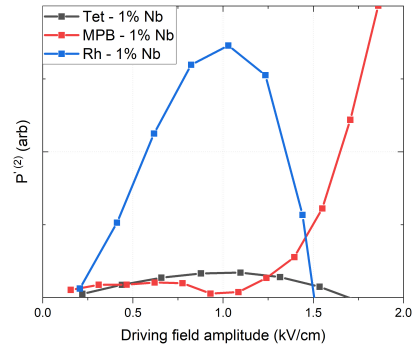


Figure E.2. Anomalies in the amplitude of the real part of the second harmonic in polarization, $P^{(2)}$ as a function of driving field amplitude E_0 of Nb-doped lead zirconate titanate ceramics with tetragonal, morphotropic, and rhombohedral composition.

F Supplementary data for Chapter 4

This appendix provides supplementary material for Chapter 4.

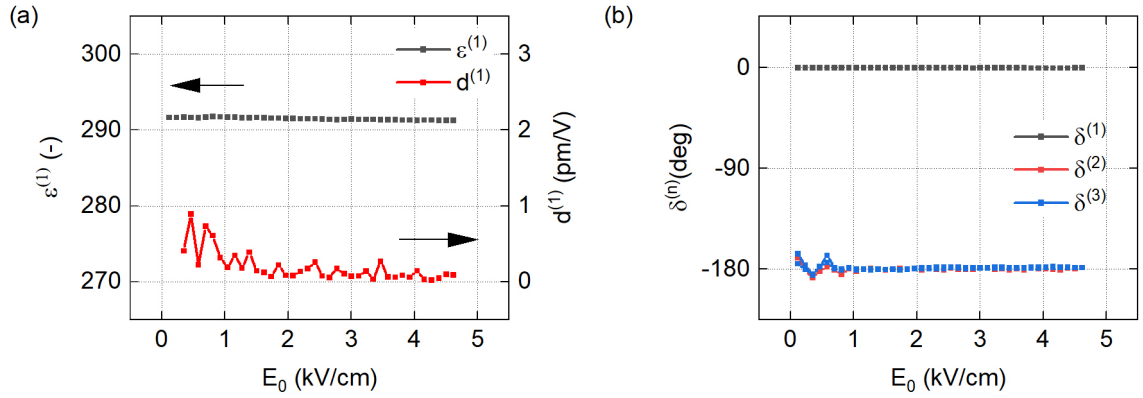


Figure F.1. Dielectric nonlinearities as a function as a function of driving field amplitude, E_0 , of [001] strontium titanate single crystal. (a) First harmonic permittivity, $\epsilon^{(1)}$, and first harmonic piezoelectric coefficient, $d^{(1)}$. (b) Phase angle of polarization $\delta^{(n)}$.

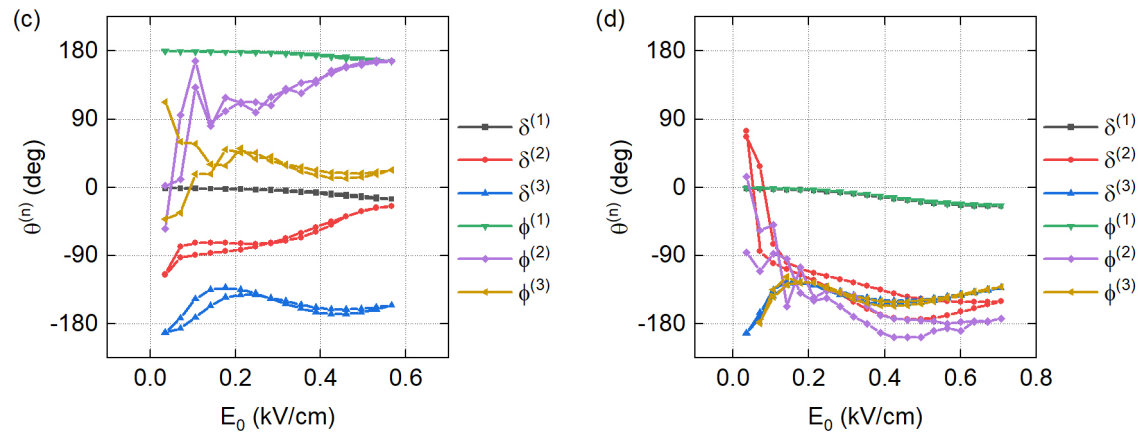


Figure F.2. Orientation dependence of harmonic phase angle, ω , for poled [111]-PMN-28PT crystal. (a) A-side, and (b) B-side.

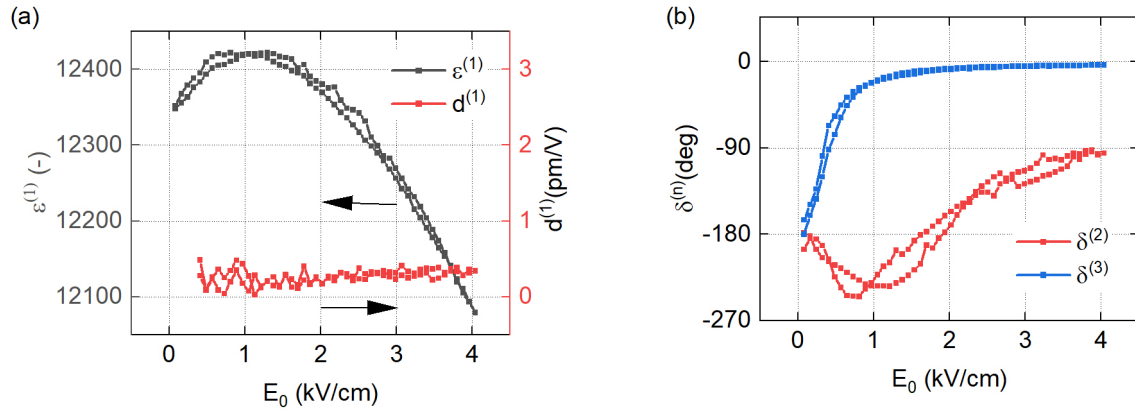


Figure E.3. Dielectric nonlinearities as a function of driving field amplitude, E_0 , of lead magnesium niobate crystal PMN-B. (a) First harmonic permittivity, $\epsilon^{(1)}$, and first harmonic piezoelectric coefficient, $d^{(1)}$. (b) Second and third phase angle of polarization, $\delta^{(2)}$ and $\delta^{(3)}$, respectively.

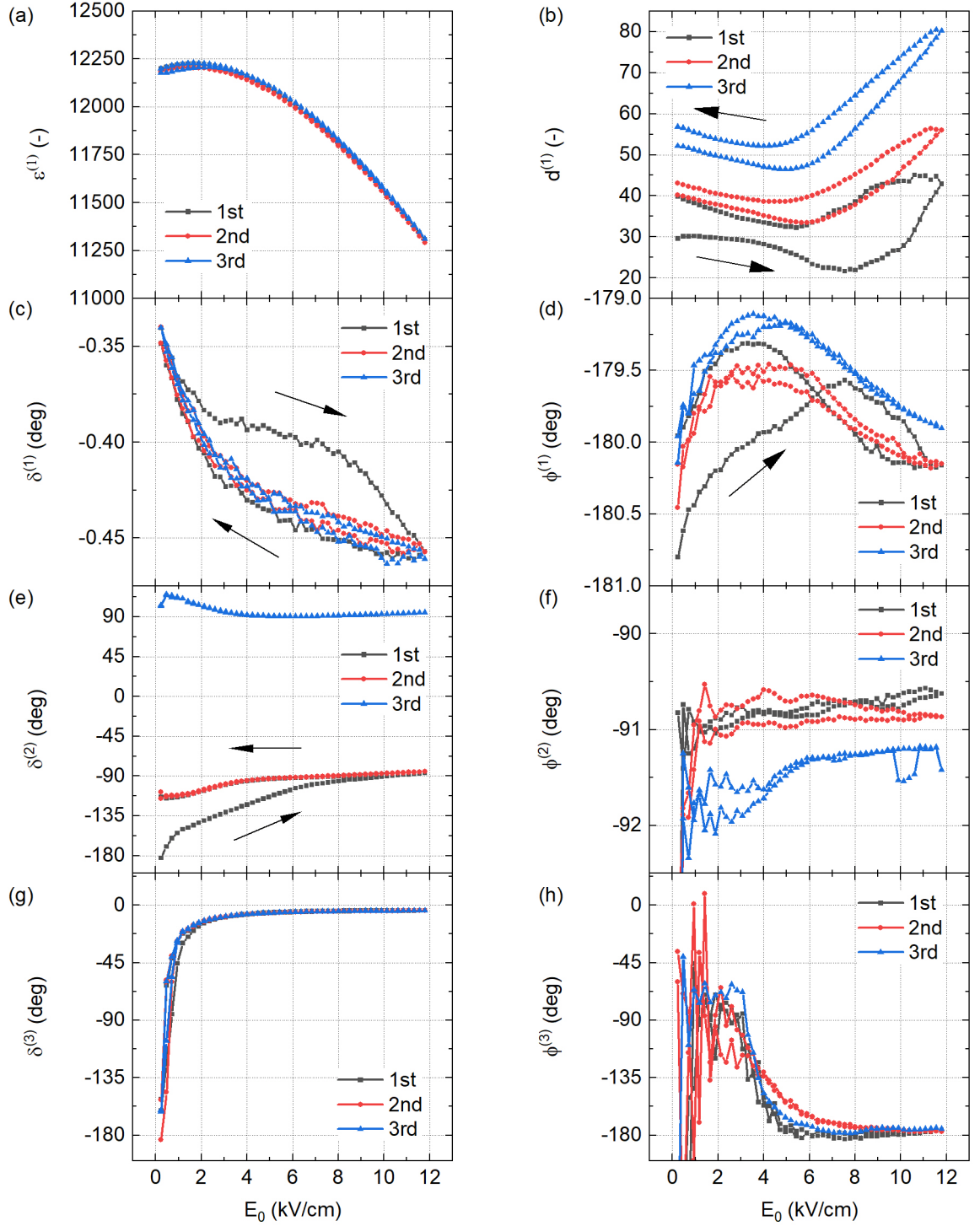


Figure E4. Dielectric and electromechanical nonlinearities as a function of driving field amplitude, E_0 , of lead magnesium niobate PMN ceramic for three subsequent measurements. (a) First harmonic permittivity, $\epsilon^{(1)}$, (b) first harmonic piezoelectric coefficient, $d^{(1)}$, (c) first harmonic phase angle of polarization, $\delta^{(1)}$, (d) first harmonic phase angle of strain, $\phi^{(1)}$, (e) second harmonic phase angle of polarization, $\delta^{(2)}$, (f) second harmonic phase angle of strain, $\phi^{(2)}$, (g) third harmonic phase angle of polarization, $\delta^{(3)}$, and (h) third harmonic phase angle of strain, $\phi^{(3)}$.

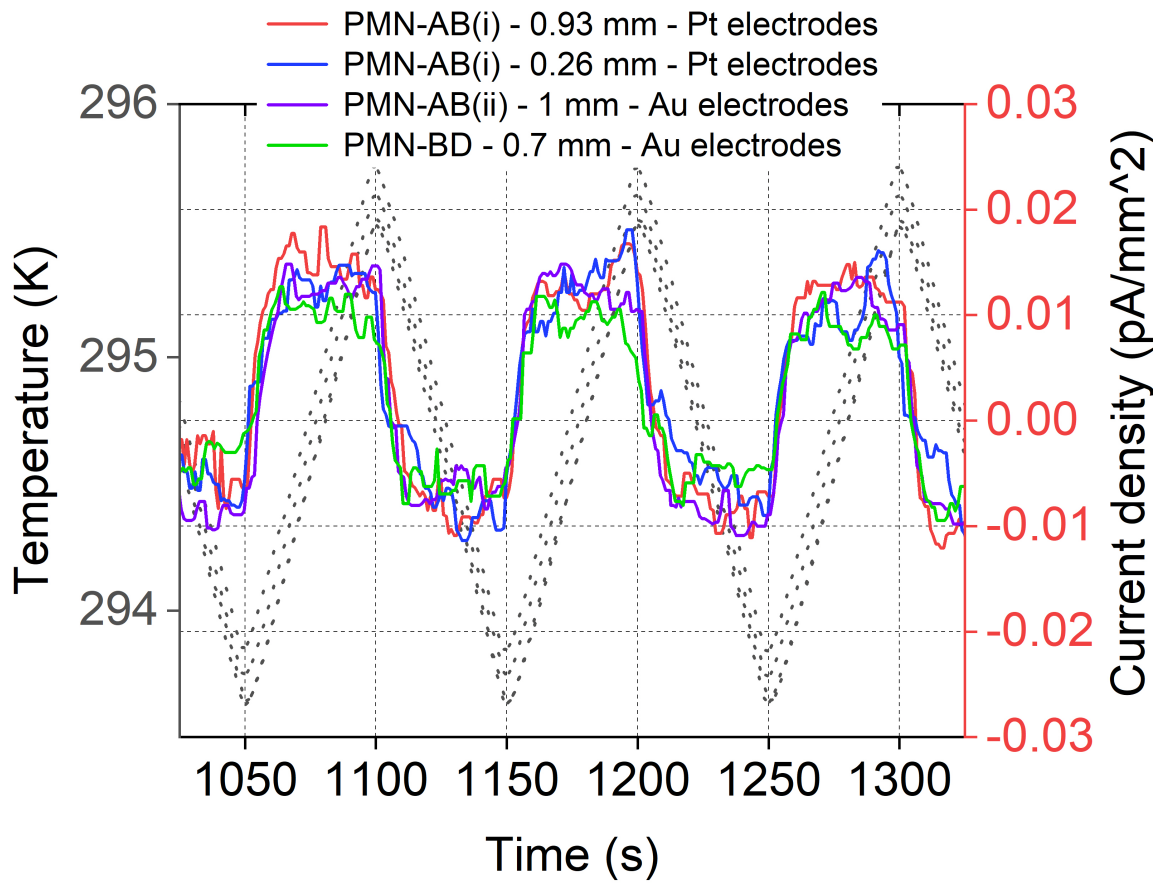


Figure E.5. Dynamic pyroelectric measurements for [001]-PMN-crystals of different origin, electrode material, thicknesses, and surface finishing. A triangular temperature, T , modulation as a function of time, t , results in a square wave current density, j_p .

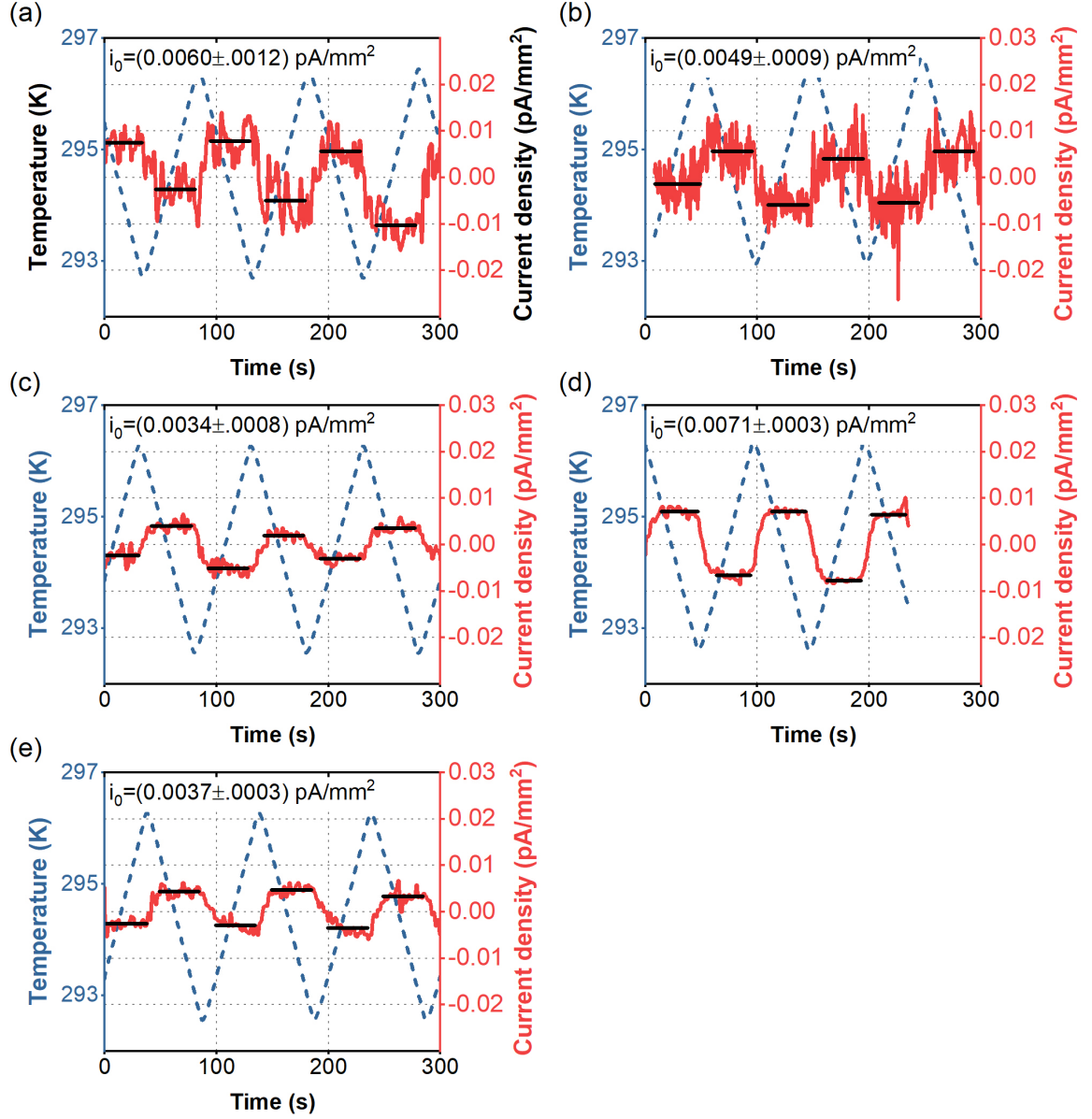


Figure E.6. Pyroelectric response of $\text{Pb}(\text{Mg}_{1/3}\text{Nb}_{2/3})\text{O}_3$ (PMN) crystals and ceramics. Pyroelectric current density amplitudes are fitted as indicated by black lines. The extracted average current density amplitudes, j_p , are indicated in the top right corner of each graph. Ceramics were annealed at 773 K before measurements. (a) Pristine (001)-cut PMN-A crystal ($2.2 \times 2.3 \times 1.0$ mm³), (b) pristine (001)-cut PMN-B crystal ($2.8 \times 2.0 \times 0.7$ mm³), (c) annealed PMN ceramic ($3.6 \times 3.2 \times 0.5$ mm³), (d) annealed PMN ceramic ($8.7 \times 3.6 \times 0.7$ mm³), and (e) annealed PMN ceramic ($3.6 \times 3.5 \times 1.5$ mm³).

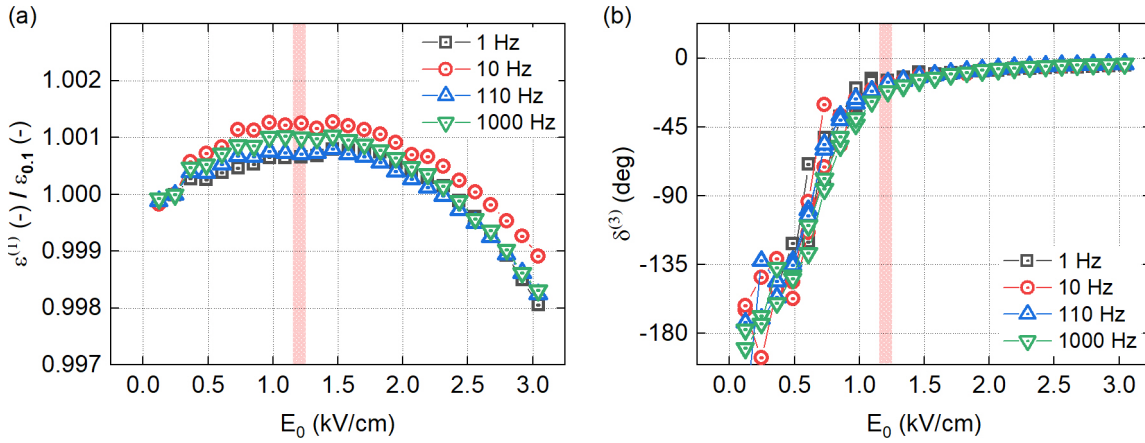


Figure E.7. Dielectric nonlinearities as a function of driving field amplitude, E_0 , of lead magnesium niobate crystal for various frequencies. (a) First harmonic permittivity normalized to the first measurement point, i.e. the value at a driving field amplitude $E_0 \approx 0.1$ kV/cm ($\epsilon_{0,1}$), and (b) third harmonic phase angle of polarization, $\delta^{(3)}$.

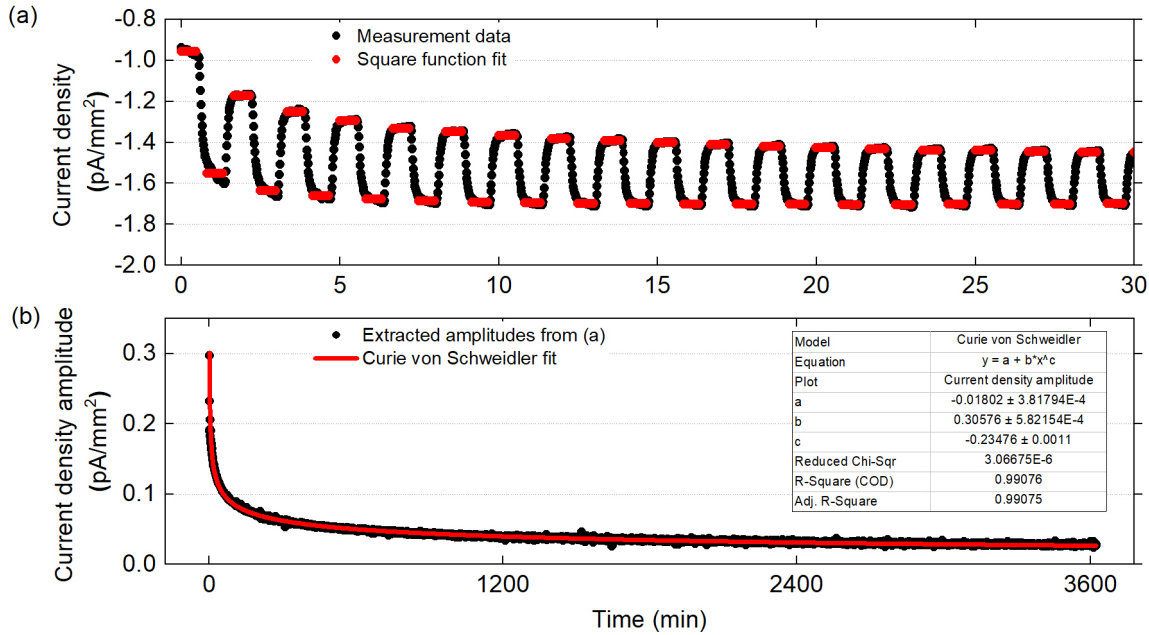


Figure E.8. Decay of pyroelectric response of [001]-PMN-A crystal after poling at 10 kV/cm for 20 minutes. (a) First 30 minutes after poling. The mean pyroelectric current density, $j_{p,m}$, for intervals of increasing and decreasing temperature are indicated in red. (b) Pyroelectric current density amplitudes, $j_{0,m}$, are calculated as the absolute value of half the difference between adjacent current levels: $j_{0,m} = \text{abs}(j_{p,m} - j_{p,m+1})/2$. The temporal evolution of $j_{0,m}$ can be fit by the Curie von Schweidler law resulting in a power exponent $n_{CVS} = -0.235 \pm 0.001$ in good agreement with results obtained from PFM measurements.²²³

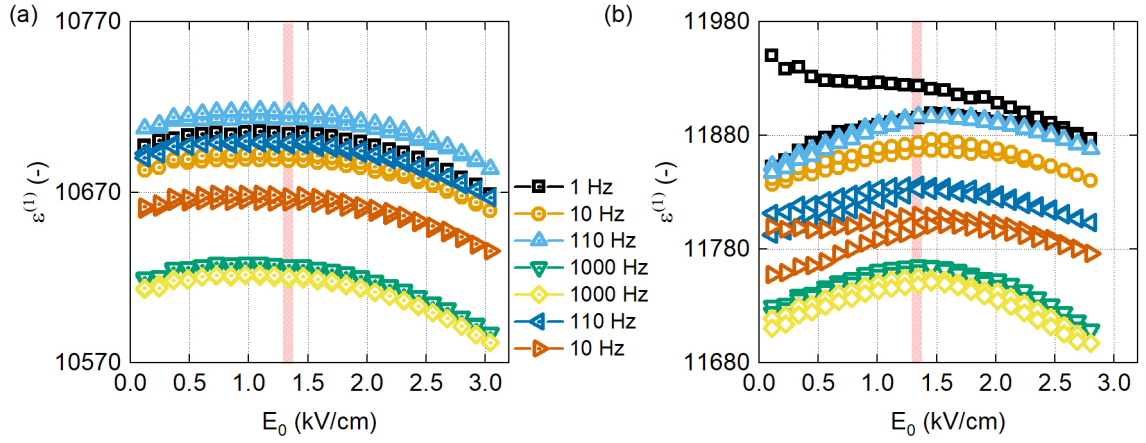


Figure F.9. Sequential measurements of the first harmonic permittivity, $\epsilon^{(1)}$, as a function of driving field amplitude, E_0 , for a PMN crystal and ceramic performed in the order presented in the figure legend. The experimentally determined field for polarization reversal $E_M = (1.35 \pm 0.05)$ kV/cm is indicated as red hatched area. The maximum dielectric permittivity is obtained for a field amplitude E_0 of approximately $E_M = (1.50 \pm 0.25)$ kV/cm. (a) PMN-A crystal, and (b) ceramic with dimensions $(3.6 \times 3.3 \times 1.0)$ mm³

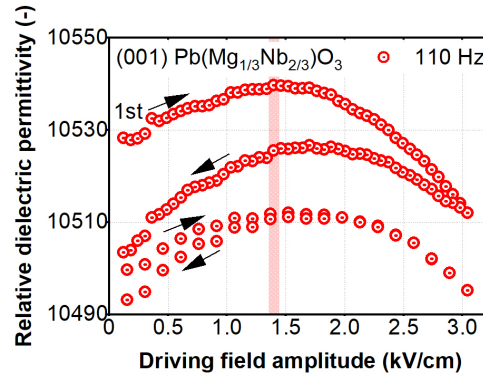


Figure F.10. Two subsequent measurements with different measurement parameters of the field dependent relative dielectric permittivity $[\epsilon_r(E_0)]$ for a PMN-A crystal. Arrows indicate the direction of field cycling starting with increasing amplitude. The experimentally determined field for polarization reversal is indicated as red hatched area. During the first measurement the maximum in dielectric permittivity increases from ≈ 1.4 kV/cm in the ascending branch to ≈ 1.7 kV/cm in the descending branch. An increase of the field amplitude increment in the second measurement cycle significantly reduces the dielectric hysteresis and confines it to field amplitudes below the maximum of permittivity. The previous increase of the field of maximum permittivity appears to be persistent.

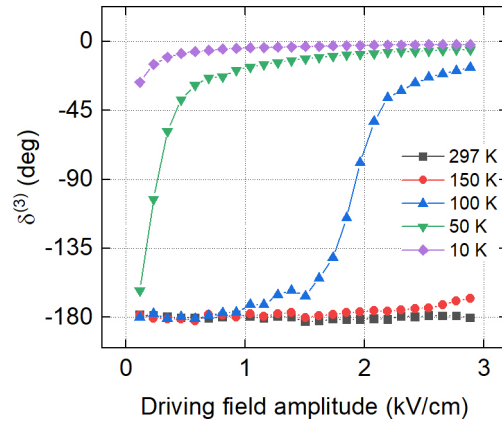


Figure F.11. Third harmonic phase angle of polarization, $\delta^{(3)}$, for [001] strontium titanate single crystal at cryogenic temperatures.

G Derivation of Bucci-Fieschi equation

In the following, the current density expected during thermally stimulated depolarization of orientational polarisation with activation energy E_a and relaxation time τ is derived following ref [238].

The temporal evolution of polarization $P(t)$ as a function of time t under the influence of a polarizing electric field E_p can be described as

$$P(t) = P_e \left[1 - \exp\left(-\frac{t}{\tau}\right) \right], \quad (\text{G.1})$$

where τ_0 is the dipolar relaxation time and P_e is the equilibrium polarization. In the intermediate electric-field range, before saturation occurs, P_e may be described by the Langevin function:

$$P_e = \frac{s N_d p_\mu^2 \kappa E_p}{k_B T_p}, \quad (\text{G.2})$$

Where s is a geometrical factor, N_d the concentration of dipoles, p_μ their dipole moment, k_B is Boltzmann's constant and κE_p the local electric field. Under the assumption that the relaxation times for polarization and depolarization are identical, the decay of the polarized equilibrium state after removal of the polarizing field is

$$P(t) = P_e \exp\left(-\frac{t}{\tau}\right), \quad (\text{G.3})$$

resulting in a depolarization current density j_D of

$$j_D = -\frac{dP(t)}{dt}. \quad (\text{G.4})$$

To account for simultaneously changing time and temperature T , the constant heating rate q is introduced as

$$q = \frac{dT}{dt}, \quad (\text{G.5})$$

and Equation (G.3) is transformed into

$$P(t) = P_e \left[\exp\left(-\int_0^t \frac{dt}{\tau}\right) \right]. \quad (\text{G.6})$$

Appendix G. Derivation of Bucci-Fieschi equation

Three postulations follow. First, Equation (G.6) is valid for changing temperature. Second, the equilibrium polarization is reached during the poling procedure at a given poling temperature T_p . Third, the temperature dependence of the τ_0 follows the Arrhenius equation

$$\tau = \tau_0 \exp\left(\frac{E_a}{k_B T}\right), \quad (\text{G.7})$$

where τ_0 is the the relaxation time at infinite temperature and E_a is the activation energy. For these conditions, the expected current density during thermally stimulated depolarization experiments with linear increasing temperature is

$$j_D(T) = \frac{P_e(T_p)}{\tau_0} \exp\left(-\frac{E_a}{k_B T}\right) \exp\left[-\frac{1}{q\tau_0} \int_{T_0}^T \exp\left(-\frac{E_a}{k_B T'}\right) dT'\right], \quad (\text{G.8})$$

where T_0 is the initial temperature. Equation (G.8) describes an asymmetric peak, which is dominated by the first exponential in the initial rise, before the exponential with the integral term dominates and suppress the response. Therefore, during the initial rise of a peak related to dipolar relaxation the second exponential can be approximated to unity and E_a determined based on²⁴¹

$$\ln j_D(T) = \text{const.} - \frac{E_a}{k_B T}. \quad (\text{G.9})$$

An expression for the maximum temperature of current density peaks can be derived by differentiating Eq. (G.8) with respect to temperature:

$$T_m = \left[\frac{E_a}{k_B} q \tau_0 \exp\left(\frac{E_a}{k_B T_m}\right) \right]^{1/2}. \quad (\text{G.10})$$

For a single ionic species moving under the influence of an electric field the total charge released during depolarization Q_D can be approximated to²⁵³

$$Q_D \approx P = 2avNqt_p \exp\left(-\frac{E_a}{k_B T}\right) \sinh\left(\frac{qaE_p}{2kT_p}\right) = Q_0 \sinh\left(\frac{qaE_p}{2kT_p}\right), \quad (\text{G.11})$$

where P is polarization, a jump distance, v is the attempt to escape frequency, N is the ion density, q is the ionic charge, H is the potential barrier height.

For a discrete set of trap states without retrapping the thermally stimulated current $I_D(T)$ takes the form of²⁴²

$$I_D(T) = n_0 \tau e \mu \nu \exp\left(-\frac{E_a}{k_B T}\right) \exp\left[-\frac{s}{q} \int_{T_0}^T \exp\left(-\frac{E}{k_B T'}\right) dT'\right], \quad (\text{G.12})$$

where n_0 is the initial density of filled trap states μ is the electron mobility.

H Supplementary data for Chapter 5

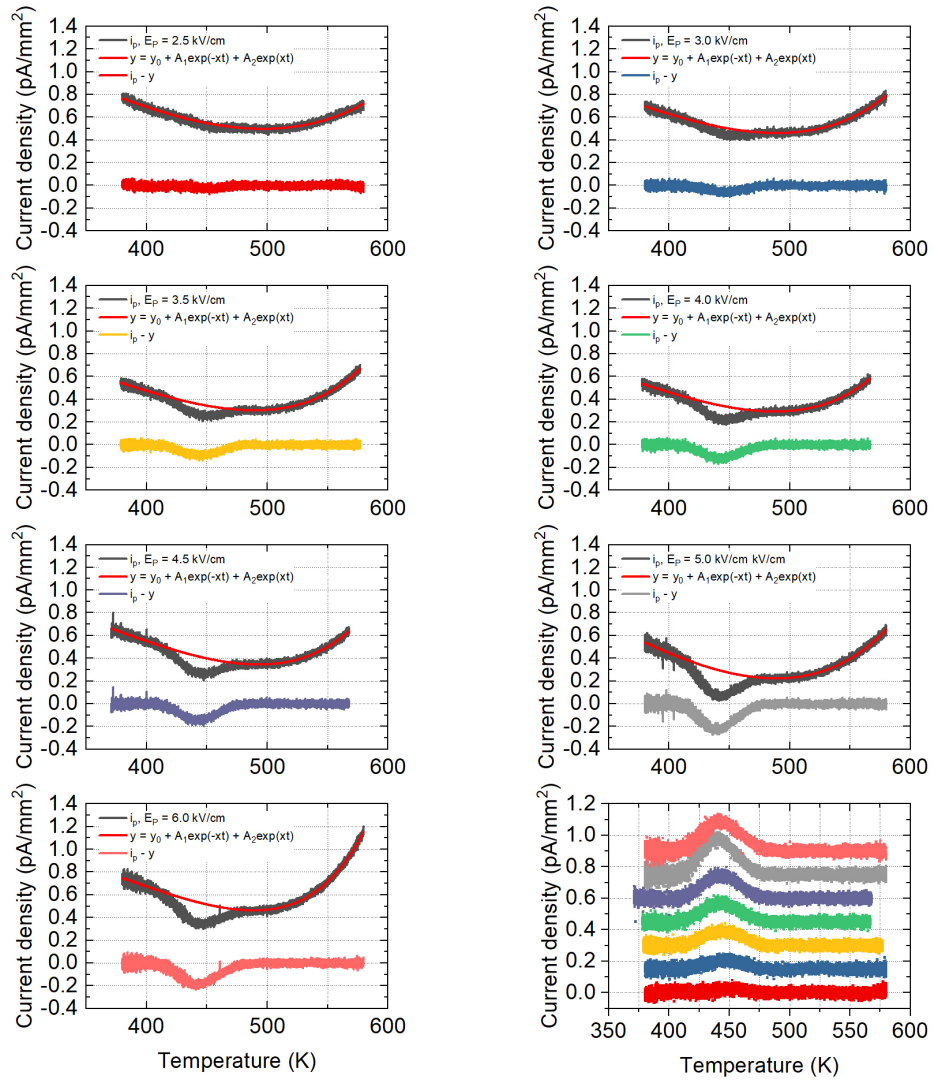


Figure H.1. Fit procedure of TSC response of [001]-PMN-A crystal.

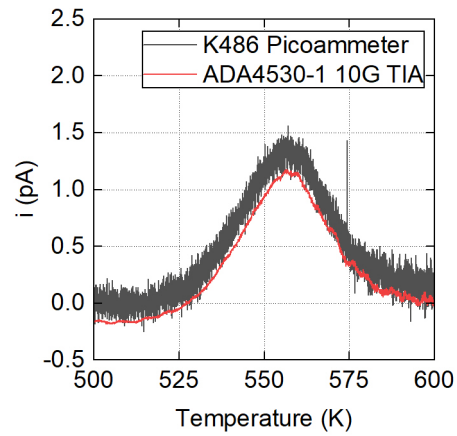


Figure H.2. Comparison between Keithley 486 Picoammeter and custom-made device based on the electrometer amplifier ADA4530-1 from Analog Devices. The current response of the ADA4530-1 has been inverted for comparison.

I Approximation of stored energy in polarized and in strained crystals

PMN crystals and ceramics where poled electrically and elastically. In an attempt to compare both poling procedures the electrically and elastically stored energy of polarized and strained samples is derived for linear material parameters under isothermal conditions and reversible processes following Ref.[136].

The energy stored in a polarized crystal, W_E , is:

$$dW_E = \nu E_i dD_i, \quad (I.1)$$

where ν is the volume of the crystal, E_i is the electric field and D_i is the displacement field. Combining this equation with the definition of D_i :

$$D_i = \epsilon_0 \epsilon_{ij} E_j, \quad (I.2)$$

with vacuum permittivity ϵ_0 and relative dielectric permittivity ϵ_{ij} , results in:

$$dW_E = \epsilon_0 \epsilon_{ij} E_i dE_j. \quad (I.3)$$

Integration of Equation (I.3) yields the final result for the electrically stored energy in a polarized crystal:

$$W_E = \frac{1}{2} \epsilon_0 \epsilon_{ij} E_i E_j. \quad (I.4)$$

The energy stored in a strained crystal, W_x , can be calculated analogous:

$$dW_x = \sigma_{ij} dx_{ij}, \quad (I.5)$$

with stress σ_{ij} and strain x_{ij} . The combination with Hooke's law,

$$\sigma_{ij} = C_{ijkl} x_{kl}, \quad (I.6)$$

Appendix I. Approximation of stored energy in polarized and in strained crystals

where $c_{ij} = c_{ji}$ is the stiffness, results in:

$$W_x = \frac{1}{2} C_{ijkl} x_{ij} x_{kl}. \quad (I.7)$$

Integration of Eq. (I.7) and simplification due to symmetry properties of the stiffness tensor ($c_{ij} = c_{ji}$) yields:

$$W_x = \frac{1}{2} C_{ijkl} x_{ij} x_{kl}. \quad (I.8)$$

Setting Equation (I.8) equal to Equation (I.4), $W_x = W_E$, results in:

$$C_{ijkl} x_{ij} x_{kl} = \epsilon_0 \epsilon_{ij} E_i E_j \quad (I.9)$$

When comparing the electrical stored energy in a crystal with plate capacitor geometry, where only one component of the electric field is applied along the (100)-axis of a cubic crystal, with the elastically stored energy stored by the same crystal for a normal force applied along an equivalent crystallographic direction, the following relation is obtained:

$$C_{1111} x_{11}^2 = \epsilon_0 \epsilon_{11} E_1^2. \quad (I.10)$$

Together with Equation (I.6) this can be written as:

$$\sigma_{11} = \sqrt{\epsilon_0 \epsilon_{11} C_{1111}} E_1 = A_c E_1. \quad (I.11)$$

For a lead magnesium niobate PMN crystal with $\epsilon \approx 10 \times 10^{-12} \frac{\text{F}}{\text{m}}$, $\epsilon_{11} \approx 1 \times 10^4$, and $C_{1111} \approx 1.5 \times 10^{11} \frac{\text{N}}{\text{m}^2}$ ^{326,327} the final results reads:

$$\sigma_{11} \approx 120 E_1. \quad (I.12)$$

This means that the electrically stored energy for a PMN crystal polarized with an electric field of $E_1 = 1 \text{ kV/cm}$ along (100)-direction is approximately equivalent to the elastically stored energy when the same crystal is strained with a normal stress of $\sigma_{11} = 12 \text{ MPa}$, under the assumption of linear, isothermal and reversible conditions.

J Estimation of flexoelectric poling efficiency

Flexoelectricity is the linear response of dielectric polarization to a strain gradient:³²⁸

$$P_l = \mu_{ijkl} \frac{\partial S_{ij}}{\partial x_k}, \quad (\text{J.1})$$

where P_l is polarization, μ_{ijkl} is the flexoelectric coefficient, S_{ij} is strain, and x_k the space coordinate. Following Ref.[329], the strain gradient for a sample in the shape of a truncated pyramid of height h with upper square face A_1 and lower square face A_2 is:

$$\frac{\partial S_{11}}{\partial x_1} = \frac{F_{11} \left(\frac{1}{A_1} - \frac{1}{A_2} \right)}{c_{1111} h}, \quad (\text{J.2})$$

According to Equation (J.1) this strain gradients results in a polarization of:

$$P_1 = \mu_{1111} \frac{\partial S_{11}}{\partial x_1} = \mu_{1111} \frac{F_{11} \left(\frac{1}{A_1} - \frac{1}{A_2} \right)}{c_{1111} h}. \quad (\text{J.3})$$

For a PMN crystal with $\mu_{1111} \approx 1 \times 10^{-3} \text{ C/m}$,^{330,331};^I $F_{11} \approx 15 \text{ N}$, $A_1 \approx 0.8 \times 2.4 \times 10^{-6} \text{ m}^2 = 1.9 \times 10^{-6} \text{ m}^2$ and $A_2 \approx 0.9 \times 2.5 \times 10^{-6} \text{ m}^2 = 2.3 \times 10^{-6} \text{ m}^2$ and height $h \approx 2.4 \times 10^{-3} \text{ m}$, $c_{1111} \approx 1.5 \times 10^{11} \text{ N/m}^2$,^{326,327} the polarization results to:

$$P_1 \approx 4 \times 10^{-4} \text{ C/m}^2. \quad (\text{J.4})$$

Dielectric polarization can be defined as:

$$P_i = (\epsilon_{ij} - 1) \epsilon_0 E_j, \quad (\text{J.5})$$

where ϵ_{ij} is the dielectric permittivity, ϵ_0 is the vacuum permittivity, and E_j is the electric field. For $\epsilon_{11} \approx 1 \times 10^4$, $\epsilon_0 \approx 1 \times 10^{-11}$, the electric field required for a polarization of $P_1 = 4 \times 10^{-5} \text{ C/m}^2$ is:

$$E_1 \approx 4 \text{ kV/m} = 4 \times 10^{-2} \text{ kV/cm}. \quad (\text{J.6})$$

^I The highest value found in the literature for μ_{1111} was taken for this approximation. It was measured for PMN ceramics with 10 at.% lead titanate.

K Supplementary data for Chapter 6

This appendix provides supplementary material for Chapter 6.

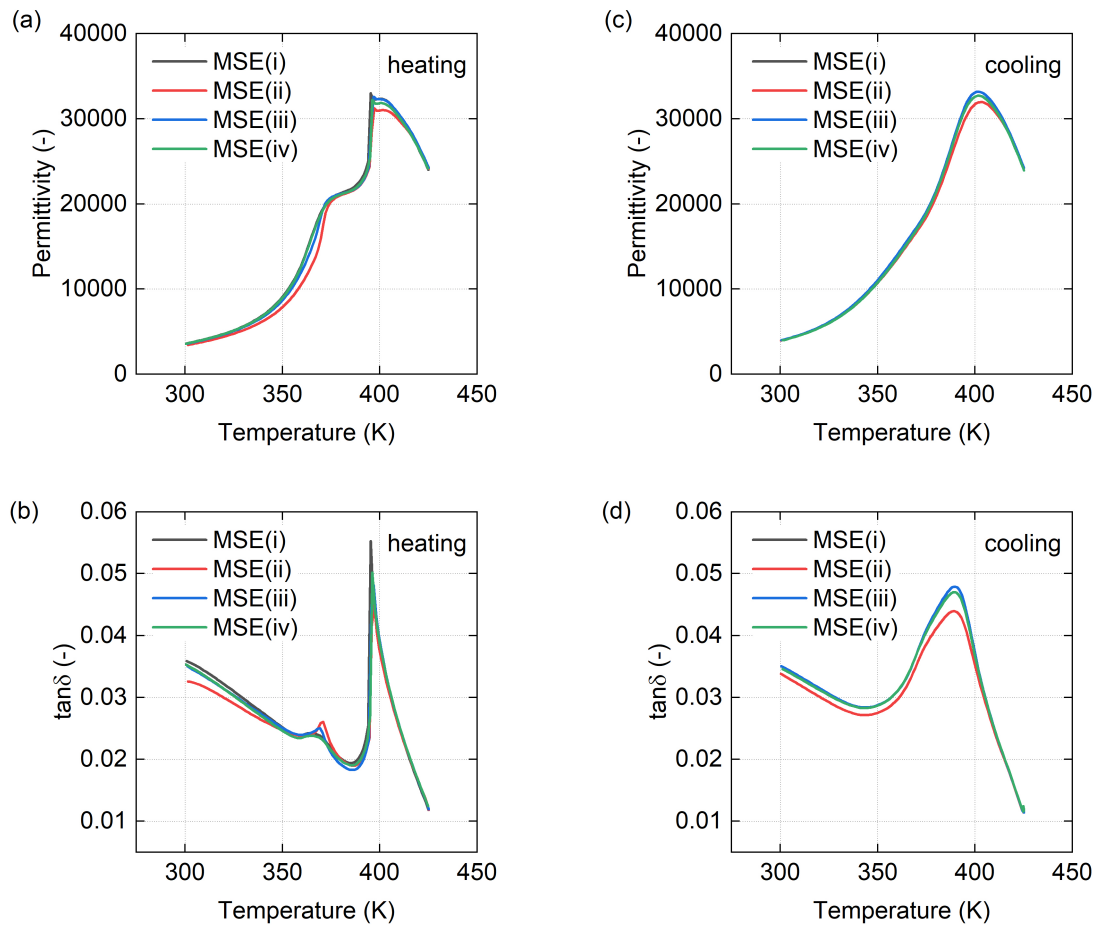


Figure K.1. Temperature dependent dielectric permittivity and loss tangent, $\tan \delta$, obtained during heating and cooling for different [001]-PMN-29PT samples. Measured during (a–b) heating, (c–d) cooling.

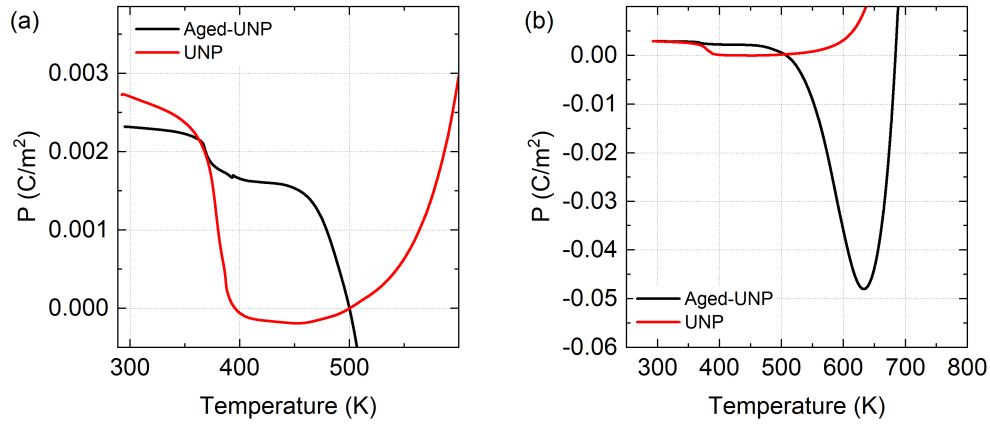


Figure K.2. Polarization for unpoled, and unpoled and then aged PMN-29PT; Sample MSE(i). (a) Similar polarization for UNP and aged-UNP is only obtained if for aged-UNP the polarization is set to zero at the coherence temperature, $T^* \approx 500$ K. (b) Aged-UNP shows large peaks around $T_B \approx 620$ K.

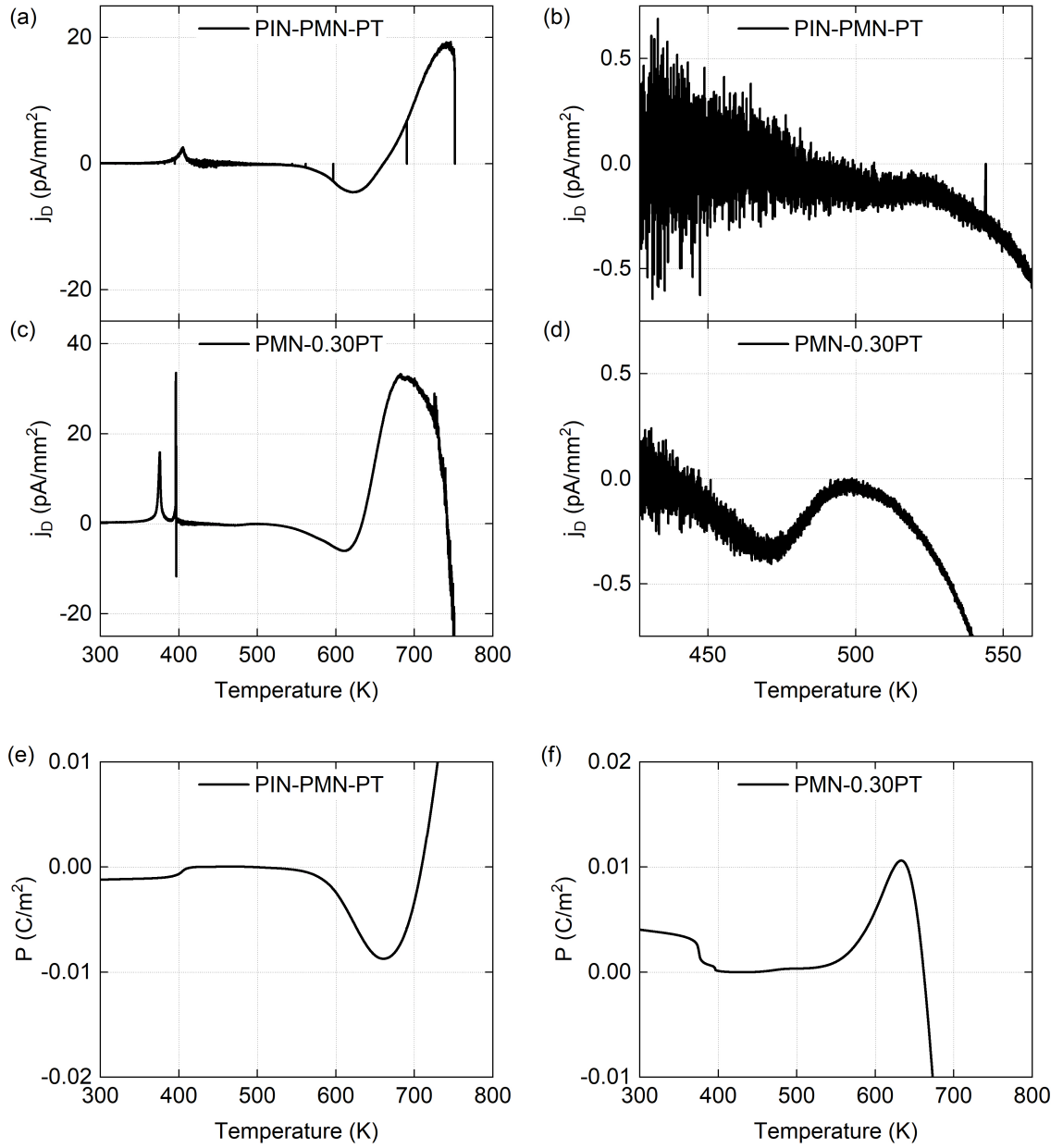


Figure K.3. Thermally stimulated current spectra and polarization for [001]- $\text{Pb}(\text{In}_{0.5}\text{Nb}_{0.5})\text{O}_3\text{-Pb}(\text{Mg}_{1/3}\text{Nb}_{2/3})\text{O}_3\text{-PbTiO}_3$ (PIN-PMN-PT), and [001]- $\text{Pb}(\text{Mg}_{1/3}\text{Nb}_{2/3})\text{O}_3\text{-PbTiO}_3$ (PMN-PT). Current density, j_D , of (a-b) PIN-PMN-PT, and (c-d) PMN-PT. Polarization, P , for (e) PIN-PMN-PT, and (f) PMN-PT.

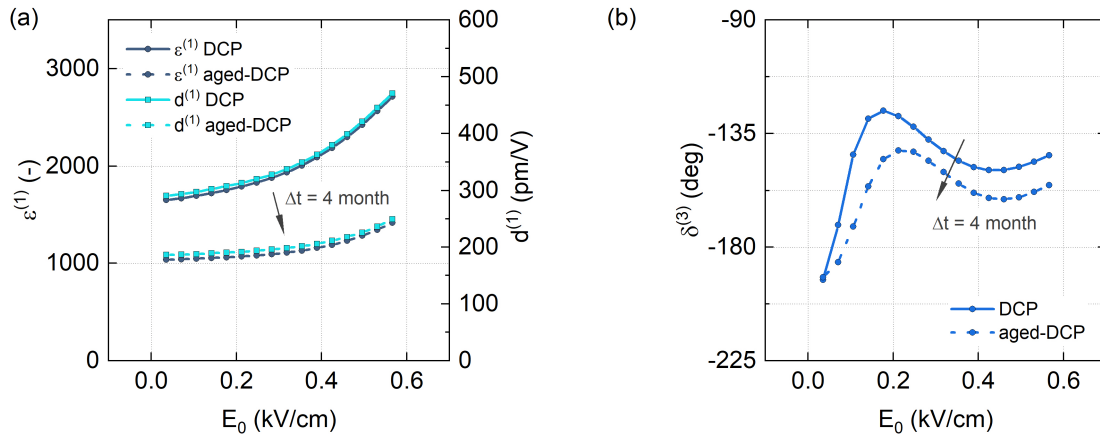


Figure K.4. Aging of direct current (electric field) polarized [111]-PMN-28PT single crystal. The sample was polarized with 5 kV/cm for 20 min at 393 K and then cooled with applied field to ambient temperatures. (a) First harmonic permittivity, $\epsilon^{(1)}$, and first harmonic piezoelectric coefficient, $d^{(1)}$, and (b) third harmonic phase angle of polarization, $\delta^{(3)}$, measured immediately after direct current poling, DCP, and after four month of aging at ambient temperatures, DCP-aged.

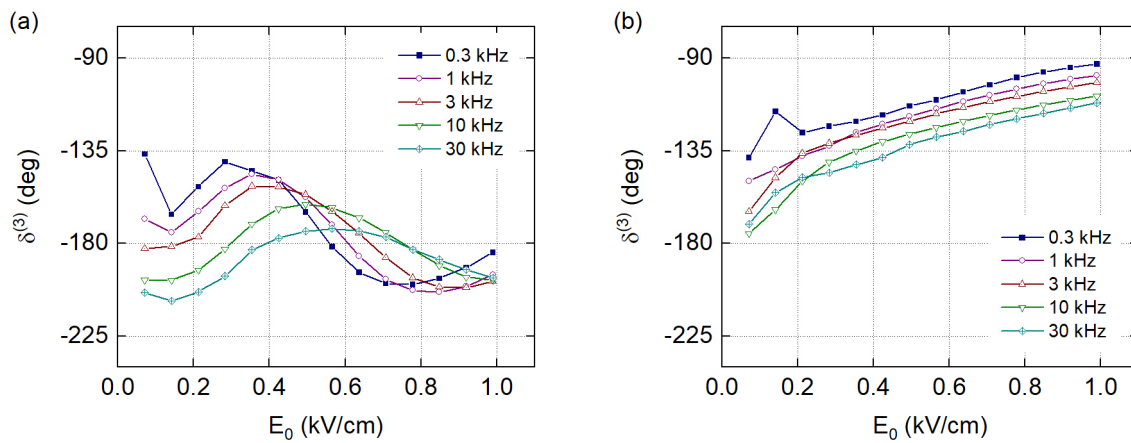


Figure K.5. Third harmonic phase angle of polarization, $\delta^{(3)}$ for various driving field frequencies of direct current polarized PMN-28PT. (a) [111]-cut, and (b) [001]-cut crystal.

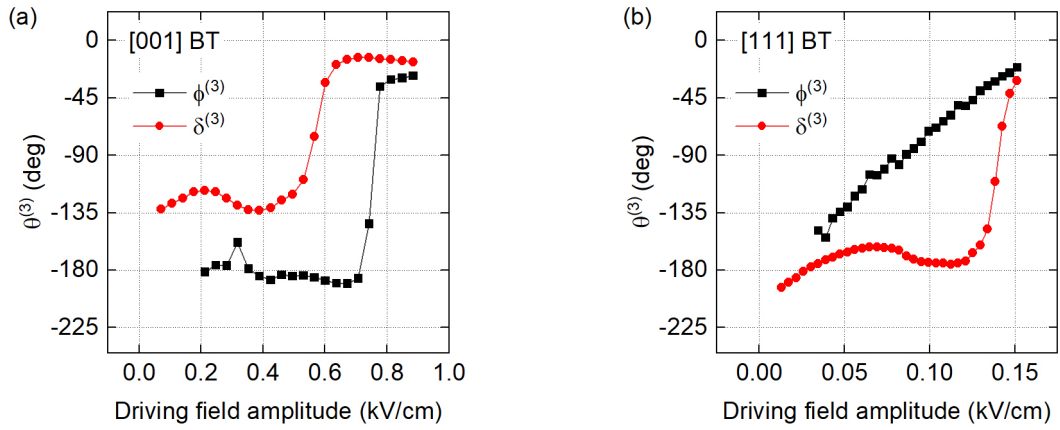


Figure K.6. Third harmonic phase angle or polarization, $\delta^{(3)}$, and strain, x , for barium titanate, BT, single crystals. (a) [001]-cut, and (b) [111]-cut.

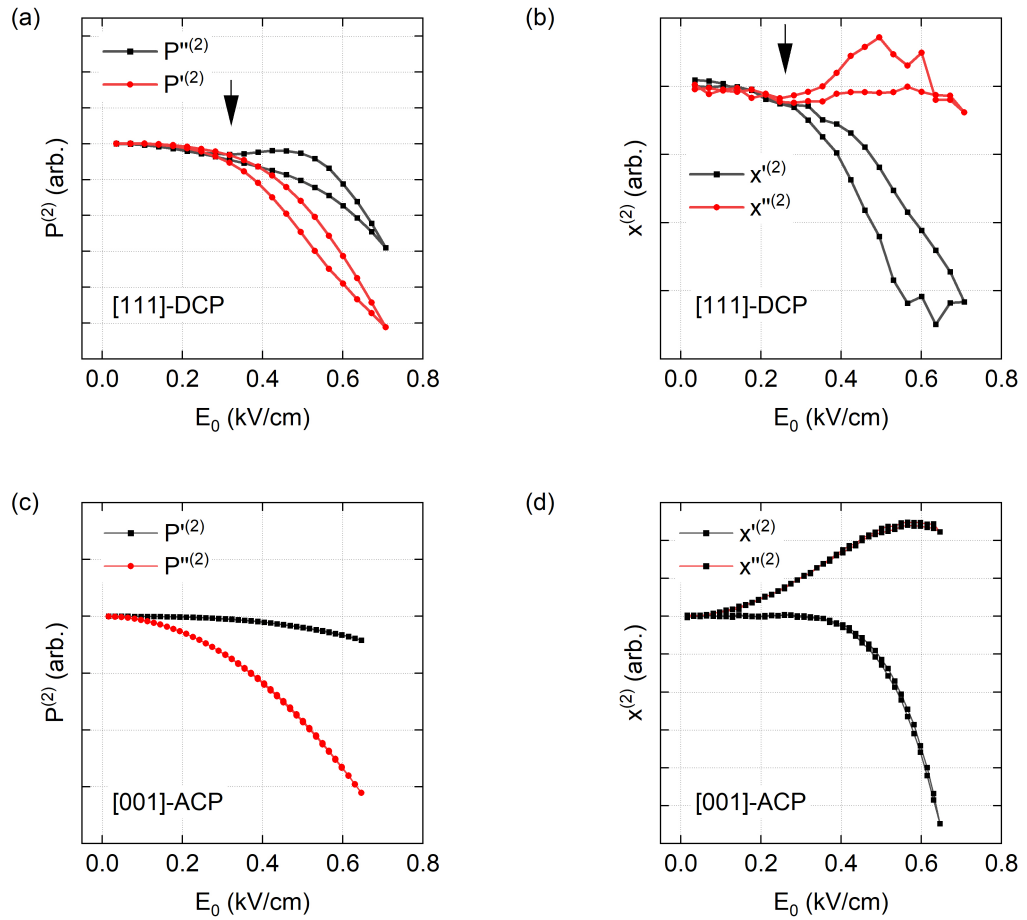


Figure K.7. Second harmonic of polarization, $P^{(2)}$, and strain, $x^{(2)}$, for direct current poled [111]-PMN-28PT. (a) Real, $P'^{(2)}$, and imaginary part, $P''^{(2)}$, of polarization and, (b) real, $x'^{(2)}$, and imaginary part, $x''^{(2)}$, of strain. Anomalies are indicated by vertical black arrows.

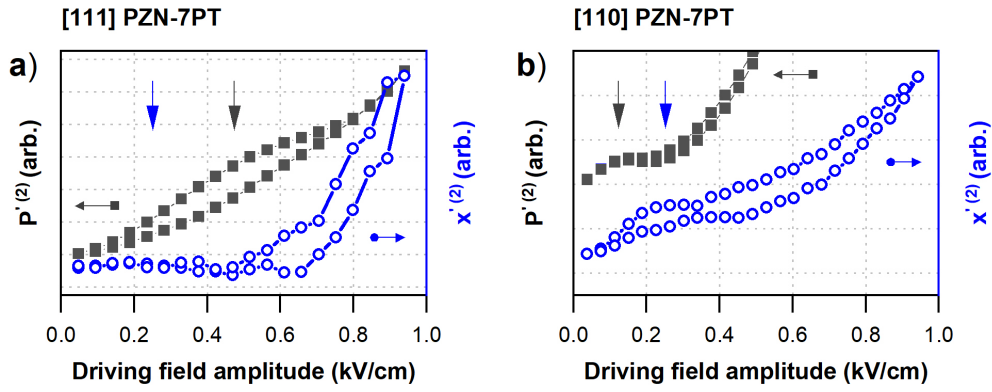


Figure K.8. Real part of the second harmonic of polarization and strain of 0.93 Pb(Zn_{1/3}Nb_{2/3})–0.07 PbTiO₃ (PZN-7PT) crystals. (a) Poled along the [111]- and (b) [011]-directions. Anomalies in the polarization and strain response are indicated as vertical black and blue arrows, respectively. They are interpreted as switching of electro-mechanically active substructures within ferroic domains.

Bibliography

- ¹A. A. Bokov and Z.-G. Ye, “Dielectric relaxation in relaxor ferroelectrics”, [Journal of Advanced Dielectrics](#) **02**, 1241010 (2012).
- ²R. D. Shannon and C. T. Prewitt, “Effective ionic radii in oxides and fluorides”, en, [Acta Crystallographica Section B: Structural Crystallography and Crystal Chemistry](#) **25**, Number: 5 Publisher: International Union of Crystallography, 925–946 (1969).
- ³P. Bonneau, P. Garnier, G. Calvarin, E. Husson, J. R. Gavarri, A. W. Hewat, and A. Morell, “X-ray and neutron diffraction studies of the diffuse phase transition in $\text{PbMg}_{1/3}\text{Nb}_{2/3}\text{O}_3$ ceramics”, [Journal of Solid State Chemistry](#) **91**, 350–361 (1991).
- ⁴P. Bonneau, P. Garnier, E. Husson, and A. Morell, “Structural study of PMN ceramics by X-ray diffraction between 297 and 1023 K”, [Materials Research Bulletin](#) **24**, 201–206 (1989).
- ⁵N. de Mathan, E. Husson, G. Calvarin, and A. Morell, “Structural study of a poled $\text{PbMg}_{1/3}\text{Nb}_{2/3}\text{O}_3$ ceramic at low temperature”, [Materials Research Bulletin](#) **26**, 1167–1172 (1991).
- ⁶S. Vakhrushev, A. Nabereznov, S. K. Sinha, Y. P. Feng, and T. Egami, “Synchrotron X-ray scattering study of lead magnoniobate relaxor ferroelectric crystals”, [Journal of Physics and Chemistry of Solids, Proceeding of the 3rd Williamsburg Workshop on Fundamental Experiments on Ferroelectrics](#) **57**, 1517–1523 (1996).
- ⁷K. Hirota, Z.-G. Ye, S. Wakimoto, P. M. Gehring, and G. Shirane, “Neutron diffuse scattering from polar nanoregions in the relaxor $\text{PbMg}_{1/3}\text{Nb}_{2/3}\text{O}_3$ ”, [Physical Review B](#) **65**, 104105 (2002).
- ⁸N. Takesue, Y. Fujii, and H. You, “X-ray diffuse scattering study on ionic-pair displacement correlations in relaxor lead magnesium niobate”, [Physical Review B](#) **64**, 184112 (2001).
- ⁹G. Xu, G. Shirane, J. R. D. Copley, and P. M. Gehring, “Neutron elastic diffuse scattering study of $\text{PbMg}_{1/3}\text{Nb}_{2/3}\text{O}_3$ ”, [Physical Review B](#) **69**, Publisher: American Physical Society, 064112 (2004).
- ¹⁰M. Eremenko, V. Krayzman, A. Bosak, H. Y. Playford, K. W. Chapman, J. C. Woicik, B. Ravel, and I. Levin, “Local atomic order and hierarchical polar nanoregions in a classical relaxor ferroelectric”, [Nature Communications](#) **10**, 2728 (2019).
- ¹¹S. Prosandeev, S. Prokhorenko, Y. Nahas, A. Al-Barakaty, L. Bellaiche, P. Gemeiner, D. Wang, A. A. Bokov, Z.-G. Ye, and B. Dkhil, “Evidence for Goldstone-like and Higgs-like structural modes in the model $\text{PbMg}_{1/3}\text{Nb}_{2/3}\text{O}_3$ relaxor ferroelectric”, [Physical Review B](#) **102**, 104110 (2020).
- ¹²G. Xu, Z. Zhong, H. Hiraka, and G. Shirane, “Three-dimensional mapping of diffuse scattering in $\text{Pb}(\text{Zn}_{1/3}\text{Nb}_{2/3})\text{O}_3 - x\text{PbTiO}_3$ ”, [Physical Review B](#) **70**, 174109 (2004).

Bibliography

- ¹³R. Blinc, V. Laguta, and B. Zalar, “Field cooled and zero field cooled ^{207}Pb NMR and the local structure of relaxor $\text{PbMg}_{1/3}\text{Nb}_{2/3}\text{O}_3$ ”, *Physical Review Letters* **91**, 247601 (2003).
- ¹⁴M. Paściak, M. Wołczyrz, and A. Pietraszko, “Interpretation of the diffuse scattering in Pb-based relaxor ferroelectrics in terms of three-dimensional nanodomains of the $\langle 110 \rangle$ -directed relative interdomain atomic shifts”, *Physical Review B* **76**, 014117 (2007).
- ¹⁵H. You and Q. M. Zhang, “Diffuse X-ray scattering study of lead magnesium niobate single crystals”, *Physical Review Letters* **79**, 3950–3953 (1997).
- ¹⁶A. D. Hilton, D. J. Barber, C. A. Randall, and T. R. Shrout, “On short range ordering in the perovskite lead magnesium niobate”, *Journal of materials science* **25**, 3461–3466 (1990).
- ¹⁷T. Egami, “Atomistic mechanism of relaxor ferroelectricity”, *Ferroelectrics* **267**, 101–111 (2002).
- ¹⁸H. Takenaka, I. Grinberg, S. Liu, and A. M. Rappe, “Slush-like polar structures in single-crystal relaxors”, *Nature* **546**, 391–395 (2017).
- ¹⁹R. E. Cohen, “Origin of ferroelectricity in perovskite oxides”, *Nature* **358**, 136–138 (1992).
- ²⁰A. Kumar, J. N. Baker, P. C. Bowes, M. J. Cabral, S. Zhang, E. C. Dickey, D. L. Irving, and J. M. LeBeau, “Atomic-resolution electron microscopy of nanoscale local structure in lead-based relaxor ferroelectrics”, *Nature Materials* **20**, 62–67 (2021).
- ²¹H. D. Rosenfeld and T. Egami, “Short and intermediate range structural and chemical order in the relaxor ferroelectric lead magnesium niobate”, *Ferroelectrics* **164**, 133–141 (1995).
- ²²S. Prosandeev and L. Bellaiche, “Effects of atomic short-range order on properties of the $\text{PbMg}_{1/3}\text{Nb}_{2/3}\text{O}_3$ relaxor ferroelectric”, *Physical Review B* **94**, 180102(R) (2016).
- ²³J. Chen, H. M. Chan, and M. P. Harmer, “Ordering structure and dielectric properties of undoped and La/Na-doped $\text{PbMg}_{1/3}\text{Nb}_{2/3}\text{O}_3$ ”, *Journal of the American Ceramic Society* **72**, 593–598 (1989).
- ²⁴D. M. Smyth, M. P. Harmer, and P. Peng, “Defect chemistry of relaxor ferroelectrics and the implications for dielectric degradation”, *Journal of the American Ceramic Society* **72**, 2276–2278 (1989).
- ²⁵A. D. Hilton, C. A. Randall, D. J. Barber, and T. R. Shrout, “TEM studies of $\text{Pb}(\text{Mg}_{1/3}\text{Nb}_{2/3})\text{O}_3$ - PbTiO_3 ferroelectric relaxors”, *Ferroelectrics* **93**, 379–386 (1989).
- ²⁶N. de Mathan, E. Husson, G. Calvarn, J. R. Gavarri, A. W. Hewat, and A. Morell, “A structural model for the relaxor $\text{PbMg}_{1/3}\text{Nb}_{2/3}\text{O}_3$ at 5 K”, *Journal of Physics: Condensed Matter* **3**, 8159 (1991).
- ²⁷P. K. Davies and M. A. Akbas, “Chemical order in PMN-related relaxors: structure, stability, modification, and impact on properties”, *Journal of Physics and Chemistry of Solids* **61**, 159–166 (2000).
- ²⁸K. Park, L. Salamanca-Riba, M. Wuttig, and D. Viehland, “Ordering in lead magnesium niobate solid solutions”, *Journal of Materials Science* **29**, 1284–1289 (1994).
- ²⁹M. Cantoni, S. Bharadwaja, S. Gentil, and N. Setter, “Direct observation of the B-site cationic order in the ferroelectric relaxor $\text{Pb}(\text{Mg}_{1/3}\text{Ta}_{2/3})\text{O}_3$ ”, *Journal of Applied Physics* **96**, 3870–3875 (2004).

- ³⁰Y. Yan, S. J. Pennycook, Z. Xu, and D. Viehland, "Determination of the ordered structures of $\text{Pb}(\text{Mg}_{1/3}\text{Nb}_{2/3})\text{O}_3$ and $\text{Ba}(\text{Mg}_{1/3}\text{Nb}_{2/3})\text{O}_3$ by atomic-resolution Z-contrast imaging", *Applied Physics Letters* **72**, 3145–3147 (1998).
- ³¹H. Z. Jin, J. Zhu, S. Miao, X. W. Zhang, and Z. Y. Cheng, "Ordered domains and polar clusters in lead magnesium niobate $\text{Pb}(\text{Mg}_{1/3}\text{Nb}_{2/3})\text{O}_3$ ", *Journal of Applied Physics* **89**, 5048–5052 (2001).
- ³²T. Egami, W. Dmowski, S. Teslic, P. K. Davies, I. W. Chen, and H. Chen, "Nature of atomic ordering and mechanism of relaxor ferroelectric phenomena in PMN", *Ferroelectrics* **206**, 231–244 (1998).
- ³³A. Al-Barakaty, S. Prosandeev, D. Wang, B. Dkhil, and L. Bellaiche, "Finite-temperature properties of the relaxor $\text{PbMg}_{1/3}\text{Nb}_{2/3}\text{O}_3$ from atomistic simulations", *Physical Review B* **91**, 214117 (2015).
- ³⁴B. P. Burton and E. Cockayne, "Why $\text{Pb}(\text{B},\text{B}')\text{O}_3$ perovskites disorder at lower temperatures than $\text{Ba}(\text{B},\text{B}')\text{O}_3$ perovskites", *Physical Review B* **60**, R12542–R12545 (1999).
- ³⁵M. J. Cabral, S. Zhang, E. C. Dickey, and J. M. LeBeau, "Gradient chemical order in the relaxor", *Applied Physics Letters* **112**, 082901 (2018).
- ³⁶C. A. Randall and A. S. Bhalla, "Nanostructural-property relations in complex lead perovskites", *Japanese Journal of Applied Physics* **29**, 327 (1990).
- ³⁷N. Setter and L. E. Cross, "The contribution of structural disorder to diffuse phase transitions in ferroelectrics", *Journal of Materials Science* **15**, 2478–2482 (1980).
- ³⁸P. Ganesh, E. Cockayne, M. Ahart, R. E. Cohen, B. Burton, R. J. Hemley, Y. Ren, W. Yang, and Z.-G. Ye, "Origin of diffuse scattering in relaxor ferroelectrics", *Physical Review B* **81**, 144102 (2010).
- ³⁹A. Pramanick and S. Nayak, "Perspective on emerging views on microscopic origin of relaxor behavior", *Journal of Materials Research* **36**, 1015–1036 (2021).
- ⁴⁰S. Tinte, B. P. Burton, E. Cockayne, and U. V. Waghmare, "Origin of the relaxor state in $\text{Pb}(\text{B}_x\text{B}'_{1-x})\text{O}_3$ perovskites", *Physical Review Letters* **97**, 137601 (2006).
- ⁴¹A. Bosak, D. Chernyshov, S. Vakhrushev, and M. Krisch, "Diffuse scattering in relaxor ferroelectrics: true three-dimensional mapping, experimental artefacts and modelling", *Acta Crystallographica Section A: Foundations of Crystallography* **68**, 117–123 (2012).
- ⁴²D. Fu, H. Taniguchi, M. Itoh, S.-y. Koshihara, N. Yamamoto, and S. Mori, "Relaxor $\text{Pb}(\text{Mg}_{1/3}\text{Nb}_{2/3})\text{O}_3$: A ferroelectric with multiple inhomogeneities", *Physical Review Letters* **103**, 207601 (2009).
- ⁴³Z. Xu, S. M. Gupta, D. Viehland, Y. Yan, and S. J. Pennycook, "Direct imaging of atomic ordering in undoped and La-doped $\text{Pb}(\text{Mg}_{1/3}\text{Nb}_{2/3})\text{O}_3$ ", *Journal of the American Ceramic Society* **83**, 181–88 (2000).
- ⁴⁴B. Dkhil, J. M. Kiat, G. Calvarin, G. Baldinozzi, S. B. Vakhrushev, and E. Suard, "Local and long range polar order in the relaxor-ferroelectric compounds $\text{PbMg}_{1/3}\text{Nb}_{2/3}\text{O}_3$ and $\text{PbMg}_{0.3}\text{Nb}_{0.6}\text{Ti}_{0.1}\text{O}_3$ ", *Physical Review B* **65**, 024104 (2001).

Bibliography

- ⁴⁵P. M. Gehring, H. Hiraka, C. Stock, S.-H. Lee, W. Chen, Z.-G. Ye, S. B. Vakhrushev, and Z. Chowdhuri, “Reassessment of the Burns temperature and its relationship to the diffuse scattering, lattice dynamics, and thermal expansion in relaxor $\text{PbMg}_{1/3}\text{Nb}_{2/3}\text{O}_3$ ”, [Physical Review B](#) **79**, 224109 (2009).
- ⁴⁶G. Burns and F. H. Dacol, “Glassy polarization behavior in ferroelectric compounds $\text{Pb}(\text{Mg}_{1/3}\text{Nb}_{2/3})\text{O}_3$ and $\text{Pb}(\text{Zn}_{1/3}\text{Nb}_{2/3})\text{O}_3$ ”, [Solid State Communications](#) **48**, 853–856 (1983).
- ⁴⁷M. A. Carpenter, J. F. J. Bryson, G. Catalan, and C. J. Howard, “Elastic and anelastic relaxations in the relaxor ferroelectric $\text{Pb}(\text{Mg}_{1/3}\text{Nb}_{2/3})\text{O}_3$: I. Strain analysis and a static order parameter”, [Journal of Physics: Condensed Matter](#) **24**, 045901 (2011).
- ⁴⁸D. Viehland, S. J. Jang, L. E. Cross, and M. Wuttig, “Deviation from Curie-Weiss behavior in relaxor ferroelectrics”, [Physical Review B](#) **46**, 8003–8006 (1992).
- ⁴⁹L. E. Cross, “Relaxor ferroelectrics”, [Ferroelectrics](#) **76**, 241–276 (1987).
- ⁵⁰M. J. Krogstad, P. M. Gehring, S. Rosenkranz, R. Osborn, F. Ye, Y. Liu, J. P. C. Ruff, W. Chen, J. M. Wozniak, H. Luo, O. Chmaissem, Z.-G. Ye, and D. Phelan, “The relation of local order to material properties in relaxor ferroelectrics”, [Nature Materials](#) **17**, 718–724 (2018).
- ⁵¹G. Xu, “Competing orders in PZN–xPT and PMN–xPT relaxor ferroelectrics”, [Journal of the Physical Society of Japan](#) **79**, 011011 (2010).
- ⁵²G. Xu, Z. Zhong, Y. Bing, Z.-G. Ye, and G. Shirane, “Electric-field-induced redistribution of polar nano-regions in a relaxor ferroelectric”, [Nature Materials](#) **5**, 134–140 (2006).
- ⁵³H. Hiraka, S.-H. Lee, P. M. Gehring, G. Xu, and G. Shirane, “Cold neutron study on the diffuse scattering and phonon excitations in the relaxor $\text{PbMg}_{1/3}\text{Nb}_{2/3}\text{O}_3$ ”, [Physical Review B](#) **70**, 184105 (2004).
- ⁵⁴R. G. Burkovsky, Y. A. Bronwald, A. V. Filimonov, A. I. Rudskoy, D. Chernyshov, A. Bosak, J. Hlinka, X. Long, Z.-G. Ye, and S. B. Vakhrushev, “Structural heterogeneity and diffuse scattering in morphotropic lead zirconate-titanate single crystals”, [Physical Review Letters](#) **109**, 097603 (2012).
- ⁵⁵A. Tkachuk and H. Chen, “Anti-ferrodistortive nanodomains in PMN relaxor”, [AIP Conference Proceedings](#) **677**, 55–64 (2003).
- ⁵⁶I. P. Swainson, C. Stock, P. M. Gehring, G. Xu, K. Hirota, Y. Qiu, H. Luo, X. Zhao, J.-F. Li, and D. Viehland, “Soft phonon columns on the edge of the Brillouin zone in the relaxor $\text{PbMg}_{1/3}\text{Nb}_{2/3}\text{O}_3$ ”, [Physical Review B](#) **79**, 224301 (2009).
- ⁵⁷H. Uršič and D. Damjanovic, “Anelastic relaxor behavior of $\text{Pb}(\text{Mg}_{1/3}\text{Nb}_{2/3})\text{O}_3$ ”, [Applied Physics Letters](#) **103**, 072904 (2013).
- ⁵⁸V. Bovtun, S. Kamba, A. Pashkin, M. Savinov, P. Samoukhina, J. Petzelt, I. P. Bykov, and M. D. Glinchuk, “Central-peak components and polar soft mode in relaxor $\text{PbMg}_{1/3}\text{Nb}_{2/3}\text{O}_3$ crystals”, [Ferroelectrics](#) **298**, 23–30 (2004).
- ⁵⁹V. Bovtun, J. Petzelt, V. Porokhonsky, S. Kamba, and Y. Yakimenko, “Structure of the dielectric spectrum of relaxor ferroelectrics”, [Journal of the European Ceramic Society](#) **21**, 1307–1311 (2001).

- ⁶⁰E. V. Colla, E. Y. Koroleva, N. M. Okuneva, and S. B. Vakhrushev, “Low-frequency dielectric response of $\text{Pb}(\text{Mg}_{1/3}\text{Nb}_{2/3})\text{O}_3$ ”, *Journal of Physics: Condensed Matter* **4**, 3671–3677 (1992).
- ⁶¹A. A. Bokov and Z. Ye, “Universal relaxor polarization in $\text{PbMg}_{1/3}\text{Nb}_{2/3}\text{O}_3$ and related materials”, *Physical Review B* **66**, 064103 (2002).
- ⁶²V. Bovtun, S. Veljko, M. Savinov, A. Pashkin, S. Kamba, and J. Petzelt, “Comparison of the dielectric response of relaxor $\text{PbMg}_{1/3}\text{Nb}_{2/3}\text{O}_3$ ceramics and single crystals”, *Integrated Ferroelectrics* **69**, 3–10 (2005).
- ⁶³V. Bovtun, S. Veljko, S. Kamba, J. Petzelt, S. Vakhrushev, Y. Yakymenko, K. Brinkman, and N. Setter, “Broad-band dielectric response of $\text{PbMg}_{1/3}\text{Nb}_{2/3}\text{O}_3$ relaxor ferroelectrics: Single crystals, ceramics and thin films”, *Journal of the European Ceramic Society, Grain Boundary Engineering of Electronic Ceramics* **26**, 2867–2875 (2006).
- ⁶⁴I. Grinberg, P. Juhás, P. K. Davies, and A. M. Rappe, “Relationship between local structure and relaxor behavior in perovskite oxides”, *Physical Review Letters* **99**, 267603 (2007).
- ⁶⁵M. Otoničar, A. Bradeško, L. Fulanović, T. Kos, H. Uršič, A. Benčan, M. J. Cabral, A. Henriques, J. L. Jones, L. Riemer, D. Damjanovic, G. Dražić, B. Malič, and T. Rojac, “Connecting the multiscale structure with macroscopic response of relaxor ferroelectrics”, *Advanced Functional Materials* **30**, 2006823 (2020).
- ⁶⁶D. Viehland, S. Jang, L. Eric Cross, and M. Wuttig, “The dielectric relaxation of lead magnesium niobate relaxor ferroelectrics”, *Philosophical Magazine B* **64**, 335–344 (1991).
- ⁶⁷C. Elissalde, J. Ravez, and P. Gaucher, “High frequency dielectric relaxation in lead magnesium niobate ceramics”, en, *Materials Science and Engineering: B* **13**, 327–333 (1992).
- ⁶⁸A. Levstik, Z. Kutnjak, C. Filipič, and R. Pirc, “Glassy freezing in relaxor ferroelectric lead magnesium niobate”, *Physical Review B* **57**, 11204–11211 (1998).
- ⁶⁹H. M. Christen, N. K. Y. R Sommer, and J. J. van der Klink, “Small-signal dielectric relaxation in the disordered perovskite $\text{PbMg}_{1/3}\text{Nb}_{2/3}\text{O}_3$ ”, *Journal of Physics: Condensed Matter* **6**, 2631–2642 (1994).
- ⁷⁰R. Pirc and R. Blinc, “Vogel-Fulcher freezing in relaxor ferroelectrics”, *Physical Review B* **76**, 020101 (2007).
- ⁷¹D. Viehland, S. J. Jang, L. E. Cross, and M. Wuttig, “Freezing of the polarization fluctuations in lead magnesium niobate relaxors”, *J. Appl. Phys.* **68**, 2916–2921 (1990).
- ⁷²A. K. Tagantsev, “Vogel-Fulcher relationship for the dielectric permittivity of relaxor ferroelectrics”, *Physical Review Letters* **72**, 1100–1103 (1994).
- ⁷³R. Sommer, N. K. Yushin, and J. J. van der Klink, “Polar metastability and an electric-field-induced phase transition in the disordered perovskite $\text{PbMg}_{1/3}\text{Nb}_{2/3}\text{O}_3$ ”, *Physical Review B* **48**, 13230–13237 (1993).
- ⁷⁴D. Viehland, J. F. Li, S. J. Jang, L. E. Cross, and M. Wuttig, “Dipolar-glass model for lead magnesium niobate”, *Physical Review B* **43**, 8316–8320 (1991).
- ⁷⁵V. Westphal, W. Kleemann, and M. D. Glinchuk, “Diffuse phase transitions and random-field-induced domain states of the “relaxor” ferroelectric $\text{PbMg}_{1/3}\text{Nb}_{2/3}\text{O}_3$ ”, *Physical Review Letters* **68**, 847–850 (1992).

Bibliography

- ⁷⁶E. V. Colla, E. Y. Koroleva, A. A. Nabereznov, and N. M. Okuneva, “The lead magnoniobate behavior in applied electric field”, *Ferroelectrics* **151**, 337–342 (1994).
- ⁷⁷A. A. Bokov and Z. G. Ye, “Recent progress in relaxor ferroelectrics with perovskite structure”, *Journal of Materials Science* **41**, 31–52 (2006).
- ⁷⁸Z. Kutnjak, B. Vodopivec, and R. Blinc, “Anisotropy of electric field freezing of the relaxor ferroelectric $\text{Pb}(\text{Mg}_{1/3}\text{Nb}_{2/3})\text{O}_3$ ”, *Physical Review B* **77**, 054102 (2008).
- ⁷⁹G. Calvarin, E. Husson, and Z. G. Ye, “X-ray study of the electric field-induced phase transition in single crystal $\text{PbMg}_{1/3}\text{Nb}_{2/3}\text{O}_3$ ”, *Ferroelectrics* **165**, 349–358 (1995).
- ⁸⁰Z.-G. Ye and H. Schmid, “Optical, dielectric and polarization studies of the electric field-induced phase transition in $\text{Pb}(\text{Mg}_{1/3}\text{Nb}_{2/3})\text{O}_3$ [PMN]”, *Ferroelectrics* **145**, 83–108 (1993).
- ⁸¹B. Dkhil, P. Gemeiner, A. Al-Barakaty, L. Bellaiche, E. Dul’kin, E. Mojaev, and M. Roth, “Intermediate temperature scale T^* in lead-based relaxor systems”, *Physical Review B* **80**, 064103 (2009).
- ⁸²J. Toulouse, “The three characteristic temperatures of relaxor dynamics and their meaning”, *Ferroelectrics* **369**, 203–213 (2008).
- ⁸³D. Nuzhnyy, J. Petzelt, V. Bovtun, S. Kamba, and J. Hlinka, “Soft mode driven local ferroelectric transition in lead-based relaxors”, *Applied Physics Letters* **114**, 182901 (2019).
- ⁸⁴S. Zhang and F. Li, “High performance ferroelectric relaxor- PbTiO_3 single crystals: Status and perspective”, *Journal of Applied Physics* **111**, 031301 (2012).
- ⁸⁵F. Li, M. J. Cabral, B. Xu, Z. Cheng, E. C. Dickey, J. M. LeBeau, J. Wang, J. Luo, S. Taylor, W. Hackenberger, L. Bellaiche, Z. Xu, L.-Q. Chen, T. R. Shrout, and S. Zhang, “Giant piezoelectricity of Sm-doped $\text{PbMg}_{1/3}\text{Nb}_{2/3}\text{O}_3$ - PbTiO_3 single crystals”, *Science* **364**, 264–268 (2019).
- ⁸⁶H. X. Fu and R. E. Cohen, “Polarization rotation mechanism for ultrahigh electromechanical response in single-crystal piezoelectrics”, *Nature* **403**, 281–283 (2000).
- ⁸⁷S.-E. Park and T. R. Shrout, “Ultrahigh strain and piezoelectric behavior in relaxor based ferroelectric single crystals”, *Journal of Applied Physics* **82**, 1804–1811 (1997).
- ⁸⁸B. Noheda, D. E. Cox, G. Shirane, J. Gao, and Z. G. Ye, “Phase diagram of the ferroelectric relaxor $(1-x)\text{PbMg}_{1/3}\text{Nb}_{2/3}\text{O}_3$ - $x\text{PbTiO}_3$ ”, *Phys. Rev. B* **66**, 054104 (2002).
- ⁸⁹V. M. Ishchuk, V. N. Baumer, and V. L. Sobolev, “The influence of the coexistence of ferroelectric and antiferroelectric states on the lead lanthanum zirconate titanate crystal structure”, *Journal of Physics: Condensed Matter* **17**, L177–L182 (2005).
- ⁹⁰F. Li, S. Zhang, D. Damjanovic, L.-Q. Chen, and T. R. Shrout, “Local structural heterogeneity and electromechanical responses of ferroelectrics: Learning from relaxor ferroelectrics”, *Advanced Functional Materials* **28**, 1801504 (2018).
- ⁹¹D. Damjanovic, “Ferroelectric, dielectric and piezoelectric properties of ferroelectric thin films and ceramics”, *Reports on Progress in Physics* **61**, 1267 (1998).
- ⁹²P. V. Yudin and A. K. Tagantsev, “Fundamentals of flexoelectricity in solids”, *Nanotechnology* **24**, 432001 (2013).

- ⁹³D. Viehland, "Symmetry-adaptive ferroelectric mesostates in oriented $\text{Pb}(\text{BI}_{1/3}\text{BII}_{2/3})\text{O}_3$ - PbTiO_3 crystals", *Journal of Applied Physics* **88**, 4794–4806 (2000).
- ⁹⁴A. Pramanick, D. Damjanovic, J. E. Daniels, J. C. Nino, and J. L. Jones, "Origins of electro-mechanical coupling in polycrystalline ferroelectrics during subcoercive electrical loading", *Journal of the American Ceramic Society* **94**, 293–309 (2011).
- ⁹⁵T. Sluka, A. K. Tagantsev, D. Damjanovic, M. Gureev, and N. Setter, "Enhanced electromechanical response of ferroelectrics due to charged domain walls", *Nature Communications* **3**, 748 (2012).
- ⁹⁶T. Rojac, H. Ursic, A. Bencan, B. Malic, and D. Damjanovic, "Mobile domain walls as a bridge between nanoscale conductivity and macroscopic electromechanical response", *Advanced Functional Materials* **25**, 2099–2108 (2015).
- ⁹⁷J. G. Swallow, J. J. Kim, J. M. Maloney, D. Chen, J. F. Smith, S. R. Bishop, H. L. Tuller, and K. J. Van Vliet, "Dynamic chemical expansion of thin-film non-stoichiometric oxides at extreme temperatures", *Nature Materials* **16**, 749–754 (2017).
- ⁹⁸K. Yan, S. Ren, M. Fang, and X. Ren, "Crucial role of octahedral untilting $\text{R3m}/\text{P4mm}$ morphotropic phase boundary in highly piezoelectric perovskite oxide", *Acta Materialia* **134**, 195–202 (2017).
- ⁹⁹G. Y. Xu, J. S. Wen, C. Stock, and P. M. Gehring, "Phase instability induced by polar nanoregions in a relaxor ferroelectric system", *Nat. Mater.* **7**, 562–566 (2008).
- ¹⁰⁰Z. Kutnjak, J. Petzelt, and R. Blinc, "The giant electromechanical response in ferroelectric relaxors as a critical phenomenon", *Nature* **441**, 956–959 (2006).
- ¹⁰¹J. Hlinka, "Do we need the ether of polar nanoregions?", *Journal of Advanced Dielectrics* **02**, 1241006 (2012).
- ¹⁰²D. Damjanovic, "Contributions to the piezoelectric effect in ferroelectric single crystals and ceramics", *Journal of the American Ceramic Society* **88**, 2663–2676 (2005).
- ¹⁰³S. J. Zhang, "Advantages and challenges of relaxor- PbTiO_3 ferroelectric crystals for electroacoustic transducers—a review", *Prog. Mater. Sci.* **68**, 1–66 (2015).
- ¹⁰⁴M. E. Manley, "Giant electromechanical coupling of relaxor ferroelectrics controlled by polar nanoregion vibrations", *Sci. Adv.* **2**, e1501814 (2016).
- ¹⁰⁵F. Li, S. Zhang, T. Yang, Z. Xu, N. Zhang, G. Liu, J. Wang, J. Wang, Z. Cheng, Z.-G. Ye, J. Luo, T. R. Shrout, and L.-Q. Chen, "The origin of ultrahigh piezoelectricity in relaxor-ferroelectric solid solution crystals", *Nature Communications* **7**, 13807 (2016).
- ¹⁰⁶Y. Sun, T. Karaki, T. Fujii, and Y. Yamashita, "Alternate current poling and direct current poling for $\text{Pb}(\text{Mg}_{1/3}\text{Nb}_{2/3})\text{O}_3$ - PbTiO_3 single crystals", *Japanese Journal of Applied Physics* **58**, SLLC06 (2019).
- ¹⁰⁷W.-Y. Chang, C.-C. Chung, C. Luo, T. Kim, Y. Yamashita, J. L. Jones, and X. Jiang, "Dielectric and piezoelectric properties of $0.7\text{Pb}(\text{Mg}_{1/3}\text{Nb}_{2/3})\text{O}_3$ - 0.3PbTiO_3 single crystal poled using alternating current", *Materials Research Letters* **6**, 537–544 (2018).

Bibliography

- ¹⁰⁸C. Qiu, B. Wang, N. Zhang, S. Zhang, J. Liu, D. Walker, Y. Wang, H. Tian, T. R. Shrout, Z. Xu, L.-Q. Chen, and F. Li, “Transparent ferroelectric crystals with ultrahigh piezoelectricity”, [Nature](#) **577**, 350–354 (2020).
- ¹⁰⁹G. Smolenskii and A. Agranovskaya, “Dielectric Polarization of a Number of Complex Compounds”, [Soviet Physics-Solid State](#) **1**, 1429–1437 (1959).
- ¹¹⁰A. E. Glazounov and A. K. Tagantsev, “A “breathing” model for the polarization response of relaxor ferroelectrics”, [Ferroelectrics](#) **221**, 57–66 (1999).
- ¹¹¹L. Jin, “Broadband dielectric response in hard and soft PZT: understanding softening and hardening mechanisms”, [PhD Thesis 4988](#), EPFL (2011).
- ¹¹²L. M. Riemer, K. Chu, Y. Li, H. Uršič, A. J. Bell, B. Dkhil, and D. Damjanovic, “Macroscopic polarization in the nominally ergodic relaxor state of lead magnesium niobate”, [Applied Physics Letters](#) **117**, 102901 (2020).
- ¹¹³M. Davis, “Phase transitions, anisotropy and domain engineering: the piezoelectric properties of relaxor-ferroelectric single crystals”, [PhD Thesis 3513](#), EPFL (2011).
- ¹¹⁴M. Daglish, “A dynamic method for determining the pyroelectric response of thin films”, [Integrated Ferroelectrics](#) **22**, 473–488 (1998).
- ¹¹⁵M. G. Cain, ed., *Characterisation of Ferroelectric Bulk Materials and Thin Films*, Vol. 2, Springer Series in Measurement Science and Technology (Springer Netherlands, Dordrecht, 2014).
- ¹¹⁶A. Devices, “Femtoampere input bias current electrometer amplifier”, [Data Sheet ADA4530-1](#), Rev. B (2017).
- ¹¹⁷Texas Instruments, “OPA627 and OPA637 precision high-speed difet operational amplifiers”, [Data Sheet SBOS165A](#), Revised Oct. 2015 (2000).
- ¹¹⁸V. Bobnar, Z. Kutnjak, R. Pirc, and A. Levstik, “Electric-field–temperature phase diagram of the relaxor ferroelectric lanthanum-modified lead zirconate titanate”, [Physical Review B](#) **60**, 6420–6427 (1999).
- ¹¹⁹B. Jaffe, W. Cook, and H. Jaffe, “The piezoelectric effect in ceramics”, [Piezoelectr. Ceram](#) **1**, 7–21 (1971).
- ¹²⁰T. Instruments, “DC parameters: Input offset voltage (V_{IO})”, [Application Report SLOA059](#) (2001).
- ¹²¹S. T. Smith, *Foundations of ultra-precision mechanism design*, Vol. 2 (CRC Press, 2003).
- ¹²²L. M. Riemer, L. Jin, H. Uršič, M. Otoničar, T. Rojac, and D. Damjanovic, “Dielectric and electro-mechanic nonlinearities in perovskite oxide ferroelectrics, relaxors, and relaxor ferroelectrics”, [Journal of Applied Physics](#) **129**, 054101 (2021).
- ¹²³A. Grigoriev, R. Sichel, H. N. Lee, E. C. Landahl, B. Adams, E. M. Dufresne, and P. G. Evans, “Nonlinear piezoelectricity in epitaxial ferroelectrics at high electric fields”, [Physical Review Letters](#) **100** (2008).
- ¹²⁴D. A. Hall, “Review nonlinearity in piezoelectric ceramics”, [Journal of Materials Science](#) **36**, 4575–4601 (2001).

- ¹²⁵A. Pramanick, D. Damjanovic, J. C. Nino, and J. L. Jones, “Subcoercive cyclic electrical loading of lead zirconate titanate ceramics I: Nonlinearities and losses in the converse piezoelectric effect”, *Journal of the American Ceramic Society* **92**, 2291–2299 (2009).
- ¹²⁶L. Jin, F. Li, and S. Zhang, “Decoding the fingerprint of ferroelectric loops: Comprehension of the material properties and structures”, *Journal of the American Ceramic Society* **97**, 1–27 (2014).
- ¹²⁷K. Kuramoto and E. Nakamura, “Nonlinear dielectric constant of KH_2PO_4 in the ferroelectric phase”, *Ferroelectrics* **157**, 57–62 (1994).
- ¹²⁸N. Bassiri-Gharb, I. Fujii, E. Hong, S. Trolier-McKinstry, D. V. Taylor, and D. Damjanovic, “Domain wall contributions to the properties of piezoelectric thin films”, *Journal of Electroceramics* **19**, 49–67 (2007).
- ¹²⁹F. Li, S. Zhang, Z. Xu, X. Wei, J. Luo, and T. R. Shrout, “Piezoelectric activity of relaxor- PbTiO_3 based single crystals and polycrystalline ceramics at cryogenic temperatures: Intrinsic and extrinsic contributions”, *Applied Physics Letters* **96**, 192903 (2010).
- ¹³⁰K. Tamm, “Theory of electric polarization”, *Berichte der Bunsengesellschaft für physikalische Chemie* **84**, 1190–1191 (1980).
- ¹³¹D. Damjanovic, “Hysteresis in piezoelectric and ferroelectric materials”, in *The science of hysteresis* (Academic Press: Oxford, 2006; Vol. III, 2006), pp. 337–465.
- ¹³²G. H. Haertling, “Ferroelectric ceramics: History and technology”, *Journal of the American Ceramic Society* **82**, 797–818 (1999).
- ¹³³D. Sundararajan, *Fourier analysis—a signal processing approach* (Springer Singapore, Singapore, 2018).
- ¹³⁴T. Furukawa, M. Date, and E. Fukada, “Hysteresis phenomena in polyvinylidene fluoride under high electric field”, *Journal of Applied Physics* **51**, 1135–1141 (1980).
- ¹³⁵M. Morozov, D. Damjanovic, and N. Setter, “The nonlinearity and subswitching hysteresis in hard and soft PZT”, *Journal of the European Ceramic Society* **25**, 2483–2486 (2005).
- ¹³⁶J. F. Nye, *Physical properties of crystals: Their representation by tensors and matrices* (Oxford University Press, Oxford, New York, 1984).
- ¹³⁷F. Li, L. Jin, Z. Xu, and S. Zhang, “Electrostrictive effect in ferroelectrics: An alternative approach to improve piezoelectricity”, *Applied Physics Reviews* **1**, 011103 (2014).
- ¹³⁸R. Pirc, R. Blinc, and V. S. Vikhnin, “Anisotropic nonlinear dielectric response of relaxor ferroelectrics”, *Physical Review B* **74** (2006).
- ¹³⁹J. Dec, W. Kleemann, S. Miga, C. Filipic, A. Levstik, R. Pirc, T. Granzow, and R. Pankrath, “Probing polar nanoregions in $\text{Pb}_{0.61}\text{Ba}_{0.39}\text{Nb}_2\text{O}_6$ via second-harmonic dielectric response”, *Physical Review B* **68**, 092105 (2003).
- ¹⁴⁰P. H. Sydenham and R. Thorn, eds., *Handbook of measuring system design* (Wiley, Chichester, England, 2005).
- ¹⁴¹M.-M. Yang, Z.-D. Luo, Z. Mi, J. Zhao, S. P. E, and M. Alexe, “Piezoelectric and pyroelectric effects induced by interface polar symmetry”, *Nature* **584**, 377–381 (2020).

Bibliography

- ¹⁴²M. I. Morozov and D. Damjanovic, “Hardening-softening transition in Fe-doped Pb(Zr, Ti)O₃ ceramics and evolution of the third harmonic of the polarization response”, [Journal of Applied Physics](#) **104**, 034107 (2008).
- ¹⁴³L. Néel, “Théorie des lois d’aimantation de Lord Rayleigh et les déplacements d’une paroi isolée”, [Cahiers de Physique](#) **12**, 1–20 (1942).
- ¹⁴⁴L. Néel, “Some theoretical aspects of rock-magnetism”, [Advances in Physics](#) **4**, 191–243 (1955).
- ¹⁴⁵G. Bertotti, *Hysteresis in magnetism: For physicists, materials scientists, and engineers*, Electromagnetism (Academic Press, San Diego, 1998), 558 pp.
- ¹⁴⁶R. Holland, “Representation of dielectric, elastic, and piezoelectric losses by complex coefficients”, [IEEE Transactions on Sonics and Ultrasonics](#) **14**, 18–20 (1967).
- ¹⁴⁷Q. M. Zhang, H. Wang, N. Kim, and L. E. Cross, “Direct evaluation of domain-wall and intrinsic contributions to the dielectric and piezoelectric response and their temperature dependence on lead zirconate-titanate ceramics”, [Journal of Applied Physics](#) **75**, 454–459 (1994).
- ¹⁴⁸M. E. Caspari and W. J. Merz, “The electromechanical behavior of BaTiO₃ single-domain crystals”, [Physical Review](#) **80**, 1082–1089 (1950).
- ¹⁴⁹R. E. Newnham, V. Sundar, R. Yimnirun, J. Su, and Q. M. Zhang, “Electrostriction: Nonlinear electromechanical coupling in solid dielectrics”, [The Journal of Physical Chemistry B](#) **101**, 10141–10150 (1997).
- ¹⁵⁰M. Sjöström, “Frequency analysis of classical preisach model”, [IEEE Transactions on Magnetics](#) **35**, 2097–2103 (1999).
- ¹⁵¹S. Hashemizadeh and D. Damjanovic, “Nonlinear dynamics of polar regions in paraelectric phase of (Ba_{1-x}Sr_x)TiO₃ ceramics”, [Applied Physics Letters](#) **110**, 192905 (2017).
- ¹⁵²L. Néel, “Théorie du traînage magnétique des substances massives dans le domaine de rayleigh”, [Journal de Physique et le Radium](#) **11**, 49–61 (1950).
- ¹⁵³L. Rayleigh, “On the behaviour of iron and steel under the operation of feeble magnetic forces”, [The London, Edinburgh, and Dublin Philosophical Magazine and Journal of Science](#) **23**, 225–245 (1887).
- ¹⁵⁴H. Kronmüller, “Statistical theory of rayleigh law”, [Zeitschrift für angewandte Physik](#) **30**, 9–13 (1970).
- ¹⁵⁵A. Turik, “Theory of polarization and hysteresis of ferroelectrics”, [Soviet Physics-Solid State](#) **5**, 885–886 (1963).
- ¹⁵⁶D. Damjanovic and M. Demartin, “The Rayleigh law in piezoelectric ceramics”, [Journal of Physics D: Applied Physics](#) **29**, 2057 (1996).
- ¹⁵⁷M. Algueró, B. Jiménez, and L. Pardo, “Rayleigh type behavior of the Young’s modulus of unpoled ferroelectric ceramics and its dependence on temperature”, [Applied Physics Letters](#) **83**, 2641–2643 (2003).
- ¹⁵⁸S. Kustov, E. Cesari, I. Liubimova, V. Nikolaev, and E. K. H. Salje, “Twinning in Ni–Fe–Ga–Co shape memory alloy: Temperature scaling beyond the Seeger model”, [Scripta Materialia](#) **134**, 24–27 (2017).

- ¹⁵⁹D. Damjanovic, "Stress and frequency dependence of the direct piezoelectric effect in ferroelectric ceramics", *Journal of Applied Physics* **82**, 1788–1797 (1997).
- ¹⁶⁰I. Urbanavičiūtė, T. D. Cornelissen, X. Meng, R. P. Sijbesma, and M. Kemerink, "Physical reality of the Preisach model for organic ferroelectrics", *Nature Communications* **9**, 1–11 (2018).
- ¹⁶¹S. A. Turik, L. A. Reznitchenko, A. N. Rybjanets, S. I. Dudkina, A. V. Turik, and A. A. Yesis, "Preisach model and simulation of the converse piezoelectric coefficient in ferroelectric ceramics", *Journal of Applied Physics* **97**, 064102 (2005).
- ¹⁶²I. D. Mayergoyz, G. Friedman, and C. Salling, "Comparison of the classical and generalized Preisach hysteresis models with experiments", *IEEE Transactions on Magnetics* **25**, 3925–3927 (1989).
- ¹⁶³F. Preisach, "Über die magnetische Nachwirkung", *Zeitschrift für Physik* **94**, 277–302 (1935).
- ¹⁶⁴H.-J. Hagemann, "Loss mechanisms and domain stabilisation in doped BaTiO₃", *Journal of Physics C: Solid State Physics* **11**, 3333 (1978).
- ¹⁶⁵G. Robert, D. Damjanovic, and N. Setter, "Preisach distribution function approach to piezoelectric nonlinearity and hysteresis", *Journal of Applied Physics* **90**, 2459–2464 (2001).
- ¹⁶⁶G. Robert, D. Damjanovic, N. Setter, and A. V. Turik, "Preisach modeling of piezoelectric nonlinearity in ferroelectric ceramics", *Journal of Applied Physics* **89**, 5067–5074 (2001).
- ¹⁶⁷Y. Saito, "Measurements of complex piezoelectric d_{33} constant in ferroelectric ceramics under high electric field driving", *Japanese Journal of Applied Physics* **34**, 5313 (1995).
- ¹⁶⁸Q. M. Zhang, W. Y. Pan, S. J. Jang, and L. E. Cross, "Domain wall excitations and their contributions to the weak-signal response of doped lead zirconate titanate ceramics", *Journal of Applied Physics* **64**, 6445–6451 (1988).
- ¹⁶⁹M. Morozov, "Softening and hardening transitions in ferroelectric Pb(Zr,Ti)O₃ ceramics", *PhD Thesis* 3368, EPFL (2005).
- ¹⁷⁰D. Berlincourt and H. H. A. Krueger, "Domain processes in lead titanate zirconate and barium titanate ceramics", *Journal of Applied Physics* **30**, 1804–1810 (1959).
- ¹⁷¹S. Li, W. Cao, and L. E. Cross, "The extrinsic nature of nonlinear behavior observed in lead zirconate titanate ferroelectric ceramic", *Journal of Applied Physics* **69**, 7219–7224 (1991).
- ¹⁷²V. Mueller and Q. M. Zhang, "Nonlinearity and scaling behavior in donor-doped lead zirconate titanate piezoceramic", *Applied Physics Letters* **72**, 2692–2694 (1998).
- ¹⁷³D. V. Taylor, D. Damjanovic, and N. Setter, "Nonlinear contributions to dielectric and piezoelectric properties in lead zirconate titanate thin films", *Ferroelectrics* **224**, 299–306 (1999).
- ¹⁷⁴D. V. Taylor, "Dielectric and piezoelectric properties of sol-gel derived Pb(Zr,Ti)O₃ thin films", *PhD Thesis* 1949, EPFL (1999).
- ¹⁷⁵C. Zhao, D. Hou, C.-C. Chung, H. Zhou, A. Kynast, E. Hennig, W. Liu, S. Li, and J. L. Jones, "Deconvolved intrinsic and extrinsic contributions to electrostrain in high performance, Nb-doped Pb(Zr_xTi_{1-x})O₃ piezoceramics (0.50 ≤ x ≤ 0.56)", *Acta Materialia* **158**, 369–380 (2018).
- ¹⁷⁶H. G. Baerwald and D. A. Berlincourt, "Electromechanical response and dielectric loss of pre-polarized barium titanate under maintained electric bias. Part I", *The Journal of the Acoustical Society of America* **25**, 703–710 (1953).

Bibliography

- ¹⁷⁷H. Jaffe, “Titanate ceramics for electromechanical purposes”, [Industrial & Engineering Chemistry](#) **42**, 264–268 (1950).
- ¹⁷⁸D. Jablonskas, R. Grigalaitis, J. Banys, A. A. Bokov, and Z.-G. Ye, “Broadband dielectric spectra in $\text{PbMg}_{1/3}\text{Nb}_{2/3}\text{O}_3$ crystals with chemical order modified by La doping”, [Applied Physics Letters](#) **107**, 142905 (2015).
- ¹⁷⁹W. Kleemann and J. Dec, “Relaxor ferroelectrics and related superglasses”, [Ferroelectrics](#) **553**, 1–7 (2019).
- ¹⁸⁰S. N. Dorogovtsev and N. K. Yushin, “Acoustical properties of disordered ferroelectrics”, [Ferroelectrics](#) **112**, 27–44 (1990).
- ¹⁸¹E. V. Colla, E. Y. Koroleva, N. M. Okuneva, and S. B. Vakhrushev, “Field induced kinetic ferroelectric phase transition in lead magnoniobate”, [Ferroelectrics](#) **184**, 209–215 (1996).
- ¹⁸²O. Aktas and E. K. H. Salje, “Macroscopic symmetry breaking and piezoelectricity in relaxor ferroelectric lead magnesium niobate”, [Applied Physics Letters](#) **113**, 202901 (2018).
- ¹⁸³J. Dec, S. Miga, W. Kleemann, and B. Dkhil, “Nonlinear dielectric properties of PMN relaxor crystals within Landau-Ginzburg-Devonshire approximation”, [Ferroelectrics](#) **363**, 141–149 (2008).
- ¹⁸⁴R. W. Whatmore, “Pyroelectric devices and materials”, [Reports on Progress in Physics](#) **49**, 1335–1386 (1986).
- ¹⁸⁵A. Biancoli, “Breaking of the macroscopic centric symmetry in $\text{Ba}_{1-x}\text{Nb}_x\text{TiO}_3$ ceramics and single crystals”, [PhD Thesis 6366, EPFL](#) (2014).
- ¹⁸⁶S. Hashemisadeh, “Origins of the macroscopic symmetry breaking in centrosymmetric phases of perovskite oxides”, [PhD Thesis 8026, EPFL](#) (2017).
- ¹⁸⁷S. Hashemizadeh, A. Biancoli, and D. Damjanovic, “Symmetry breaking in hexagonal and cubic polymorphs of BaTiO_3 ”, [Journal of Applied Physics](#) **119**, 094105 (2016).
- ¹⁸⁸A. Biancoli, C. M. Fancher, J. L. Jones, and D. Damjanovic, “Breaking of macroscopic centric symmetry in paraelectric phases of ferroelectric materials and implications for flexoelectricity”, [Nature Materials](#) **14**, 224–229 (2015).
- ¹⁸⁹A. Bencan, E. Oveisi, S. Hashemizadeh, V. K. Veerapandiyan, T. Hoshina, T. Rojac, M. Deluca, G. Drazic, and D. Damjanovic, “Atomic scale symmetry and polar nanoclusters in the paraelectric phase of ferroelectric materials”, [Nature Communications](#) **12**, 3509 (2021).
- ¹⁹⁰M. Tyunina and J. Levoska, “Effect of ac field on the dielectric behavior in epitaxial films of relaxor ferroelectric $\text{PbMg}_{1/3}\text{Nb}_{2/3}\text{O}_3$ ”, [Physical Review B](#) **72**, 104112 (2005).
- ¹⁹¹Z.-R. Liu, B.-L. Gu, and X.-W. Zhang, “Effects of ac field amplitude on the dielectric susceptibility of relaxors”, [Physical Review B](#) **62**, 1–4 (2000).
- ¹⁹²A. E. Glazounov and A. K. Tagantsev, “Crossover in a non-analytical behaviour of dielectric non-linearity in $\text{PbMg}_{1/3}\text{Nb}_{2/3}\text{O}_3$ relaxor ferroelectric”, [Journal of Physics: Condensed Matter](#) **10**, 8863 (1998).
- ¹⁹³A. Glazounov, “Non-linear dielectric response of $\text{Pb}(\text{Mg}_{1/3}\text{Nb}_{2/3})\text{O}_3$ relaxor ferroelectric”, [PhD Thesis 1665, EPFL](#) (1997).

- ¹⁹⁴X. Zhao, W. Qu, X. Tan, A. A. Bokov, and Z.-G. Ye, “Electric field-induced phase transitions in (111)-, (110)-, and (100)-oriented $\text{Pb}(\text{Mg}_{1/3}\text{Nb}_{2/3})\text{O}_3$ single crystals”, [Physical Review B](#) **75**, 104106 (2007).
- ¹⁹⁵A. E. Glazounov and A. K. Tagantsev, “Comparison of DC and AC field effects on dielectric properties of lead magnesium niobate relaxor: Study of single crystals and ceramics”, [Ferroelectrics](#) **201**, 305–315 (1997).
- ¹⁹⁶A. Bradeško, L. Fulanović, M. Vrabelj, M. Otoničar, H. Uršič, A. Henriques, C.-C. Chung, J. L. Jones, B. Malič, Z. Kutnjak, and T. Rojac, “Electrocaloric fatigue of lead magnesium niobate mediated by an electric-field-induced phase transformation”, [Acta Materialia](#) **169**, 275–283 (2019).
- ¹⁹⁷H. Simons, A. B. Haugen, A. C. Jakobsen, S. Schmidt, F. Stöhr, M. Majkut, C. Detlefs, J. E. Daniels, D. Damjanovic, and H. F. Poulsen, “Long-range symmetry breaking in embedded ferroelectrics”, [Nature Materials](#) **17**, 814 (2018).
- ¹⁹⁸G. Arlt, “Twinning in ferroelectric and ferroelastic ceramics: Stress relief”, [Journal of Materials Science](#) **25**, 2655–2666 (1990).
- ¹⁹⁹N. Bassiri-Gharb, S. Trolier-McKinstry, and D. Damjanovic, “Strain-modulated piezoelectric and electrostrictive nonlinearity in ferroelectric thin films without active ferroelastic domain walls”, [Journal of Applied Physics](#) **110**, 124104 (2011).
- ²⁰⁰K. Uchino, S. Nomura, L. E. Cross, S. J. Jang, and R. E. Newnham, “Electrostrictive effect in lead magnesium niobate single crystals”, [Journal of Applied Physics](#) **51**, 1142–1145 (1980).
- ²⁰¹T. R. Shrout, W. Huebner, C. A. Randall, and A. D. Hilton, “Aging mechanisms in $\text{PbMg}_{1/3}\text{Nb}_{2/3}\text{O}_3$ -based relaxor ferroelectrics”, [Ferroelectrics](#) **93**, 361–372 (1989).
- ²⁰²Y. Wang, L. T. Li, and Z. L. Gui, “Initial dielectric aging in a lead magnesium niobate ceramic under strong alternating current fields”, [Materials Letters](#) **37**, 40–43 (1998).
- ²⁰³J. Kuwata, K. Uchino, and S. Nomura, “Electrostrictive coefficients of $\text{Pb}(\text{Mg}_{1/3}\text{Nb}_{2/3})\text{O}_3$ ceramics”, [Japanese Journal of Applied Physics](#) **19**, 2099 (1980).
- ²⁰⁴M. Otoničar, A. Bradeško, S. Salmanov, C. C. Chung, J. L. Jones, and T. Rojac, “Effects of poling on the electrical and electromechanical response of PMN-PT relaxor ferroelectric ceramics”, [Open Ceramics](#) **7**, 100140 (2021).
- ²⁰⁵J. Erhart and L. Burianová, “What is really measured on a d_{33} -meter?”, [Journal of the European Ceramic Society](#) **21**, 1413–1415 (2001).
- ²⁰⁶S. Prosandeev, B. Xu, and L. Bellaiche, “Polarization switching in the $\text{PbMg}_{1/3}\text{Nb}_{2/3}\text{O}_3$ relaxor ferroelectric: An atomistic effective Hamiltonian study”, [Physical Review B](#) **98**, 024105 (2018).
- ²⁰⁷W. S. Lau, T. C. Chong, L. S. Tan, C. H. Goo, and K. S. Goh, “The characterization of traps in semi-insulating gallium arsenide buffer layers grown at low temperature by molecular beam epitaxy with an improved zero-bias thermally stimulated current technique”, [Japanese Journal of Applied Physics, Part II](#) **30**, L1843 (1991).
- ²⁰⁸Z. Kighelman, D. Damjanovic, and N. Setter, “Electromechanical properties and self-polarization in relaxor $\text{PbMg}_{1/3}\text{Nb}_{2/3}\text{O}_3$ thin films”, [Journal of Applied Physics](#) **89**, 1393–1401 (2000).

Bibliography

- ²⁰⁹J. Kim, H. Takenaka, Y. Qi, A. R. Damodaran, A. Fernandez, R. Gao, M. R. McCarter, S. Saremi, L. Chung, A. M. Rappe, and L. W. Martin, “Epitaxial strain control of relaxor ferroelectric phase evolution”, [Advanced Materials](#) **31**, 1901060 (2019).
- ²¹⁰A. I. Frenkel, D. Ehre, V. Lyahovitskaya, L. Kanner, E. Wachtel, and I. Lubomirsky, “Origin of polarity in amorphous SrTiO₃”, [Physical Review Letters](#) **99**, 215502 (2007).
- ²¹¹K. Wieczorek, A. Ziebiniska, Z. Ujma, K. Szot, M. Górny, I. Franke, J. Koperski, A. Soszyński, and K. Roleder, “Electrostrictive and piezoelectric effect in BaTiO₃ and PbZrO₃”, [Ferroelectrics](#) **336**, 61–67 (2006).
- ²¹²W. P. Mason, “Electrostrictive effect in barium titanate ceramics”, [Physical Review](#) **74**, 1134–1147 (1948).
- ²¹³J. Aufort, O. Aktas, M. A. Carpenter, and E. K. Salje, “Effect of pores and grain size on the elastic and piezoelectric properties of quartz-based materials”, [American Mineralogist](#) **100**, 1165–1171 (2015).
- ²¹⁴P. Ren, J. Wang, Y. Wang, L. K. V., and G. Zhao, “Origin of enhanced depolarization temperature in quenched Na_{0.5}Bi_{0.5}TiO₃-BaTiO₃ ceramics”, [Journal of the European Ceramic Society](#) **40**, 2964–2969 (2020).
- ²¹⁵L. K. V., J. Koruza, and J. Rödel, “Propensity for spontaneous relaxor-ferroelectric transition in quenched (Na_{1/2}Bi_{1/2})TiO₃ compositions”, [Applied Physics Letters](#) **113**, 252902 (2018).
- ²¹⁶A. Dwivedi, C. A. Randall, and G. A. Rossetti, “Thermal history induced variable relaxor behavior in the high T_C ternary ferroelectric 0.6Bi(Mg_{1/2}Ti_{1/2})O₃-0.05Bi(Zn_{1/2}Ti_{1/2})O₃-0.35PbTiO₃”, [Materials Letters](#) **65**, 3034–3036 (2011).
- ²¹⁷F. Chu, I. M. Reaney, and N. Setter, “Spontaneous (zero-field) relaxor-to-ferroelectric-phase transition in disordered Pb(Sc_{1/2}Nb_{1/2})O₃”, [Journal of Applied Physics](#) **77**, 1671–1676 (1995).
- ²¹⁸S. Liu and D. Long, “Pyroelectric detectors and materials”, [Proceedings of the IEEE](#) **66**, 14–26 (1978).
- ²¹⁹G. Xu, P. M. Gehring, and G. Shirane, “Persistence and memory of polar nanoregions in a ferroelectric relaxor under an electric field”, [Physical Review B](#) **72**, 214106 (2005).
- ²²⁰A. A. Bokov and Z.-G. Ye, “Double freezing of dielectric response in relaxor PbMg_{1/3}Nb_{2/3}O₃ crystals”, [Physical Review B](#) **74**, 132102 (2006).
- ²²¹E. V. Colla, E. L. Furman, S. M. Gupta, N. K. Yushin, and D. Viehland, “Dependence of dielectric relaxation on ac drive in [Pb(Mg_{1/3}Nb_{2/3})O₃](1-x)-(PbTiO₃)x single crystals”, [Journal of Applied Physics](#) **85**, 1693–1697 (1999).
- ²²²W. Kleemann, J. Dec, and S. Miga, “The cluster glass route of relaxor ferroelectrics”, [Phase Transitions](#) **88**, 234–244 (2015).
- ²²³V. V. Shvartsman and A. L. Kholkin, “Spontaneous and induced surface piezoresponse in PbMg_{1/3}Nb_{2/3}O₃ single crystals”, [Zeitschrift für Kristallographie](#) **226**, 108–112 (2011).
- ²²⁴S. V. Kalinin, B. J. Rodriguez, J. D. Budai, S. Jesse, A. N. Morozovska, A. A. Bokov, and Z.-G. Ye, “Direct evidence of mesoscopic dynamic heterogeneities at the surfaces of ergodic ferroelectric relaxors”, [Physical Review B](#) **81**, 064107 (2010).

- ²²⁵A. K. Tagantsev and A. E. Glazounov, "Mechanism of polarization response in the ergodic phase of a relaxor ferroelectric", [Physical Review B](#) **57**, 18–21 (1998).
- ²²⁶A. Tagantsev, V. Sherman, K. Astafiev, J. Venkatesh, and N. Setter, "Ferroelectric materials for microwave tunable applications", [Journal of Electroceramics](#) **11**, 5–66 (2003).
- ²²⁷M. Tyunina, J. Levoska, and I. Jaakola, "Polarization relaxation in thin-film relaxors compared to that in ferroelectrics", [Physical Review B](#) **74**, 104112 (2006).
- ²²⁸F. W. Lytle, "X-ray diffractometry of low-temperature phase transformations in strontium titanate", [Journal of Applied Physics](#) **35**, 2212–2215 (1964).
- ²²⁹P. A. Fleury, J. F. Scott, and J. M. Worlock, "Soft phonon modes and the 110°K phase transition in SrTiO₃", [Physical Review Letters](#) **21**, 16–19 (1968).
- ²³⁰C. Stock, M. Songvilay, P. M. Gehring, G. Xu, and B. Roessli, "Broadband critical dynamics in disordered lead-based perovskites", [Journal of Physics: Condensed Matter](#) **32**, 374012 (2020).
- ²³¹R. Wang, Y. Zhu, and S. M. Shapiro, "Electron diffraction studies of phonon and static disorder in SrTiO₃", [Physical Review B](#) **61**, 8814–8822 (2000).
- ²³²M. Holt, M. Sutton, P. Zschack, H. Hong, and T.-C. Chiang, "Dynamic fluctuations and static speckle in critical x-ray scattering from SrTiO₃", [Physical Review Letters](#) **98**, 065501 (2007).
- ²³³B. I. Halperin and C. M. Varma, "Defects and the central peak near structural phase transitions", [Physical Review B](#) **14**, 4030–4044 (1976).
- ²³⁴J. B. Hastings, S. M. Shapiro, and B. C. Frazer, "Central-peak enhancement in hydrogen-reduced SrTiO₃", [Physical Review Letters](#) **40**, 237–239 (1978).
- ²³⁵F. Cordero, A. Franco, V. Calderone, P. Nanni, and V. Buscaglia, "Anelastic spectroscopy for studying O vacancies in perovskites", [Journal of the European Ceramic Society](#) **26**, 2923–2929 (2006).
- ²³⁶R. Palmer, "Broken ergodicity", [Advances in Physics](#) **31**, 669–735 (1982).
- ²³⁷G. Teyssedre, F. Zheng, L. Boudou, and C. Laurent, "Charge trap spectroscopy in polymer dielectrics: a critical review", [Journal of Physics D: Applied Physics](#) **54**, 263001 (2021).
- ²³⁸P. Bräunlich, *Thermally stimulated relaxation in solids*, Topics in Applied Physics 37 (Springer, Berlin Heidelberg New York, 1979).
- ²³⁹J. van Turnhout, *Thermally stimulated discharge of polymer electrets: a study on nonisothermal dielectric relaxation phenomena* (Elsevier Scientific Pub. Co, Amsterdam ; New York, 1974), 335 pp.
- ²⁴⁰A. K. Jonscher, *Dielectric relaxation in solids* (Chelsea Dielectrics Press, London, 1983), 380 pp.
- ²⁴¹T. Hino, "Thermally stimulated characteristics in solid dielectrics", [IEEE Transactions on Electrical Insulation](#) **EI-15**, 301–311 (1980).
- ²⁴²G. F. J. Garlick and A. F. Gibson, "The electron trap mechanism of luminescence in sulphide and silicate phosphors", [Proceedings of the Physical Society](#) **60**, 574–590 (1948).
- ²⁴³C. Bucci and R. Fieschi, "Ionic thermoconductivity. method for the investigation of polarization in insulators", [Physical Review Letters](#) **12**, 16–19 (1964).

Bibliography

- ²⁴⁴C. Bucci, R. Fieschi, and G. Guidi, “Ionic thermocurrents in dielectrics”, [Physical Review](#) **148**, 816–823 (1966).
- ²⁴⁵J. Vanturnhout, “Thermally stimulated discharge of polymer electrets”, [Polymer Journal](#) **2**, 173–191 (1971).
- ²⁴⁶M. L. Williams, R. F. Landel, and J. D. Ferry, “The temperature dependence of relaxation mechanisms in amorphous polymers and other glass-forming liquids”, [Journal of the American Chemical Society](#) **77**, 3701–3707 (1955).
- ²⁴⁷W. Kleemann, “Relaxor ferroelectrics: Cluster glass ground state via random fields and random bonds”, [physica status solidi \(b\)](#) **251**, 1993–2002 (2014).
- ²⁴⁸J. P. Stott and J. H. Crawford, “Dipolar complexes in KCl resulting from 1.5-MeV-electron bombardment”, [Physical Review B](#) **6**, 4660–4667 (1972).
- ²⁴⁹H. Lee, J. R. Kim, M. J. Lanagan, S. Trolier-McKinstry, and C. A. Randall, “High-energy density dielectrics and capacitors for elevated temperatures: $\text{Ca}(\text{Zr,Ti})\text{O}_3$ ”, [Journal of the American Ceramic Society](#) **96**, 1209–1213 (2013).
- ²⁵⁰S. Zhao, S. J. Zhang, W. Liu, N. J. Donnelly, Z. Xu, and C. A. Randall, “Time dependent dc resistance degradation in lead-based perovskites: $0.7\text{Pb}(\text{Mg}_{1/3}\text{Nb}_{2/3})\text{O}_3$ - 0.3PbTiO_3 ”, [Journal of Applied Physics](#) **105**, 053705 (2009).
- ²⁵¹M. Hafid, S. Moudeden, C. Proust, E. Husson, S. Takeoka, S. Nishida, T. Fukami, and J. Sheng, “Dielectric and conduction properties in nickel doped barium strontium titanate ceramics”, [Japanese Journal of Applied Physics](#) **37**, 3370 (1998).
- ²⁵²G. Blaise, “Charge localization and transport in disordered dielectric materials”, [Journal of Electrostatics](#) **50**, 69–89 (2001).
- ²⁵³W. Liu and C. A. Randall, “Thermally stimulated relaxation in Fe-doped SrTiO_3 systems:I. single crystals”, [Journal of the American Ceramic Society](#) **91**, 3245–3250 (2008).
- ²⁵⁴J. G. Simmons and G. W. Taylor, “High-field isothermal currents and thermally stimulated currents in insulators having discrete trapping levels”, [Physical Review B](#) **5**, 1619–1629 (1972).
- ²⁵⁵G. S. Nadkarni and J. G. Simmons, “Determination of the defect nature of MoO_3 films using dielectric-relaxation currents”, [Journal of Applied Physics](#) **43**, 3650 (2003).
- ²⁵⁶S. W. S. McKeever and D. M. Hughes, “Thermally stimulated currents in dielectrics”, [Journal of Physics D: Applied Physics](#) **8**, 1520–1529 (1975).
- ²⁵⁷T. Fukami, M. Kusunoki, and H. Tsucniya, “TSC study on Fe-doped barium-strontium titanate ceramics”, [Japanese Journal of Applied Physics](#) **26**, 46 (1987).
- ²⁵⁸X. Zhao, J. Wang, Z. Peng, K. .-H. Chew, H. L. W. Chan, C. L. Choy, and H. Luo, “Electric field effect on polarization and depolarization behavior of the $\langle 001 \rangle$ -oriented relaxor-based $0.7\text{Pb}(\text{Mg}_{1/3}\text{Nb}_{2/3})\text{O}_3$ - 0.3PbTiO_3 single crystal”, [Physica B: Condensed Matter](#) **339**, 68–73 (2003).
- ²⁵⁹J. J. Carter, T. J. M. Bayer, and C. A. Randall, “Degradation and recovery of iron doped barium titanate single crystals via modulus spectroscopy and thermally stimulated depolarization current”, [Journal of Applied Physics](#) **121**, 145106 (2017).

- ²⁶⁰S. B. Vakhrushev, R. G. Burkovsky, S. Shapiro, and A. Ivanov, “Two-mode behavior of the $\text{PbMg}_{1/3}\text{Nb}_{2/3}\text{O}_3$ relaxor”, *Physics of the Solid State* **52**, 889–893 (2010).
- ²⁶¹C. Lynch, “The effect of uniaxial stress on the electro-mechanical response of 8/65/35 PLZT”, *Acta Materialia* **44**, 4137–4148 (1996).
- ²⁶²T. Sumigawa, K. Hikasa, A. Kusunose, H. Unno, K. Masuda, T. Shimada, and T. Kitamura, “*In Situ* TEM observation of nanodomain mechanics in barium titanate under external loads”, *Physical Review Materials* **4**, 054415 (2020).
- ²⁶³M. N. Shetty, V. C. S. Prasad, and E. C. Subbarao, “90° domain-wall motion in barium titanate under uniaxial compression”, *Physical Review B* **10**, 4801–4802 (1974).
- ²⁶⁴S. Zhang, S. Taylor, F. Li, J. Luo, and R. J. Meyer, “Piezoelectric property of relaxor- PbTiO_3 crystals under uniaxial transverse stress”, *Applied Physics Letters* **102**, 172902 (2013).
- ²⁶⁵H. Lu, C.-W. Bark, D. Esque de los Ojos, J. Alcala, C. B. Eom, G. Catalan, and A. Gruverman, “Mechanical writing of ferroelectric polarization”, *Science* **336**, 59–61 (2012).
- ²⁶⁶J. Narvaez and G. Catalan, “Origin of the enhanced flexoelectricity of relaxor ferroelectrics”, *Applied Physics Letters* **104**, 162903 (2014).
- ²⁶⁷E. A. McLaughlin, T. Liu, and C. S. Lynch, “Relaxor ferroelectric PMN-32PT crystals under stress, electric field and temperature loading: II-33-mode measurements”, *Acta Materialia* **53**, 4001–4008 (2005).
- ²⁶⁸M. A. Carpenter, J. F. J. Bryson, G. Catalan, S. J. Zhang, and N. J. Donnelly, “Elastic and anelastic relaxations in the relaxor ferroelectric $\text{Pb}(\text{Mg}_{1/3}\text{Nb}_{2/3})\text{O}_3$: II. strain-order parameter coupling and dynamic softening mechanisms”, *Journal of Physics: Condensed Matter* **24**, 045902 (2011).
- ²⁶⁹B. Chaabane, J. Kreisel, B. Dkhil, P. Bouvier, and M. Mezouar, “Pressure-induced suppression of the diffuse scattering in the model relaxor ferroelectric $\text{PbMg}_{1/3}\text{Nb}_{2/3}\text{O}_3$ ”, *Physical Review Letters* **90**, 257601 (2003).
- ²⁷⁰M. Ahart, M. Somayazulu, Z.-G. Ye, R. E. Cohen, H.-k. Mao, and R. J. Hemley, “High-pressure Brillouin scattering of $\text{Pb}(\text{Mg}_{1/3}\text{Nb}_{2/3})\text{O}_3$ ”, *Physical Review B* **79**, 132103 (2009).
- ²⁷¹S.-H. Yoon, J.-B. Lim, S.-H. Kim, and D.-Y. Kim, “Influence of Dy on the dielectric aging and thermally stimulated depolarization current in Dy and Mn-codoped BaTiO_3 multilayer ceramic capacitor”, *Journal of Materials Research* **28**, 3252–3256 (2013).
- ²⁷²X. Song, T. Zhang, Y. Zhang, K. Hu, Z. Zhao, and I. Baturin, “Impedance spectroscopy and thermally simulated depolarization current study of barium strontium titanate glass ceramics: Effect of thermal annealing atmosphere on dielectric property”, *Ceramics International* **44**, 5668–5672 (2018).
- ²⁷³B. Akkopru-Akgun, T. J. M., K. Tsuji, K. Wang, C. A. Randall, M. T. Lanagan, and S. Trolier-McKinstry, “Leakage current characteristics and DC resistance degradation mechanisms in Nb doped PZT films”, *Journal of Applied Physics* **129**, 174102 (2021).
- ²⁷⁴W. Wu, Z. Liu, Y. Gu, Z. Yue, and Y. Li, “Thermally stimulated depolarization current study on barium titanate single crystals”, *AIP Advances* **8**, 045005 (2018).

- ²⁷⁵J. A. Bock, S. Trolier-McKinstry, G. D. Mahan, and C. A. Randall, "Polarization-based perturbations to thermopower and electronic conductivity in highly conductive tungsten bronze structured (Sr, Ba)Nb₂O₆: Relaxors vs normal ferroelectrics", [Physical Review B](#) **90**, 115106 (2014).
- ²⁷⁶J. Handerek, Z. Ujma, C. Carabatos-Nédelec, G. E. Kugel, D. Dmytrow, and I. El-Harrad, "Dielectric, pyroelectric, and thermally stimulated depolarization current investigations on lead-lanthanum zirconate-titanate-x/95/5 ceramics with La content x=0.5%–4%", [Journal of Applied Physics](#) **73**, 367–373 (1993).
- ²⁷⁷D. I. Woodward, I. M. Reaney, G. Y. Yang, E. C. Dickey, and C. A. Randall, "Vacancy ordering in reduced barium titanate", [Applied Physics Letters](#) **84**, 4650–4652 (2004).
- ²⁷⁸J. Carrasco, F. Illas, N. Lopez, E. A. Kotomin, Y. F. Zhukovskii, R. A. Evarestov, Y. A. Mastrikov, S. Piskunov, and J. Maier, "First-principles calculations of the atomic and electronic structure of *F* centers in the bulk and on the (001) surface of SrTiO₃", [Physical Review B](#) **73**, 064106 (2006).
- ²⁷⁹A. J. Bell, P. M. Shepley, and Y. Li, "Domain wall contributions to piezoelectricity in relaxor-lead titanate single crystals", [Acta Materialia](#) **195**, 292–303 (2020).
- ²⁸⁰F. Bai, N. Wang, J. Li, D. Viehland, P. M. Gehring, G. Xu, and G. Shirane, "X-ray and neutron diffraction investigations of the structural phase transformation sequence under electric field in 0.7Pb(Mg_{1/3}Nb_{2/3})-0.3PbTiO₃ crystal", [Journal of Applied Physics](#) **96**, 1620–1627 (2004).
- ²⁸¹E. W. Sun and W. W. Cao, "Relaxor-based ferroelectric single crystals: growth, domain engineering, characterization and applications", [Prog. Mater. Sci.](#) **65**, 124–210 (2014).
- ²⁸²J. Xiong, Z. Wang, X. Yang, R. Su, X. Long, and C. He, "Impact of thickness and poling condition on dielectric and piezoelectric properties of Pb(In_{0.5}Nb_{0.5})O₃-PbTiO₃ Ferroelectric Crystals", [physica status solidi \(b\)](#), 2100287.
- ²⁸³S. Wada, K. Muraoka, H. Kakemoto, T. Tsurumi, and H. Kumagai, "Enhanced piezoelectric properties of potassium niobate single crystals by domain engineering", [Japanese Journal of Applied Physics](#) **43**, 6692 (2004).
- ²⁸⁴S. Wada, S. Suzuki, T. Noma, T. Suzuki, M. Osada, M. Kakihana, S.-E. Park, L. E. Cross, and T. R. Shrout, "Enhanced piezoelectric property of barium titanate single crystals with engineered domain configurations", [Japanese Journal of Applied Physics](#) **38**, 5505–5511 (1999).
- ²⁸⁵H. Wan, C. Luo, W.-Y. Chang, Y. Yamashita, and X. Jiang, "Effect of poling temperature on piezoelectric and dielectric properties of 0.7Pb(Mg_{1/3}Nb_{2/3})O₃-0.3PbTiO₃ single crystals under alternating current poling", [Applied Physics Letters](#) **114**, 172901 (2019).
- ²⁸⁶C. Qiu, J. Liu, F. Li, and Z. Xu, "Thickness dependence of dielectric and piezoelectric properties for alternating current electric-field-poled relaxor-PbTiO₃ crystals", [Journal of Applied Physics](#) **125**, 014102 (2019).
- ²⁸⁷C. Qiu, Z. Xu, Z. An, J. Liu, G. Zhang, S. Zhang, L.-Q. Chen, N. Zhang, and F. Li, "In-situ domain structure characterization of Pb(Mg_{1/3}Nb_{2/3})O₃-PbTiO₃ crystals under alternating current electric field poling", [Acta Materialia](#) **210**, 116853 (2021).

- ²⁸⁸H. Wan, C. Luo, C. Liu, W.-Y. Chang, Y. Yamashita, and X. Jiang, "Alternating current poling on sliver-mode rhombohedral $\text{Pb}(\text{Mg}_{1/3}\text{Nb}_{2/3})\text{O}_3$ – PbTiO_3 single crystals", *Acta Materialia* **208**, 116759 (2021).
- ²⁸⁹H. Wan, C. Luo, C.-C. Chung, Y. Yamashita, and X. Jiang, "Enhanced dielectric and piezoelectric properties of manganese-doped $\text{Pb}(\text{In}_{1/2}\text{Nb}_{1/2})\text{O}_3$ – $\text{Pb}(\text{Mg}_{1/3}\text{Nb}_{2/3})\text{O}_3$ – PbTiO_3 single crystals by alternating current poling", *Applied Physics Letters* **118**, 102904 (2021).
- ²⁹⁰M. Ma, S. Xia, K. Song, H. Guo, Z. Xu, and Z. Li, "Temperature dependence of the transverse piezoelectric properties in the [001]-poled $0.25\text{Pb}(\text{In}_{1/2}\text{Nb}_{1/2})\text{O}_3$ – $0.42\text{Pb}(\text{Mg}_{1/3}\text{Nb}_{2/3})\text{O}_3$ – 0.33PbTiO_3 single crystal with alternating current treatment", *Journal of Applied Physics* **129**, 114102 (2021).
- ²⁹¹W. A. Schulze and K. Ogino, "Review of literature on aging of dielectrics", *Ferroelectrics* **87**, 361–377 (1988).
- ²⁹²Y. A. Genenko, J. Glaum, M. J. Hoffmann, and K. Albe, "Mechanisms of aging and fatigue in ferroelectrics", *Materials Science and Engineering: B, Electrical Fatigue* **192**, 52–82 (2015).
- ²⁹³G. H. Jonker, "Nature of Aging in Ferroelectric Ceramics", *Journal of the American Ceramic Society* **55**, 57–58 (1972).
- ²⁹⁴P. V. Lambeck and G. H. Jonker, "The nature of domain stabilization in ferroelectric perovskites", *Journal of Physics and Chemistry of Solids* **47**, 453–461 (1986).
- ²⁹⁵L. X. Zhang and X. Ren, "*In Situ* observation of reversible domain switching in aged Mn-doped BaTiO_3 single crystals", *Physical Review B* **71**, 174108 (2005).
- ²⁹⁶N. Luo, S. Zhang, Q. Li, Q. Yan, Y. Zhang, T. Ansell, J. Luo, and T. R. Shrout, "Crystallographic dependence of internal bias in domain engineered Mn-doped relaxor- PbTiO_3 single crystals", *Journal of Materials Chemistry C* **4**, 4568–4576 (2016).
- ²⁹⁷R.-A. Eichel, "Structural and dynamic properties of oxygen vacancies in perovskite oxides - analysis of defect chemistry by modern multi-frequency and pulsed EPR techniques", *Phys. Chem. Chem. Phys.* **13**, 368–384 (2011).
- ²⁹⁸U. Robels and G. Arlt, "Domain wall clamping in ferroelectrics by orientation of defects", *Journal of Applied Physics* **73**, 3454–3460 (1993).
- ²⁹⁹X. Liu, B. Fang, Z. Chen, J. Ding, X. Zhao, H. Xu, and H. Luo, "Aging behavior and mechanical properties of $0.69\text{Pb}(\text{Mg}_{1/3}\text{Nb}_{2/3})\text{O}_3$ – 0.31PbTiO_3 ceramics", *Ferroelectrics* **467**, 115–125 (2014).
- ³⁰⁰W. Y. Pan, T. R. Shrout, and L. E. Cross, "Modelling the ageing phenomena in 0.9PMN – 0.1PT relaxor ferroelectric ceramics", *Journal of Materials Science Letters* **8**, 771–776 (1989).
- ³⁰¹X. Liu, D. Wu, B. Fang, J. Ding, X. Li, X. Zhao, H. Luo, J.-H. Ko, and C. W. Ahn, "Aging characteristics of $0.7\text{Pb}(\text{Mg}_{1/3}\text{Nb}_{2/3})\text{O}_3$ – 0.3PbTiO_3 single crystals with different crystal orientations", *Applied Physics A* **119**, 1469–1476 (2015).
- ³⁰²W. Pan, E. Furman, G. O. Dayton, and L. E. Cross, "Dielectric ageing effects in doped lead magnesium niobate: Lead titanate relaxor ferroelectric ceramics", *Journal of Materials Science Letters* **5**, 647–649 (1986).

Bibliography

- ³⁰³R. Zhu, X. Li, Z. Fu, J. Chen, H. Xu, and H. Luo, "Investigations of defects in $\text{Pb}(\text{Mg}_{1/3}\text{Nb}_{2/3})\text{O}_3$ - PbTiO_3 single crystals grown along [001] direction", *Ceramics International* **45**, 13354–13361 (2019).
- ³⁰⁴X. Wu, L. Liu, X. Li, X. Zhao, D. Lin, H. Luo, and Y. Huang, "The influence of defects on ferroelectric and pyroelectric properties of $\text{Pb}(\text{Mg}_{1/3}\text{Nb}_{2/3})\text{O}_3$ –0.28 PbTiO_3 single crystals", *Materials Chemistry and Physics* **132**, 87–90 (2012).
- ³⁰⁵E. V. Colla, N. K. Yushin, and D. Viehland, "Dielectric properties of $(\text{PMN})_{(1-x)}(\text{PT})_x$ single crystals for various electrical and thermal histories", *Journal of Applied Physics* **83**, 3298–3304 (1998).
- ³⁰⁶D. Phelan, E. E. Rodriguez, J. Gao, Y. Bing, Z.-G. Ye, Q. Huang, J. Wen, G. Xu, C. Stock, M. Matsuura, and P. M. Gehring, "Phase diagram of the relaxor ferroelectric $(1-x)\text{Pb}(\text{Mg}_{1/3}\text{Nb}_{2/3})\text{O}_3+x\text{PbTiO}_3$ revisited: a neutron powder diffraction study of the relaxor skin effect", *Phase Transitions* **88**, 283–305 (2015).
- ³⁰⁷F. Li, S. Zhang, Z. Xu, X. Wei, J. Luo, and T. R. Shrout, "Composition and phase dependence of the intrinsic and extrinsic piezoelectric activity of domain engineered $(1-x)\text{Pb}(\text{Mg}_{1/3}\text{Nb}_{2/3})\text{O}_3$ – $x\text{PbTiO}_3$ crystals", *Journal of Applied Physics* **108**, 034106 (2010).
- ³⁰⁸Y. Gao, K. Uchino, and D. Viehland, "Time dependence of the mechanical quality factor in "hard" lead zirconate titanate ceramics: Development of an internal dipolar field and high power origin", *Japanese Journal of Applied Physics* **45**, 9119–9124 (2006).
- ³⁰⁹Z. Zhang, J. Xu, L. Yang, S. Liu, J. Xiao, R. Zhu, X. Li, X. Wang, and H. Luo, "The performance enhancement and temperature dependence of piezoelectric properties for $0.7\text{Pb}(\text{Mg}_{1/3}\text{Nb}_{2/3})\text{O}_3$ – 0.30PbTiO_3 single crystal by alternating current polarization", *Journal of Applied Physics* **125**, 034104 (2019).
- ³¹⁰P. Chandra and P. B. Littlewood, "A Landau Primer for ferroelectrics", in *Physics of ferroelectrics: A modern perspective*, Topics in Applied Physics (Springer Berlin Heidelberg, Berlin, Heidelberg, 2007), pp. 69–116.
- ³¹¹J. Ma, K. Zhu, D. Huo, X. Qi, E. Sun, and R. Zhang, "Performance enhancement of the piezoelectric ceramics by alternating current polarizing", *Applied Physics Letters* **118**, 022901 (2021).
- ³¹²C. Luo, H. Wan, W.-Y. Chang, Y. Yamashita, A. R. Paterson, J. Jones, and X. Jiang, "Effect of low-frequency alternating current poling on 5-mm-thick $0.7\text{Pb}(\text{Mg}_{1/3}\text{Nb}_{2/3})\text{O}_3$ – 0.3PbTiO_3 single crystals", *Applied Physics Letters* **115**, 192904 (2019).
- ³¹³L. X. Zhang, W. Chen, and X. Ren, "Large recoverable electrostrain in Mn-doped $(\text{Ba},\text{Sr})\text{TiO}_3$ ceramics", *Applied Physics Letters* **85**, 5658–5660 (2004).
- ³¹⁴Z. Chen, Y. Zhang, S. Li, X.-M. Lu, and W. Cao, "Frequency dependence of the coercive field of $0.71\text{Pb}(\text{Mg}_{1/3}\text{Nb}_{2/3})\text{O}_3$ – 0.29PbTiO_3 single crystal from 0.01 Hz to 5 MHz", *Applied Physics Letters* **110**, 202904 (2017).
- ³¹⁵C. Deng, L. Ye, C. He, G. Xu, Q. Zhai, H. Luo, Y. Liu, and A. J. Bell, "Reporting excellent transverse piezoelectric and electro-optic effects in transparent rhombohedral PMN-PT single crystal by engineered domains", *Advanced Materials* **33**, 2103013 (2021).

- ³¹⁶D. Morikawa and K. Tsuda, “Electric-field response of polar nanodomains in BaTiO₃”, [Applied Physics Letters](#) **119**, 052904 (2021).
- ³¹⁷G. Xu, J. Wen, C. Stock, and P. M. Gehring, “Phase instability induced by polar nanoregions in a relaxor ferroelectric system”, [Nature Materials](#) **7**, 562–566 (2008).
- ³¹⁸F. Cordero, “Anelastic (dielectric) relaxation of point defects at any concentration, with blocking effects and formation of complexes”, [Physical Review B](#) **47**, 7674–7685 (1993).
- ³¹⁹P. Jakes, E. Erdem, R.-A. Eichel, L. Jin, and D. Damjanovic, “Position of defects with respect to domain walls in Fe³⁺-doped Pb[Zr_{0.52}Ti_{0.48}]O₃ piezoelectric ceramics”, [Applied Physics Letters](#) **98**, 072907 (2011).
- ³²⁰E. Erdem, R.-A. Eichel, H. Kungl, M. J. Hoffmann, A. Ozarowski, H. van Tol, and L. Claude Brunel, “Local symmetry-reduction in tetragonal (La, Fe)-codoped Pb[Zr_{0.4}Ti_{0.6}]O₃ piezoelectric ceramics”, [Physica Scripta](#) **T129**, 12–16 (2007).
- ³²¹X. Ren, “Large electric-field-induced strain in ferroelectric crystals by point-defect-mediated reversible domain switching”, [Nature Materials](#) **3**, 91–94 (2004).
- ³²²C. Stock, P. M. Gehring, H. Hiraka, I. Swainson, G. Xu, Z.-G. Ye, H. Luo, J.-F. Li, and D. Viehland, “Evidence for anisotropic polar nanoregions in relaxor Pb(Mg_{1/3}Nb_{2/3})O₃: A neutron study of the elastic constants and anomalous TA phonon damping in PMN”, [Physical Review B](#) **86**, 104108 (2012).
- ³²³A. Naberezhnov, S. Vakhrushev, B. Dorner, D. Strauch, and H. Moudden, “Inelastic neutron scattering study of the relaxor ferroelectric Pb(Mg_{1/3}Nb_{2/3})O₃ at high temperatures”, [The European Physical Journal B - Condensed Matter and Complex Systems](#) **11**, 13–20 (1999).
- ³²⁴P. M. Gehring, S. Wakimoto, Z.-G. Ye, and G. Shirane, “Soft mode dynamics above and below the Burns temperature in the relaxor Pb(Mg_{1/3}Nb_{2/3})O₃”, [Physical Review Letters](#) **87**, 277601 (2001).
- ³²⁵M. E. Lines and A. M. Glass, *Principles and applications of ferroelectrics and related materials* (Oxford University Press, Oxford, New York, 2001).
- ³²⁶C.-S. Tu, V. H. Schmidt, and I. G. Siny, “Hypersound anomalies and elastic constants in single-crystal PbMg_{1/3}Nb_{2/3}O₃ by Brillouin scattering”, [Journal of Applied Physics](#) **78**, 5665–5668 (1995).
- ³²⁷S. G. Lushnikov, A. I. Fedoseev, S. N. Gvasaliya, and S. Kojima, “Anomalous dispersion of the elastic constants at the phase transformation of the PbMg_{1/3}Nb_{2/3}O₃ relaxor ferroelectric”, [Physical Review B](#) **77**, 104122 (2008).
- ³²⁸A. K. Tagantsev, “Piezoelectricity and flexoelectricity in crystalline dielectrics”, [Physical Review B](#) **34**, 5883–5889 (1986).
- ³²⁹L. Cross, “Flexoelectric effects: Charge separation in insulating solids subjected to elastic strain gradients”, [Journal of Materials Science](#) **41**, 53–63 (2006).
- ³³⁰P. Hana, M. Marvan, L. Burianova, S. J. Zhang, E. Furman, and T. R. Shrout, “Study of the inverse flexoelectric phenomena in ceramic lead magnesium niobate-lead titanate”, [Ferroelectrics](#) **336**, 137–144 (2006).

Bibliography

- ³³¹B. Wang, Y. Gu, S. Zhang, and L.-Q. Chen, “Flexoelectricity in solids: Progress, challenges, and perspectives”, [Progress in Materials Science](#) **106**, 100570 (2019).

Curriculum Vitae

Lukas Max Riemer

[linkedin.com/in/lukas-riemer](https://www.linkedin.com/in/lukas-riemer)

Personal information

Date of birth: 5th November 1987
Place of birth: Korneuburg, Austria
Nationality: Austrian

Education

- 2022 Ecole Polytechnique Federale de Lausanne (EPFL)
 Doctoral Assistant in Materials Science and Materials Engineering
 Group for Ferroelectrics and Functional Oxides, Prof. Dragan Damjanovic
- 2016 Technical University of Darmstadt (TUD)
 Master of Science in Materials Science and Engineering
 Group for Nonmetallic-Inorganic Materials (NAW), Prof. Jürgen Rödel
- 2014 Technical University of Darmstadt (TUD)
 Bachelor of Science in Materials Science and Engineering
 State Materials Testing Institute Darmstadt (MPA), Prof. Matthias Oechsner

Publications

1. D.-S. Park, M. Hadad, [L.M. Riemer](#), R. Ignatans, D. Spirito, V. Esposito, V. Tileli, N. Gauquelin, D. Chezganov, D. Jannis, J. Verbeeck, S. Gorfman, Pryds, N. P. Muralt, and D. Damjanovic, “Induced giant piezoelectricity in centrosymmetric oxides”, *Science* **accepted** (2021)
2. M. Höfling, X. Zhou, [L.M. Riemer](#), E. Bruder, B. Liu, L. Zhou, P. B. Groszewicz, F. Zhuo, B.-X. Xu, K. Durst, X. Tan, D. Damjanovic, J. Koruza, and J. Rödel, “Control of polarization in bulk ferroelectrics by mechanical dislocation imprint”, *Science* **372**, 961–964 (2021)
3. [L.M. Riemer](#), L. Jin, H. Uršič, M. Otoničar, T. Rojac, and D. Damjanovic, “Dielectric and electro-mechanic nonlinearities in perovskite oxide ferroelectrics, relaxors, and relaxor ferroelectrics”, *Journal of Applied Physics* **129**, 054101 (2021)

4. L.M. Riemer, K. Chu, Y. Li, H. Uršič, A. J. Bell, B. Dkhil, and D. Damjanovic, “Macroscopic polarization in the nominally ergodic relaxor state of lead magnesium niobate”, [Applied Physics Letters](#) **117**, 102901 (2020)
5. M. Otoničar, A. Bradeško, L. Fulanović, T. Kos, H. Uršič, A. Benčan, M. J. Cabral, A. Henriques, J. L. Jones, L.M. Riemer, D. Damjanovic, G. Dražić, B. Malič, and T. Rojac, “Connecting the multiscale structure with macroscopic response of relaxor ferroelectrics”, [Advanced Functional Materials](#), 2006823 (2020)
6. X. Meng, C. Hu, D.-S. Park, L.M. Riemer, K. Chu, Z. Zhou, D. Damjanovic, and H. Tian, “Ultra-high piezoresponse in tantalum doped potassium sodium niobate single crystal”, [Applied Physics Letters](#) **116**, 112902 (2020)
7. C. S. Sandu, F. Parsapour, D. Xiao, R. Nigon, L.M. Riemer, T. LaGrange, and P. Muralt, “Impact of negative bias on the piezoelectric properties through the incidence of abnormal oriented grains in $\text{Al}_{0.62}\text{Sc}_{0.38}\text{N}$ thin films”, [Thin Solid Films](#) **697**, 137819 (2020)
8. L.M. Riemer, K. V. Lalitha, X. Jiang, N. Liu, C. Dietz, R. W. Stark, P. B. Groszewicz, G. Buntkowsky, J. Chen, S.-T. Zhang, J. Rödel, and J. Koruza, “Stress-induced phase transition in lead-free relaxor ferroelectric composites”, [Acta Materialia](#) **136**, 271–280 (2017)
9. K. V. Lalitha, L.M. Riemer, J. Koruza, and J. Rödel, “Hardening of electromechanical properties in piezoceramics using a composite approach”, [Applied Physics Letters](#) **111**, 022905 (2017)